A Detailed Study of the Pulsar Wind Nebula MSH 15−52 in X-rays and TeV γ-rays

Detaillierte Analyse der Röntgen- und
TeV-Gammastrahlung des Pulsarwindnebels
MSH 15−52

Der Naturwissenschaftlichen Fakultät
der Friedrich-Alexander-Universität Erlangen-Nürnberg
zur Erlangung des Doktorgrades Dr. rer. nat.

vorgelegt von
Fabian Matthias Schöck
aus Dachau

Als Dissertation genehmigt von der Naturwissenschaftlichen Fakultät der Friedrich-Alexander-Universität Erlangen-Nürnberg

Tag der mündlichen Prüfung: 26. Oktober 2010

Vorsitzender der Promotionkommission:	Prof. Dr. Rainer Fink
Erstberichterstatter:	Prof. Dr. Christian Stegmann
Zweitberichterstatter:	Prof. Dr. Jörn Wilms

Kurzfassung

In der vorliegenden Dissertation wird eine detaillierte Studie der Röntgen- und TeV-Gammastrahlung des Pulsarwindnebels MSH 15−52 vorgestellt. Im Rahmen der Arbeit wird die erste Analyse der Beobachtungen von MSH 15−52 mit dem *XMM-Newton* Röntgensatelliten präsentiert. Mit der Analyse der H. E. S. S. Beobachtungen von MSH 15−52 wird die präziseste Vermessungen des Pulsarwindnebels im Energiebereich der hochenergetischen Gammastrahlung vorgestellt. Anhand eines theoretischen Models werden schließlich die physikalischen Grundlagen des Ursprungs der beobachteten nichtthermischen Emission untersucht. Die räumliche Änderung der Energiespektren, die im Röntgenbereich mit *XMM-Newton* gemessen wird, kann durch das Model erklärt werden. Das Spektrum der hochenergetischen Gammastrahlung wird durch das Model mit den an den Röntgendaten optimierten Parametern nicht exakt reproduziert, der berechnete Fluss liegt jedoch in der Größenordnung des mit H. E. S. S. gemessenen Flusses. Die Ergebnisse der Modelierung sind ein zusätzlicher Indikator dafür, dass die mit *XMM-Newton* und H. E. S. S. gemessene Strahlung dadurch erklärt werden kann, dass Leptonen im Pulsarwindnebel Synchrotronstrahlung erzeugen, und mittels des inversen Compton-Effekts Photonen aus niederenergetischen Strahlungsfeldern auf Energien im TeV-Bereich beschleunigen.

Abstract

In the present thesis a detailed study of the pulsar wind nebula MSH 15−52 in X-rays and TeV γ-rays is introduced. This study encompasses the first analysis of observations of the *XMM-Newton* satellite on MSH 15−52 in the X-ray energy range. In the VHE γ-ray range, the most sensitive analysis of MSH 15−52 so far is carried out using data from the H. E. S. S. experiment. Finally, a leptonic model of the PWN is constructed to investigate the physics of the particles in the PWN. The results from the X-ray analysis are used to constrain the parameters of our model. It shows, that the model is able to reproduce the spatial evolution of the spectral characteristics observed in the analysis of the *XMM-Newton* data. Using the model parameters that were optimized on the X-ray results, the prediction of our model for the TeV emission from inverse Compton interaction with target photon fields is calculated. The model does not exactly reproduce the observed H. E. S. S. spectrum, although the predicted flux is in the same order of magnitude. The model supports the scenario that the X-ray and TeV γ-ray emission observed from the pulsar wind nebula MSH 15−52 is mainly due to leptons interacting with the magnetic field and target photon fields.

Contents

Introduction

The look at the bright stars in the dark night sky has always fascinated humankind. The distant phenomena evoke the most fundamental questions and leave us wondering about the origin of the light from above. The picture became even more complex at the end of the 19th century, when it was found out, that the visible light is but one small part of the broad spectrum of electromagnetic radiation. Since then, scientists have studied the spectral composition of the light from stars and other astronomical objects. However, it was not before 1933 that Karl Jansky discovered cosmic radio emission and laid the foundation for the field of radio astronomy (Jansky 1933). It took even longer to get a first glimpse of the light at further wavelengths, because an observation of this radiation is not easily possible from the ground. The Earth's atmosphere is opaque to most parts of the spectrum of electromagnetic radiation. This is illustrated in Fig. 0.1, where the opacity of the atmosphere is plotted against the wavelength of the radiation. A direct measurement of photons with ground-based instruments is only possible in three distinct wavelength ranges, the so-called optical, infrared and radio windows. For all other wave bands, the light is absorbed in the atmosphere and does not reach the ground.

Electromagnetic radiation with a wavelength of less than about 100 nm (which corresponds to an energy in the order of a few electron volt) can only be detected with instruments outside the influence of the atmosphere. Therefore, astronomy in this energy range was not possible until the beginning of the space age after the Second World War. First measurements of X-ray photons (with energies in the order of a few keV) were conducted with rocket- and balloon-borne experiments in the 1960s. With the beginning of satellite-based X-ray astronomy, the number of known sources quickly rose to more than 100 and has increased rapidly ever since, breaking the barrier of $1,000,000$ X-ray sources possibly this year (Drake 2007). With the modern generation of X-ray satellites it is possible to measure the spatial and spectral properties of astrophysical sources with great detail.

The upper energy bound for spaceborne measurements is set by the decreasing photon flux, since the detection area of satellite experiments is limited. Recently, the *Fermi* Gamma-ray Space Telescope was launched and now extends the energy range for the satellite-borne detection of photons to energies around 300 GeV. *Fermi* has successfully completed its first year of operations and has detected $1,451$ sources in eleven months

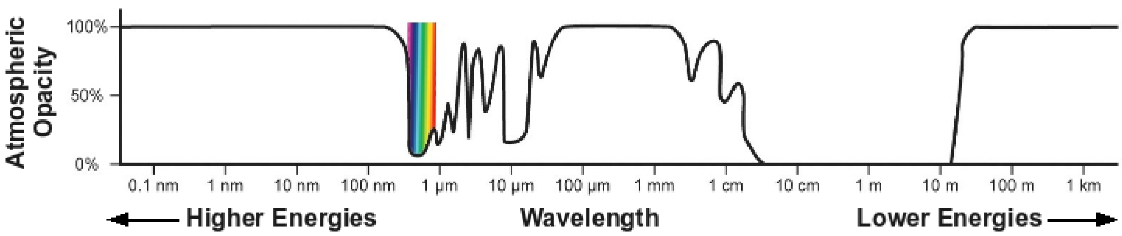

Fig. 0.1: *Plot of the opacity of Earth's atmosphere for different wavelength of electromagnetic radiation (Image courtesy: NASA/JPL).*

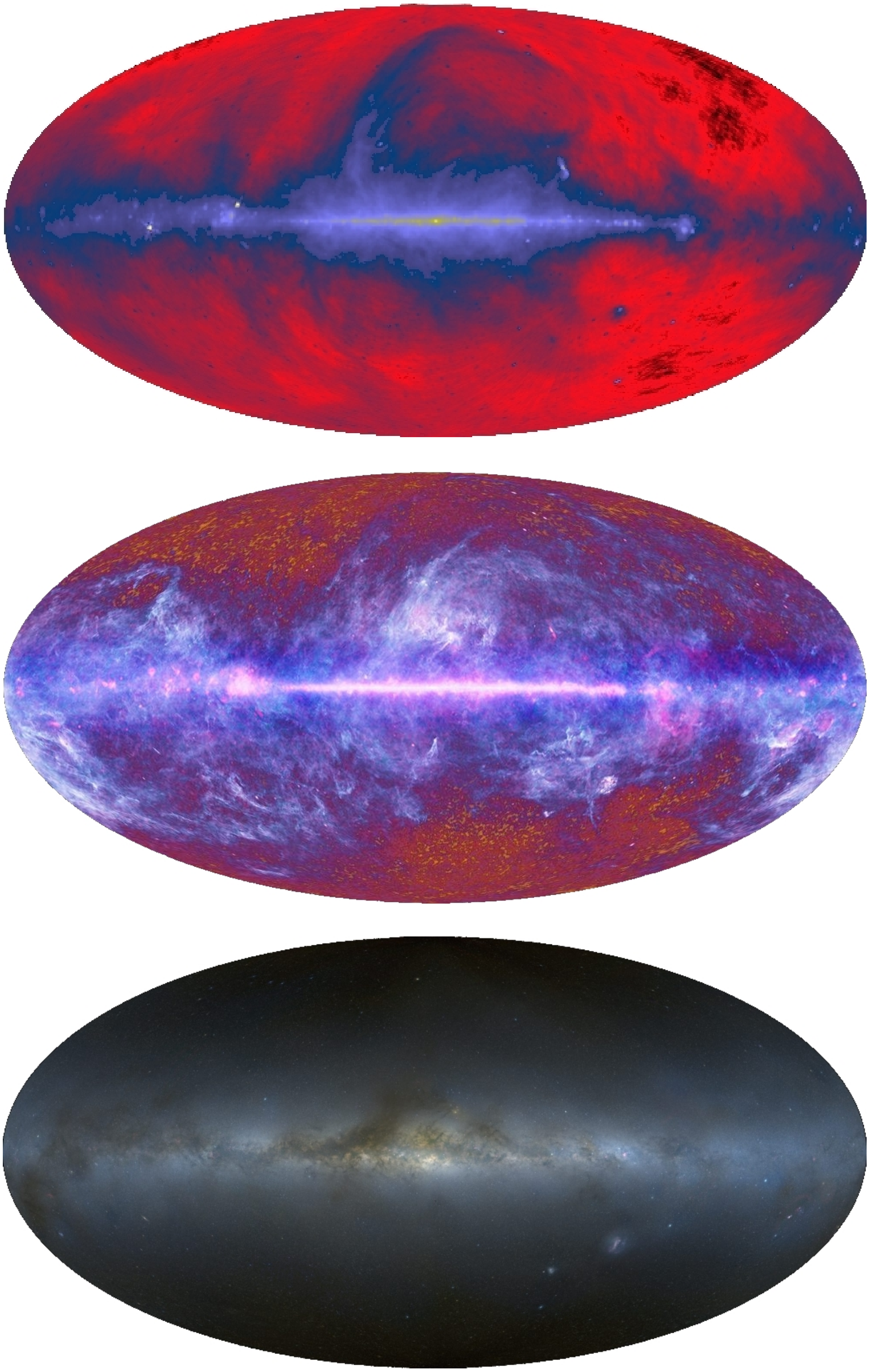

Fig. 0.2: *Top: False-color image of the sky at 408 MHz, composed from the data of several radio telescopes. Middle: First survey result of the Planck satellite in the range from 30 to 857 GHz. Bottom: All-sky panorama in optical light, composed from more than 3,000 individual images. (Credits: Top: Haslam et al. (1982), MPIfR, SkyView; Middle: ESA, Planck HFI & LFI Consortia; Bottom: Axel Mellinger, Central Michigan University)*

of data taking (Abdo et al. 2010a). For photon energies beyond the scope of satellite experiments, it is again possible to detect photons with ground-based instruments, making use of indirect measurement methods. A very successful approach for energies in the GeV to TeV range is the imaging air Cherenkov technique (IACT) utilized by H. E. S. S. and other experiments. In this technique, the Cherenkov radiation of particle cascades in the atmosphere is measured. These air showers are generated when very high-energy (VHE, $100\,\mathrm{GeV} \lesssim E \lesssim 100\,\mathrm{TeV}$) γ-rays are absorbed by the Earth's atmosphere. Calculating back from the measured Cherenkov radiation, it is possible to obtain information about the origin and the energy of the primary VHE γ-ray photons. Since the first detection of cosmic TeV photons from the Crab Nebula (Weekes et al. 1989), the number of sources has increased significantly. At present, 108 sources of VHE γ-rays have been detected (Wakely & Horan 2010).

The range of wavelengths, for which astronomical measurements are possible with the different detection methods described above, currently extends over more than 20 orders of magnitude, from wavelengths as small as 10^{-20} m to radio waves with more than 10 m. Many different physical processes are responsible for the emission observed in the different wave bands and therefore the appearance of the night sky changes accordingly. This is illustrated in Figs. 0.2 and 0.3, which show the view of the whole sky observed with different instruments in a Galactic coordinate system. The top panel of Fig. 0.2 displays the radio emission observed at a frequency of 408 MHz. In the center of the sky map is the Galactic Center, visible as a bright spot of radio emission. The Galactic Plane extends to the left and the right of the Galactic Center. The diffuse radio emission along the Plane is synchrotron radiation, emitted by electrons that spiral along the Galactic magnetic field. In the middle panel, the all-sky view of the first survey of the Planck satellite, which observes photons with microwave energies, is shown. The bright emission along the Galactic Plane arises from the interstellar medium in the Galaxy. At high latitudes, in the top and the bottom of the sky map, the Galactic emission is less bright and the structure of the cosmic microwave background can be seen. The bottom panel of Fig. 0.2 shows the view of the sky as it can be observed by eye. The Galactic Plane is visible as a bright band, but is obscured by dark filaments of dust. The two bright sources that are to the South of the Galactic Plane are the Small and the Large Magellanic Cloud. The two sky maps in Fig. 0.3 illustrate the electromagnetic radiation at higher energies. At the top, the map of the *ROSAT* all-sky survey gives an impression of the X-ray emission in the energy range from 0.1 to 2 keV, which is also known as the soft X-ray band. For these energies, the absorption due to the intersteller medium plays a major role. In Fig. 0.3 this effect becomes apparent through the dark band that obscures the X-ray emission along the Galactic Plane. The absorption is dominant for the low-energy part of the X-ray band. Therefore, only sources with a hard spectrum are visible in the Galactic Plane and appear as bluish dots, due to the absorption of the low-energy part of their emission (which is colored in red and green). At energies beyond the X-ray band, the absorption effects are less and less dominant. This becomes especially clear when looking at the GeV γ-ray sky map from the *Fermi* satellite, which is shown in the lower panel of Fig. 0.3. The Galactic Plane is again apparent as a bright band of emission. Many of the Galactic sources seen in this energy range are pulsars, rotating neutron stars that lose energy via the slowdown of their rotation.

The highest photon energies that are currently accessible to measurements are VHE γ-rays in the TeV energy range. The map of the 108 VHE γ-ray sources that have been detected so far is shown in Fig. 0.4, where different source types are marked with colored labels.

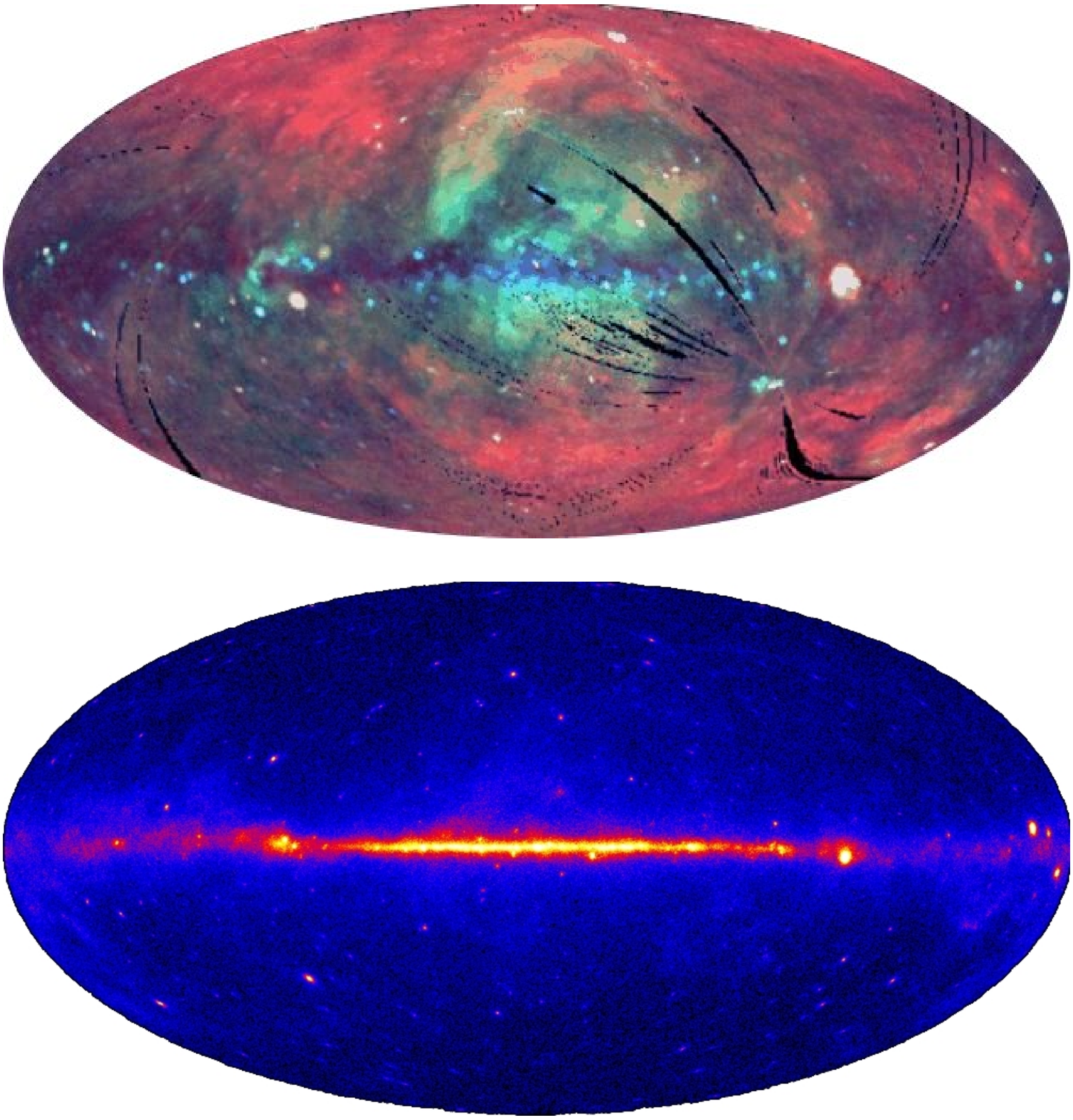

Fig. 0.3: *Top: All-sky three-color image from the ROSAT survey. The colors represent different energies of the photons (red: 0.1 – 0.4 keV, green: 0.4 – 0.9 keV, blue: 0.9 – 2.0 keV). Bottom: Map of the GeV γ-ray sky constructed from three months of observation with the* Fermi *satellite. (Credits: Top: S. Digel and S. Snowden (USRA/ LHEA/ GSFC), ROSAT Project, MPE, NASA; Bottom: NASA/DOE/Fermi-LAT Collaboration)*

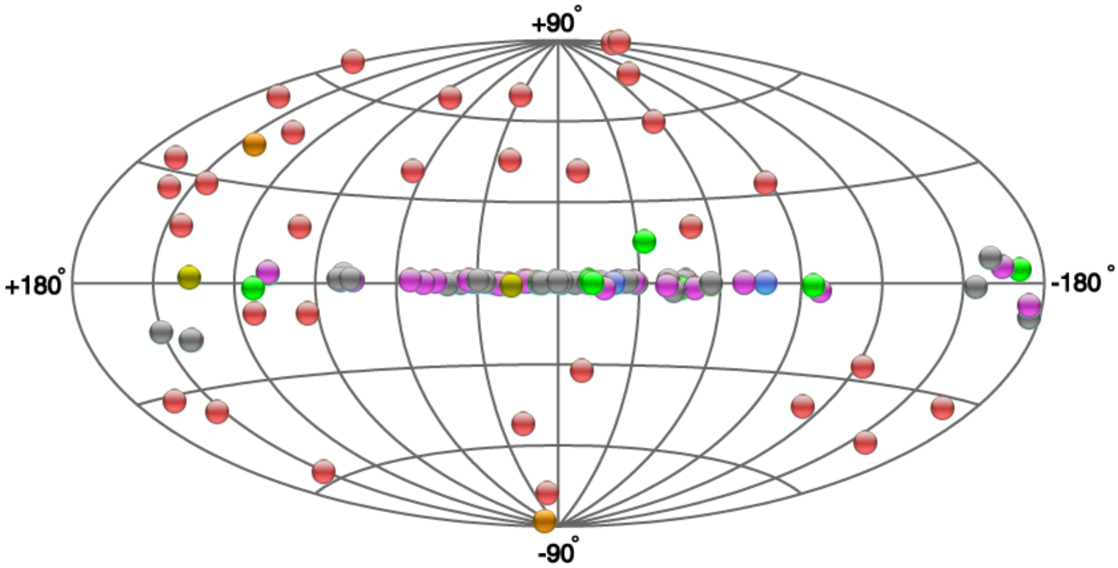

Fig. 0.4: *Sky map in Galactic coordinates of the currently known sources of VHE γ-rays. Different source types are color-labeled: extragalactic sources are Starburst Galaxies (orange) and Active Galactic Nuclei (AGN, red); Galactic sources include X-ray/γ-ray binaries (yellow), PWN (purple), shell-type SNR (green) and associations with microquasars, cataclysmic variables or Wolf-Rayet stars (blue); sources without a clear identification (Galactic and extragalactic) are marked with gray color labels. Figure from the online γ-ray catalog TeVCat (Wakely & Horan 2010).*

The sky map illustrates that the majority of Galactic TeV sources are clustered along the Galactic Plane, whereas the extragalactic sources seem to be isotropically distributed. Among the approximately 60 Galactic TeV sources, there are many objects that are identified as a pulsar wind nebula (PWN, marked with purple labels in Fig. 0.4). Most of the newly discovered Galactic sources of TeV γ-rays were unveiled in the scan of the Galactic Plane with the H. E. S. S. telescope array (Aharonian et al. 2005a, 2006b; Chaves et al. 2009). Figure 0.5 shows an excerpt of the H. E. S. S. view of the inner region of our Galaxy in the Galactic longitude of $-50°$ to $30°$ and Galactic latitude of $-3°$ to $2°$. It is a map of the significance of the γ-ray events above an energy of about 200 GeV measured by the H. E. S. S. experiment. The significance at a certain position of the sky map is a measure of the statistical compatibility of the observed emission with isotropic background emission. A higher significance is thus an indication that the observed VHE γ-ray emission is from an individual source rather than from background events. The color scale of the sky map is truncated at a significance of $14\,\sigma$, because otherwise the Galactic Center (GC; visible in the upper panel) would be the by far brightest object. The map also serves as an introduction to the VHE γ-ray view on the PWN MSH 15−5*2*, which is the source that is studied in the present thesis. It is located at a position of $l = 320.4°$ and $b = -1.4°$ (Galactic coordinates) and is visible toward the right side of the lower panel of Fig. 0.5, where it is also labeled as HESS J1514 − 591.

The topic of the present thesis is the analysis of observations and the modeling of the PWN MSH 15−5*2*. The first Chapter will therefore provide a general overview on pulsar wind nebulae, presenting the current understanding of the structure and the evolution of this class of astrophysical objects. Following this, the relevant acceleration and radiation mechanisms important for the context of this study are introduced. In Chapter 2, a detailed introduction to the region around MSH 15−52 is given. This includes a summary of the observations on the pulsar, the PWN and the shell of the supernova remnant that have been carried out with various instruments at different wavelengths. The topic of Chapter 3 is the first analysis of *XMM-Newton* observations of the PWN MSH 15−52. Following a brief introduction of the detection techniques for cosmic X-rays and the *XMM-Newton* satellite, the analysis of the data on MSH 15−52 is presented. Chapter 4 is the second data analysis Chapter and covers the analysis of VHE γ-rays from MSH 15−52 that have been observed with the H. E. S. S. experiment. The indirect detection method that H. E. S. S. uses to observe γ-rays is explained in detail, as it is not as straight-forward as the detection of photons with direct measurement techniques. After this, the most sensitive analysis of MSH 15−52 in this energy range is presented, making use of a considerably extended data set (with respect to earlier analyses) and an advanced γ-ray reconstruction method. Following the X-ray and TeV γ-ray data analysis, a model of the nonthermal emission of PWN is presented in Chapter 5. In contrast to the widely established one-zone models of PWN, the model describes the spatial evolution of the leptons in a spherically symmetric, steady-state approach. The optimum values for the free model parameters are determined by comparing the results of the spatially-resolved spectral analysis of the X-ray data presented in Chapter 3 with the model prediction of the emission in the same regions of the PWN. Afterwards, a comparison of the TeV emission predicted by the model and measured with the H. E. S. S. experiment is presented.

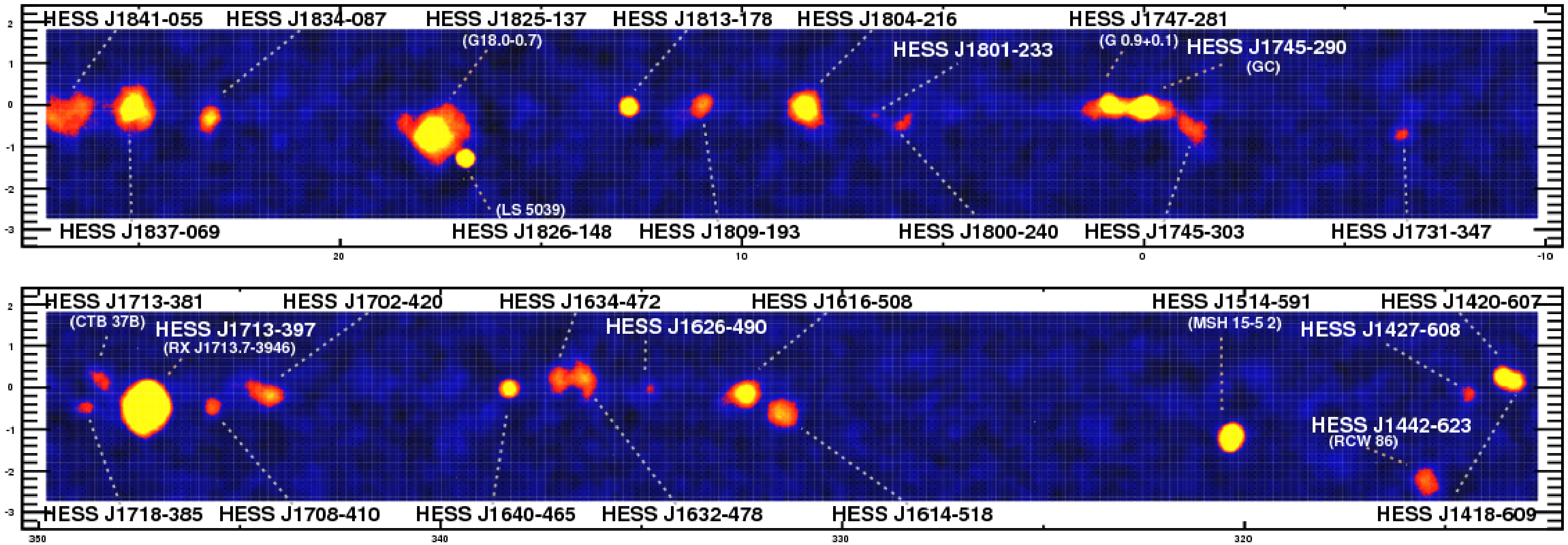

Fig. 0.5: *VHE γ-ray significance map of the Galactic Plane between a Galactic longitude of $-50°$ to $30°$ and a Galactic latitude of $-3°$ to $2°$. The background is estimated using a ring-region around the test position and the on-source counts were summed within a radius of $0.22°$. The color scale is between a significance of $-4\,\sigma$ and $14\,\sigma$. The upper end of the scale is truncated, since the Galactic Center (labeled GC) is far above this level. The labels indicate the H. E. S. S. names of the detected γ-ray sources and, in case of clear associations, the common name from the literature is also given. MSH 15–52 (HESS J$1514-591$) is on the lower panel at a Galactic longitude of $l \approx 320.4°$ (reproduced from Hoppe 2008).*

1 Pulsar Wind Nebulae

Before we look in detail at the pulsar wind nebula MSH 15−5*2*, an introduction to this class of astrophysical objects is given in this chapter. The first section comprises an overview of the general structure, including the different constituents that make up the PWN in the current understanding. After that, the different evolutionary stages of PWNe are discussed. The last two sections deal with the proposed mechanisms of particle acceleration that are apparent and the processes in which the accelerated particles emit radiation. An understanding of these physical concepts is one of the key goals in astronomy and allows the study of physics at energy scales unachievable with the current generation of particle accelerators on Earth. As in many fields of science, there is also a prototype for the research on PWNe: the Crab Nebula, the remnant of the historical supernova of 1054 AD, is the best-studied specimen of this source class. Before discussing the properties of PWN and turning our attention to MSH 15−5*2*, let us thus have a quick look at a beautiful composite image of the Crab Nebula from observations by three different telescopes. Figure 1.1 is a composite image of the emission of the Crab Nebula in three different wavelengths, radio emission in red, visible light in green and X-ray emission in blue, measured respectively by the Very Large Array (VLA), the Hubble Space Telescope (HST) and the *Chandra* X-ray Observatory. The dot at the center of the central blue torus structure is the pulsar that powers the large-scale emission of the PWN seen in the three wavelengths.

Figure 1.1 highlights one of the central properties of the definition of a PWN: contrary to the class of shell-type supernova remnants, pulsar wind nebulae have a center-filled appearance and are thus also known as plerions (derived from the Ancient Greek word “pleres”, translating to “full” or “covered”). Another characteristic of pulsar wind nebulae is the observed spectrum. It is of nonthermal nature and covers a broad range of wavelengths, from radio to VHE γ-rays. The energy source of a PWN is its pulsar, which supplies energy to the nebula through the loss of rotational energy. These criteria, alongside with the suggestion of the name plerion, were first introduced in a work on “Crab-type supernova remnants” by Weiler & Panagia (1978). Newer observations have put the first properties of plerions into a different perspective, but the basic definition is still used today.

1.1 Structure

As already mentioned in the Introduction, pulsar wind nebulae are one possible type of a supernova remnant. The first step in unveiling their typical structure will be to look at the energy source that powers the emission seen across the electromagnetic spectrum: the pulsar. How is the pulsar formed? What are the properties of its magnetic field? And in which form does it supply the energy to power a large-scale structure such as the PWN? What are the relevant emission processes? These questions will be treated in the first sections, whereas the further sections will then deal with the flow of the particles that are accelerated by the pulsar and which form the features of the pulsar wind observed at different distances from the pulsar.

1.1.1 The Pulsar

As the name already suggests, pulsars are named after the pulsed nature of the emission that is observed[1]. The radiation is believed to be emitted in a narrow cone by a neutron star that is rapidly rotating. The treatment of pulsars is thus always directly linked to the properties of neutron stars. Although the first pulsar was only detected in 1968 by Hewish et al., the existence of neutron stars was theoretically predicted much earlier. Already in 1934, Baade & Zwicky suggested that a neutron star could be the final state of a star after a supernova explosion, although no prediction for visible emission was made. Shortly before the observational discovery of the first pulsar, Pacini (1967) made the prediction, that a rapidly rotating neutron star could provide the energy source for a surrounding nebula, like e.g. the Crab Nebula. The discovery of the Crab Pulsar in 1968 by Staelin & Reifenstein confirmed this prediction and also provided a clear evidence for the initial proposition by Baade & Zwicky. Gold (1968) suggested that the rotating neutron stars have a strong magnetic field and that pulsars slow down due to the emission of magnetic dipole radiation. These basic principles are still valid and have been confirmed by precise measurements of a growing population of known pulsars. The field of pulsar astronomy has rapidly expanded and to date, more than 1500 pulsars have been detected at radio wavelengths alone (Manchester et al. 2005).

Fig. 1.1: *Composite multi-wavelength image of the Crab Nebula. Red represents the radio emission measured by the VLA, green represents visible emission observed by the HST and blue represents the X-ray emission measured by the Chandra X-ray Observatory (Image credit: J. Hester (ASU), CXC, HST, NRAO, NSF, NASA).*

Formation and Structure

The formation of neutron stars occurs in core-collapse supernovas of stars. These violent explosions take place when a massive star has burnt its supply of material the nuclear fusion. The decreasing outward thermal pressure is then unable to counter-balance the inward gravitational pressure and the star collapses. For certain masses of the progenitor star, the collapse is halted when the core transforms into a neutron star and the outer envelope is blown outwards in a gigantic explosion (see more detailed explanation below). It is believed that an energy of up to 10^{46} J is released in such an explosion, making these events visible to the naked eye, when they happen in our Galaxy or close-by. An impressive image of the most noticeable supernova in modern times is shown in Figure 1.2 as a composite image across two wavelength ranges from observations with the Hubble Space Telescope and the *Chandra* X-ray observatory. The optical emission observed is color-coded in pink and white colors, whereas the X-ray emission is displayed in blue and purple colors. The image impressively visualizes the effects of the supernova shock wave as it moves outwards. Depending on the mass of the progenitor star before the explosion, it will end up as a white dwarf, a neutron star or a black hole. A neutron star will form for a progenitor star with a mass between about six to 15 solar masses (Lyne & Graham-Smith 2006). In this case, the density of the stellar core becomes high enough, so that the inverse β-decay process

$$\mathrm{p} + \mathrm{e}^- \rightarrow \mathrm{n} + \nu_\mathrm{e}\,, \tag{1.1}$$

takes place, in which the electrons react with the protons to form neutrons and neutrinos. The complete collapse of the core is balanced by the degeneracy pressure of the electrons,

[1] The word "pulsar" was coined from a contraction of the expression "pulsating star". The abbreviation PSR stands for "pulsating source of radio".

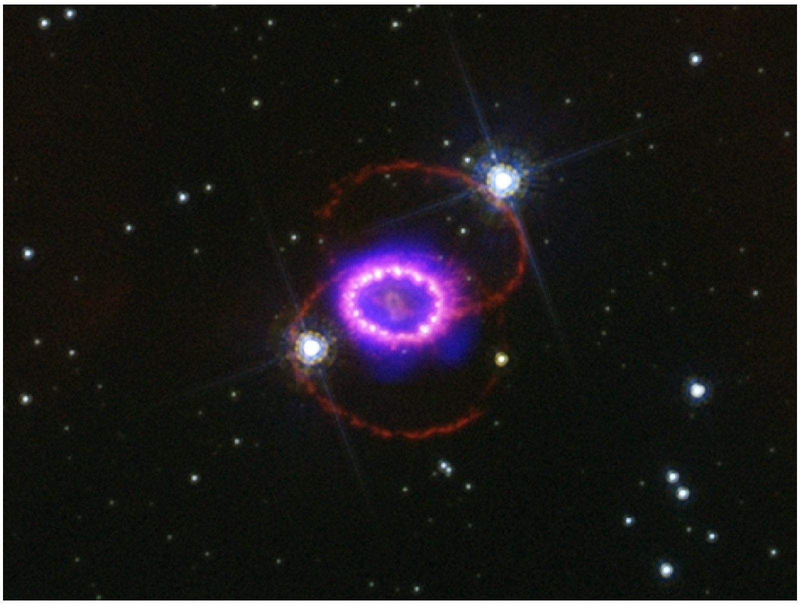

Fig. 1.2: *Composite multi-wavelength image of the sky around the supernova SN1987A. The optical emission was observed by the HST and is pink-white-colored, the emission in X-rays was observed by the Chandra X-ray observatory and is blue-purple-colored (Credit: X-ray: NASA/CXC/PSU/S.Park & D.Burrows.; Optical: NASA/STScI/CfA/P.Challis).*

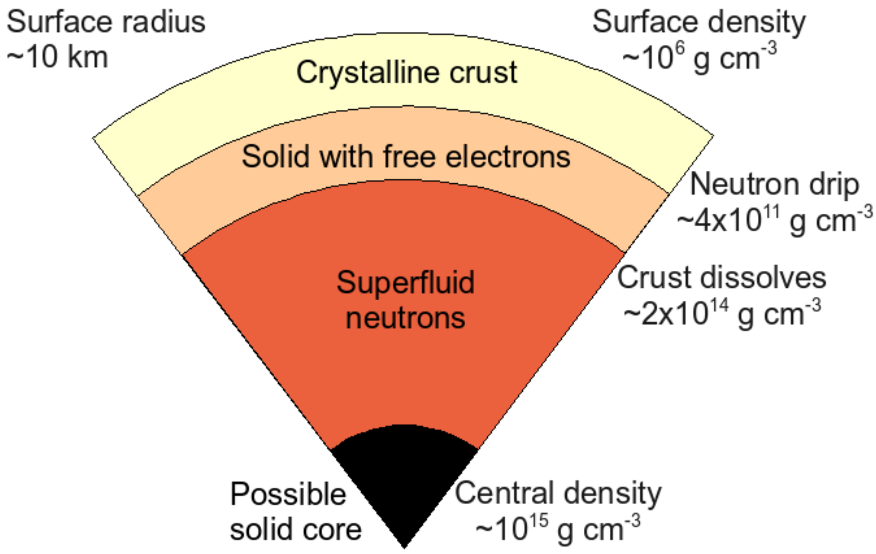

Fig. 1.3: *Schematic illustration of the inner structure of a neutron star with a mass of* $1.4\,\mathrm{M}_\odot$ *and a radius of* 10 *km. The density decreases by approximately nine orders of magnitude from the core to the surface of the neutron star (Figure adopted from Lyne & Graham-Smith (2006)).*

because a further increase in density would require that electrons occupy the same energy state. At this point, the temperature has no effect on the physical properties of the neutron star and the equation of state (EOS) of the system is only governed by the pressure and the density. The EOS of neutron stars rests on the fundamental physics of the strong force and for such dense matter, there are still many open questions and therefore a wide variety of models for the EOS. A good overview of different models is given e.g. in Lattimer & Prakash (2001). A simplified view of the typical structure of a neutron star with a mass of 1.4 solar masses is displayed in Fig. 1.3. The central core, which is possibly solid, is surrounded by a neutron superfluid. The outer crust is about 1 km thick and of solid, crystalline structure. It is assumed to consist of heavy nuclei and electrons. In Fig. 1.3, the densities at different positions inside the neutron star are labeled. For a neutron star with typical parameters for the radius of $R = 10\,\mathrm{km}$ and a mass of $M = 1.4\,\mathrm{M}_\odot$ the mean density is $\rho = 6.7 \times 10^{14}\,\mathrm{g\,cm^{-3}}$. From the center to the surface, the density decreases by approximately nine orders of magnitude, leading to different state of matters within the neutron star.

Magnetic Field

The presence of strong magnetic fields in pulsars has been theoretically predicted and measurements of the polarization of the radio emission have provided the experimental evidence for it. Magnetic field strengths of the order of 10^{12} Gauss can be derived from the observed cyclotron features in X-ray spectra of pulsars, e.g. for Her X-1 (Truemper et al. 1978). These extremely strong magnetic fields originate in the collapse of the progenitor star. The typical magnetic field of a star like the Sun is in the order of 10^2 G. Due to the magnetic flux freezing, the magnetic field is bound to the stellar plasma. If the star collapses by a factor of 10^{-5} in radius, then this collapse can account for the expected magnetic field strengths of pulsars. An estimate of the surface magnetic field strength of a pulsar can be derived from the observation of the rotation period P and its time derivative $\dot{P}$. For a slow-down of the rotation which is due to magnetic dipole radiation, the surface magnetic field B_S is equal to (Lorimer & Kramer 2005)

$$B_\mathrm{S} = \sqrt{\frac{3c^3}{8\pi^2 R^6 \sin^2\Psi} P\dot{P}}\,, \tag{1.2}$$

where R is the radius of the pulsar and Ψ the angle between the rotation axis and the axis of the magnetic field.

One would suspect that such a strong magnetic field dominates the structure of the pulsar, but due to the high density of the pulsar, this is not the case. Outside of the pulsar, however, the physical processes are dominated by the magnetic field. An illustration of a pulsar is shown in Fig. 1.4. The rotation axis and the axis of the magnetic field are misaligned. This leads to the emission of magnetic dipole radiation, as will be pointed out in more detail in the next paragraph. The light cylinder (see Fig. 1.4) marks the distance at which a particle rotating with the pulsar period would be traveling at the speed of light ($R_\mathrm{LC} = c/\Omega$). The region inside the light cylinder is called the magnetosphere of the pulsar. It is filled up by a high-energy plasma which is rotating with the same period as the pulsar. Goldreich & Julian (1969) pioneered the theoretical description of the properties of this region for the case of the aligned rotator, in which the magnetic field and rotational axes fall together. For the magnetosphere, which is highly conducting along the magnetic field lines, Goldreich & Julian (1969) derived the Goldreich-Julian density n_GJ, the space-charge density of electric charges in the co-rotating zone:

$$n_\mathrm{GJ} = 7 \times 10^{-2} B_z P^{-1}\,\mathrm{cm}^{-3}\,. \tag{1.3}$$

A general approach for non-aligned rotators has so far not been carried out, but already the special case of a perfect alignment of the axes provides important insights into the characteristics of the pulsar magnetosphere.

Rotation and Spin-down Characteristics

In the previous paragraph it was already pointed out that the rotation period of the pulsar P changes with time. Just like in the case of the magnetic field, the fast rotation originates in the collapse of the progenitor star. Angular momentum is conserved, and during the dramatic collapse of the radius of the star, a moderate rotation period of the star becomes a period in the order of seconds and less for the remaining neutron star. Since the discovery of the first pulsar in 1968, the experimental techniques have improved significantly and have allowed for precise measurements of the pulsar period for many pulsars. For most of the pulsars, it is also possible to measure the time derivative of the pulsar period, $\dot{P}$, and for some of the pulsars, the second and third derivative of the period is also measurable. The change in the rotation period is related to the braking index n, which is defined as

$$\dot{\Omega} = -K\Omega^n\,, \tag{1.4}$$

where $\Omega = 2\pi/P$ is the angular frequency of the rotation of the pulsar and K is assumed to be a constant. The braking index of a pulsar can directly be calculated if the second derivative of the period can be measured. The braking index is then equal to

$$n = \frac{\Omega\ddot{\Omega}}{\dot{\Omega}^2} = 2 - \frac{P\ddot{P}}{\dot{P}^2}\,. \tag{1.5}$$

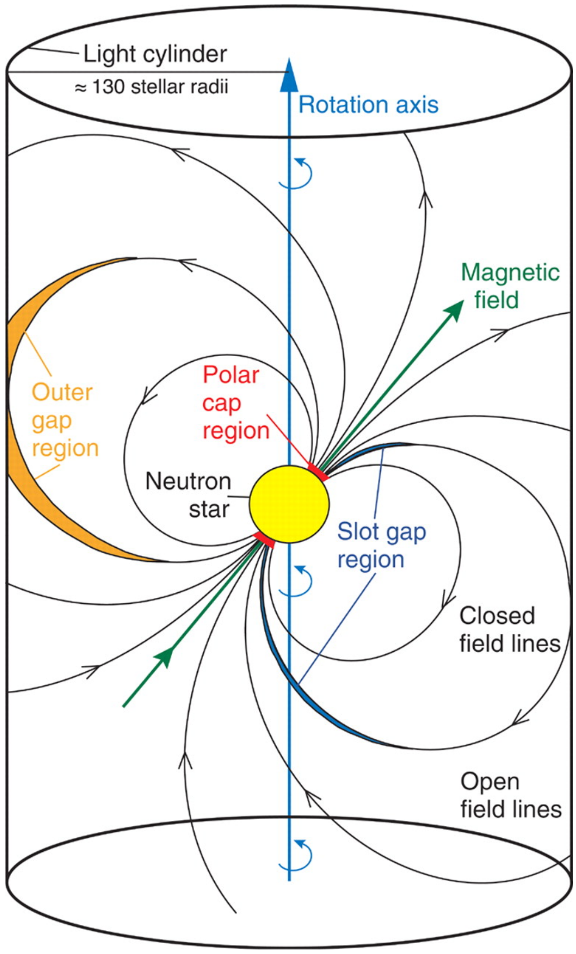

Fig. 1.4: *Illustration of the magnetosphere and possible emission regions of a pulsar. Three emission models are considered in this image, the polar cap, outer gap and slot-gap model. The radius of the light cylinder of* 130 *stellar radii is stated for the Crab pulsar. Figure taken from Albert et al. (2008).*

The value of the braking index provides information about the energy loss mechanisms which lead to the change in the pulsar period. The currently best-established approach to explain the slow-down in the rotation is by the process of magnetic braking. In this case, the magnetic axis is misaligned with respect to the rotational axis. Figure 1.4 shows a sketch of a pulsar for which the rotational axis and the magnetic field axis are misaligned. The varying dipole moment leads to the conversion of rotational energy of the pulsar into electromagnetic radiation. For a magnetic dipole with a moment of $|\mathbf{m}|$, the radiation power is equal to

$$P_{\rm rad} = \dot{E}_{\rm dipole} = \frac{2}{3c^3}|\mathbf{m}|^2\Omega^4\sin^2\Psi\,, \tag{1.6}$$

where the angle between the rotation axis and the magnetic axis of the pulsar is denoted as Ψ. The loss of rotational energy of the pulsar is called spin-down luminosity or spin-down power and is commonly denoted as $\dot{E}$ or L. It is the total power per time interval that the pulsar supplies by the slow-down of its rotation. For a given moment of inertia I of the pulsar, it amounts to

$$\dot{E} = -\frac{\mathrm{d}E_{\rm rot}}{\mathrm{d}t} = -\frac{\mathrm{d}(\frac{1}{2}I\Omega^2)}{\mathrm{d}t} = -I\Omega\frac{\mathrm{d}\Omega}{\mathrm{d}t}\,. \tag{1.7}$$

If one assumes that the loss of rotational energy is entirely converted into magnetic dipole radiation, then it follows from Eqs. 1.6 and 1.7, that

$$\dot{\Omega} \propto -\Omega^3, \tag{1.8}$$

indicating a braking index of $n = 3$ for this process. As laid out in Eq. 1.5, the braking index can be measured, if the second derivative of the pulsar period can be measured. This is the case for a small number of pulsars and the measured braking indices range from 1.4 ± 0.2 for the Vela pulsar (Lyne et al. 1996) to 2.91 ± 0.05 for the pulsar PSR J1119−6127 (Camilo et al. 2000). For PSR B1509−58, an analysis of 21 years of radio timing data and 8 years of X-ray timing data yielded a braking index of $n = 2.839 \pm 0.003$ (Livingstone et al. 2005). Clearly, the braking index deviates from what would be the expectation for pure magnetic dipole radiation. One explanation for this is, that the energy flow from the pulsar is not only by electromagnetic radiation, but does also have a contribution from the particle outflow. Since the magnetic field dominates the physics of the outer magnetosphere, Eq. 1.6 will still give a good approximation of the total energy flow (Lyne & Graham-Smith 2006).

An integration of Eq. 1.4 yields a relation for the age t of the pulsar as a function of the angular frequency and its derivative:

$$t = -\frac{\Omega}{\dot{\Omega}(n-1)} \left(1 - \left(\frac{\Omega}{\Omega_i} \right)^{n-1} \right) . \tag{1.9}$$

In this equation, Ω_i denotes the initial angular frequency of the pulsar at its formation. If we now assume that $n \neq 1$ and that the angular frequency of the pulsar at birth is much greater than the current frequency ($\Omega_i \gg \Omega$), we get an estimate of the pulsar age of

$$\tau_\mathrm{c} = -\frac{\Omega}{\dot{\Omega}(n-1)} = \frac{P}{\dot{P}(n-1)} , \tag{1.10}$$

which is called the characteristic age of the pulsar. In most cases, the characteristic age is stated under the implicit assumption of magnetic dipole radiation ($n = 3$) and is then equal to (Lyne & Graham-Smith 2006)

$$\tau_\mathrm{c} = \frac{P}{2\dot{P}} \approx 15.8 \left(\frac{\dot{P}}{10^{-5}} \right)^{-1} \mathrm{Myr} . \tag{1.11}$$

The characteristic age provides a good estimate for many pulsars, but there are also significant deviations found for pulsars, for which the true age is known from an association with a historical supernova. This may be due to a braking index $n \neq 3$ or a non-negligible birth period P_0 of the pulsar. Pulsars that are associated with a historical supernova provide a unique opportunity to study the birth periods of pulsars. Assuming a constant braking index throughout the lifetime of the pulsar, the birth period can be calculated using Eqs. 1.9 and 1.10 as

$$P_0 = P \left(1 - \frac{n-1}{2} \frac{t}{\tau_\mathrm{c}} \right)^{1/(n-1)} . \tag{1.12}$$

For the Crab pulsar, an initial spin period of 19 ms was calculated by Lyne et al. (1993), but values of up to 139 ms for PSR J0538+2817 (Kramer et al. 2003) have been found.

Particle Acceleration and Emission Processes Close to the Pulsar

The region close to the pulsar emits radiation over a broad spectral range. Apart from the thermal radiation that is emitted from the surface of the pulsar, there is also nonthermal emission apparent. Three regions for the origin of the nonthermal emission within the pulsar's magnetosphere are typically considered: the polar cap region (e.g. Daugherty & Harding 1982), slot gap region (e.g. Muslimov & Harding 2004) and the outer gap region (e.g. Hirotani 2008). The three emission regions are indicated in Fig. 1.4. In these (vacuum) gaps, the density of the plasma is lower than the Goldreich-Julian density. This leads to the acceleration of electrons to very high energies. The processes by which these electrons emit nonthermal radiation will be presented in more detail in Section 1.4 (Radiation Processes in Pulsar Wind Nebulae). High-energy photons that are emitted are in turn absorbed via magnetic pair production and photon-photon pair production. Thus, a cascade of charged particles and photons is created in the pulsar magnetosphere. Further out in the magnetosphere, the photons are attenuated via photon-photon collisions. This leads to a high-energy cutoff at around 10 GeV, so that the nonthermal emission from regions close to the pulsar is not observable at TeV energies.

1.1.2 The Unshocked Wind

The leptons that are accelerated inside the gaps of the pulsar's magnetosphere are propagating outwards at relativistic speeds. In current model scenarios, the unshocked wind is dominated by the Poynting flux of the electromagnetic field rather than the particle energy flux (Gaensler & Slane 2006). This unshocked wind is also called a "high-σ wind". In this expression, σ is the magnetization parameter of the wind and is defined as the ratio of the Poynting flux to the energy flux of the particles (Gaensler & Slane 2006):

$$\sigma = \frac{F_{E\times B}}{F_{\text{particle}}} = \frac{B^2}{4\pi\rho\gamma c^2}\,, \tag{1.13}$$

where B, ρ and γ are parameters of the wind, namely the magnetic field, mass density of the particles and the Lorentz factor. The typical Lorentz factors in the unshocked wind are in the order of $10^4 - 10^7$. This is far below the values that would be expected for a freely expanding wind (Arons 2002). No synchrotron emission is expected to be emitted from this region, since the magnetic field is frozen into the plasma and thus the particle outflow moves together with the magnetic field. However, IC emission is expected from the interaction of the unshocked wind with low-energy photons, e.g. from the thermal emission originating at the pulsar's surface. Depending on the Lorentz factor of the wind, these IC photons should have energies in the range of 10 GeV to 10 TeV (Aharonian & Bogovalov 2003). A sketch of the different components of a PWN and the emission that is expected from each site is shown in Fig. 1.5. The different energy ranges of the emitted radiation are labeled with R, O, X, MeV, GeV and TeV (see image caption for details). As described in Section 1.1.1, the pulsed emission from the magnetosphere only extends to GeV energies and then cuts off sharply, whereas the unshocked wind should only be visible through the IC channel. Since the size of this region is comparatively small and the expected fluxes are rather low, current VHE γ-ray telescopes have so far not been able to measure the emission from the unshocked pulsar wind. These predictions are therefore still lacking experimental proof.[2]

[2]For the current generation of satellites measuring GeV photons the expected fluxes are below the sensitivity and the small region of the unshocked wind cannot be resolved, given the present angular

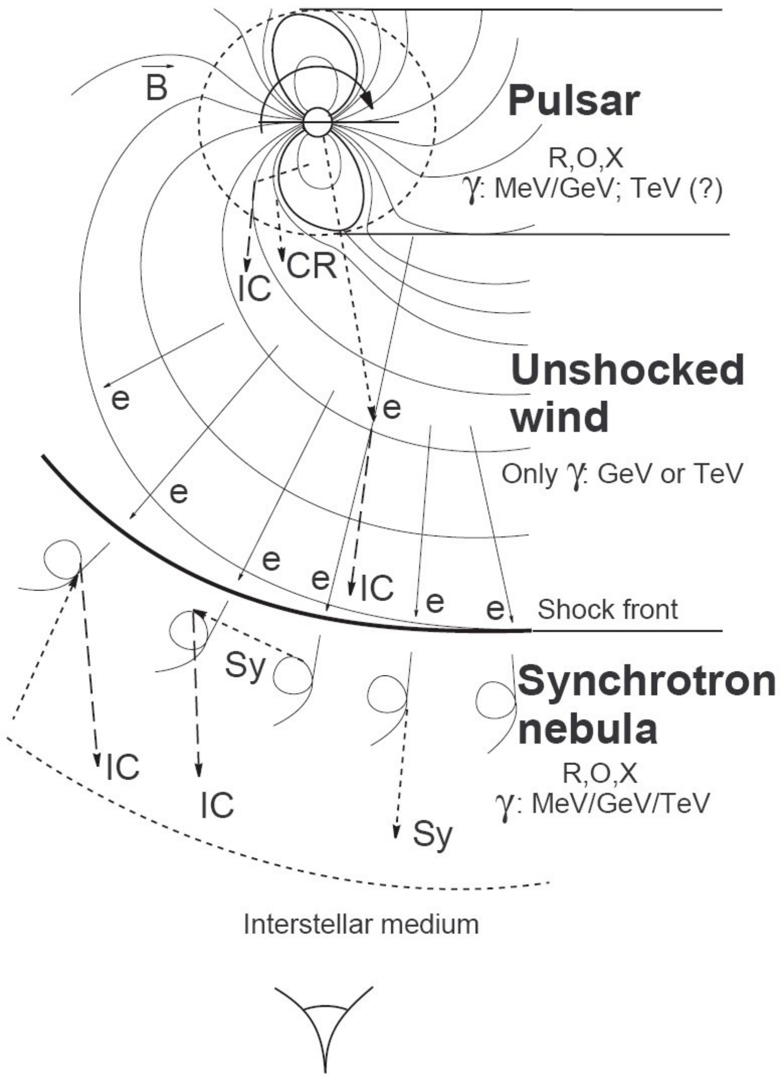

Fig. 1.5: *Schematic view of a pulsar wind nebula and the emission from each region. The radiation that can be observed from each region is marked with the labels R (radio wavelengths), O (optical wavelengths), X (X-ray emission in the keV energy range). The tags MeV, GeV and TeV indicate that photons with energies in the respective range should be emitted from these regions. In this picture, the region around the pulsar is the magnetosphere inside the light cylinder (cf. 1.1.1). Pulsed emission in a broad range from radio to GeV energies is observed from this region. In the unshocked wind, only VHE γ-rays from inverse Compton (IC) scattering processes are expected. Beyond the shock front, the synchrotron nebula (pulsar wind nebula) is visible from radio to TeV energies. The emission processes in the PWN are mainly synchrotron and IC emission. Figure taken from Aharonian & Bogovalov (2003).*

1.1.3 The Wind Termination Shock

Already in 1974, Rees & Gunn concluded for the Crab nebula that there must be some kind of shock transition occurring inside the PWN. Since the outer edge of the PWN is confined by the expanding ejecta of the SNR, the total energy must be confined within the nebula. At a typical distance of R_S (the shock radius), the ram pressure of the unshocked wind is balanced by the internal pressure of the PWN. The shock radius can be calculated as (Gaensler & Slane 2006)

$$R_{\mathrm{S}} = \sqrt{\frac{\dot{E}}{4\pi\omega c P_{\mathrm{PWN}}}}\,, \tag{1.14}$$

where ω is the equivalent filling factor for an isotropic wind and P_{PWN} is the total pressure in the shocked nebula interior. For the Crab nebula, Rees & Gunn (1974) connected the boundary of an underluminous region apparent in X-ray observations to the unshocked wind bordered by the termination shock. This feature can be seen in the X-ray part of Fig. 1.1 as a the inner ring around the pulsar. It lies at a distance of around 0.1 pc, a value which is typical for PWNe in which the termination shock has been observationally resolved (Bamba et al. 2010).

Within the shock, particles are re-accelerated and have Lorentz factors of up to 10^6, a value derived from X-ray observations of termination shocks (Gaensler & Slane 2006). Furthermore, a large part of the energy in the electromagnetic field is transferred to particles. Magnetohydrodynamic (MHD) simulations of the Crab nebula showed that the termination shock also marks a transition from high σ values to values of around $\sigma = 3 \times 10^{-3}$ in the PWN (Kennel & Coroniti 1984a). The exact nature of this transition is, however, not yet clear to date (Gaensler & Slane 2006).

An expression to calculate the magnetic field strength at the shock, B_S, in terms of the spin-down power of the pulsar is given by Kennel & Coroniti (1984b):

$$B_{\mathrm{S}} = \frac{\kappa}{R_{\mathrm{S}}}\sqrt{\frac{\sigma \dot{E}}{(1+\sigma)c}}\,, \tag{1.15}$$

where σ is the magnetization at the shock. The magnetic compression ratio is denoted by κ, and is in the range of $1-3$ (Kennel & Coroniti 1984b). For strong shocks, in which $\sigma \ll 1$, a compression in the order of 3 is expected, whereas values of $\kappa \approx 1$ are found for weaker shocks, e.g. for the Vela pulsar (Sefako & de Jager 2003).

1.1.4 The Pulsar Wind Nebula

The actual pulsar wind nebula, referring to the observationally most prominent part in size and luminosity, is the flow of particles from the termination shock outwards. Emission from this region is unpulsed and can be observed at almost all wavelengths. It extends to distances in the order of 10 pc, compared to a typical radius of the termination shock of 0.1 pc. In Fig. 1.5, it is marked as the synchrotron nebula, since most of the radiation observed from radio up to hard X-ray wavelengths is from synchrotron radiation of the leptons in the magnetic field of the PWN. It is believed that the magnetic field in the PWN is toroidal and frozen into the particle outflow. This means that the ideal MHD limit holds true and thus

$$\frac{\partial \mathbf{B}}{\partial t} = \nabla \times (\mathbf{v} \times \mathbf{B})\,, \tag{1.16}$$

resolution.

where $\mathbf{v}$ is the velocity of the particle outflow. Simulations show that $\sigma < 1$ for the nebula beyond the termination shock. This means that the largest part of the energy flow is carried by the particles and not by the electromagnetic field. Typical magnetic fields in the PWN are in the range of 1 to 100 μG.

At radio wavelengths, the emission spectrum of PWNe shows a flat power-law characteristic with $F_\nu \sim \nu^{-\alpha}$, where the index α is typically between 0 and 0.3. At X-ray wavelengths, the spectrum is then considerably steeper and the index changes to values between approximately 1.5 and 2.5. For many pulsar wind nebulae, a spectral steepening is observed at X-ray energies, with a harder spectrum close to R_S and a steeper spectrum further out in the PWN. This is interpreted as the synchrotron cooling of the lepton population: the high-energy leptons lose energy via synchrotron radiation and this leads to a steepening of the observed photon spectrum at larger distances from the pulsar. The current generation of γ-ray instruments also enabled observations of pulsar wind nebulae at higher energies. The detected emission is most likely due to the IC emission that is produced in the up-scattering of background photons by the leptons. The typical spectrum of a PWN in the TeV energy range can be fitted by a power-law spectrum with an index of ~ 2.

Looking at the observed morphological properties of pulsar wind nebulae, one can observe that the dimension of the synchrotron nebula gets smaller with larger energies. Typically the largest extent is seen at radio wavelengths. This is attributed to the synchrotron cooling effects on the lepton outflow in the wind. There is, however, a detailed structure within the PWN that can be resolved with high-resolution instruments. For one, the termination shock is not symmetric around the pulsar, but is linked to the rotation and magnetic axis of the pulsar. In some PWNe, jet-like features are observed, that distort the appearance of the shock and the synchrotron nebula. Furthermore, it is also assumed that the shock has an elliptical shape depending on the orientation of the axes of the pulsar. Beyond the shock, the PWN also shows substructures, referred to as wisps, knots and filaments. The exact nature of the formation of these features is yet unknown. However, it is assumed that in these features the mass density and magnetic field strength is greater and that they are sites of re-acceleration of the particle outflow (Gaensler et al. 2002).

1.2 Evolution

There are four important phases of evolution for a PWN according to Gaensler & Slane (2006):

- free expansion into the unshocked ejecta,
- interaction with the reverse shock of the supernova remnant,
- a PWN inside a Sedov SNR, and finally
- a pulsar in the interstellar gas.

During the phase of free expansion, the pulsar is located at the center of the SNR, surrounded by the unshocked ejecta of the supernova explosion. The PWN undergoes a phase of rapid expansion at supersonic speeds and drives a shock into the ejecta of the SNR. Chevalier (1977) derived an expression of the radius of the forward shock of the PWN, R_PWN, in the case of spherical symmetry:

$$R_\mathrm{PWN} = 1.1\,\mathrm{pc}\left(\frac{\dot{E}_0}{10^{38}\mathrm{erg\,s^{-1}}}\right)^{1/5}\left(\frac{E_\mathrm{SN}}{10^{51}\mathrm{erg}}\right)^{3/10}\left(\frac{M_\mathrm{ej}}{10\,\mathrm{M}_\odot}\right)^{-1/2}\left(\frac{t}{10^3\,\mathrm{yr}}\right)^{6/5}, \tag{1.17}$$

where $\dot{E}_0$ is the initial spin-down luminosity and E_{SN} and M_{ej} are the energy and ejected mass released in the supernova explosion. This evolutionary phase is valid for young pulsars with an age of up to a couple of thousand years.

After the phase of free expansion, the SNR enters the Sedov-Taylor phase. In this stage, the total energy is conserved. Two shocks are now present, a forward shock which leads to a compression and heating of the gas surrounding the SNR, and a reverse shock, which decelerates the ejecta of the supernova. The reverse shock passes the PWN on time scales of 10^3 to 10^4 years and leads to a significant compression of the PWN (Chevalier 1998). Thereby, the pressure and the magnetic field are increased, causing a more rapid expansion with an increased synchrotron luminosity. The best-known example of a PWN in this evolutionary stage is the nebula around the Vela pulsar with a characteristic age of $\approx 11\,\mathrm{kyr}$.

In the third phase of the evolution, the PWN now expands into the shocked and heated ejecta (Gaensler & Slane 2006). The age of the system makes it probable, that the pulsar has traveled a significant distance due to its randomly orientated space velocity obtained in the supernova explosion. This leads to the class of offset pulsar wind nebulae, in which it is possible that the pulsar leaves the older PWN and creates a younger, smaller PWN around its position. Depending on the initial velocity of the pulsar and the surrounding medium, it is also possible for the pulsar to develop a bow-shock. In the last evolutionary phase, the energy output of the pulsar will not be sufficient to power a synchrotron nebula and the only visible signature of the pulsar will be the forward shock of the pulsar due to its movement through the neutral gas (Gaensler & Slane 2006).

1.3 Acceleration Mechanisms in Pulsar Wind Nebulae

In this Section, a short overview of the mechanisms that are responsible for accelerating the particles in pulsar wind nebulae will be given. Diffusive shock acceleration is currently regarded to be the most probable mechanism for the production of high-energy particles in all types of supernova remnants (for a detailed review see e.g. Reynolds 2008). In Section 1.3.1 this mechanism will be briefly introduced, together with the stochastic acceleration, the other mechanism referred to as Fermi-type acceleration. In the further context, other processes which might play a role in the acceleration of particles in a PWN are reviewed and the limits on the energies that can be reached in the wind termination shock will be discussed at the end of the Section.

1.3.1 Fermi-type Processes

In 1949, Enrico Fermi first proposed a mechanism for the stochastic acceleration of particles to high energies in interactions with molecular clouds (Fermi 1949). He used this mechanism to explain the formation of cosmic rays in the interstellar medium. In this approach, irregularities of the interstellar magnetic field act as randomly moving magnetic mirrors with which the particles collide. Fermi showed that particles gain energy on average, since the probability of a head-on collision is higher than that for a head-tail collision. The average energy gain per collision is

$$\left\langle \frac{\Delta E}{E} \right\rangle = \frac{8}{3}\left(\frac{V}{c}\right)^2 , \tag{1.18}$$

where V is the velocity of the magnetic mirrors, i.e. the irregularities in the magnetic field. In this type of acceleration, the energy gain of the particle is proportional to $(V/c)^2$ and it is thus called the second order Fermi acceleration. For an explicit derivation of this result, see e.g. Longair (2004b). An important result of this mechanism was, that it predicts a power-law spectrum and can thus explain the shape of the spectra that many sources of cosmic rays exhibit. However, taking into account the small velocities of interstellar clouds, the neglected ionization losses and the small gain in energy achieved in this process, it becomes apparent that this mechanism cannot account for the observed high-energy cosmic rays.

The first order Fermi acceleration mechanism is also known as the diffusive shock acceleration and currently regarded as the most likely explanation of particle acceleration in supernova remnants. In this process, high-energy particles diffusively cross a passing shock multiple times. In each cycle they gain energy in the order of $\Delta E/E \approx V/c$. Due to the escape probability of the particles, the resulting energy spectrum has a power-law shape, $N(E) \sim E^{-p}$, with an index of $p \approx 2$. Although this spectral index is at odds with many observations, the first order Fermi acceleration for the first time provided a mechanism with which particles can efficiently be accelerated and in which a unified spectral shape is plausibly obtained for a variety of astrophysical sources.

1.3.2 Other Processes

Besides the Fermi-type processes, there also have been numerous modifications and suggestions for alternative acceleration mechanisms. A steeper spectrum of the accelerated particles can, for example, be obtained for weaker shocks (Hinton & Hofmann 2009). In another mechanism proposed by Amato & Arons (2006), ions play an important role in the acceleration of leptons. If the wind has a large component of ions, these ions will emit cyclotron waves at the shock. Leptons can then be accelerated by a resonant absorption of these cyclotron waves. In a publication by Kirk et al. (2009) it is proposed that this process, together with an acceleration mechanism based on the reconnection of magnetic field lines (Pétri & Lyubarsky 2007), might be responsible for an acceleration of the low-energy leptons emitting synchrotron photons at radio wavelengths. Fermi-type acceleration processes would then account for the high-energy leptons emitting synchrotron radiation at X-ray energies. Such a scenario would provide a theoretical backing for the broken power-law spectra that are needed to model the emission in one-zone models of PWN (de Jager & Djannati-Ataï 2009).

1.3.3 Limit on Energies

Although the exact nature of the acceleration mechanisms taking place in the wind termination shock of a PWN are yet unclear, it is possible to derive important results on the maximum energies that can be obtained. Two limits provide a useful estimate of the maximum energy: the synchrotron and the gyroradius limit for the maximum lepton energy (de Jager & Djannati-Ataï 2009).

Synchrotron Limit

The synchrotron limit was first discussed by de Jager et al. (1996) who stated that leptons in a relativistic pulsar wind shock can be accelerated via first order Fermi acceleration at a rate as fast as the gyroperiod. The acceleration rate of a lepton occurs with a rate of $t_{\mathrm{acc}} = \alpha\nu_{\mathrm{g}}$, where $\alpha \leq 1$ is a constant depending on the shock geometry. The second parameter, ν_{g}, is the gyrofrequency, i.e. the number of times per second that a charged particle rotates about the magnetic field direction. It is given by (Longair 2004a)

$$\nu_{\mathrm{g}} = \frac{ZeB}{2\pi\gamma m}\,, \tag{1.19}$$

with the charge of the particle given Ze. For a non-relativistic electron, the gyrofrequency is $\nu_{\mathrm{g}} = eB/(2\pi m_{\mathrm{e}}) = 2.8\,\mathrm{MHz\,G^{-1}}$. Coming back to the synchrotron limit on the maximum energy that a lepton in a relativistic shock can obtain, we now consider a particle moving in a strong magnetic field. In this case, the acceleration will have to compete against the energy loss due to synchrotron radiation. Following de Jager et al. (1996) this can be expressed as

$$\frac{\mathrm{d}E_{\mathrm{e}}}{\mathrm{d}t} = \alpha\frac{ecB_{\mathrm{S}}}{2\pi} - \frac{2e^4B_{\mathrm{S}}^2\sin^2\theta\gamma^2}{3m_e^2c^3}\,, \tag{1.20}$$

where θ is the pitch angle of the lepton toward the magnetic field. The first part of this equation corresponds to the energy gain obtained in a first order Fermi acceleration and the second part corresponds to the synchrotron losses of the accelerated particles. The maximum lepton energy that can be obtained is then equal to

$$E_{\mathrm{e,max}} = \gamma_{\mathrm{max}}m_ec^2 = 6.1\times10^{14}\left(\frac{\alpha}{\langle\sin^2\theta\rangle B_{-3}}\right)^{1/2}\mathrm{eV}. \tag{1.21}$$

In this expression, B_{-3} is the magnetic field strength in units of $10^{-3}\,\mathrm{G}$. The maximum energy for synchrotron photons from the leptons in the shock can be calculated to be

$$E_{\gamma,\mathrm{max}} = \frac{hc}{r_e}\frac{D\alpha}{\sin\theta}\left(\frac{3}{4\pi}\right)^2 = 25\left(\frac{D\alpha}{\sin\theta}\right)\mathrm{MeV}, \tag{1.22}$$

where D is the Doppler factor of the emitting particle to the observer and the factor $D\alpha/\sin\theta$ is expected to be of order unity (de Jager et al. 1996). Interestingly, this maximum photon energy does not depend on the lepton energy, magnetic field or radius of the shock, but solely on the Doppler factor of the emitting particle.

Gyroradius Limit

The energy losses of an accelerated particle via synchrotron losses places one limit on the maximum energy that can be reached. Another constraint comes from the condition, that a particle is only accelerated as long as it is still within the shock. This is stated in the gyroradius limit, which was first introduced by Harding & Gaisser (1990). The gyroradius (= Larmor radius) of the particles with the maximum energy must be smaller than the shock radius:

$$r_{\mathrm{L}} = \frac{E_{\mathrm{e,max}}}{eB_{\mathrm{S}}} = \epsilon R_{\mathrm{S}} < R_{\mathrm{S}}\,, \tag{1.23}$$

where the factor ϵ must be smaller than 1, for a particle to be contained inside the acceleration zone. This limit becomes applicable in weaker magnetic fields, where the synchrotron losses do not constrain the maximum energy. Rearranging Eq. 1.23, one obtains an expression for the maximum lepton energy depending on the shock radius and the magnetic field strength at the shock:

$$E_{\mathrm{e,max}} = e\epsilon R_{\mathrm{S}}B_{\mathrm{S}}\,. \tag{1.24}$$

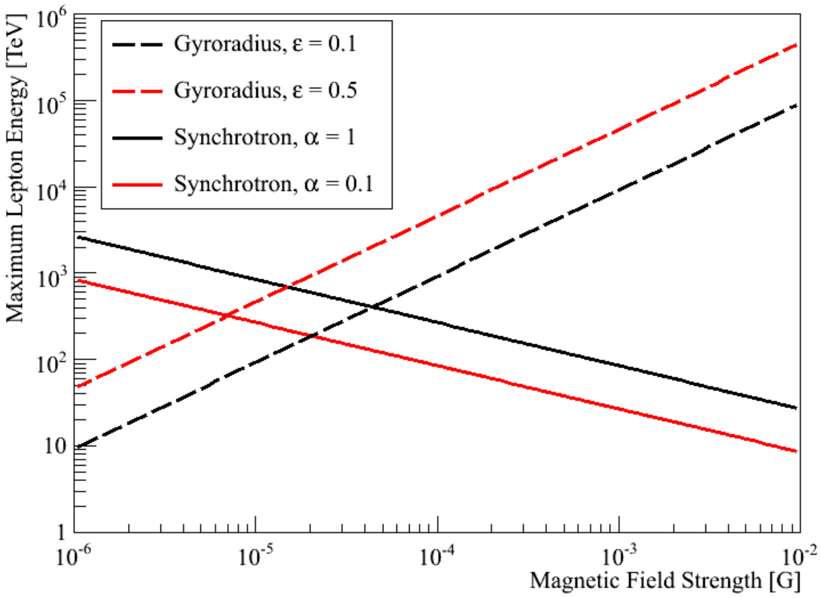

Fig. 1.6: *Maximum lepton energy in a PWN shock that can be obtained according to the gyroradius limit and the synchrotron limit. The maximum lepton energy in units of TeV is plotted against the magnetic field strength in the PWN shock. For the calculation of the gyroradius limit a shock radius of $R_S = 0.1\,\mathrm{pc}$ was used, whereas for the synchrotron limit an isotropic distribution of the pitch angles θ was assumed.*

If one takes into account the expression derived by Kennel & Coroniti (1984b) for the magnetic field (1.15), it is possible to obtain the maximum energy in terms of the spin-down luminosity $\dot{E}$ and the shock parameters σ and κ:

$$E_{\mathrm{e,max}} = e\epsilon\kappa\sqrt{\frac{\sigma}{1+\sigma}\frac{\dot{E}}{c}} = \kappa\left(\frac{\epsilon}{0.2}\right)\left(\frac{\sigma}{0.1}\dot{E}_{36}\right)^{1/2} 110\,\mathrm{TeV}, \qquad (1.25)$$

where $\dot{E}_{36}$ is the spin-down luminosity of the pulsar in units of $10^{36}\,\mathrm{erg\,s^{-1}}$. The gyroradius limit is believed to become important for older remnants, where the magnetic field strength is lower. This expression for the gyroradius limit was used by de Jager & Djannati-Ataï (2009) to estimate a maximum lepton energy of 350 TeV for a Vela-like pulsar, using a value of $\epsilon = 0.2$.

Figure 1.6 illustrates the constraints on the maximum lepton energy in the two limits discussed above. For the synchrotron limit, two curves with $\alpha = 0.1$ and $\alpha = 1$ are shown. An isotropic distribution of the pitch angle θ was assumed in the calculation. The two dashed lines visualize the maximum lepton energy in the gyroradius limit for $\epsilon = 0.1$ and $\epsilon = 0.5$. As can be seen from Fig. 1.6, the energy loss due to synchrotron radiation places the more constraining limit on the highest lepton energy that can be achieved for magnetic field strengths above roughly 10 to 20 μG. For lower magnetic fields at the shock, the maximum lepton energy is constrained by the gyroradius limit, as leptons with higher energies would escape from the regions where the acceleration is taking place.

1.4 Radiation Processes in Pulsar Wind Nebulae

In the previous Sections of this Chapter, the focus was placed mainly on introducing the current understanding of the characteristics of pulsars and their nebulae, and on how particles are accelerated in such objects. At this point, we will turn our attention to the reason why we are actually able to detect nonthermal radiation from these objects. The term “nonthermal radiation” “refers” to any radiation process which emits radiation that does not follow a blackbody distribution. Blackbody radiation is emitted by particles in thermal equilibrium, so the emission of nonthermal radiation is an indication that the particle population is not in a thermal equilibrium state. Nonthermal radiation is emitted by charged particles interacting with the electromagnetic field or with other particles in the pulsar wind nebula. The following processes are relevant for the study of pulsar wind nebulae:

- synchrotron radiation,
- curvature radiation,
- inverse Compton radiation,
- bremsstrahlung, and
- hadronic production of γ-rays via π_0-decay.

In the present study, only synchrotron radiation from leptons in the magnetic field of the PWN and inverse Compton radiation from the interaction of leptons with background photon fields will be relevant. Therefore, we will put our focus on these two processes and only mention the other ones briefly.

1.4.1 Synchrotron Radiation

An important process in the study of Galactic and extragalactic astrophysical objects is synchrotron radiation. It is emitted by relativistic charged particles gyrating in a magnetic field (in the non-relativistic case, it is called cyclotron radiation). The main contribution to synchrotron radiation comes from light particles, mainly leptons, since the radiated power from synchrotron radiation scales with the inverse of the squared particle mass. The synchrotron energy loss rate ($\widehat{=}$ emitted power) for a lepton is given by

$$P_{\mathrm{Sy}} = -\dot{E} = \frac{4}{3}\sigma_{\mathrm{T}} c U_B \beta^2 \gamma^2 \,, \tag{1.26}$$

where $U_B = B^2/8\pi$ is the energy density of the magnetic field and $\beta = v/c$ the velocity of the lepton relative to the speed of light.

$$\sigma_{\mathrm{T}} = \frac{8\pi}{3} r_{\mathrm{e}}^2 = 6.65 \times 10^{-25}\,\mathrm{cm}^2 \tag{1.27}$$

is the Thomson cross section and r_{e} the classical electron radius. The Thomson cross section is applicable for the interaction of a non-relativistic lepton with a photon. In the relativistic case, there are deviations from this expression and the more general Klein-Nishina cross section must be used. It will be discussed in more detail in the section on inverse Compton radiation.

The spectral distribution from synchrotron radiation by a single lepton is given by (see e.g. Blumenthal & Gould 1970)

$$P_{\mathrm{emitted}}(\nu) = \frac{\mathrm{d}W}{\mathrm{d}\nu \mathrm{d}t} = \frac{\sqrt{3}e^3 B \sin\theta}{m_{\mathrm{e}}c^2} \frac{\nu}{\nu_{\mathrm{c}}} \int_{\nu/\nu_{\mathrm{c}}}^{\infty} K_{5/3}(\xi)\,\mathrm{d}\xi\,. \tag{1.28}$$

In this expression, ν_{c} is the critical frequency of the lepton, which is defined as

$$\nu_{\mathrm{c}} = \frac{3eB}{4\pi m_{\mathrm{e}} c}\gamma^2 \sin\theta\,. \tag{1.29}$$

$K_{5/3}$ is a modified Bessel function of order 5/3. For the calculation of the synchrotron spectra, the approximation of

$$F(\nu/\nu_{\mathrm{c}}) = \frac{\nu}{\nu_{\mathrm{c}}} \int_{\nu/\nu_{\mathrm{c}}}^{\infty} K_{5/3}(\xi)\,\mathrm{d}\xi \approx 1.7826 \left(\frac{\nu}{\nu_{\mathrm{c}}}\right)^{0.3005} \exp\left(\frac{\nu}{\nu_{\mathrm{c}}}\right) \tag{1.30}$$

is used, which was derived from a fit of tabulated values of the Bessel function. The approximation is illustrated in Fig. 1.7 in comparison to the tabulated function values.

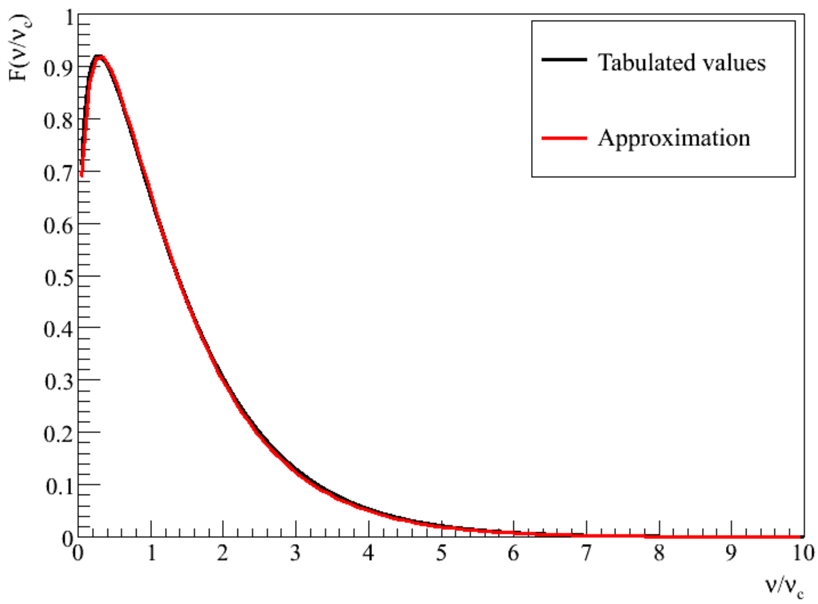

Fig. 1.7: *Plot of tabulated values for $F(\nu/\nu_{\mathrm{c}})$ and comparison to the function used for the approximation (see Eq. 1.30).*

The next step is to look at the synchrotron spectrum that is emitted by an ensemble of leptons. Below, we assume that the number of leptons, N, is distributed according to γ, the respective Lorentz factor of the particle (which is equivalent to its energy). The lepton distribution, $N(\gamma)$, has a power-law shape of the form

$$N(\gamma) = k\gamma^{-p} N(\theta)/4\pi\,. \tag{1.31}$$

If there is no pitch angle dependancy for the leptons, then Eq. 1.31 reduces to $k\gamma^{-p}$. The total synchrotron emission for this lepton spectrum is then equal to (Blumenthal & Gould 1970):

$$\frac{\mathrm{d}W}{\mathrm{d}\nu \mathrm{d}t} = \frac{\sqrt{3}ke^3 B}{4\pi m_{\mathrm{e}} c^2} \int N(\theta) \sin\theta\,\mathrm{d}\Omega_\theta \int_{\gamma_1}^{\gamma_2} \gamma^{-p}\,\mathrm{d}\gamma \frac{\nu}{\nu_{\mathrm{c}}} \int_{\nu/\nu_{\mathrm{c}}}^{\infty} K_{5/3}(\xi)\,\mathrm{d}\xi\,. \tag{1.32}$$

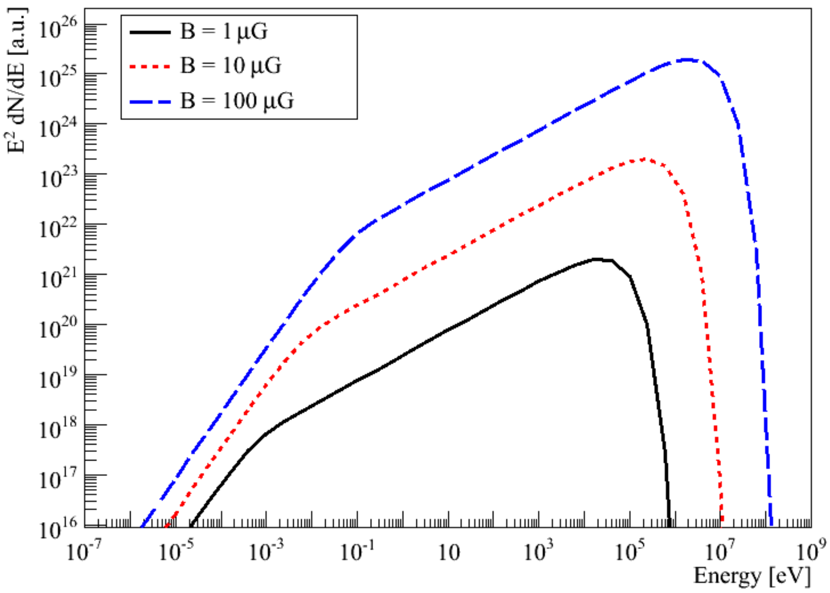

Fig. 1.8: *Differential synchrotron spectrum for three different magnetic field strengths of* $B = 1\,\mu G$, $B = 10\,\mu G$ *and* $B = 100\,\mu G$. *For all curves, the same lepton spectrum with an index of* $p = 2$ *in the energy range of* $10^{11} - 10^{15}$ *eV was used.*

Here, Ω_θ denotes the solid angle. A simplification of this expression is possible by making two assumptions. If the leptons are locally isotropic, then $N(\theta) = 1$ and the integral over the pitch angles can be calculated. Furthermore, if one assumes that the end points of the lepton spectrum do not contribute, the integration boundaries for the lepton spectrum can be set to zero and infinity. The resulting synchrotron spectrum is then of the form:

$$\frac{\mathrm{d}W}{\mathrm{d}\nu\mathrm{d}t} = \frac{4\pi k e^3 B^{(p+1)/2}}{m_\mathrm{e}c^2}\left(\frac{3e}{4\pi m_\mathrm{e}c}\right)^{(p-1)/2} a(p)\nu^{-(p-1)/2}\,, \tag{1.33}$$

with

$$a(p) = \frac{2^{(p-1)/2}\sqrt{3}\Gamma[(3p-1)/12]\Gamma[(3p+19)/12]\Gamma[(p+5)/4]}{8\pi^{1/2}(p+1)\Gamma[(p+7)/4]}\,. \tag{1.34}$$

Blumenthal & Gould (1970) give a table of values for $a(p)$, but for values of p between 1.5 and 5, $a(p)$ is approximately equal to 0.1. For arbitrary lepton distributions, Eq. 1.32 must be evaluated replacing the power-law spectrum with the desired function. For a power-law distribution of leptons, however, Eq. 1.33 gives an important result: if the lepton spectrum has an index of p, then the emitted synchrotron spectrum also follows a power-law distribution and has an index of $\Gamma = (p+1)/2$, regardless of the magnetic field. For different magnetic field strengths, the energy range of the emitted radiation and the total emitted flux change. This is illustrated in Fig. 1.8, where the synchrotron spectrum is plotted for three different magnetic field strengths. For all curves, the same lepton spectrum was used. The lepton spectrum has an index of $p = 2$, with a minimum energy of 10^{11} eV and a maximum energy of 10^{15} eV. The resulting spectral index for the synchrotron spectrum is $\Gamma = 1.5$, which is true for the energy range from roughly 10^{-3} eV to 10^5 eV in Fig. 1.8. Outside that range, the synchrotron spectrum shows cutoff effects due to the minimum and maximum energy.

Before moving on to the inverse Compton radiation, we will have a look at two useful estimates for synchrotron radiation. Following de Jager & Djannati-Ataï (2009), the lepton energy that is required for the emission of synchrotron photons with a certain energy can be calculated as

$$E_\mathrm{e} = B^{-1/2} E_\mathrm{keV}^{1/2} (70\,\mathrm{TeV})\,, \tag{1.35}$$

where B_{-5} is the magnetic field in units of 10^{-5} G and E_keV is the mean energy of the synchrotron photons in keV. The synchrotron lifetime is the ratio of the lepton energy to the energy losses due to synchrotron radiation and can be estimated as

$$\tau_\mathrm{Sy} = B_{-5}^{-3/2} E_\mathrm{keV}^{-11/2} (1.2\,\mathrm{kyr})\,. \tag{1.36}$$

1.4.2 Inverse Compton Radiation

While synchrotron radiation originates in the interaction of charged particles with the magnetic field, inverse Compton radiation is emitted when high-energy particles interact with photons. In principle, it is possible to have IC emission from the collision of nuclei and photons. For all practical purposes, however, the interaction of leptons and photons is the only relevant case, since the cross section for heavier particles is far smaller than for leptons. In astrophysical objects the leptons can interact with a number of different target photon populations. The most common case is the interaction with the photons of the cosmic microwave background radiation (CMBR). In such interactions, leptons in a PWN can scatter the low-energy photons up to TeV-energies. Other target photon fields can be infrared photons emitted by dust, starlight or the synchrotron radiation emitted by the leptons. The IC emission from the synchrotron radiation field (synchrotron-self Compton, SSC) is only an issue for very young systems with a very strong magnetic field, e.g. for the Crab nebula. For MSH 15−5*2* the SSC emission is many orders of magnitude lower than the IC emission off other radiation fields and therefore it will not be considered in the further context.

The cross section for the interaction between a lepton and a photon was mentioned earlier, when the Thomson cross section, σ_T, was introduced in Eq. 1.27. For relativistic leptons, Klein & Nishina (1929) derived the cross section from quantum electrodynamics, which is known as the Klein-Nishina cross section. The cross section is given by (Rybicki & Lightman 1979):

$$\sigma_\text{K-N} = \sigma_\mathrm{T} \frac{3}{4} \left[\frac{1+x}{x^3} \left(\frac{2(1+x)}{1+2x} - \frac{1}{x} \ln(1+2x) \right) + \frac{1}{2x} \ln(1+2x) - \frac{1+3x}{(1+2x)^2} \right]\,. \tag{1.37}$$

In this expression, $x = h\nu / m_\mathrm{e} c^2$ is the energy of the incident photon in units of the electron rest energy.

For the nonrelativistic case ($x \ll 1$), the Klein-Nishina cross section reduces to the classical Thomson cross section and can be approximated by (Aharonian 2004):

$$\sigma_\text{K-N} \approx \sigma_\mathrm{T} \left(1 - 2x + \frac{26x^2}{5} + \ldots \right) \approx \sigma_\mathrm{T}(1-2x) \approx \sigma_\mathrm{T}\,. \tag{1.38}$$

For photons with very high energies in the ultrarelativistic limit ($x \gg 1$), the cross section simplifies to

$$\sigma_\text{K-N} \approx \sigma_\mathrm{T} \frac{3}{8} \left(\frac{\ln(4x)}{x} \right)\,, \tag{1.39}$$

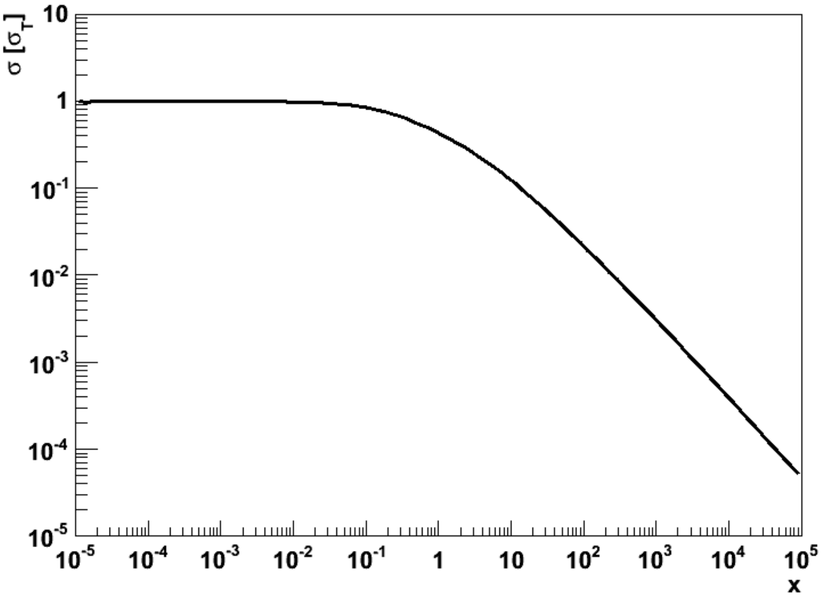

Fig. 1.9: *Klein-Nishina cross section as given by Eq. 1.37. The total cross section is given in units of the Thompson cross section, the variable x is the energy of the incident photon in units of the electron rest energy.*

and becomes roughly proportional to $1/x$. Figure 1.9 shows the cross section in units of the Thompson cross section plotted against the variable x, and illustrates the cross section in the nonrelativistic and the ultra-relativistic limit.

The inverse Compton spectrum from high-energy leptons is derived in detail in Blumenthal & Gould (1970). The important results for this work will now be briefly introduced. We will denote the initial photon energy in the lab system with ϵ and the energy of the scattered photon with ϵ_1. The ratio of the scattered photon energy to the initial electron energy is denoted as E_1 and given by

$$E_1 = \frac{\epsilon_1}{\gamma m_\mathrm{e} c^2} \, . \tag{1.40}$$

The photon gas is assumed to be isotropic and its differential density is given by $\mathrm{d}n = n(\epsilon)\mathrm{d}\epsilon$. A high-energy electron passing through the photon gas will lead to a scattered photon spectrum of

$$\frac{\mathrm{d}N_{\gamma,\epsilon}}{\mathrm{d}t\,\mathrm{d}E_1} = \frac{2\pi r_\mathrm{e}^2 m_\mathrm{e} c^3}{\gamma} \frac{n(\epsilon)\mathrm{d}\epsilon}{\epsilon} \left[2q \ln q + (1+2q)(1-q) + \frac{(\Gamma_\epsilon q)^2}{2(1+\Gamma_\epsilon q)}(1-q) \right] . \tag{1.41}$$

In this expression, the dimensionless parameters Γ_ϵ and q are defined as

$$\Gamma_\epsilon = \frac{4\epsilon\gamma}{m_\mathrm{e} c^2} \tag{1.42}$$

and

$$q = \frac{E_1}{\Gamma_\epsilon (1 - E_1)} \tag{1.43}$$

The parameter Γ_ϵ indicates, whether the scattering occurs in the Thomson regime or in the Klein-Nishina regime. For $\Gamma_\epsilon \ll 1$, the Thomson limit applies. In this case, $E_1 \ll 1$

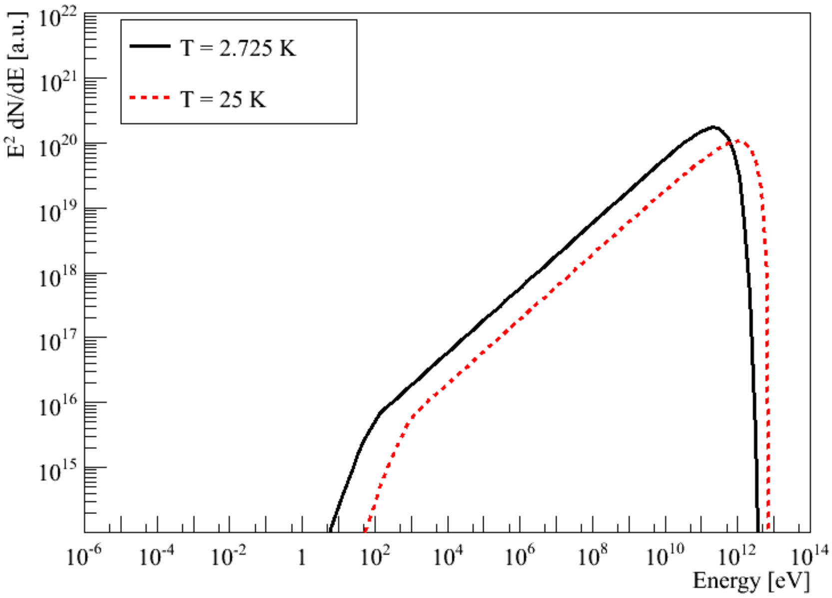

Fig. 1.10: *Inverse Compton spectrum for two different target photon fields of $T = 2.725\,K$ and $T = 25\,K$ and an energy density of $U_{\rm rad} = 0.25\,eV\,cm^{-3}$. For this plot, a lepton spectrum with an index of $p = 2$ in the energy range from $10^8 - 10^{13}$ eV was used.*

and the last term in the brackets of Eq. 1.41 is negligible (Blumenthal & Gould 1970). For $\Gamma_\epsilon \gg 1$, the Klein-Nishina regime applies. The possible range of values for E_1 and q can be restricted by the kinematics of the scattering process. For E_1 the range is

$$1 \gg \frac{\epsilon}{\gamma m_{\rm e} c^2} \leq E_1 \leq \frac{\Gamma_\epsilon}{1+\Gamma_\epsilon}\,, \tag{1.44}$$

and for q it is

$$1 \gg \frac{1}{4\gamma^2} \leq q \leq 1\,. \tag{1.45}$$

Equation 1.41 gives the resulting spectrum for one lepton. To obtain the total IC spectrum from a distribution of leptons, we now have to integrate this equation over all values of the lepton Lorentz factor γ:

$$\frac{\mathrm{d}N_{\rm tot}}{\mathrm{d}t\,\mathrm{d}\epsilon_1} = \int\int N_\epsilon(\gamma)\frac{\mathrm{d}N_{\gamma,\epsilon}}{\mathrm{d}t\,\mathrm{d}\epsilon}\,\mathrm{d}\gamma\,. \tag{1.46}$$

With this equation, it is possible to calculate the IC spectra for any lepton spectra and it was used to obtain the results presented in Chapter 5. Figure 1.10 shows the IC emission spectra from the scattering of a power-law distribution of leptons off two different target photon fields with temperatures of $T = 2.725$ K and $T = 25$ K, respectively. The energy densities of both photon distributions was set to the same value of $U_{\rm rad} = 0.25\,\mathrm{eV\,cm^{-3}}$, the energy density of the CMBR. The IC spectra show that for the same lepton spectrum, the peak of the emitted IC radiation gets shifted to higher energies, approaching a maximum energy set by the maximum energy of the leptons.

For a power-law distribution of the leptons, it is possible to evaluate the integrals in Eq. 1.46 (Blumenthal & Gould 1970). It is assumed that the lepton spectrum has the shape

$$N_{\rm e}(\gamma) = K_{\rm e}\gamma^{-p}\,. \tag{1.47}$$

The spectrum is limited by the low-energy cutoff γ_0 and at high energies by $\gamma_{\rm max}$, so that $\gamma_0 < \gamma < \gamma_{\rm max}$. It is furthermore assumed, that the low- and high-energy endpoints of the photon spectrum do not contribute significantly and that the photon distribution has a blackbody characteristic of the form

$$n(\epsilon) = \frac{1}{\pi^2(\hbar c)^3}\frac{\epsilon^2}{e^{\epsilon/kT}-1}\,. \tag{1.48}$$

Equation 1.46 then simplifies to a power law in ϵ_1 (Blumenthal & Gould 1970)

$$\frac{\mathrm{d}N_{\rm tot}}{\mathrm{d}t\,\mathrm{d}\epsilon_1} = \frac{r_{\rm e}^2}{\pi\hbar^3c^2}K_{\rm e}(kT)^{(p+5)/2}F(p)\epsilon_1^{-(p+1)/2}\,, \tag{1.49}$$

where $F(p)$ is equal to

$$F(p) = 2^{p+3}\frac{p^2+4p+11}{(p+3)^2(p+1)(p+5)}\Gamma\left[\frac{p+5}{2}\right]\zeta\left[\frac{p+5}{2}\right]\,. \tag{1.50}$$

Here, ζ is the Riemann zeta function. A tabulated list of values for $F(p)$ is given as Table 1 in Blumenthal & Gould (1970). The resulting IC spectrum for a power-law lepton spectrum is then proportional to

$$\frac{\mathrm{d}W}{\mathrm{d}\nu\,\mathrm{d}t} \propto \nu^{-(p+1)/2}\,. \tag{1.51}$$

This highlights an important aspect of the relation between synchrotron and IC radiation in the Thomson regime: a lepton spectrum with a power-law shape will lead to synchrotron and IC spectra with the same photon index ($(p+1)/2$). This has its foundation in the underlying physics, as the process of synchrotron radiation can be regarded as an inverse Compton scattering of a lepton off the virtual photon from the magnetic field. We will now have a look at the energy losses of a lepton due to IC scattering and will arrive at similar expression as well.

The total energy loss rate for per electron can be computed from (Blumenthal & Gould 1970)

$$-\frac{\mathrm{d}E}{\mathrm{d}t} = \int(\epsilon_1-\epsilon)\frac{\mathrm{d}N}{\mathrm{d}t\,\mathrm{d}\epsilon_1}\,\mathrm{d}\epsilon_1\,. \tag{1.52}$$

For the Thomson regime ($\Gamma_\epsilon \ll 1$), this expression simplifies to

$$-\frac{\mathrm{d}E}{\mathrm{d}t} = \frac{4}{3}\sigma_{\rm T}c\gamma^2U_{\rm rad}\,, \tag{1.53}$$

where $U_{\rm rad}$ is the energy density of the radiation field. In the Klein-Nishina case ($\Gamma_\epsilon \gg 1$), the expression is more complicated and the energy loss is equal to

$$-\frac{\mathrm{d}E}{\mathrm{d}t} = \pi r_{\rm e}^2\frac{(m_{\rm e}ckT)^2}{6\hbar^3}\left(\ln\frac{4\gamma kT}{m_{\rm e}c^2} - \frac{5}{6} - C_E - C_l\right)\,, \tag{1.54}$$

where $C_E \approx 0.5772$ is the Euler-Mascheroni constant[3] and $C_l = 0.5700$[4]. It should be noticed that in the comparison of the energy losses in the two limits, the energy loss in the

[3]The Euler-Mascheroni constant is defined as the difference between the harmonic series and the natural logarithm: $C_E = \lim\limits_{n\to\infty}\left(\sum_{k=1}^{n}\frac{1}{k} - \ln(n)\right) = \int_1^\infty\left(\frac{1}{\lfloor x\rfloor} - \frac{1}{x}\right)dx$.

[4]C_l is defined as $C_l = \frac{6}{\pi^2}\sum_{k=2}^{\infty}\frac{\ln k}{k^2}$

Klein-Nishina regime increases only logarithmically in energy, whereas in the Thomson regime the loss is proportional to $\propto E^2$.

In the Thomson limit, it is also possible to derive a simple expression for the mean and the maximum energy of the scattered photon. Following the derivation of Longair (2004a), the maximum energy for the scattered photon, $\epsilon_{1,\mathrm{max}}$, is equal to

$$\epsilon_{1,\mathrm{max}} \approx 4\gamma^2\epsilon\,. \tag{1.55}$$

The average energy of a scattered photon, $\bar{\epsilon}_1$, is

$$\bar{\epsilon}_1 \approx \frac{1}{3}\epsilon_{1,\mathrm{max}} \approx \gamma^2\epsilon\,. \tag{1.56}$$

Similar to the synchrotron radiation, we will also give two useful expressions for the energy and the lifetime of leptons that emit TeV γ-rays via IC radiation. The expressions are valid for the interaction with the CMBR photons. This is the dominant component in many cases. Corrections for the Klein-Nishina regime, which becomes important for the IC scattering off infrared or optical photons are given e.g. by de Jager (2005). For the up-scattering of a CMBR photon to the energy E_{TeV} via the IC process, one needs a mean electron energy of

$$E_{\mathrm{e}} = E_{\mathrm{TeV}}^{1/2}(18\,\mathrm{TeV})\,. \tag{1.57}$$

Thus, a lepton energy of $\approx 20\,\mathrm{TeV}$ is required if IC photons in the TeV range are observed. This translates to Lorentz factors greater than 10^7. Combining Eq. 1.57 with the expression for synchrotron radiation (Eq.1.35), it is possible to relate the two processes:

$$E_{\mathrm{keV}} = 0.06 B_{-5} E_{\mathrm{TeV}}\,. \tag{1.58}$$

If IC photons with energy E_{TeV} are observed, then the emitting leptons should also be visible via their synchrotron radiation at an energy E_{keV}. According to de Jager & Djannati-Ataï (2009), the synchrotron lifetime of the leptons that scatter the CMBR photons to TeV energies can be expressed (in the Thomson limit) as

$$\tau_{\mathrm{IC}} = B_{-5}^{-2} E_{\mathrm{TeV}}^{-1/2}\,. \tag{1.59}$$

A contribution of the energy losses due to IC emission is only relevant for very low magnetic fields below the average Galactic magnetic field strength. In all other cases, the synchrotron losses will dominate by far over the IC losses.

1.4.3 Other radiation processes

For the modeling of the radiation in the PWN MSH 15−52 (see Chapter 5), only the synchrotron and IC processes are relevant. However, in other regions of a supernova remnant and in other astrophysical objects further radiation processes are important. We will now briefly discuss these.

Curvature radiation

Curvature radiation is very similar to synchrotron radiation and usually treated in the same context. It is emitted by charged particles that are accelerated along the magnetic field lines, contrary to synchrotron radiation, where the particles are accelerated perpendicular to the magnetic field. Curvature radiation becomes important in the presence of very strong magnetic fields and is, for example, relevant for the radiation emitted close to a pulsar. In a PWN, the curvature radiation is suppressed by many orders of magnitude compared to the synchrotron radiation and we will thus not consider it in more detail.

Bremsstrahlung

When a charged particle is accelerated due to the interaction with the Coulomb field of another charged particle, radiation is emitted which is called bremsstrahlung (or braking radiation). In its original definition, bremsstrahlung refers to any process, in which radiation is emitted due to the acceleration of a charged particle and thus includes synchrotron radiation. However, the prevalent usage is for radiation emitted in the interaction of charged particles with matter. Thermal and nonthermal bremsstrahlung are important in the investigation of a broad variety of sources, among them Galaxy clusters as an example for thermal bremsstrahlung and shell-type supernova remnants with a sufficient particle density for nonthermal bremsstrahlung. For MSH 15−5*2* the density is too low by far for any significant contribution of bremsstrahlung (see e.g. Dubner et al. (2002)), so we will not elucidate this process at this point and instead refer the interested reader to the detailed derivation of Blumenthal & Gould (1970).

γ-rays from Hadronic Processes

The hadronic production of VHE γ-ray photons refers to the decay of neutral π^0 mesons into two photons. Neutral and charged π mesons are generated, when high-energy protons interact with the protons of ambient matter. While the charged pions decay mainly into muons and neutrinos, the neutral pion predominantly decays as

$$\pi^0 \longrightarrow 2\gamma\,. \tag{1.60}$$

An investigation of the relevance of this radiation process for the PWN MSH 15−5*2* was conducted by Bednarek & Bartosik (2003) and they concluded that the IC radiation should dominate over the radiation from the hadronic interactions for this object. For an effective production of VHE γ-rays via this channel, two requirements must be fulfilled. Firstly, the energetics must allow for an efficient acceleration of a sufficient amount of protons. Secondly, these protons need a target medium for the proton-proton interaction, i.e. the proton density in the target region must be sufficiently large. Both factors disfavor a significant contribution of this process to the high-energy radiation observed from MSH 15−5*2* and thus, a detailed treatment for this process will not be given here. A good reference for the γ-ray production via π^0-decay is e.g. Aharonian (2004).

2 Introducing MSH 15−52

In the previous Chapter the general characteristics of pulsar wind nebulae were introduced, alongside with the acceleration and radiation mechanisms taking place in these objects. Now we will turn our focus on MSH 15−52, the pulsar wind nebula that is treated in this study in detail. The abbreviation "MSH" stands for the radio catalog composed by Mills, Slee and Hill (see Section 2.2 for references). The first two numbers in the name correspond to the first two digits of the right ascension coordinate. The sign and the third number indicate the first digit of the declination of the source, the fourth number is an ordinal number from the catalog and does not stand for any coordinate information[1]. The first part of the Chapter will give an overview of the properties of the pulsar PSR B1509−58, which supplies energy to the system via its spin-down losses. The second part will deal with the pulsar wind nebula and in the last part, the radio shell of the pulsar will be covered shortly.

In the literature, there is a historical ambiguity about the meaning of the name MSH 15−52, on the one hand referring to the whole supernova remnant (also known as G320.4−1.2), on the other hand referring to the central pulsar wind nebula inside the remnant only. In the following, we will also stick to this twofold usage, making it clear from the context which part of the system is currently being treated.

2.1 The Pulsar PSR B1509−58

Unlike many other pulsars, PSR B1509−58 was not discovered in one of the radio surveys. Seward & Harnden (1982) discovered PSR B1509−58 at X-ray energies in the range of 0.2 − 4 keV with the *Einstein* satellite and measured a pulsar period of 150 ms. Making use of the observed increase in pulsar period, they derived a spin-down luminosity of $5 \times 10^{37}\,\mathrm{erg\,s^{-1}}$ and a characteristic age of 1600 years. Shortly after the discovery, confirmation was provided by Manchester et al. (1982) with the detection of the pulsar at radio wavelengths.

A first detailed measurement of the pulsar parameters was conducted by Kaspi et al. (1994) using 11 yr of radio timing data. This work was later extended by Livingstone et al. (2005), who used 21 yr of radio and X-ray timing data obtained with the *MOST* radio telescope and the *RXTE* X-ray telescope to characterize the pulsar. The derived parameters of this analysis are shown in Table 2.1. Uncommon for such a young pulsar, no glitches in the pulsar period have been observed over the 21 years of data. Figure 2.1 shows the braking index over time and illustrates that there is no significant change. With its low characteristic age, its high spin-down luminosity and an inferred surface magnetic field of $B_p = 1.5 \times 10^{13}$ G, PSR B1509−58 is one of the youngest, most energetic, and highest field pulsars known (Gaensler et al. 2002). van der Swaluw & Wu (2001) inferred an initial spin period at the pulsar's birth of $P_0 = 69$ ms, using a scaling law between

[1] The names and coordinates in the MSH catalog are given for the B1950.0 epoch. A good overview of the astronomical catalog designations is given by Zombeck (2010).

Table 2.1: *Parameters for PSR B1509−58 from the phase-coherent and partially coherent analysis of Livingstone et al. (2005).*

Parameter	Value
Dates (Modified Julian Date)	45114 − 52925
ν [Hz]	6.633598804(3)
$\dot{\nu}$ [$10^{-11}\,\mathrm{s}^{-2}$]	−6.75801754(4)
$\ddot{\nu}$ [$10^{-21}\,\mathrm{s}^{-3}$]	1.95671(2)
$\dddot{\nu}$ [$10^{-31}\,\mathrm{s}^{-4}$]	−1.28(21)
Braking index, n	2.84209(3)
Second braking index, m	18.3(2.9)
Dispersion measure [$\mathrm{pc\,cm}^{-3}$]	253.2

the size of the SNR shell and the radius of the plerion. This result, derived from a modeling of the pulsar birth period, agrees well with the characteristic age estimate from the period measurements. The position of PSR B1509−58 ($\alpha_{J2000} = 15^h13^m55\overset{s}{.}61 \pm 0\overset{s}{.}02$; $\delta_{J2000} = -59°08'08\overset{''}{.}67 \pm 0\overset{''}{.}26$) was determined by Gaensler et al. (1999) from an analysis of observations with the *ATCA* radio telescope. The analysis of these authors also suggests, that the components of MSH 15−5*2*, radio shell, wind nebula and pulsar, are associated and lie at a distance of 5.2 ± 1.4 kpc.

At optical wavelengths, Caraveo et al. (1994) proposed to have found a counterpart for PSR B1509−58. They derived a very high optical luminosity in comparison to other young pulsars like the Crab pulsar. Furthermore, they did not detect any pulsations, unlike for other young pulsars. Kaplan & Moon (2006) analyzed data taken with the *PANIC* near-infrared camera and concluded for a different, less bright, counterpart. This candidate had already been proposed by Wagner & Seifert (2000), based on a detailed analysis of optical observations. In Fig. 2.2, three images of the region around PSR B1509−58 at near-infrared wavelengths are shown and the counterpart is marked with an “A” in the rightmost (K_S-band) image. The derived X-ray to infrared flux ratio for this counterpart is similar to that of the Crab pulsar.

Going up in energy, Kawai et al. (1991) detected pulsed emission from PSR B1509−58 in the energy range of 2 − 60 keV with the Ginga satellite. In the energy range of 0.75 − 30 MeV, Kuiper et al. (1999) reported the detection using *COMPTEL* data and confirming the pulse phase relation obtained earlier. The most sensitive measurement at these energies was recently published by Abdo et al. (2010b), who detected PSR B1509−58 with the *Fermi*-Large Area Telescope (LAT). The measured pulsar lightcurve shows two peaks, which are offset from the radio peaks by phases of 0.96 and 0.33, respectively. The spectral analysis of the pulsed emission in the energy range of 1 keV to 1 GeV indicates the presence of a low cut-off or a spectral break, rendering the detection of PSR B1509−58 at VHE γ-ray energies unlikely with the current instruments.

2.2 The Pulsar Wind Nebula

Similar to the pulsar, the observations of the pulsar wind nebula MSH 15−5*2* also span the whole range of wavelengths accessible to observations with the current-generation instruments. Remarkably, the extended emission of the PWN was already detected long

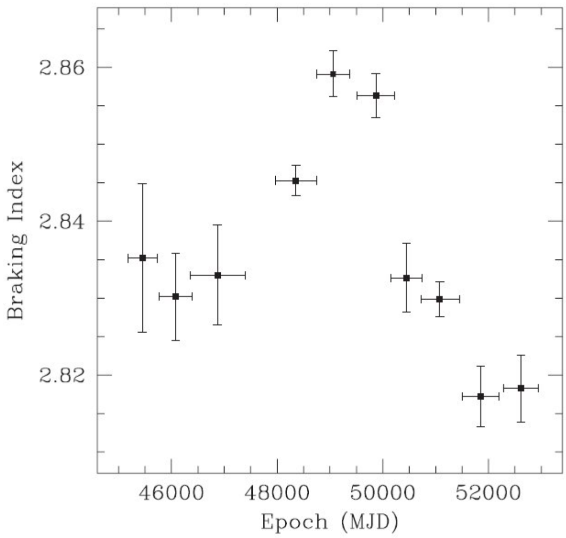

Fig. 2.1: *Calculated braking index of the pulsar PSR B1509−58 at different epochs. No statistically significant deviation from a constant braking index over the 21.3 yr of data is observed. The average value of the braking index is 2.839 ± 0.003. Figure taken from Livingstone et al. (2005).*

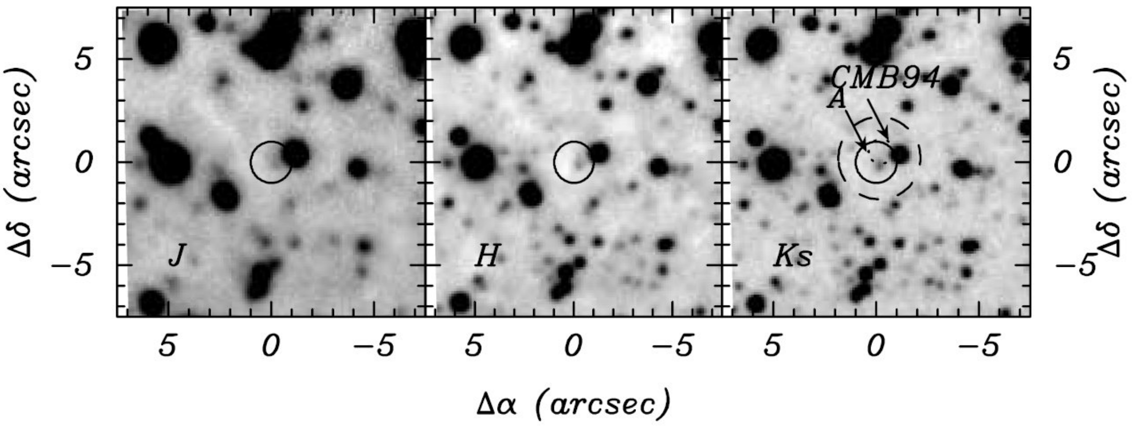

Fig. 2.2: *Near-infrared images of the region around PSR B1509−58 in three different wavelength bands taken with the PANIC camera. From left to right, the images are in the J-band (1.25 μm), H-band (1.65 μm) and K_S-band (2.0 – 2.3 μm). Figure taken from Kaplan & Moon (2006). The candidate counterpart found by Kaplan & Moon is marked with "A" and the counterpart suggested by Caraveo et al. as "CMB94".*

before the pulsed emission from PSR B1509−58 was finally discovered. Already in the survey of Mills et al. in 1961, MSH 15−52 was detected as an extended source of radio emission. The nonthermal nature of the diffuse radio emission was unveiled by Caswell et al. in 1981. The appearance of the PWN in radio and X-ray observations can be seen from Fig. 2.3. In this figure, the white contours mark the *ROSAT* PSPC data in the energy range from 0.6 – 2.1 keV from Trussoni et al. (1996). The gray scale corresponds to the MOST radio data at 843 MHz (Whiteoak & Green 1996). The radio appearance of MSH 15−52 is rather unusual, consisting of a partial shell visible in the southeast of PSR B1509−58 and a bright component to the northwest, which is centered on the optical

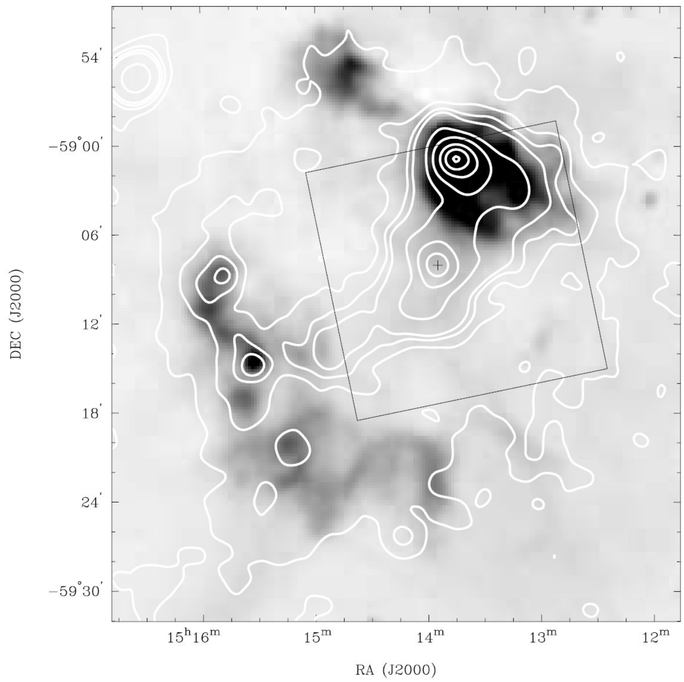

Fig. 2.3: *View of MSH 15−52 at radio and X-ray wavelengths. The gray scale corresponds to the* 843 *MHz MOST radio data (Whiteoak & Green 1996), the white contours are smoothed ROSAT PSPC data from Trussoni et al. (1996). The position of PSR B1509−58 is marked with a cross and the black box illustrates the field of view of the Chandra ACIS-I camera from the observation analyzed by Gaensler et al. (2002).*

nebula RCW 89. The X-ray picture of MSH 15−52 can be seen as the white contours in Fig. 2.3. At these energies, the source exhibits a similarly complicated morphology, comprising the pulsed emission from the pulsar, the nonthermal emission from the pulsar wind nebula and thermal emission coincident with RCW 89. Furthermore, there is also faint X-ray emission coinciding with the radio emission in the southeast of the SNR. With the increased angular resolution and higher sensitivity of newer X-ray instruments like the *Chandra* X-ray telescope, a more detailed analysis of the morphology of the PWN is possible. Figure 2.4 shows a *Chandra* image in the energy range from 0.3 to 8.0 keV of the region marked with the black box in Fig. 2.3. The diffuse, nonthermal emission from the pulsar wind nebula is clearly visible around the position of the pulsar. The emission is elongated and Gaensler et al. (2002) derived a position angle of 150 ± 5 (north through east) to define the main axis of the system. In the northeast of the pulsar, there are bright clumps of emission coinciding with the optical nebula RCW 89 on top of the diffuse emission. While Gaensler et al. (1999) argued that these might be synchrotron-emitting clumps in a diffuse thermal nebula, Gaensler et al. (2002) favor a scenario in which the clumps are thermal emission embedded in the diffuse synchrotron nebula, a scenario already proposed by Tamura et al. (1996). Gaensler et al. (2002) conducted a spectral analysis of the *Chandra* data for various regions. The spectrum of the photons from the diffuse pulsar wind is fitted well by an absorbed power law, where the best-fit parameters are an absorbing column of $N_\mathrm{H} = (9.5 \pm 0.3) \times 10^{21}\,\mathrm{cm}^{-2}$ and a photon index $\Gamma = 2.05 \pm 0.04$.

Two more recent publications present detailed analyses of a larger *Chandra* data set,

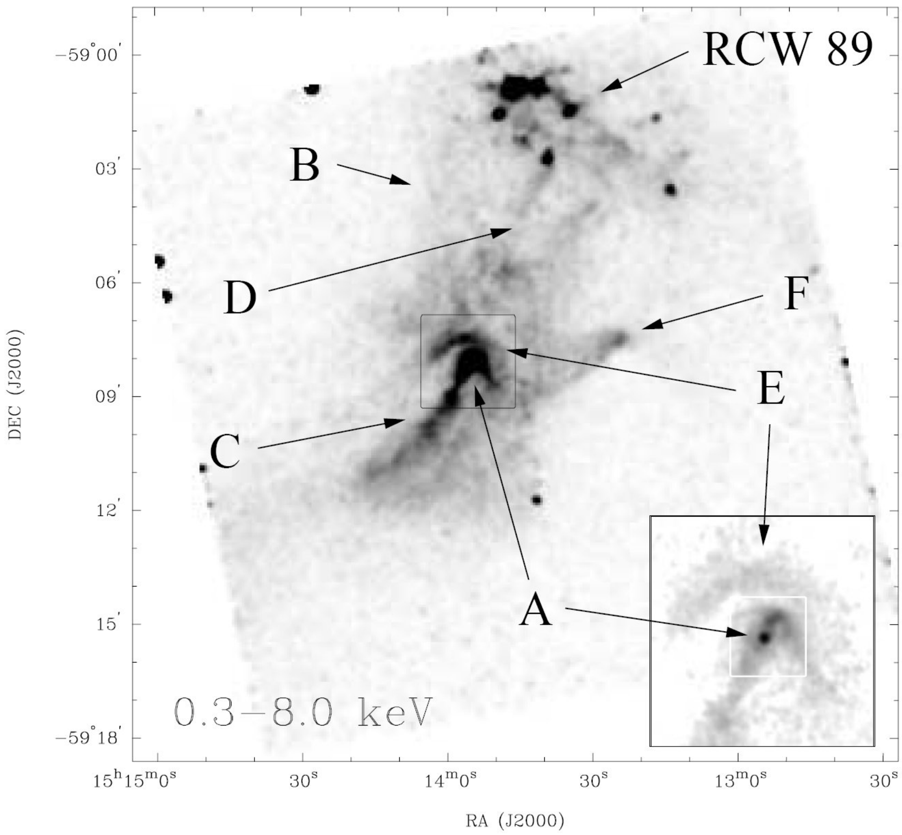

Fig. 2.4: *Chandra image of MSH 15−52 in the energy range from 0.3 to 8.0 keV. The image is exposure-corrected and convolved with a Gaussian of FWHM 10″. The central black box marks the extension of the panel on the lower right side. In this panel, the gray scale is logarithmic and the data are smoothed with a Gaussian of FWHM 4″. Figure is taken from Gaensler et al. (2002).*

extending the work of Gaensler et al. (2002). DeLaney et al. (2006) analyzed *Chandra* observations with a total exposure of $\approx$ 60 ks taken between August 2000 and October 2003 to study the time variability of MSH 15−52. Additionally, they also included archival *ROSAT* data in their analysis. DeLaney et al. (2006) found a variability of the size, number and brightness of compact knots close to the pulsar, which might be explained by turbulences in the flows surrounding the pulsar. Furthermore, a 30% increase of the brightness of the jet-like feature to the southeast of the pulsar (cf. feature C in Fig 2.4) over a time-span of 9 years was found. A spatially resolved spectral analysis of the emission from the jet-like feature shows that the spectral index steepens with increasing distance, which might be due to synchrotron cooling of the lepton population emitting the synchrotron radiation. The study with the largest data set of *Chandra* observations was conducted by Yatsu et al. (2009), who used a total exposure of 190 ks for their detailed study of the vicinity of PSR B1509−58. Figure 2.5 shows the overview image of MSH 15−52 in the left panel and a zoom on the position of PSR B1509−58 in the right panel, together with a schematic illustration of the structures as interpreted by Yatsu et al. (2009). The extension of the right-hand image is marked as a white box in the image on the left side. A ring-like feature is apparent at a distance of 10″ from the pulsar, which might correspond to a wind termination shock as observed around the Crab pulsar. Yatsu et al. (2009) also analyzed the spectral features of MSH 15−52 in annular regions around the pulsar

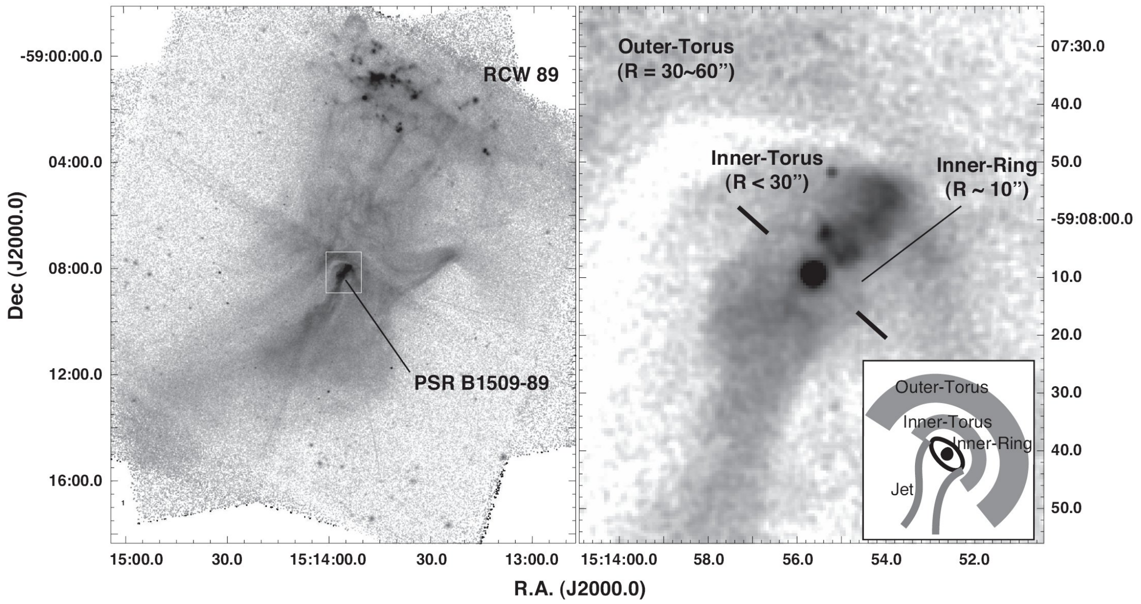

Fig. 2.5: *Overview image of MSH 15−52 using Chandra data with a total exposure of 190 ks. The image was smoothed with a Gaussian of $\sigma = 2.0''$. The right panel shows a close-up of the region around PSR B1509−58, indicated by a white box in the left panel. The inner panel of the right side shows a schematic illustration of the observable structures as interpreted by the authors. Figure taken from Yatsu et al. (2009).*

position. The resulting spatial evolution of the surface brightness and the spectral index of a power-law fit to the data are shown in Fig. 2.6 as a function of the increasing radius. A systematic steepening of the spectrum with increasing distance is observed, consistent with the results of DeLaney et al. (2006). An analysis of *XMM-Newton* observations of MSH 15−52 is part of this work and is presented in Chapter 3.

In the energy range of 20 − 200 keV, MSH 15−52 was observed by *INTEGRAL* (Forot et al. 2006) and *BeppoSAX* (Mineo et al. 2001). Besides the pulsed emission from PSR B1509−58, unpulsed emission was detected from the pulsar wind nebula, consistent with the morphology observed by *Chandra*. Figure 2.7 shows the significance map of the emission between 17 and 40 keV after the removal of the point-source contribution of PSR B1509−58. A fit of an asymmetric Gaussian to the emission yields a rotation angle of $155° \pm 4°$ measured from north through east and a width of $\sigma \approx 8'$ along the major axis. The spectrum of the combined *INTEGRAL* and *BeppoSAX* data is best fitted by a power-law spectrum with an index of $\Gamma = 2.12 \pm 0.05$ up to an energy of 160 keV. A possible spectral break at this energy is marginally significant with $\sigma = 2.9$. Forot et al. (2006) derive a magnetic field of 22 − 33 μG and a bulk velocity of 0.3 − 0.5 c in the nebula, which corresponds to a maximum energy of 400 − 730 TeV of the leptons in the outflow.

High-energy emission in the MeV and GeV energy range from the pulsar wind nebula was first detected with the *Fermi*-LAT (Abdo et al. 2010b). Above 1 GeV there is extended γ-ray emission which is spatially coincident with the X-ray and TeV PWN. In Fig. 2.8, a smoothed *Fermi*-LAT count map above 10 GeV is shown, overlaid in black are the H. E. S. S. significance contours. The morphologies in both energy ranges show a good agreement, taking into account the lower angular resolution of the *Fermi*-LAT image.

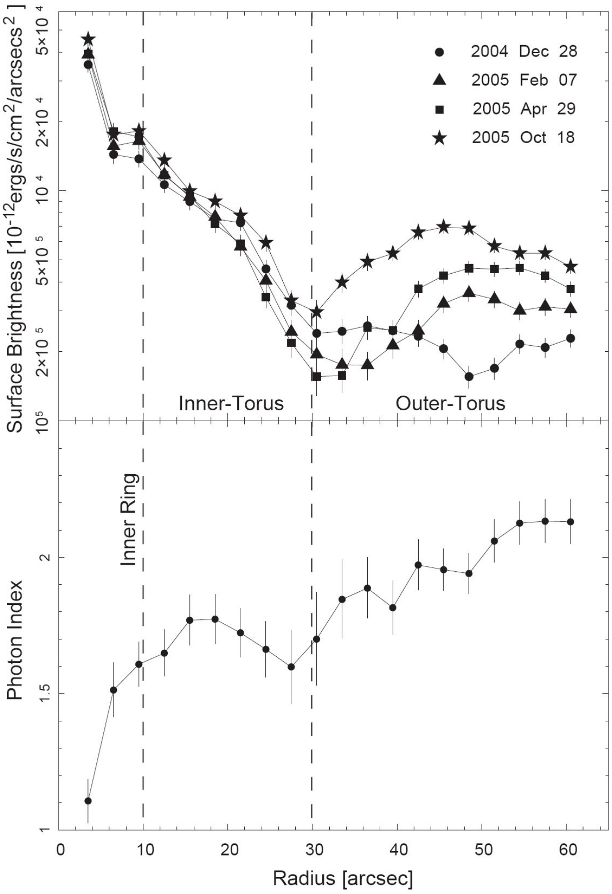

Fig. 2.6: *Top panel: spatial evolution of the X-ray surface brightness with increasing distance around the position of PSR B1509−58. Results from different epochs are shown. Bottom panel: spectral index of a power-law fit to the data for regions with increasing distance to PSR B1509−58. Figure taken from Yatsu et al. (2009).*

The spectrum of the nebula is best fitted by a power law with a spectral index of $\Gamma = 1.57 \pm 0.17 \pm 0.13$ and a flux above 1 GeV of $(2.91 \pm 0.79 \pm 1.35) \times 10^{-9}\,\mathrm{cm^{-2}\,s^{-1}}$, where the first error represents the statistical fit error and the second error is the systematic uncertainty. The spectral energy distribution (SED) of MSH 15−52 is shown in Fig. 2.9 from radio to VHE γ-ray energies. The model curves (dotted, dashed and solid lines) are from the model discussed in Abdo et al. (2010b). In this model, the photons in the radio to keV energy range are from synchrotron emission of the leptons in the nebular magnetic field. The high-energy part of the spectrum is most likely the IC emission from leptons interacting with target photon fields. The different components of the IC emission are labeled in the legend of Fig. 2.9. The mean nebular magnetic field strength for this model is $B = 17\,\mu$G, a value consistent with the lower limit of $B \geq 8\,\mu$G obtained by Gaensler et al. (2002). A hadronic model for the VHE γ-ray emission is also shown in Fig. 2.9 as the thick gray curve. However, Abdo et al. (2010b) disfavor this scenario based on the energetics, since even for a very high density in this region the pulsar cannot provide the necessary energy.

In the VHE γ-ray range (100 GeV to 100 TeV), the *CANGAROO* experiment reported a marginal detection at the 4.1 σ level (Sako et al. 2000). MSH 15−52 was later detected as

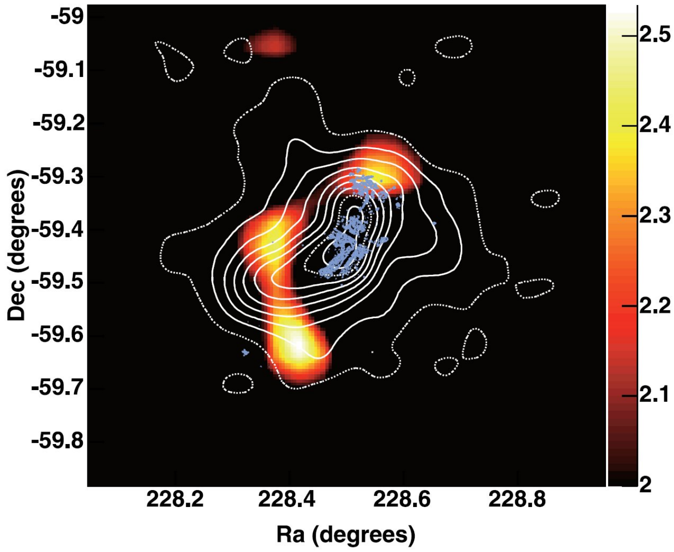

Fig. 2.7: *INTEGRAL smoothed significance map of emission from MSH 15−52 in the energy range of 17 to 40 keV after removal of the point-source contribution from PSR B1509−58 (Forot et al. 2006). The white contours correspond to the emission at TeV energies, measured with H. E. S. S.. The blue contours mark the Chandra measurement by Gaensler et al. (2002) (cf. Fig. 2.4).*

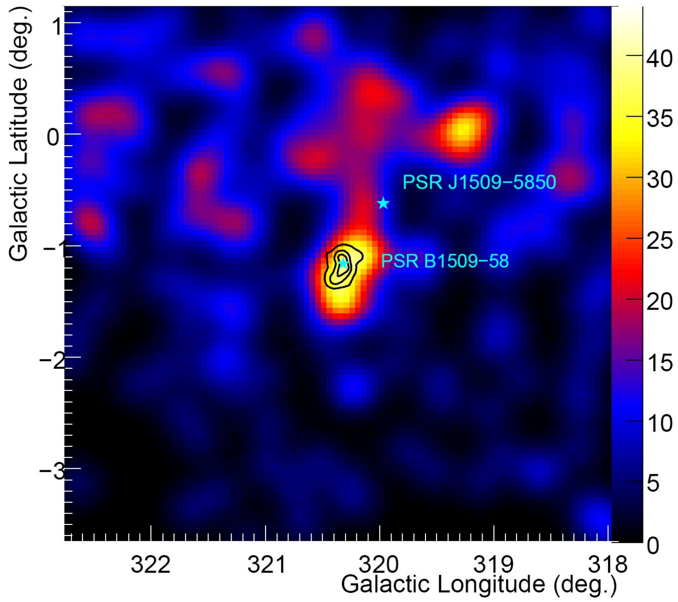

Fig. 2.8: *Smoothed Fermi-LAT count map of the region around MSH 15−52 above a photon energy of 10 GeV. The sky map is smoothed with a Gaussian of $\sigma = 0.15°$. Blue stars mark the positions of two pulsars in the field of view and the black contours are the significance contours of the VHE γ-ray emission measured with H. E. S. S.*

an extended source of VHE γ-ray emission by the H. E. S. S. experiment with a significance of 25 σ above the background level (Aharonian et al. 2005b) using 22 hours of observation. Figure 2.10 shows the smoothed VHE γ-ray excess map of MSH 15−52 in the energy

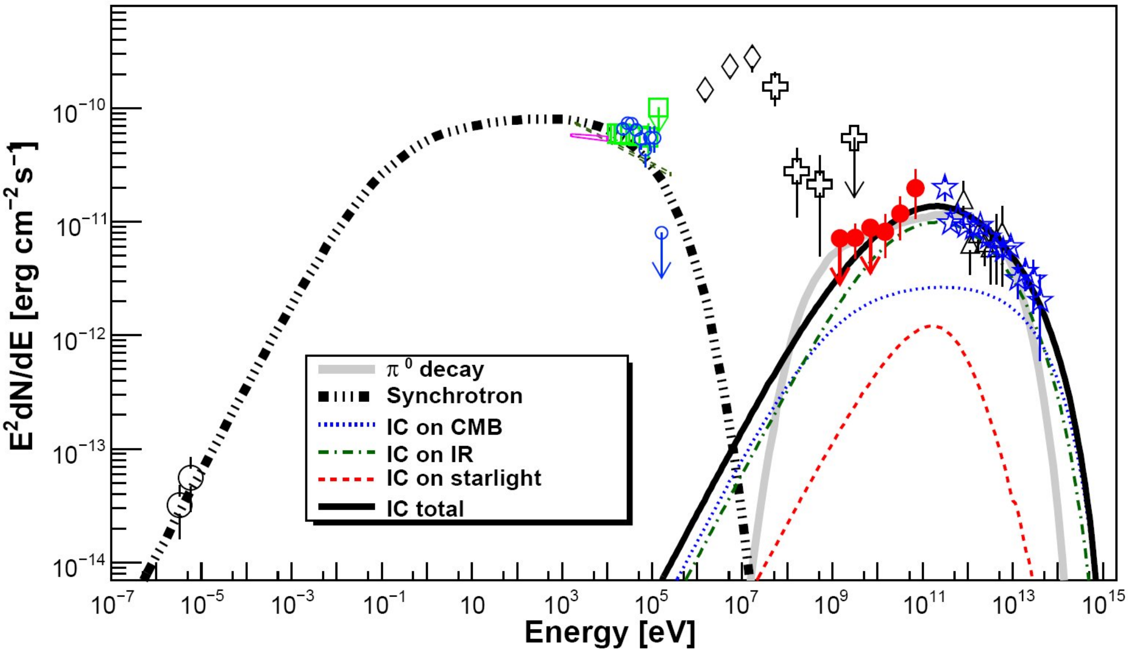

Fig. 2.9: *Spectral energy distribution of the pulsar wind nebula MSH 15−52 from radio to VHE γ-rays by Abdo et al. (2010b). Predicted model spectra for synchrotron and inverse Compton emission are overlaid and labeled in the legend. The thick gray curve is from a hadronic γ-ray model for the VHE γ-ray emission. References for the observational data points are given in Abdo et al. (2010b). The red dots are the data points from the Fermi-LAT measurement, using one year of survey data. Diamond points and open crosses mark the COMPTEL and EGRET data, which are dominated by the pulsar PSR B1509−58 and might also be contaminated by the nearby γ-ray pulsar PSR J1509 − 5850.*

range of 280 GeV to 40 TeV. The emission has an elliptical shape and follows the X-ray morphology (indicated with the white contours from the *ROSAT* measurement in Fig. 2.10). The best fit of a two-dimensional Gaussian convolved with the PSF to the unsmoothed excess map yields a centroid significantly displaced from the pulsar position. The major axis of the fit lies at $131° \pm 13°$ (measured north through east), the intrinsic standard deviation of the Gaussian is $6.4' \pm 0.7'$ along the major and $2.3' \pm 0.5'$ along the minor axis. Spectral analysis of the VHE γ-ray data yields a power-law spectrum with a photon index of $\Gamma = 2.27 \pm 0.03 \pm 0.20$ and a differential flux at 1 TeV of $(5.7 \pm 0.2 \pm 1.4) \times 10^{-12}\,\mathrm{TeV^{-1}\,cm^{-2}\,s^{-1}}$ as the best fit, where the first error is the statistical fit error and the second error the systematic uncertainty of the measurement. A detailed analysis of an extended H. E. S. S. data set of MSH 15−52 using improved analysis methods is presented in Chapter 4.

2.3 The SNR Shell

Besides the central pulsar and the pulsar wind nebula surrounding it, the composite SNR MSH 15−52 also shows a partial shell morphology, visible mainly at radio wavelengths and as diffuse X-ray emission (cf. Fig. 2.3). This complex structure lead to suggestions by some authors, that MSH 15−52 might consist of two or three separate SNRs. However,

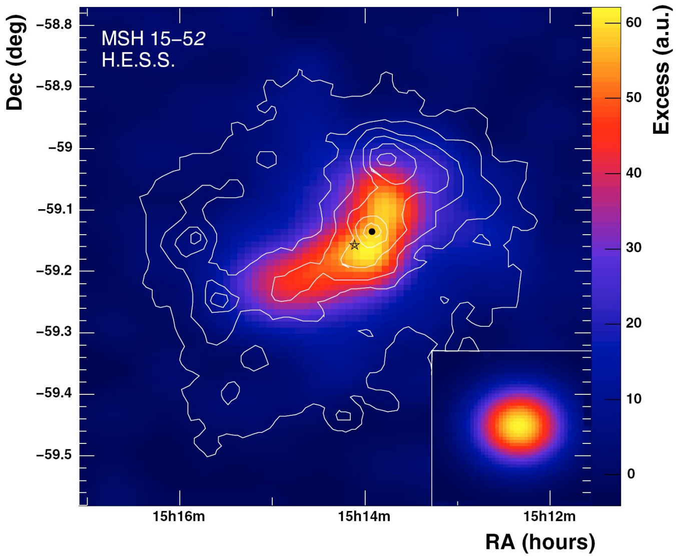

Fig. 2.10: *Smoothed H. E. S. S. VHE γ-ray excess map of MSH 15−52 (Aharonian et al. 2005b). The map was smoothed with a Gaussian of $\sigma = 0.04°$. The white contours mark the ROSAT (0.6 – 2.4 keV) count rate, the black point indicates the position of PSR B1509−58 and the black star the VHE γ-ray excess centroid. In the lower right corner, the smoothed PSF is shown.*

Gaensler et al. (1999) used a comparison of X-ray and radio data to conclude that the different components are part of only one SNR. The distance to MSH 15−52 was estimated to be 5.2 ± 1.4 kpc using H I absorption measurements. Seward et al. (1983) discuss several scenarios for the nature of MSH 15−52. Using the diameter of the partial shell to the southeast and assuming the age-diameter relationship of Clark & Caswell (1976), an age of 10^4 years was estimated. The Sedov relationship with an initial energy of 10^{51} erg and an interstellar density of 1 atom cm^{-3} gives an age estimate of 6 to 20 kyr. Both estimates are in contradiction to the characteristic age of the pulsar ($\tau_c \approx 1700$ yr). One possible explanation for this discrepancy given by Seward et al. (1983) is, that the supernova explosion occurred in a region of inhomogeneous density. This could lead to a faster propagation towards the southeast into a region of lower density and a slower expansion towards the denser northwest. Recent H I observations by Dubner et al. (2002) support this scenario.

3 The *XMM-Newton* View of MSH 15−52

In the previous Chapters it was already mentioned that the analysis of photons in the keV energy range provides crucial information about the nature of astrophysical sources. For the PWN MSH 15−52, an overview of the detailed observations that have been carried out with the *Chandra* X-ray observatory was given in Chapter 2. The *Chandra* X-ray observatory provides the highest angular resolution of the current instruments in the X-ray energy range. In this Chapter, the first analysis of the data taken with the *XMM-Newton* satellite on MSH 15−52 will be presented. The instruments on the *XMM-Newton* satellite provide the highest effective area for the detection of X-ray photons. In comparison to *Chandra*, *XMM-Newton* is therefore ideally suited for the spectral analysis of extended sources. The emphasis of our work was therefore the spatially-resolved spectral analysis of MSH 15−52. The results of this analysis are used in Chapter 5 to constrain the free parameters of a model of the nonthermal emission of MSH 15−52. In the first Sections of

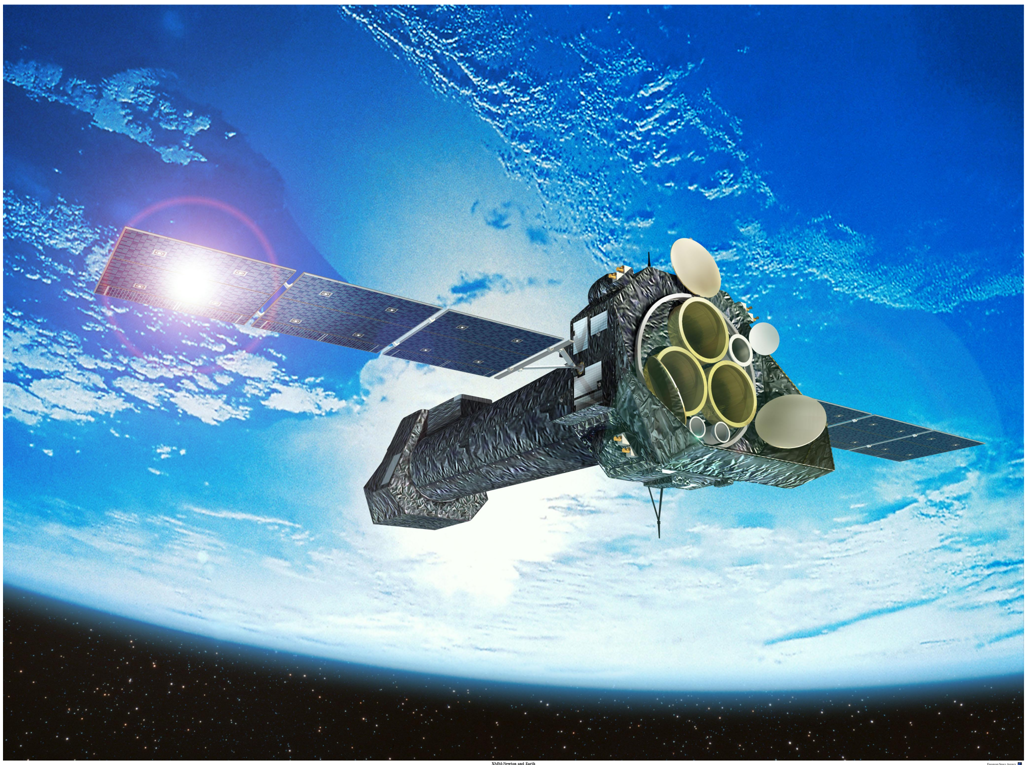

Fig. 3.1: *Artist's impression of the XMM-Newton satellite. The hatches of the three main telescopes are opened. Toward the upper right, the optical monitor with its opened hatch can be seen, the two smaller telescopes toward the bottom are the star tracker telescopes (Image courtesy of ESA).*

this Chapter the basic detection principles for cosmic X-rays are described, followed by a short introduction of the *XMM-Newton* satellite. After these introductory remarks, the available data and the analysis thereof will be presented. The results of our *XMM-Newton* analysis are part of our publication on MSH 15−52 (Schöck et al. 2010).

3.1 Detection of cosmic X-rays

The Earth's atmosphere is opaque for radiation in the X-ray energy range[1]. Therefore, a detection of cosmic X-rays is only feasible outside the influence of Earth's atmosphere. First measurements where conducted with detectors installed on rockets or high-flying balloons (cf. the Introduction), but satellite-borne instruments quickly replaced this technique and have been successfully operating for many years.

Several techniques for the detection of X-rays are in use, e.g. scintillator detectors, proportional counters and charge-coupled device (CCD) detectors. At hard X-ray energies, many experiments employ scintillators, but in the energy range of $0.1 - 10$ keV, CCD detectors are most commonly used. In this technique, a photo-sensitive semiconductor is exposed to the X-ray photons. An incident photon produces secondary charges, which are then read out to calculate the energy of the photon, which is proportional to the measured charge. To reconstruct the direction of the incoming photons, the photo-sensitive semiconductor is subdivided into pixels.

Unlike for optical wavelengths, no suitable transparent materials for mirrors are available for X-rays. Two techniques provide an alternative solution for focussing light at X-ray energies: grazing incidence mirrors and coded masks. The latter are mainly used at higher energies, where the use of grazing incidence is not possible anymore due to the lack

[1]The range from ≈ 0.1 keV to ≈ 10 keV is usually defined as the X-ray range, with lower energies denoted as soft X-rays and photons with energies up to several hundred keV labeled as hard X-rays.

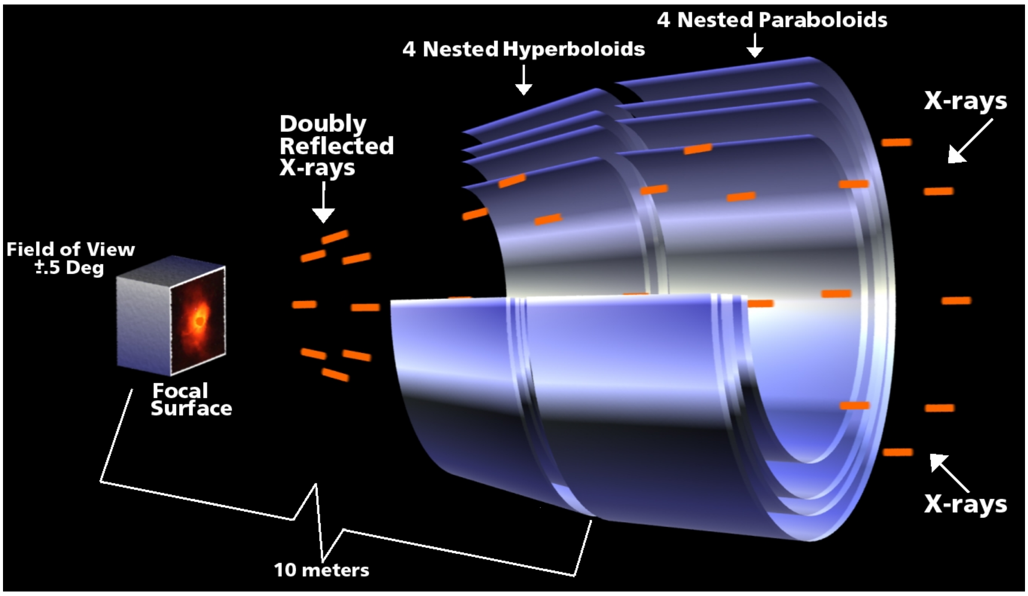

Fig. 3.2: *Schematic illustration of the grazing incidence technique (Image courtesy of NASA/CXC/D.Berry).*

of adequate materials. Furthermore, the sensitivity is also lower for coded mask optics, since a significant fraction of the incoming photons is absorbed by the mask. Therefore, grazing incidence mirrors are most commonly used for the optics of X-ray instruments for energies up to 10 keV. Three possible working principles for this type of mirror were laid out by Hans Wolter (Wolter 1952) and hence the mirror types are known as Wolter I, II and III grazing incidence mirrors.

A schematic illustration of the Wolter type I mirror design and the detection principle of modern X-ray instruments is shown in Fig. 3.2. The X-ray photons are illustrated by orange dashes that travel from the right side of the picture to the left side. The light first impacts on the mirror system, which consists of a number of nested mirrors (4 in this illustration). Each mirror shell is in turn made up of a paraboloid and a hyperboloid mirror. The X-rays are reflected twice, once on the paraboloid and once on the hyperboloid mirrors, and then hit the camera which is placed in the focal surface of the optical system. Typically, CCD detectors are used as the camera for X-ray photons with energies up to 10 keV

3.2 The *XMM-Newton* Satellite

The *XMM-Newton* satellite (X-ray Multi-Mirror Mission, Jansen et al. 2001), named after Sir Isaac Newton, is an X-ray observatory launched on 10 December 1999. Operated by the European Space Agency, it orbits Earth on an elliptical 48 hour orbit with an apogee of $114,000$ km and a perigee of $7,000$ km. *XMM-Newton* carries three X-ray telescopes, each equipped with 58 Wolter-type I mirrors nested in a coaxial and cofocal configuration. The largest mirror has a diameter of 70 cm and the focal length of the telescope amounts to 7.5 m. A special emphasis in the design of the mirrors was placed on a great effective area over a wide range of energies. In the range from 0.1 to 10 keV the mirrors are most efficient. The on-axis PSF has a FWHM of $\approx 6''$ and a HEW of $\approx 15''$ with only a minor dependance on the photon energy[2]. The three telescopes have the largest effective area in the X-ray energy range as yet, making *XMM-Newton* ideally suited for highly sensitive studies of astrophysical X-ray sources. An artistic view of the *XMM-Newton* satellite is shown in Fig. 3.1, where the openings of the three main telescopes can be seen. The two small openings belong to the star trackers and the medium-sized telescope is the optical monitor on board the *XMM-Newton* spacecraft. A detailed front view on the mirrors during the integration in the laboratory can be seen in the left panel of Fig. 3.3.

Each of the three main telescopes is equipped with an X-ray CCD camera, named the European Photon Imaging Camera (EPIC). Two of the cameras are MOS (Metal Oxide Semiconductor, Turner et al. 2001) CCD arrays, installed behind telescopes that are also equipped with reflection grating spectrometers (RGS). About one half of the incoming photons is deflected by mirrors onto these gratings, which allow for a high-resolution spectral analysis of the radiation. Altogether, about 44% of the incident photons reach the MOS cameras. The pixel size of the MOS cameras is approximately $1''$. Both cameras, MOS 1 and MOS 2, comprise seven silicon chips made up of a matrix of 600×600 pixels. The chips in the MOS 1 and MOS 2 cameras are aligned orthogonal to each other, so that MOS 1 is able to cover the gaps between the chips of MOS 2 and vice versa.

The third camera, EPIC-pn (Strüder et al. 2001), does not suffer from any losses in its optical path and receives the whole incoming flux. It is a new type of camera, especially

[2]FWHM is the full width at half maximum, HEW the half energy width.

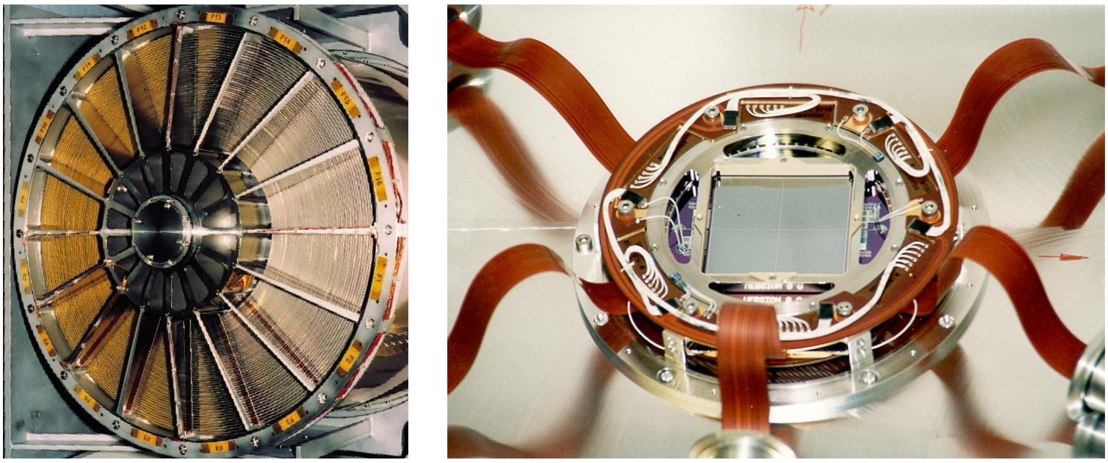

Fig. 3.3: *Left panel: The XMM-Newton Wolter-type I mirrors during the integration in the laboratory (Image courtesy of Dornier Satellitensysteme GmbH and ESA). Right panel: View of the 12 CCDs of the EPIC-pn camera. The four quadrants each have three CCD subunits. (Image courtesy of MPI-semiconductor laboratory, MPE, Astronomisches Institut Tuebingen, Germany and ESA.)*

developed for the *XMM-Newton* telescope and is made of a single high-purity silicon wafer. The name "pn" derives from the positive and negative doping of the silicon wafer. With its sensitive area of $36\,\mathrm{cm}^2$ it is the largest X-ray CCD detector ever built. The four quadrants of the pn-array (see Fig. 3.3) each have three CCD subunits, so that the pn-detector comprises twelve CCDs in total. The pixels of the pn-detector have a size of about $4''$.

The EPIC cameras can be operated in three different modes of data acquisition, suited for various scientific tasks. These are the full frame, partial window and timing mode. In the full frame mode the time resolution is 73.4 ms (pn)/2.6 s (MOS). The maximum count rate to avoid deterioration due to pile-up[3] is 1000/15 (pn/MOS) counts per second for diffuse emission and 0.7/0.24 (pn/MOS) mCrab[4] for point sources. In the partial window and the timing mode only some of the CCDs are read out and thus a better time resolution and a greater maximum count rate can be achieved.

In comparison to the instruments of the *Chandra* X-ray observatory (HEW $\approx 0.5''$), *XMM-Newton* has a worse angular resolution by almost one order of magnitude. However, the effective area of *XMM-Newton* is $4650\,\mathrm{cm}^2$ at 1 keV compared to $555\,\mathrm{cm}^2$ for the *Chandra* ACIS-S CCD array. This large effective area makes *XMM-Newton* the ideal observatory for the detailed spectral analysis of extended emission. For the PWN MSH 15−52 the results of detailed *Chandra* analyses with a high angular resolution were already presented in Section 2.2. In the further course of this Chapter, an analysis of the extended emission of the PWN observed with the *XMM-Newton* satellite will be presented. The focus of this analysis is on the spectral analysis, since the *Chandra* analyses by Gaensler et al. (2002) and Yatsu et al. (2009) already discussed the morpholgy in great detail. Our analysis of the *XMM-Newton* data on MSH 15−52 was published in a refereed journal and the text

[3] Pile-up refers to the arrival of more than one photon in one pixel or in an adjacent pixel before the camera is read out. This can lead to systematic effects in the spatial and energy resolution of the camera, because two low-energy photons arriving within one readout frame will be detected as one photon with the summed energy.

[4] In the energy range of 2 − 10 keV, $1\,\mathrm{mCrab} = 2.4 \times 10^{-11}\,\mathrm{erg\,s^{-1}\,cm^{-2}}$.

Table 3.1: *Details of the XMM-Newton EPIC-pn observations on MSH 15−52 used for the analysis.*

Observation ID	Exposures (ks) performed$^{(1)}$	net$^{(2)}$
0207050201	23.135	5.9
0302730201	16.130	3.6
0302730301	8.235	2.0

$^{(1)}$ Exposure time without background screening
$^{(2)}$ Net exposure time after background screening

in the further section will follow along the lines of Schöck et al. (2010).

3.3 Observations

The region around MSH 15−52 has been observed eight times with *XMM-Newton* with the EPIC-MOS and EPIC-pn cameras. Two of these observations (Observation ID: 0128120301 and 0128120401) were routine calibration runs centered on the position of the pulsar. In one of the other six observations (Observation ID: 0312590101), all three cameras were also centered on PSR B1509−58 and operated in timing mode. This observation mode allows for a better timing resolution, but does not provide the direction of the incoming photons. Therefore, this observation was not considered further for the spatially-resolved spectral study of the extended, steady emission of the PWN.

In order to reduce the systematics on the spectral analysis of the extended emission of the PWN, we require the whole area of our intereset to be within the *XMM-Newton* field of view (FOV). Only three of the five observations taken in full-frame mode match this criterion. The observations with the IDs 0302730101 and 0207050101 were pointing towards the southeast of MSH 15−52 and only a part of the source is contained in the FOV. So this leaves the three observations with the IDs listed in Table 3.1 fulfilling the criteria for the spectral analysis. These three observations pointed towards the same position ($\alpha_{J2000} = 15^h13^m46\overset{s}{.}46$; $\delta_{J2000} = -59°00'49\overset{''}{.}5$) in the northern part of MSH 15−52. In each of these observations the detectors were operated in full-frame mode with medium optical blocking filters.

3.4 Data Analysis

For the analysis of the X-ray data the *XMM-Newton* Science Analysis Software (SAS) version 8.0.0 was used. Additional tasks were performed with tools from the FTOOLS software package distributed by the NASA High Energy Astrophysics Science Archive Research Center (HEASARC, Blackburn 1995). The spectral modeling of the data was done with version 12.5.0 of the XSPEC X-ray spectral fitting package (Arnaud 1996). The 7 to 15 keV lightcurve extracted from the full FOV provided by the standard SAS analysis chain was used to screen the data from periods of high background-flaring activity. Since a good understanding of the background is crucial for the analysis of extended sources like MSH 15−52, a conservative background threshold of ten background counts per second

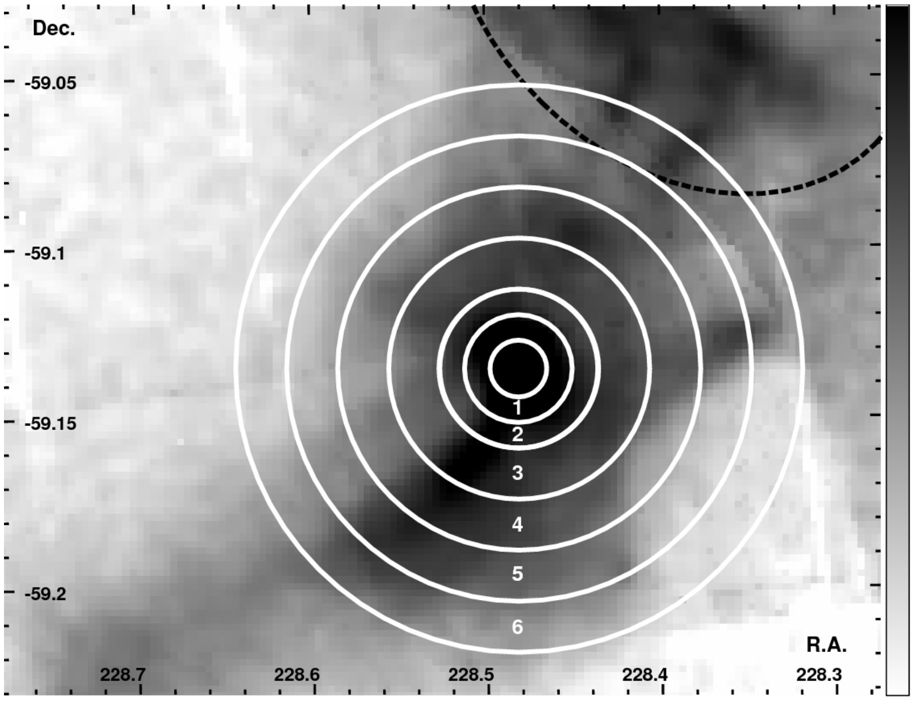

Fig. 3.4: *Exposure-corrected XMM-Newton count map of the region around MSH 15−52 (from Schöck et al. 2010). The regions indicated on the maps are used for the spectral analysis discussed in Section 3.6. The extraction regions are centered on the position of the pulsar PSR B1509−58 and are marked with white lines and numbers. The black dashed line marks the exclusion region which was chosen to encompass the thermal emission from the H*II *region RCW* 89.

was applied for the definition of good time intervals (GTI). Furthermore, for the spectral analysis shown in Section 3.6, the data of the pn-camera were used, since it is more sensitive than the MOS cameras and the statistics were sufficient for the spectral analysis. Only events flagged as good (FLAG=0) were selected. Another filter was applied on the pattern of the events. Since the flux of the extended emission of MSH 15−5*2* is too low for pattern pile-up, we used single and double events (PATTERN<=4) for higher statistics in the analysis. Deterioration in the spectral analysis due to pixel pile-up is also not an issue, since the extraction regions used in Section 3.6 only start at a radius of 30″ from the bright pulsar PSR B1509−58. The total exposure and the net exposure after background screening is displayed in Table 3.1. Since all of the observations were affected by long periods of background flaring or a full scientific buffer of the EPIC-pn camera, the net exposures are rather short. However, the statistics are still sufficient for a spectral analysis of the extraction regions defined in Section 3.1.

3.5 Imaging

As already pointed out before, the key feature of *XMM-Newton* is the large effective area in comparison to other X-ray instruments, which allows for an excellent spatially-resolved spectral analysis. For the detailed morphological study of X-ray sources, the resolution of the *Chandra* ACIS camera is unsurpassed. The sky map presented here is therefore mainly shown to illustrate the extraction regions for the spectral analysis discussed in

Table 3.2: *Extraction regions for the XMM-Newton spectral analysis of the PWN MSH 15−52.*

Ring No.	Radius (arcsec) inner	outer	mean	No. of Obs.
1	30	57	43.5	2
2	57	84	70.5	2
3	84	138	111	3
4	138	192	165	3
5	192	246	219	1
6	246	300	273	2

Section 3.6. The *Chandra* sky map from the analysis of Yatsu et al. (2009) is shown in Fig. 2.5 on page 46.

Figure 3.4 shows the *XMM-Newton* count map of the region around the pulsar PSR B1509−58. The map is exposure-corrected and uses the EPIC-pn data from the three observations listed in Table 3.1. The annular extraction regions for the spectral analysis presented in the next section are marked in white color and are labeled with numbers from 1 through 6. The annuli are centered on the position of the pulsar ($\alpha_{J2000} = 15^h13^m55^s$; $\delta_{J2000} = -59°08'09''$) (Livingstone et al. 2005) and go out to a distance of $300''$.

3.6 Spectral Analysis

The spectral analysis was conducted for the annular regions shown in the sky map in Fig. 3.4. The location and shape of the regions was chosen to study the changes of the spectral properties with increasing distance from the pulsar. Full annuli were used in contrast to wedge-shaped regions to extract the integral flux for each region. This is of special importance for the modeling of the nonthermal emission of the PWN that is presented in Chapter 5. The parameters for the extraction regions are listed in Table 3.2. In the numbering scheme, the regions are labeled beginning with ring 1, which is the region closest to PSR B1509−58. It goes out to region 6, for which the outer radius lies at a distance of $300''$ from the pulsar position. Beyond the distance of $300''$, the X-ray emission starts to show a pronounced sideway bending (cf. Fig. 3.4) and the brightness of the source also starts to decrease. Furthermore, the model that will be introduced in Chapter 5 assumes a spherical symmetry for the bulk motion of the leptons in the PWN and thus we restricted the X-ray analysis to distances closer than $300''$ to the pulsar.

In order to avoid systematic effects from the CCD borders, we extracted the spectra for each detector CCD separately. The background for each CCD was estimated using infield background regions from the same chip. This minimizes systematic uncertainties on the flux, compared to a background estimation from blank-sky observations. The effective areas and energy responses for each detector CCD were calculated by weighting the contribution from each pixel with the flux using a detector map from the 0.2 − 7.0 keV energy band. The spectra from the different CCDs for each extraction region were then merged by weighting the responses (rmf) and auxiliary responses (arf) with the size of the respective region.

For each ring, the spectra were fitted in parallel with an absorbed power-law model ("phabs" absorption model from the XSPEC fitting package). In the individual observations that were used, the bad columns and the CCD borders have different orientations. This leads to a difference in the norm and thus in the flux of the fitted spectra. In the case where bad columns obscure a large fraction of the extraction region, a wrong flux is obtained. We added a selection criterion on the observations used for the spectral analysis of each ring to circumvent this problem. Only those observations were used in which the bad columns do not obscure parts of the particular extraction region. In this way we obtained the correct integral flux for each region. The resulting number of observations for each extraction region is given in Table 3.2.

The parameters of the spectral power-law fit — absorption column density, photon index and normalization — were linked for the fitting of the different observations. The absorption column density does not vary significantly between the different regions and was fixed to the value of the first ring. The fit range was from 0.5 − 9.0 keV for rings 1 to 5, while for ring 6 we chose a narrower fit range of 3.0 − 9.0 keV, due to the insufficient statistics at low energies.

Figure 3.5 shows the fit of absorbed power laws to the observed emission of rings 1 through 6. The resulting parameters for the spectral analysis of each ring are listed in Table 3.3. The data are fitted very well by absorbed power laws. Due to the increasing size of the extraction region and the constant area of the infield background, the statistical uncertainty of the spectra of the outer regions is greater, resulting in a lower value of χ^2/dof. We obtained an absorption density of $N_{\mathrm{H}} = (1.15 \pm 0.03) \times 10^{21}\,\mathrm{cm}^{-2}$ using the abundance tables of Wilms et al. (2000). This is in good agreement with results of previous X-ray analyses of this source in which other abundance tables were used (see e.g. Gaensler et al. 2002).

The extended emission of MSH 15−5*2* shows variation in the spectral properties with increasing radial distance to the pulsar. The photon index Γ of the fitted absorbed power law increases from the inner regions to the outer regions by roughly 0.5, reflecting a softening of the nonthermal X-ray spectrum of the PWN. Figure 3.6 shows this variation of the photon index with increasing distance to the position of PSR B1509−58. Besides a change in the index of the fitted power-law spectrum, a change in flux and surface brightness is also observed. Table 3.3 gives the unabsorbed flux and the surface brightness in the energy range from 0.5 to 9.0 keV for each of the extraction regions as well as the χ^2 and the number of degrees of freedom (dof) of the fit. The surface brightness decreases with increasing distance of the extraction region to the pulsar, as can be seen in Fig 3.7. A decrease of the X-ray surface brightness by more than two order of magnitude is observed between the innermost region around PSR B1509−58 and region 6 with a mean distance of 273″.

For the parameter optimization of the model (see Chapter 5), we divided the spectrum for each of the annular extraction regions in six intervals in energy and calculated the unabsorbed flux in these bins. This is shown in Fig. 3.8, where as an example the fitted spectra for region 1 and 6 are shown. Only four bins were used for the analysis of the ring 6 region, due to the narrower energy range (3.0 − 9.0 keV). The approach of using individual flux points rather than only using the index and the total flux of a power-law fit is better suited for the parameter optimization that will be described in the Chapter on the modeling of the nonthermal emission (Chapter 5 on page 111). In this way we compare the data and the model results directly, without assuming power-law distributions for fits of the X-ray spectra.

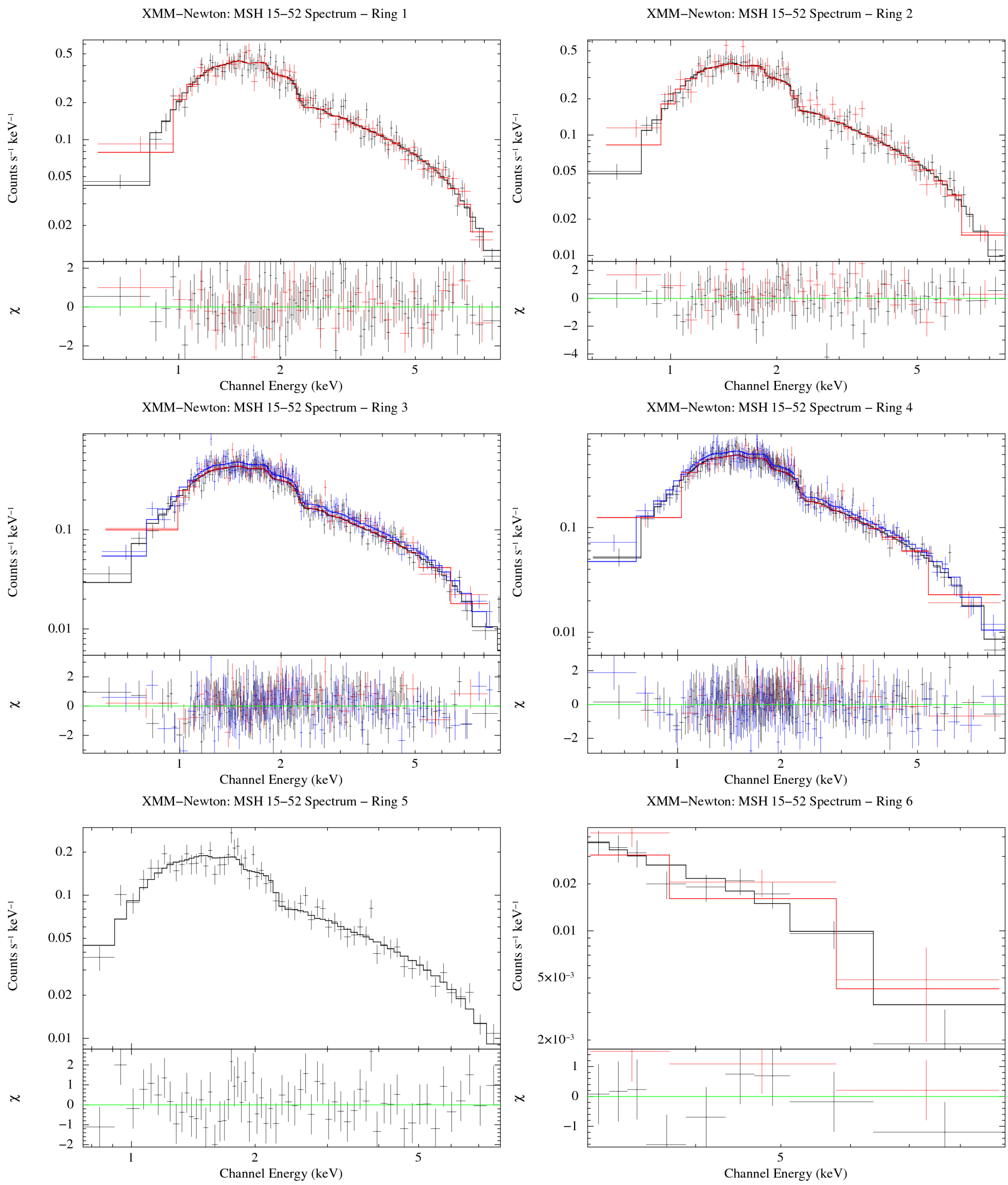

Fig. 3.5: *XMM-Newton spectra of the regions displayed in Fig. 3.4. The number of counts per second per keV is plotted against the energy of the photons in keV. The different colors mark the data and models from the different observations. In the lower panels of the figures, the fit residuals are plotted. From top to bottom and left to right the data points and the fitted absorbed power-law spectra for the regions 1 through 6 are shown. The number of observations varies due to the different location of the bad columns that obscure the extraction regions. Table 3.2 shows the number of observations that were used for each region.*

Table 3.3: *Results of the spectral analysis of the extraction regions shown in Fig. 3.4. The data were fitted with an absorbed power-law spectrum using the abundance tables of Wilms et al. (2000).*

Ring No.	Γ	Flux (10^{-12} erg s^{-1} cm^{-2})	Surface Brightness (10^{-17} erg s^{-1} cm^{-2} arcsec^{-2})	χ^2/dof
1	1.66 ± 0.02	12.0 ± 0.3	162 ± 4.5	147/161
2	1.78 ± 0.03	10.0 ± 0.3	92 ± 3.0	161/147
3	1.88 ± 0.02	2.9 ± 0.07	9.2 ± 0.2	431/459
4	1.96 ± 0.02	3.1 ± 0.09	6.1 ± 0.2	356/536
5	2.07 ± 0.05	2.4 ± 0.1	3.4 ± 0.2	97/156
6	2.24 ± 0.28	0.4 ± 0.2	0.5 ± 0.3	62/107

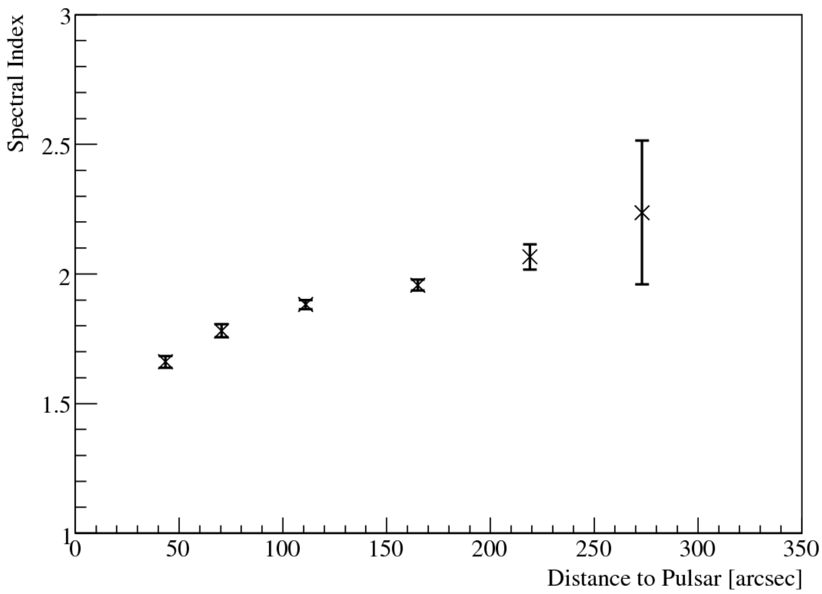

Fig. 3.6: *Spectral index of the power-law fit to the XMM-Newton data in the energy range of 0.5 − 9 keV of the different regions versus the mean distance of the extraction regions to the pulsar PSR B1509−58. A steepening of the spectrum is observed with increasing distance.*

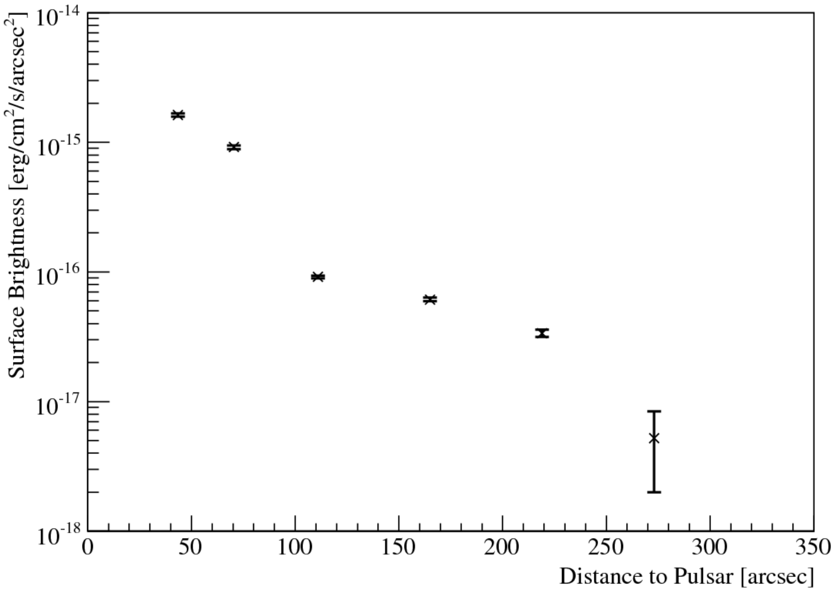

Fig. 3.7: *Surface brightness in the* 0.5 – 9.0 keV *band of the X-ray emission from the annular extraction regions as a function of the distance to the pulsar PSR B1509−58. The surface brightness decreases by more than two orders of magnitude.*

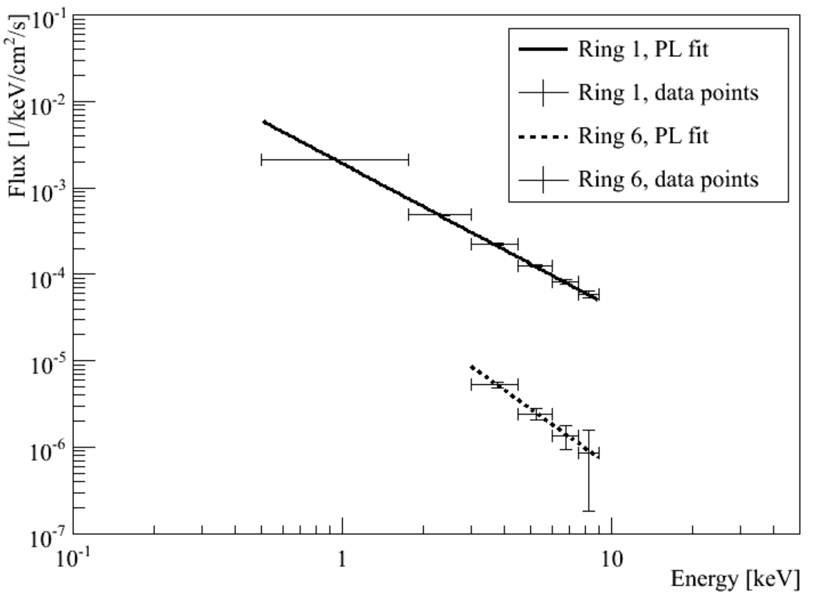

Fig. 3.8: *Illustration of the flux points as they were used for the parameter optimization discussed in Chapter 5. As an example, the power-law fits of the spectra for ring 1 and 6 are shown in this plot, together with the flux points that were derived for the extraction regions. Due to the limited energy range, we use only four flux points for ring 6, for all other rings, six flux points are used.*

4 The H. E. S. S. View of MSH 15−52

In the previous Chapter, an analysis of the extended X-ray emission of the pulsar wind nebula MSH 15−52 was presented. Now we turn our focus to higher energies and move up to the energy range of VHE γ-rays[1]. This range of wavelengths has only become accessible to measurements in recent years and the most successful experiment so far is the H. E. S. S. array of Cherenkov telescopes. This experiment utilizes the imaging atmospheric Cherenkov technique (IACT) to indirectly measure VHE γ-rays. In this Chapter, the most sensitive analysis of the VHE γ-ray emission of MSH 15−52 measured with the H. E. S. S. experiment will be presented. To this end, an introduction to the physics of air showers and Cherenkov radiation is given first. Thereafter, the imaging atmospheric Cherenkov technique is discussed and the H. E. S. S. experiment introduced. After explaining the different steps in the analysis of the H. E. S. S. data, the results of the data analysis of MSH 15−52 are shown in detail.

The detection of VHE γ-rays is not possible with a direct measurement method. An indirect approach has to be used which is not quite as intuitive as, for example, the detection of optical or X-ray photons. Therefore, the first parts of this Chapter will give a detailed introduction to the measurement technique and the H. E. S. S. experiment. For the results that are shown in Section 4.5 of this Chapter, a publication is currently in preparation (HESS Collaboration et al. in prep.).

4.1 Air Showers

The Earth's atmosphere is not transparent to VHE γ-rays (for a plot of the atmospheric opacity for different photon energies, see Fig. 0.1 in the Introduction). When a high-energy photon hits the upper layers of the atmosphere, a cascade of new particles is induced. The secondary particles can then again interact with the atmosphere and induce further particles. In that way, the impact of one photon can create a large number of secondary particles, the so-called air shower. The number of particles in the air shower keeps on growing continuously until absorption effects in the atmosphere start to dominate over the production of new particles. If the primary particle is a photon, the air shower is governed by electromagnetic processes, the dominant interaction of the γ-ray being pair production. This type of air shower, which is also induced for an incident electron as the primary particle, is called electromagnetic air shower. If the primary particle is a cosmic-ray proton or nucleus, there is also an air shower initiated. In this type of air shower, interactions of the strong and the weak force take place, besides electromagnetic interactions. Therefore, it is called hadronic air shower. The two types of air showers will be explained in more detail in the following.

[1] Typically, the VHE γ-ray energy range comprises γ-ray photons with an energy between roughly 100 GeV and 100 TeV.

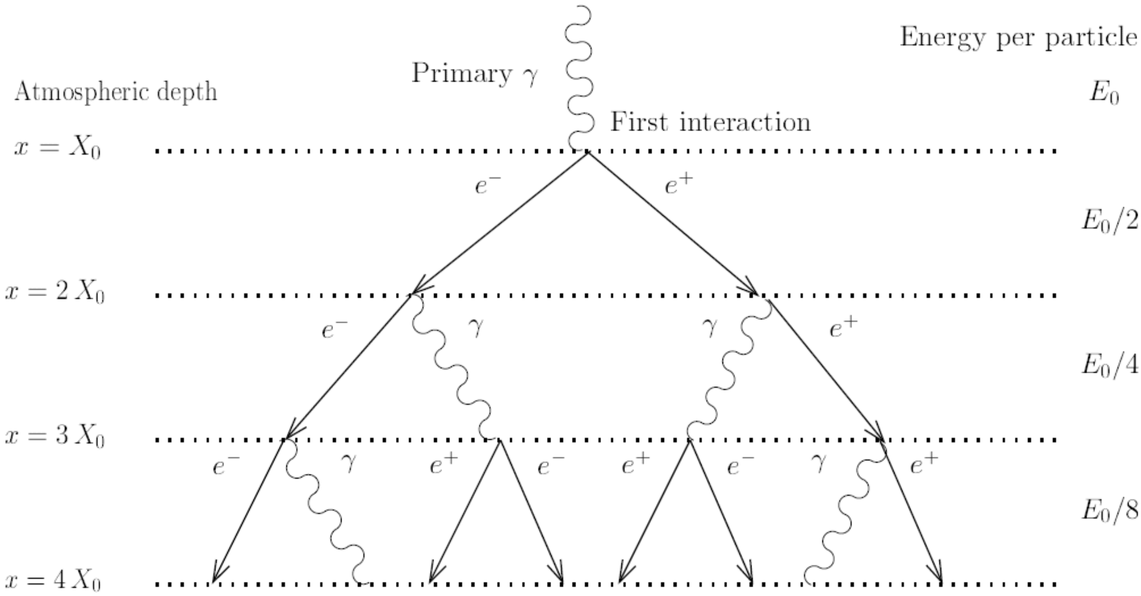

Fig. 4.1: *Depiction of the Heitler model of an electromagnetic air shower induced by an incident VHE γ-ray. Figure adopted from Funk (2005).*

4.1.1 Electromagnetic Showers

The development of electromagnetic showers is governed by the processes of pair production and bremsstrahlung. A γ-ray interacting with the electromagnetic field of a nucleus in the atmosphere forms an electron-positron pair. The induced leptons will then emit high-energy bremsstrahlung photons. These processes occur again and again to form the electromagnetic air shower. The production of new particles continues until the energy of the leptons reaches the so-called critical energy, E_c. At this energy, the losses due to ionization dominate over the bremsstrahlung and the production of new particles ceases. The shower then dies out due to the ionization losses of the leptons. In the atmosphere, the critical energy is in the order of 80 MeV. The production of leptons by pair production is only possible, if the γ-rays have an energy above a threshold of

$$E_{\mathrm{min}} = 2 m_e c^2 (1 + m_e/M) \approx 1.02\,\mathrm{MeV}. \tag{4.1}$$

In this equation, m_e is the electron mass and M the mass of the nucleon.

A model to describe the formation of electromagnetic showers was developed by Heitler (1954). In this model (schematically illustrated in Fig. 4.1), the only processes taken into account are pair production and bremsstrahlung. The characteristic length scales of the two processes (denoted as X_0) are assumed to be equal. This neglects that the mean free path for pair creation is 9/7 times the radiation length for bremsstrahlung (Particle Data Group et al. 2008). Further assumptions are, that the energy is divided equally among the leptons created in a pair production process and that the bremsstrahlung occurs exactly after X_0 and generates a photon with half of the energy of the emitting lepton. The number of particles at an atmospheric depth of $n = X/X_0$ radiation lengths is then given by:

$$N_n = 2^n. \tag{4.2}$$

The mean energy E_n of the particles at radiation length n decreases with the same exponent, so that

$$E_n = E_0 2^{-n}. \tag{4.3}$$

E_0 is the energy of the primary photon. The number of particles is at its maximum at the critical energy. This maximum occurs at a distance of

$$X_{\max} = X_0 \frac{\ln(E_0/E_c)}{\ln 2}. \tag{4.4}$$

The maximum number of particles in this shower model is then

$$N_{\max} = 2^{X_{\max}/X_0} = \frac{E_0}{E_c}. \tag{4.5}$$

With this straightforward model, the most important properties of an electromagnetic shower can already be deduced. The number of particles in the shower grows exponentially up to a maximum number of particles given by Eq. 4.5. This number is proportional to the energy of the primary particle E_0. The maximum depth of the shower is proportional to the logarithm of E_0. Although there are a number of simplifying assumptions in this model, the qualitative conclusions remain unaltered when applying more sophisticated models of electromagnetic air showers.

The lateral extension of an electromagnetic shower is determined by multiple Coulomb scattering. The angular distribution is fairly narrow. 99% of the particles of the electromagnetic cascade are contained in a radius of $3.5R_M$, where R_M is the Molière radius and is defined as (Particle Data Group et al. 2008)

$$R_M = \frac{X_0 E_s}{\rho E_c}. \tag{4.6}$$

E_s is the scale energy and has a value of 21.2 MeV. For a vertical 1 TeV shower the Molière radius at the shower maximum is $R_M \approx 200$ m (Aharonian et al. 2008).

4.1.2 Hadronic Showers

The physical processes of hadronic air showers are more complicated than those of electromagnetic air showers. When protons or other nuclei hit the Earth's atmosphere, the dominating part of the interactions occurs via the strong force. Inelastic scattering off nuclei in the atmosphere leads to the production of a variety of secondary particles, among them mesons, nucleons and hyperons (see Fig. 4.2 for an illustration). A large fraction of the secondary particles is made up of pions ($\pi^0, \pi^\pm$). The neutral pions have a very short life time of $(8.4\pm0.6)\times10^{-17}$ seconds and decay quickly into two photons. These two γ-rays in turn generate electromagnetic sub-showers, as described in the previous section. The charged pions, on the other hand, have a considerably longer life time of 2.6×10^{-8} seconds and decay almost to 100% into muons ($\mu^\pm$) and muon neutrinos. However, due to the long life time of the charged pions, they can again interact with atmospheric nuclei via the strong force. This leads to the generation of hadronic sub-showers. The muons do not take part in the generation of further particles in the air shower and escape the shower region.

The lateral extension of hadronic air showers is broader and more inhomogeneous than for electromagnetic showers. Due to the strong interactions in the shower, the secondary particles gain large transverse momenta. The occurrence of electromagnetic and hadronic

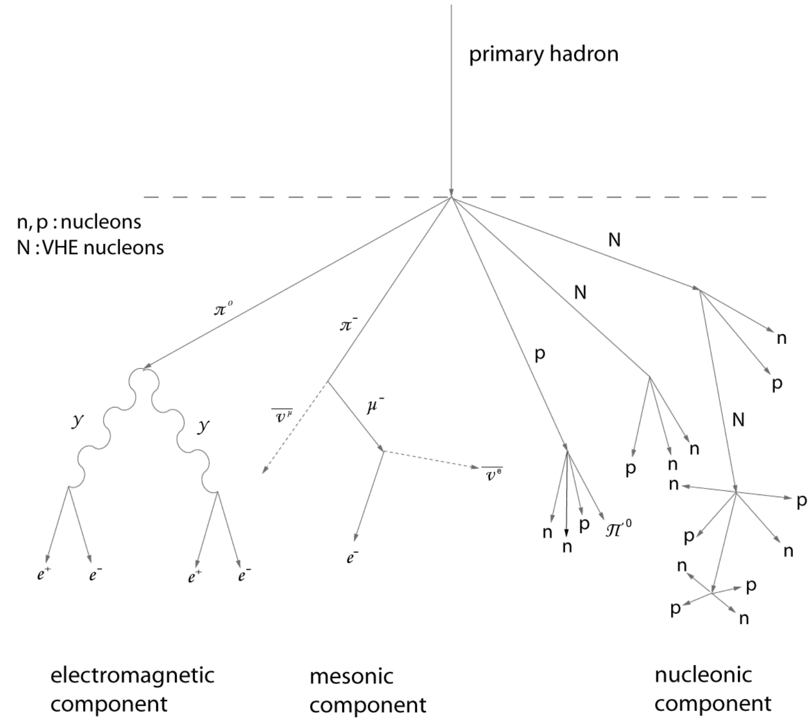

Fig. 4.2: *Illustration of the different components (electromagnetic, mesonic, nucleonic) of a hadronic air shower in the Earth's atmosphere. Figure adopted from Funk (2005).*

sub-showers in the main hadronic air shower leads to a less regular appearance compared to electromagnetic air showers, where there is only the main shower present. A comparison of the longitudinal development of both shower types is shown in Fig. 4.3. The electromagnetic shower is closely aligned with the shower axis, whereas the hadronic shower exhibits strong deviations from the axis and the electromagnetic sub-showers within the hadronic air shower can be seen.

Another difference between the shower types is the number of particles that are contained in the electromagnetic part of the shower. Since the long-lived muons and neutrinos escape the shower region, a significant part of the primary energy does not take part in the electromagnetic sub-showers of a hadronic showers. Only the interactions of π_0 lead to electromagnetic sub-showers. This means that about one-third of the energy of the primary particle is contained in the electromagnetic sub-showers, whereas for a purely electromagnetic air shower, all of its energy is contained in the electromagnetic part.

4.2 Cherenkov Radiation

A charged particle that travels through a dielectric medium with a velocity that is larger than the speed of light in this medium emits Cherenkov radiation. The charge of the moving particle leads to a polarization of the atoms in the medium and they emit electromagnetic radiation. If the particle has a velocity, v, that is smaller than the speed of light in the medium, c/n (where c is the speed of light in vacuum and n is the refractive index of the medium), then the emitted radiation interferes destructively and no radiation is visible to the observer. If, however, $v > c/n$ constructive interference occurs and

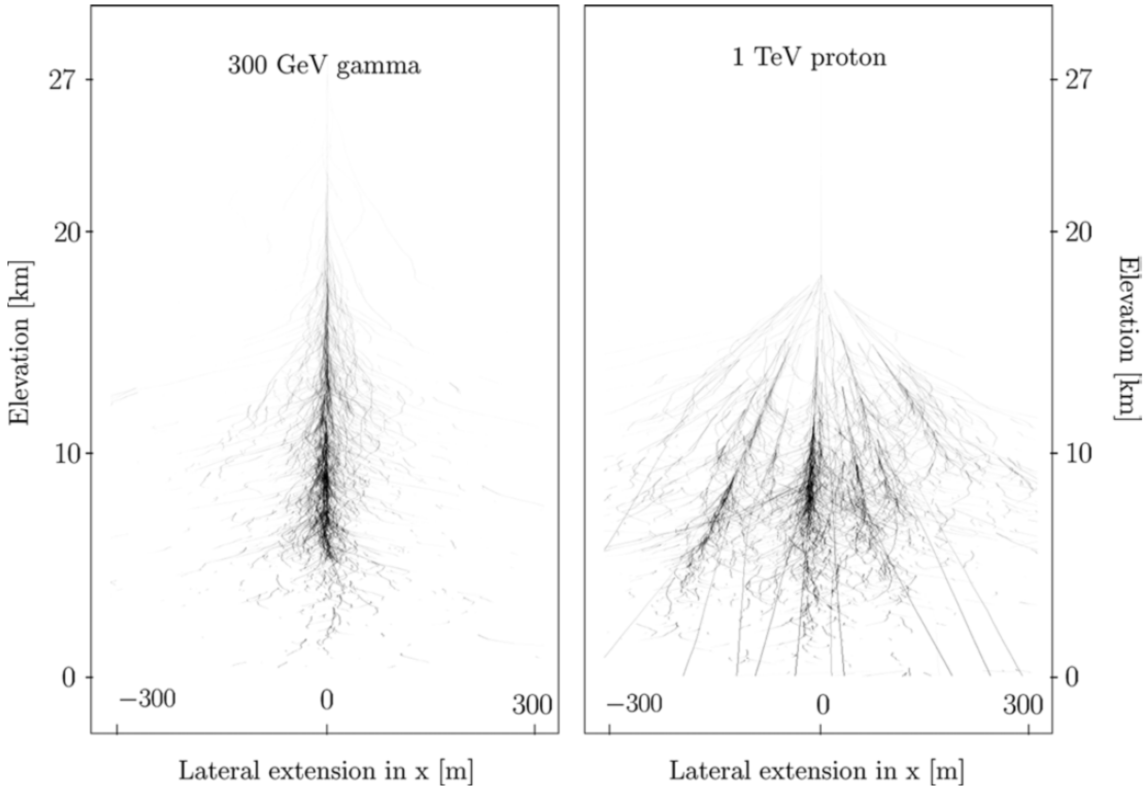

Fig. 4.3: *Longitudinal development of an air shower induced by a 300 GeV γ-ray (left panel) and by a 1 TeV proton (right panel). The images were created with a Monte Carlo simulation and show the projected tracks of individual particles in the air shower (Bernlöhr 2010).*

Cherenkov photons can be observed. The construction of the wavefront of the Cherenkov radiation using the Huygens principle is illustrated in Fig. 4.4.

The Cherenkov radiation is emitted with a very narrow opening angle. The characteristic angle ϑ_c between the path of the emitting particle and the wavefront of the Cherenkov light is

$$\vartheta_c = \arccos \frac{c}{vn} = \arccos \frac{1}{\beta n}. \tag{4.7}$$

In this equation β is the velocity of the particle in units of the speed of light, $\beta = v/c$. Cherenkov emission is thus only possible, if $\beta > 1/n$ and the maximum of the opening angle occurs for ultrarelativistic particles with $\beta \approx 1$. The minimum energy for a charged particle to emit Cherenkov light is then

$$E_{\min} = \gamma_{\min} m_0 c^2 = \frac{m_0 c^2}{\sqrt{1 - \beta_{\min}^2}} = \frac{m_0 c^2}{\sqrt{1 - n^{-2}}}, \tag{4.8}$$

where m_0 is the rest mass of the charged particle and γ its Lorentz factor. The threshold energy for the Cherenkov radiation scales linearly with the mass of the particles and thus the emission from air showers is dominated by the lightest charged particles in the shower, namely electrons and positrons. A more detailed treatment of Cherenkov radiation in general is given e.g. by Longair (2004a) and Jackson (1998).

The opening angle and the threshold energy both depend on the refractive index of the medium that the charged particle passes through (Eqns. 4.7 and 4.8). The refraction in the Earth's atmosphere changes due to the change in density. A simple density profile of the atmosphere is given by the expression

$$\rho = \rho_0 \exp\left(-h/h_0\right), \tag{4.9}$$

where h is the height above sea level, $h_0 \approx 8.5\,\mathrm{km}$ the scale height of the atmosphere and $\rho_0 \approx 1.205 \times 10^{-3}\,\mathrm{g\,cm^{-3}}$ the typical atmospheric density at sea level (Aharonian et al. 2008). This leads to the expression of

$$n(h) = 1 + n_0 \exp\left(-h/h_0\right) \tag{4.10}$$

for the refractive index n of the atmosphere. In this equation $n_0 = 0.00029$ and $h_0 = 7.25\,\mathrm{km}$, differing slightly from the standard scale height of the atmosphere. The change in the refractive index results in a change of the opening angle of the emitted Cherenkov radiation, thus the emission from a lepton moving through the atmosphere does not exhibit a perfect circular shape on the ground, but rather is smeared out as can be seen in Fig. 4.5. In this image, the distribution of the Cherenkov light emitted by a photon-induced and a proton-induced air shower are shown for a comparison. The photon-induced shower is purely of electromagnetic nature and thus has smeared out circular shape, whereas the proton-induced shower exhibits stronger fluctuations and the different electromagnetic sub-showers are clearly visible. For electromagnetic showers, the circle of the emitted Cherenkov light has a radius of $\approx 100\,\mathrm{m}$ and all photons from the shower arrive on the ground within a time interval of the order of nanoseconds.

The resulting spectrum of Cherenkov light is strongly peaked at short wavelengths (UV to blue). For a single, charged particle, the source spectrum is given by the Franck-Tamm relation (Aharonian et al. 2008):

$$\frac{\mathrm{d}^2 N_{\mathrm{ph}}}{\mathrm{d}x\,\mathrm{d}\lambda} = \frac{2\pi\alpha}{\lambda^2}\sin^2(\vartheta_c), \tag{4.11}$$

which gives the differential number of photons emitted in a wavelength interval $\mathrm{d}\lambda$ per unit length $\mathrm{d}x$ for a Cherenkov angle ϑ_c. The peak of this distribution lies in the UV region. However, the Cherenkov light is attenuated by scattering and absorption processes in the atmosphere. The two most important scattering processes are Rayleigh and Mie scattering. For the absorption, the dominant process is the absorption of photons by the ozone (O_3) in the atmosphere. These three effects lead in combination to an attenuated spectrum which is sharply cut off at wavelengths below 300 nm (Bernlöhr 2000). For a primary γ-ray with an energy of 1 TeV about 100 Cherenkov photons per square meter are observed at a height of 2 km a.s.l.

4.3 The Imaging Atmospheric Cherenkov Technique

The flux of cosmic γ-rays is rapidly decreasing with higher energies and for energies above $\sim 100\,\mathrm{GeV}$ the low flux makes the measurement of γ-rays with satellite instruments inefficient. The Imaging Atmospheric Cherenkov Technique (IACT) allows the detection of cosmic VHE γ-rays with ground-based telescopes and makes it possible to extend the measurements of γ-rays to an energy range of up to 100 TeV. With this technique, an incident γ-ray is measured via the Cherenkov radiation that is emitted by the secondary particles in the electromagnetic air shower. By mapping the Cherenkov light onto a camera, it

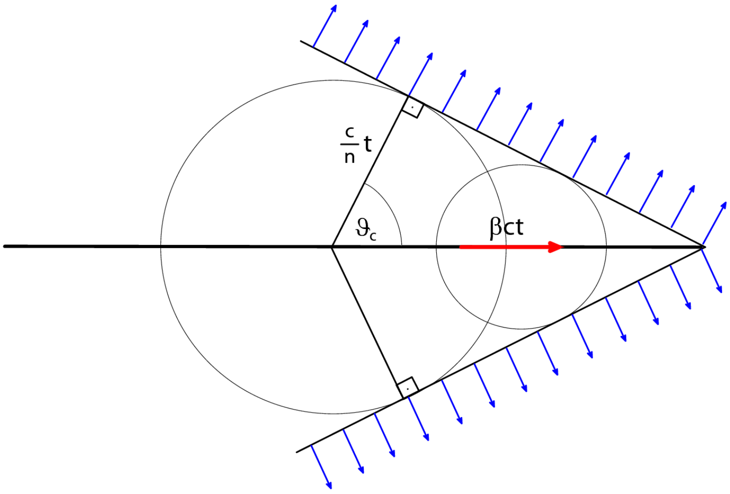

Fig. 4.4: *Depiction of the Cherenkov light emitted by a charged particle that travels with a larger speed than the speed of light in the local medium. The circles illustrate the construction of the wavefront using the Huygens principle (Figure from Hupfer 2008).*

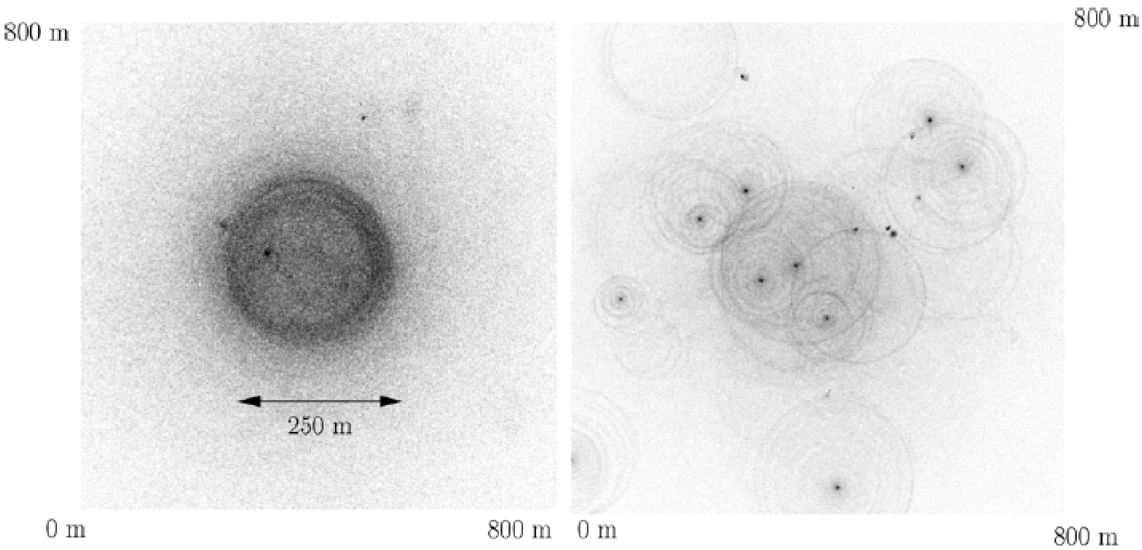

Fig. 4.5: *Distribution of the Cherenkov light emitted by the particles in the air shower induced by a 300 GeV γ-ray (left panel) in comparison to the Cherenkov emission by an air shower induced by a 1 TeV proton (right panel). The images were created with a Monte Carlo simulation for a height of 2200 m a.s.l. (Bernlöhr 2010). The simulations correspond to the simulations shown in Fig. 4.3.*

is possible to reconstruct the direction of the primary γ-ray as well as its energy. The information contained in an air shower can be measured by a telescope that is located at any place in its Cherenkov light pool. Thus, the effective detection area of an IACT experiment is in the order of $10^5\,\mathrm{m}^2$, which is many orders of magnitudes above the effective areas of current-generation satellite experiments.

The first source of cosmic VHE γ-rays to be detected with an IACT experiment was the Crab Nebula by the *Whipple* collaboration (Weekes et al. 1989). The HEGRA collaboration for the first time used a stereoscopic approach for an IACT instrument (Daum et al. 1997). This has several advantages and has become the standard for most of the IACT experiments. By placing several telescopes in the Cherenkov light pool, it is possible to reduce background events, obtain a higher sensitivity and improve the energy and angular resolution of reconstructed γ-ray events significantly. The current generation of IACT telescopes consists of the experiments MAGIC (Albert et al. 2008) and VERITAS (Holder et al. 2008) in the Northern Hemisphere and CANGAROO III (Tanimori et al. 1998) and H. E. S. S. (Aharonian et al. 2006a) in the Southern Hemisphere. A vast number of new VHE γ-ray sources was detected within the last years by these four experiments, most prominently by the Galactic Plane scan of the H. E. S. S. experiment, in which 14 sources were observed in VHE γ-rays for the first time (Aharonian et al. 2005a, 2006b). At the moment, there are efforts to upgrade or extend the current-generation experiments. With the construction of a second telescope, MAGIC is currently upgraded to the stereoscopic telescope system MAGIC II (Goebel et al. 2009) and the VERITAS experiment is also upgrading its telescope system to achieve a higher sensitivity (Otte et al. 2009). The H. E. S. S. collaboration is currently constructing the new H. E. S. S. II telescope, which will be placed inside the existing telescope and will be the largest Cherenkov telescope ever built (Punch et al. 2005). With this new telescope, H. E. S. S. phase II will lower its energy threshold significantly and improve its sensitivity, as can be seen in Fig. 4.6, where the sensitivity curves for H. E. S. S. phases I and II are plotted in comparison. The lowered energy threshold of $\sim 20\,\mathrm{GeV}$ will enable a crosscheck of the measurements with the *Fermi* Gamma-ray Space Telescope.

The basic layout of the IACT telescopes is the same for all of the above-mentioned experiments. Telescopes are placed in the Cherenkov light pool of air showers triggered by incident VHE γ-rays. A schematic view of four IACT telescopes placed in the Cherenkov light pool of an air shower from an incident VHE γ-ray is shown in Fig. 4.7. The light is collected by the telescope mirrors and mapped onto a camera consisting of fast photodetectors. The mirrors typically have a spherical or parabolic shape and are made up of many mirror facets to form one large reflector. The collection area of the mirrors is proportional to the energy threshold of IACT telescopes, since the air shower from less energetic primary γ-rays emit a smaller number of Cherenkov photons. A ray of light emitted at a point (x, y, z) in the atmosphere is mapped onto the camera coordinate system as

$$\begin{pmatrix} u \\ v \end{pmatrix} = -\frac{f}{z} \begin{pmatrix} x \\ y \end{pmatrix}, \tag{4.12}$$

where (u, v) are the camera coordinates of the detected ray of light and f is the focal length of the telescope. Figure 4.8 illustrates how the Cherenkov light emission from an air shower is mapped onto the focal plane of the telescope. For this picture it is assumed that the Cherenkov light is emitted isotropically along the shower axis. The resulting images have an elliptical shape, in which the shower axis corresponds to the main axis of the ellipse. Since the mapping is nonlinear, the resulting ellipses are slightly distorted, as

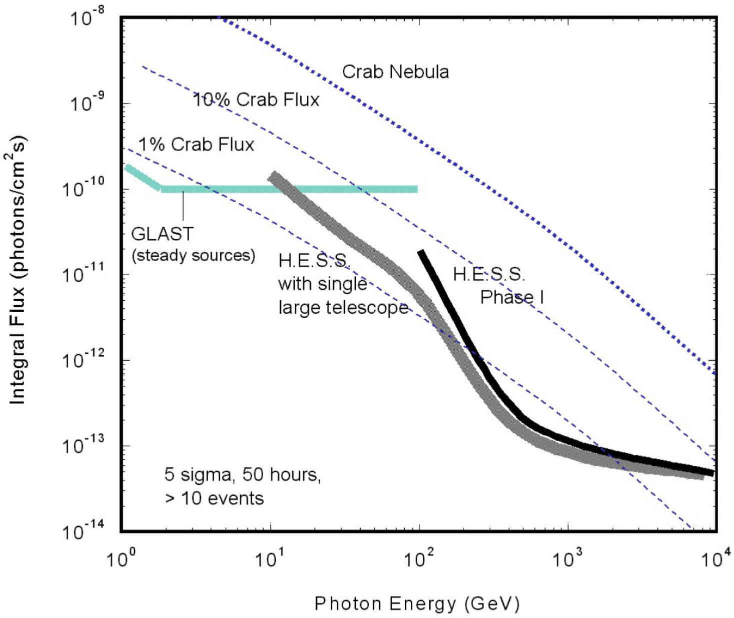

Fig. 4.6: *Sensitivity plot for phase II of the H. E. S. S. experiment. The detection threshold will be lower and the sensitivity higher than for H. E. S. S. Phase I (Figure from Punch et al. 2005).*

can be seen in the right panel of Fig. 4.8. However, this does not affect the image of the shower axis and thus, does not affect the direction reconstruction of the primary γ-ray.

The camera of IACT telescopes need to fulfill several requirements. Since all of the Cherenkov photons from an air shower arrive on the ground within an interval of a few nanoseconds, the photo detectors need to be very fast. Furthermore, the total amount of light emitted by the particles in an air shower is very small, and thus very sensitive detectors are needed to measure the Cherenkov light. In current-generation IACT telescopes, photomultiplier tubes (PMT) make up the individual pixels of the cameras. Sophisticated triggering schemes for the cameras are required to discriminate the faint signal from the background. Typically, the camera is divided into different sectors and only triggers if enough pixels within one sector record a signal above a certain threshold. This is crucial to discriminate the faint Cherenkov light from air showers among the dominating night sky background (NSB) from star light and other light sources. In order to reduce the NSB it is also common to observe only during the time of total darkness, meaning that there is no moon visible. For stereoscopic IACT telescope systems there is also a central trigger, which requires that the camera triggers from multiple telescopes have recorded a signal. Due to this central trigger it is possible to reject camera triggers from muons almost completely, since the muons interact at a low altitude and only lead to a signal in single telescopes. Additionally, a stereoscopic central trigger also leads to a suppression of the hadronic background events. The Cherenkov light pool of air showers triggered by hadrons is much more inhomogeneous, and thus the central trigger leads to a suppression of the hadronic events compared to the γ-ray events.

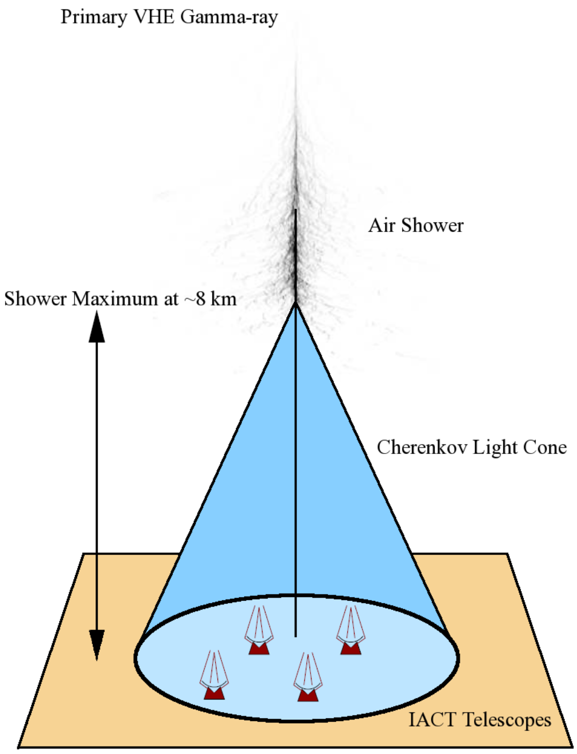

Fig. 4.7: *Schematic layout of a stereoscopic IACT experiment. Four telescopes are placed inside the Cherenkov light pool of the air shower triggered by the incident VHE γ-ray. The properties of the primary particles can be reconstructed by using the light collected with the telescopes (Figure adopted from Funk 2005).*

4.4 H. E. S. S. — The High Energy Stereoscopic System

H. E. S. S., the High Energy Stereoscopic System, is a system of four telescopes that uses the IACT to detect γ-ray photons via the Cherenkov light of the air showers that are induced when the photons interact with the Earth's atmosphere. In the previous Section, the IACT principle was introduced. Now we will examine how the H. E. S. S. experiment realizes this technique to detect VHE γ-rays with a ground-based telescope system. The first part of the section will deal with the general layout of the H. E. S. S. telescope array and its components, whereas the second part will focus on two different data analysis techniques for H. E. S. S., namely the standard Hillas analysis and the more sophisticated Model++ analysis based on a semi-analytical model of the air shower.

4.4.1 The Telescope Array

H. E. S. S. is an array of four IACT telescopes situated in the Khomas highland of Namibia. The telescope array lies at a position of 23°16′ S and 16°30′ N at an altitude of 1800 m a.s.l. near the Gamsberg mountain. The experiment is located on the Farm Göllschau, which is about 160 km to the south-west of the Namibian capital Windhoek. Figure 4.9 shows a map of Namibia on which the location of the Farm Göllschau is marked. The telescope site in Namibia satisfies the high requirements concerning the atmospheric conditions necessary for the observations. Of the moon-less nights in which H. E. S. S. observations

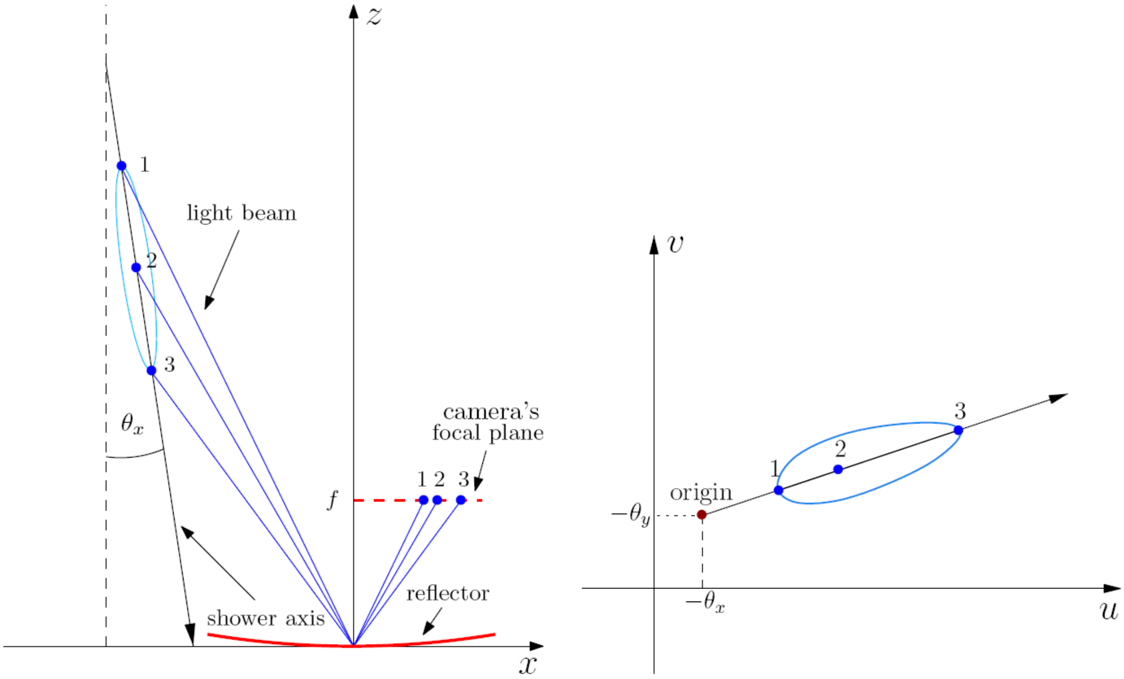

(a) Shower image mapping (b) Corresponding camera image

Fig. 4.8: *Imaging of the Cherenkov light of an air shower with an IACT telescope (Figure from Nowak 2008).*

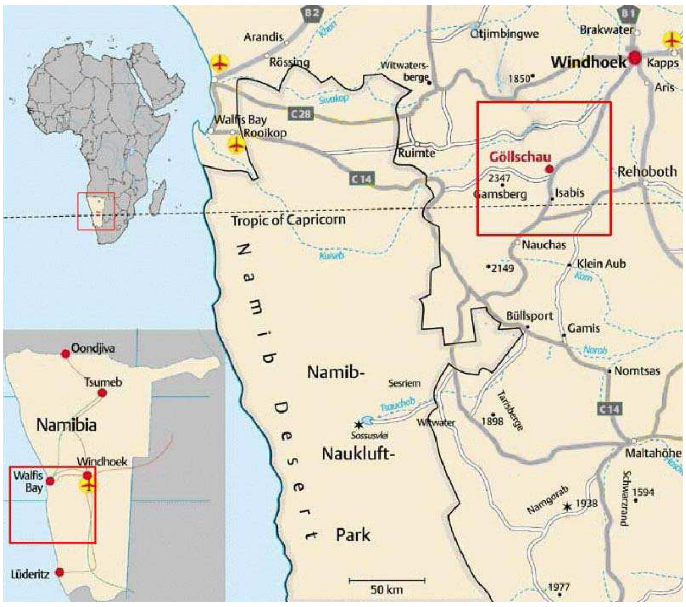

Fig. 4.9: *A map of Namibia on which the location of the H. E. S. S. experiment on the Farm Göllschau in the Khomas highland is indicated (Figure from Berge 2006).*

Fig. 4.10: *Photograph of the four telescopes of the H. E. S. S. experiment. The building in front houses the control room for the operation of the telescope system. The picture was taken in January 2004 after the completion of the telescope array (Figure from Berge 2006).*

are possible, 57% are cloud-free and in 94% of these nights, the humidity is below 90%. This makes the site ideally suited for observations with an IACT telescope system. The location in the Southern Hemisphere furthermore enables observations of the inner region of the Milky Way close to the Galactic center. This is especially important for the survey of the Galactic plane conducted with the H. E. S. S. telescope system.

In Fig. 4.10 the four telescopes of the H. E. S. S. array can be seen shortly after the completion of the full array in 2004. The telescopes are positioned in a square with a side length of 120 m. Two conditions are important when choosing the spacing of the telescopes. Firstly, a large distance between the telescopes is advantageous for the stereoscopic imaging of the air showers and increases the effective area for the collection of γ-rays. On the other hand, the radius of the Cherenkov light pool on the ground is roughly ≈ 100 m (cf. Sec. 4.2). Thus, a smaller distance between the telescopes increases the probability that a shower is observed by multiple telescopes.

Each of the four telescopes of the H. E. S. S. array has a hexagonal dish which is equipped with 382 round mirrors. A front view of a telescope is shown in Fig. 4.11. The mirrors have a diameter of 60 cm and add up to a total reflecting area of 107 m^2. The mirrors initially had a reflectivity of more than 80%, but due to external causes (e.g. sand storms) the reflectivity has decreased over the years. Therefore, a re-coating of the mirrors is currently under way to restore the initial reflectivity. The mirrors are arranged in a Davies-Cotton design, which is especially suited for the imaging of off-axis light rays. In this design, the mirrors are situated on a sphere with a radius that is equal to the focal length. For the H. E. S. S. telescopes, the focal length is equal to 15 m and the flat-to-flat diameter of the dish is 12 m. The dish is moved by an altazimuth mount, which is favorable due to the simplicity and mechanical robustness of the design. For the azimuthal movement, the telescopes are rotated on a rail with a diameter of 13.6 m at a maximum speed of 100° per minute, while for the elevation the full range from 0° to 90° is accessible. The positioning of the telescopes is monitored on a regular basis with so-called pointing runs, in which the pointing of the telescope is calibrated via optical photographs with the known position of bright stars.

The four telescopes are each equipped with identical cameras that have a diameter of 1.4 m. Since the length of the Cherenkov light pulses of the air showers is only a few nanoseconds and the Cherenkov light is very faint, the camera is made up of photomultiplier tubes (PMT). A total of 960 PMTs, operated at high voltage, are used as the pixels for each

Fig. 4.11: *Front view of a H. E. S. S. telescope that has been moved out of the parking position.*

camera. Figure 4.12 shows a front view on the pixels of one of the cameras. The individual pixel each have a field of view of 0.16° so that the total FOV of the camera is 5°. The circular PMTs are covered with hexagonal Winston cones that collect the light falling in the space between the PMTs, thus increasing the light collecting efficiency of the cameras. The PMTs are arranged in 60 drawers, with 16 PMTs in each drawer, as can be seen on Fig. 4.12. For the triggering of the telescope, each camera is divided into 38 overlapping sectors with 64 pixels in each sector. A camera is triggered, when the preset conditions on the number of triggered pixel above a threshold value of photoelectrons are exceeded in the triggering window of $\approx 1.3\,\mathrm{ns}$. Apart from the camera trigger, H. E. S. S. also has a central trigger, which checks for coincident camera triggers in multiple telescopes. Only events that can be observed stereoscopically, i.e. that trigger at least two telescopes, pass the central trigger.

4.4.2 H. E. S. S. Data Analysis

In the following, a short overview of the analysis of data taken with the H. E. S. S. experiment is given. After briefly outlining the calibration of the data, two analysis methods used for the analysis of the MSH 15−5*2* data set will be presented. Firstly, the Hillas analysis method, based on the calculation of the second moments of the pixel intensity distribution in the cameras. The second analysis method is called the Model++ analysis and employs a comparison of the observed intensities with a semi-analytical model for the reconstruction of the γ-ray events. Since the results presented in Section 4.5 are mainly from the (more sensitive) Model++ analysis, the Hillas analysis will not be discussed in great detail. An introduction, however, is given because of two reasons: on the one hand, the Hillas analysis follows an easily comprehensible approach and has been the "standard" analysis methods for IACT experiments for a long time. On the other hand, the results from the Hillas analysis serve as the starting parameters for the fit procedure in the Model++ analysis.

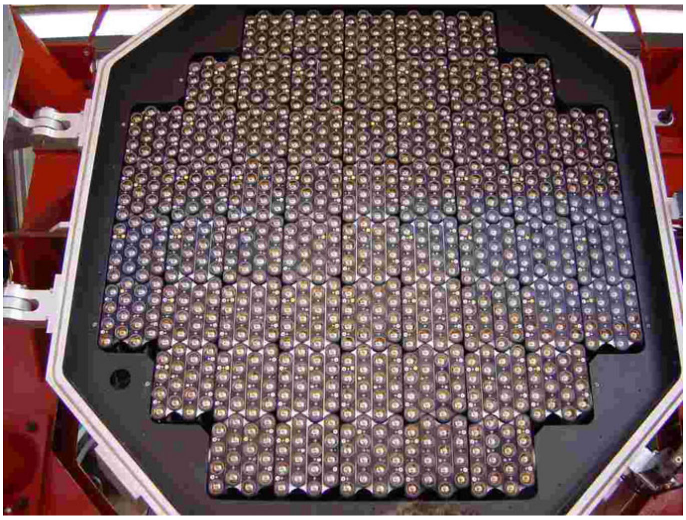

Fig. 4.12: *View of a camera of one of the H. E. S. S. telescopes. The image shows a front view on the camera with its 960 PMTs and the Winston cones that cover them (Vincent et al. 2003).*

4.4.2.1 Calibration

Besides the signal of the camera PMTs that is used for the trigger, the PMTs are read out via two channels, a low gain and a high gain. These two channels are optimized for different signal strengths and provide a good coverage of the expected signals from the Cherenkov radiation from air showers. The signal coming from the PMT is an analog signal and is digitized via an analog-to-digital converter (ADC). The conversion of the digital count value in the low and high gain channels requires a careful calibration process in which several parameters need to be determined, namely the pedestal values of the two channels[2], the respective gain values[3] and the flat-field coefficient[4]. During the calibration process pixels are also flagged as bad and excluded from the further analysis if they were affected by missing drawers, broken pixels or bright stars in the FOV.

4.4.2.2 Hillas Analysis

The Hillas analysis method is used by most of the current IACT experiments. It was first introduced by Hillas and uses the second moments of the intensities in the pixels of the cameras for the reconstruction of the primary γ-ray events and for the separation of these events from the dominating cosmic-ray background (Hillas 1985). This approach has proven to be very time-efficient and robust. Thus, this method is also used for the data analysis with the H. E. S. S. experiment. In the following the basic principles of this analysis method will therefore briefly introduced.

Image Cleaning
Before the second moments of the intensities in the pixels are calculated, the image is first cleaned of pixels that are not due to the Cherenkov light from air showers. This noise

[2]The pedestal value is the number of ADC counts if no Cherenkov photons can be observed by the PMT.
[3]The gain factor between ADC counts and number of photoelectrons (p.e.).
[4]Correction factor for differences between single PMTs.

consists of the night sky background (NSB) from star light, other ambient light sources and the camera electronics noise. A tailcut cleaning is applied to remove the noise and keep the signal from the air shower. In the standard tailcut cleaning, all pixels are left unmodified, that fulfill one of the following criteria:

- the pixel has an amplitude larger than 10 p.e. and has at least one neighbor with an amplitude larger than 5 p.e.
- the pixel has an amplitude larger than 5 p.e. and has at least one neighbor with an amplitude larger than 10 p.e.

All pixels that do not match one of these criteria are discarded. The Hillas parameters that are introduced in the next paragraph are then calculated for the pixels that passed the tailcut cleaning.

Hillas Parameters

The image of an air shower in the camera has an elliptical shape, which is due to the small lateral spread of the air shower compared to its large extension along the shower axis. The parametrization of the shower ellipses with the Hillas parameters provides information about the nature of the primary particle as well as its origin and energy. Figure 4.13 shows the definition of the Hillas parameters in the camera coordinate system. The parameters are the following:

- Center of gravity (COG) of the image;
- Length: the major axis of the shower ellipse;
- Width: the minor axis of the shower ellipse;
- ϑ: the orientation angle of the major axis of the shower ellipse in the camera coordinate system;
- Size: the total sum of the pixel amplitudes in the shower ellipse;
- Local distance: the distance between camera center and COG.

As mentioned before, a good discrimination between air showers of hadronic and electromagnetic origin can be obtained by looking at the length and the width of the image in the camera. However, the shape of the camera image also depends on the energy of the primary particle and the orientation of the shower compared to the telescope. This orientation is quantified via the impact parameter, which is defined as the distance between the telescope and the impact point of the shower axis on the ground. For a good classification of the showers, the deviation of the Hillas parameters length and width to expected values from Monte Carlo simulations is calculated in units of the standard deviation. Furthermore, the parameters for all telescopes are averaged. The mean reduced scaled length (MRSL) is thus defined as:

$$\mathrm{MRSL} = \frac{1}{N_{\mathrm{tel}}} \sum_{i=1}^{N_{\mathrm{tel}}} \frac{\mathrm{length}_i - \langle \mathrm{length} \rangle_i}{\sigma_i}. \tag{4.13}$$

In this expression N_{tel} denotes the number of telescopes that observed the air shower and length_i is the measured length of the shower image. The parameter $\langle \mathrm{length} \rangle_i$ is the mean value of the length from the Monte Carlo simulations and σ_i is its RMS spread. These values are tabulated in look-up tables as a function of the impact parameter and the image size. The mean reduced scaled width (MRSW) is calculated in the same fashion.

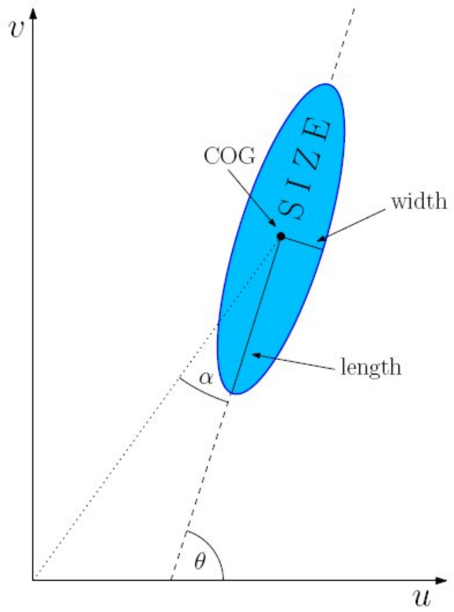

Fig. 4.13: *Sketch of a shower ellipse. The Hillas parameters that are used to characterize the image are shown (Figure from Nowak 2008).*

Analysis Cuts and Event Reconstruction
Due to the low signal to noise ratio in VHE γ-ray observations with IACT experiments, it is crucial to achieve a good separation between γ-ray and background events. In the standard H. E. S. S. data analysis based on the Hillas parameters, there are two layers of cuts that are applied to the shower parameters. Before the reconstruction of the direction and the energy of the primary, the preselection cuts are applied. Only events with camera images above a certain threshold of the size pass this cut, since for events with a small size the reconstruction gets increasingly difficult and inaccurate. In addition, a cut on the local distance is applied in this step to remove events that were recorded close to the camera edge and for which a reconstruction thus is also difficult. After the preselection cuts have been applied, the events are reconstructed and secondary cuts, the postselection cuts, are applied on the properties of the events. In the postselection, there is a cut on the MRSL and MRSW of the events, which is the most powerful discriminator between hadronic showers and electromagnetic showers used in the Hillas analysis. With the postselection cuts it is possible to suppress a large fraction of the isotropic hadronic background. The typical signal-to-noise ratio before cuts is about 1 : 100. After the application of the pre- and postselection cuts, a ratio of around 1 : 1 can be reached, depending on the observed source and the set of analysis cuts that is used.

Following the selection cuts, an event reconstruction is carried out to obtain the direction of the primary particle and its energy from the observed shower images. As stated earlier, the stereoscopic imaging of air showers provides a huge advantage for the reconstruction of the primary particle's origin. An overview of algorithms used in the geometrical reconstruction of the shower direction in IACT experiments is given in Hofmann et al. (1999). Method I from the algorithms introduced in this paper is used for the standard H. E. S. S. analysis. The direction of origin is uniquely defined by the intersection of the shower axes of the two or more images in the cameras. An illustration of the geometric direction reconstruction is illustrated in Fig. 4.14. The image shows the overlaid images of four cameras after the image cleaning has been carried out. The color scale corresponds to the signal in units of

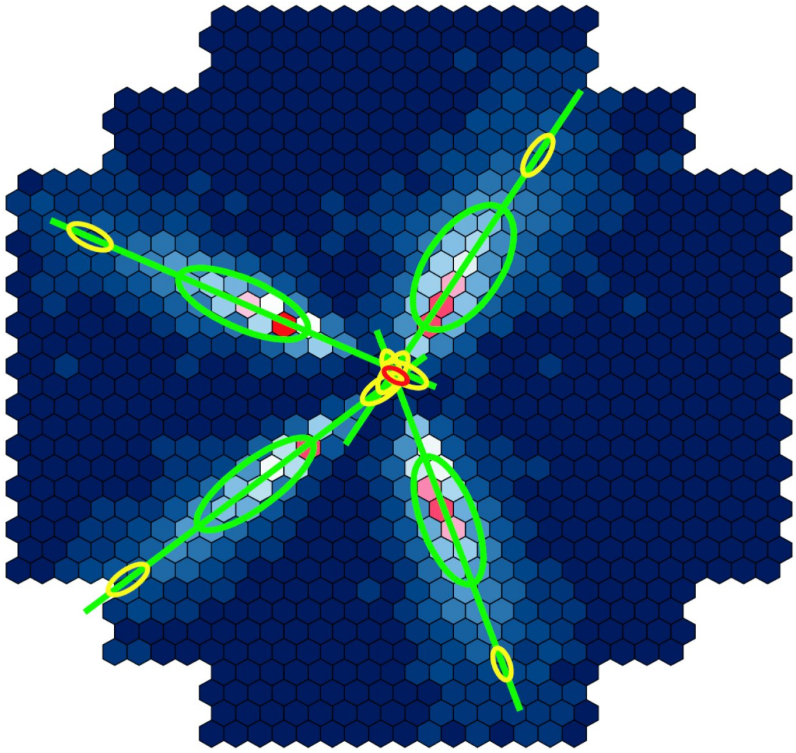

Fig. 4.14: *Illustration of the direction reconstruction in the H. E. S. S. Hillas analysis. The shower images of a γ-ray event with an energy of 7 TeV from four cameras are overlaid in the nominal system. The reconstructed Hillas ellipses are drawn in green, the yellow ellipses mark the estimated region for the source position and the red ellipse is the weighted average of all intersection points. Figure taken from Nowak (2008).*

p.e. in each pixel. The ellipse from the Hillas parametrization is marked in light green and the yellow ellipses mark the source region estimated from each image individually. The red ellipse shows the weighted average of all the intersection points. If a shower is observed by N cameras, then there are $N(N-1)/2$ intersection points, which are weighted based on the size, angular orientation of the shower axis and on the ratio of length to width of the shower ellipse. The geometric reconstruction is carried out in the nominal system, which is centered on the pointing direction of the system. The quality of the direction reconstruction is checked by comparing observations of point sources with Monte Carlo simulations. The measurements show an excellent agreement with the simulations, as is shown e.g. for the Crab Nebula in Aharonian et al. (2006a). A measure for the angular resolution of an optical system is the point spread function. The H. E. S. S. PSF depends on observational parameters such as the zenith angle, azimuthal angle and wobble offset[5], as well as the energy of the primary particle. It can be approximated by the sum of two one-dimensional Gaussian functions (Aharonian et al. 2006a):

$$PSF = A_1 \exp\left(\frac{-\theta^2}{2\sigma_1^2}\right) + A_2 \exp\left(\frac{-\theta^2}{2\sigma_2^2}\right). \tag{4.14}$$

[5]To enable a good background subtraction it is favorable to observe the source not directly, but with a small offset. Typically, sources are offset 0.5° or 07.° of the camera center. This offset is wobbled in different directions from the source, therefore the name wobble offset. For more details, see Section 4.4.2.4.

In general, the direction reconstruction works better for particles with higher energies and for observations close to the zenith. This is illustrated in the comparison plot (Fig. 4.17) of the angular resolution between Hillas and Model++ analysis that is shown in the Section on the Model++ analysis.

The initial energy of the primary particle is reconstructed under the assumption that all showers passing the preselection cuts are γ-ray events. The reconstruction is carried out via a look-up table created from Monte Carlo simulations of air showers and the telescope system. The accuracy of the energy reconstruction is displayed in the Section on the Model++ analysis, where the energy resolution is plotted against the primary energy of the particle for the two different analysis methods in Fig. 4.16.

4.4.2.3 Model++ Analysis

While the analysis based on the Hillas parameters is robust and efficient, the Model++ analysis uses a more sophisticated analysis approach which requires considerably more computation time. It is based on the comparison of the observed Cherenkov light distribution with calculated Cherenkov light distributions from a model of the air shower. An implementation of this concept was first introduced by the CAT experiment (Cherenkov Array at Themis, Le Bohec et al. 1998). Right from the start of the H. E. S. S. experiment, it was also used for the analysis of H. E. S. S. data (de Naurois et al. 2003). Since then it has been continuously improved and become more and more sophisticated (de Naurois 2005). The analysis presented in this work makes use of the latest version of this analysis approach by de Naurois & Rolland (2009). Below, the event reconstruction will be introduced, before the cuts used for the analyses are stated and a short comparison of the performance of the Hillas analysis and the Model++ analysis is given.

Event Reconstruction

The parameters of the primary γ-ray determine the longitudinal, lateral and angular distribution of charged particles in an electromagnetic air shower. The distribution of charged particles, in turn, defines the distribution of Cherenkov light from the shower. In the Model++ analysis, an analytical expression for the Cherenkov light distribution from the shower is used, the shower model, which is derived from a parametrization of extensive Monte Carlo simulations. The calculation of the shower images not only takes into account instrumental effects, such as the point spread function of the system, but also the light in each pixel due to the night sky background. The shower model thus gives a prediction of the Cherenkov light distribution on the ground based on the primary particle's energy, direction, impact parameter and the depth of the first interaction in the atmosphere (primary depth, t_0).

Contrary to the Hillas parameter analysis, the Model++ analysis does not require an image cleaning before the analysis. All sources leading to a signal in the pixels are taken into account in the modeling of the shower image. As an example for the shower model, four images of the simulated Cherenkov light distribution of an air shower are shown in Fig. 4.15. The primary γ-ray for this shower has an energy of 1 TeV and the different pictures show the light distribution for a shower with different distances to the telescope and different points of first interaction in the atmosphere. The shower models are generated for different zenith angles, impact distances, energies and first interaction depths of the primary γ-ray photon. All in all, 624000 shower templates are generated (de Naurois &

Rolland 2009) and an interpolation procedure is used for parameter values for which no simulated light distribution has been calculated.

The reconstruction of the direction and the energy of the primary γ-ray photon is then carried out via a log-likelihood minimization on the χ^2 value between the recorded shower image and the simulated shower models. The simulated shower images give the density of the Cherenkov light in the focal plane. To calculate the expected signal for each pixel, the pixel size and the response of the photomultiplier have to be taken into account. The conditional probability density (likelihood) to observe a signal with strength s (in p.e.) is given by (de Naurois & Rolland 2009):

$$P(s|\mu, \sigma_p, \sigma_\gamma) = \sum_n \frac{\mu^n e^{-\mu}}{n!\sqrt{2\pi(\sigma_p^2 + n\sigma_\gamma^2)}} \exp\left(-\frac{(s-n)^2}{2(\sigma_p^2 + n\sigma_\gamma^2)}\right) . \tag{4.15}$$

In this equation, μ is the expectation value and n the number of photoelectrons. The resolution of the photomultiplier is represented by a Gaussian with a width of $\sqrt{(\sigma_p^2 + n\sigma_\gamma^2)}$, where σ_p is the pedestal width and σ_γ the width of a single photoelectron peak. The pixel log-likelihood is then defined as

$$\ln L = -2 \ln P(s|\mu, \sigma_p, \sigma_\gamma) . \tag{4.16}$$

The likelihood function for each telescope follows as the sum over all the pixel in the camera. The pixels are assumed to be independent, so that the telescope likelihood is merely a sum of the pixel likelihoods:

$$\ln L_{\mathrm{tel}} = \sum_{\mathrm{pixel}\, i} \ln L_i = -2 \sum_{\mathrm{pixel}\, i} \ln P(s_i|\mu_i, \sigma_p, \sigma_\gamma) . \tag{4.17}$$

The properties of the primary γ-ray are now reconstructed via a pixel-by-pixel comparison of the observed camera image and the shower model. This is done using a minimization procedure on the telescope likelihood which makes use of the Levenberg-Marquardt fit algorithm. Since the starting point is crucial for the correct convergence of the fit, the results from the Hillas analysis of the shower are used as the starting values. In this process, the optical efficiency of the telescope is also taken into account. The model prediction for the image amplitude is scaled according to the results of single muon events obtained in calibration runs (Aharonian et al. 2004). For the reconstruction of a single event, a computing time of 50 to 100 ms is needed on a typical desktop machine. The output of the minimization are now the six parameters characterizing the primary particle[6], the correlation matrix of the fit and the log-likelihood value of the shower.

For the discrimination between electromagnetic and hadronic air showers, the Model++ analysis uses an approach which is based on the goodness-of-fit of a shower, G. It is defined as:

$$G = \frac{\sum_{\mathrm{pixel}\, i} \left[\ln L(s_i|\mu_i) - \langle \ln L \rangle|_{\mu_i}\right]}{\sqrt{2 \times \mathrm{dof}}} , \tag{4.18}$$

with dof the number of degrees of freedom[7]. At the end of the likelihood fit, pixels are also sorted into two categories, depending on whether they belong to the shower core or are

[6] These are energy, direction (2 parameters), impact parameter (2 parameters) and the depth of the first interaction.

[7] The number of degrees of freedom is the number of camera pixel minus six.

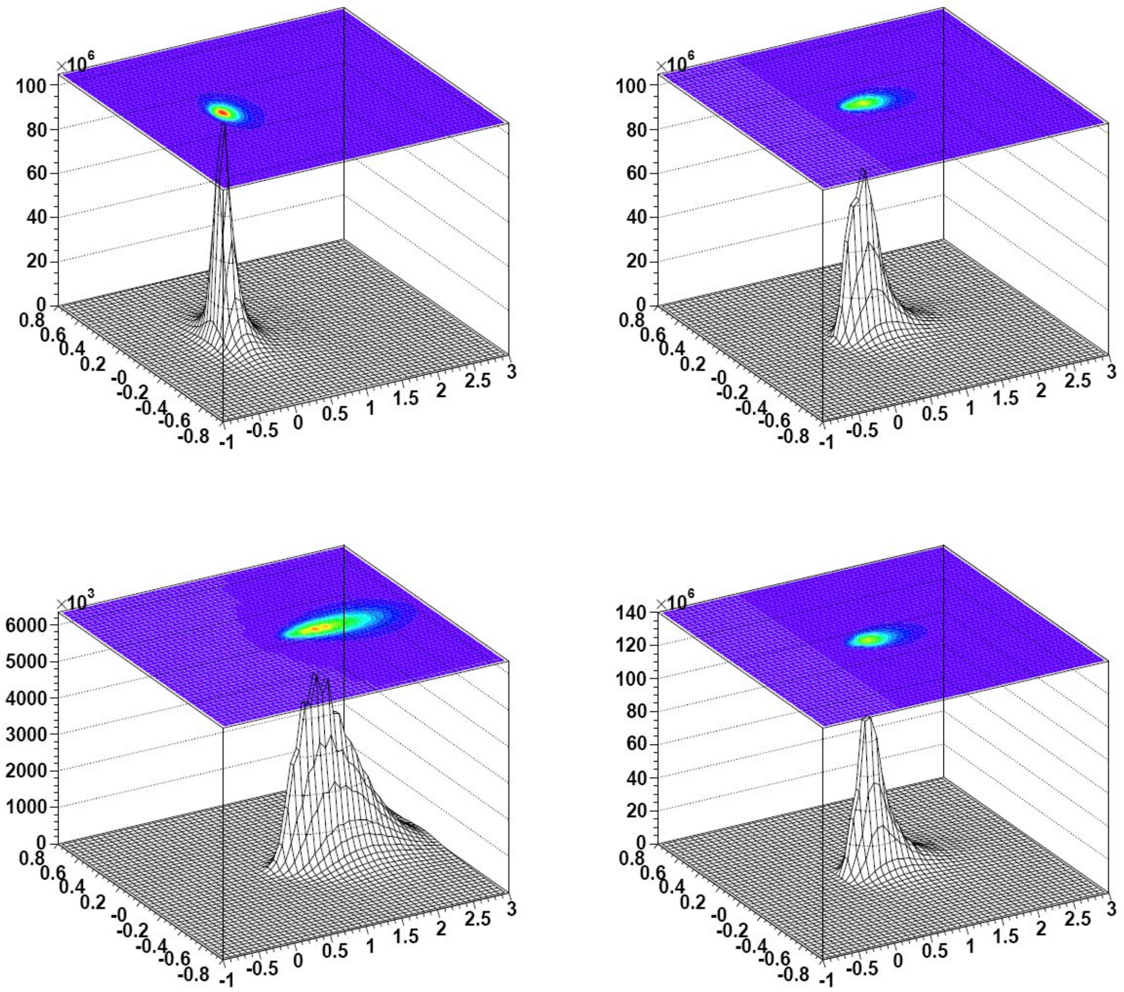

Fig. 4.15: *Model of the Cherenkov light distribution for a primary γ-ray with an energy of 1 TeV. For the top-left image, the shower has its first interaction in the atmosphere at one radiation length of the primary particle and the shower axis falls 20 m away from the telescope. The images in the top-right and the bottom-left show the Cherenkov light distribution from the same shower at a distance of 100 m and 250 m to the telescope. The lower-right image is the light distribution from a shower with the same primary energy, but with a primary depth of three radiation lengths and a distance of 100 m. The x- and the y-coordinates are given in the camera system in units of degrees, the color scale corresponds to the image amplitude. Figure taken from de Naurois & Rolland (2009).*

Table 4.1: *Parameter cut values for the different analysis configurations used in the Model++ analysis.*

Name	Size Min. [p.e.]	Nom. Dist. Max. [°]	N_{tel} Min.	$MSSG$	BG Max.	t_0 $[X_0]$	L_{NSB} Max.
Standard	60	2	2	$(-3, 0.6)$	2	$(-1, 4)$	-1
Faint Source	120	2	2	$(-3, 0.4)$	2	$(-1, 4)$	-1
Loose Cuts	40	2	2	$(-2, 0.9)$	2	—	—

considered as background[8]. Similar to Eq. 4.18, a shower goodness (SG) and a background goodness (BG) is calculated for the pixels from these categories. The analysis cuts in the γ-hadron separation are applied on the mean scaled values of these two parameters, using the information of all runs observing the corresponding event. The mean scaled shower goodness, $MSSG$, is given by a sum over all telescopes:

$$\mathrm{MSSG} = \frac{1}{\sqrt{N_{\mathrm{tel}}}} \sum_{i=1}^{N_{\mathrm{tel}}} \frac{\mathrm{SG}_i - \langle \mathrm{SG} \rangle_i}{\sigma_i}. \tag{4.19}$$

The mean scaled background goodness, $MSBG$, is defined in the same manner. In the next paragraph the cut values on these parameters used in the H. E. S. S. data analysis will be discussed.

Analysis Cuts

The separation of γ-ray and hadron-induced events is crucial for a good performance of any analysis method in γ-ray astronomy. With a cut on the shower goodness, the Model++ analysis is able to reject more than 95% of the background events, while keeping 70% of the γ-ray events (de Naurois & Rolland 2009). This leads to a sensitivity that is in the order of two times higher than the sensitivity achieved with the standard Hillas analysis.

The cut values used for the data analysis presented in Section 4.5 are given in Table 4.1. The largest discrimination between γ-ray events and hadrons is achieved by using the parameter $MSSG$. Two additional cuts on the background goodness and L_{NSB}[9] filter additional hadronic events while having no influence on γ-ray events. For point-like sources, there is also a cut on θ^2 (i.e. the squared radial distance of the reconstructed direction of the event to the source position), whereas for the analysis of extended regions, a value corresponding to the source size is typically used for this cut.

Performance of the Model++ analysis

As already stated in the last paragraph, the Model++ analysis has a sensitivity that is in the order of a factor two larger than the sensitivity of the standard Hillas analysis. Figure 4.16 shows a comparison of the energy resolution and the energy bias for the

[8] A pixel belongs to the shower core, if it has a predicted amplitude above 0.01 p.e.

[9] L_{NSB} is the likelihood value when comparing the observed camera image to pure Gaussian noise caused by fluctuations of the night sky background.

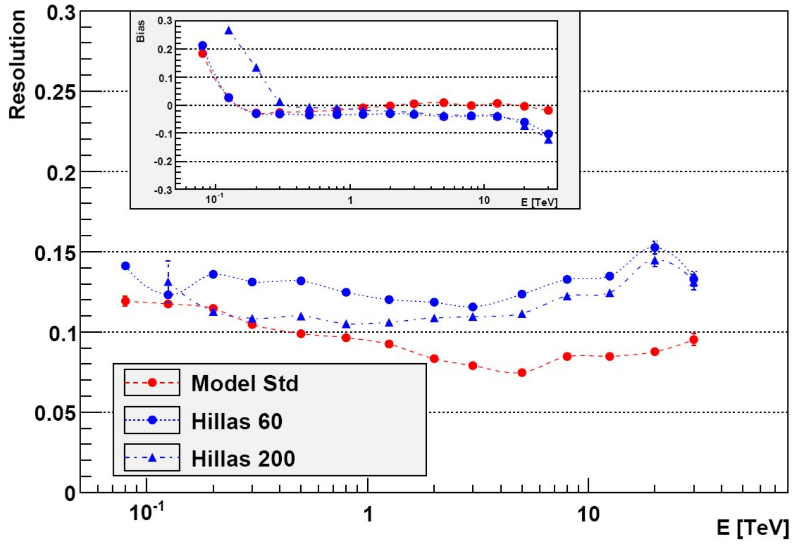

Fig. 4.16: *Comparison of the energy resolution (main plot) and the energy bias (inset) between the Model++ analysis and the Hillas analysis as a function of energy. The red circles (dashed line) correspond to the Model++ analysis, blue circles (dotted line) and triangles (dot-dashed line) to the Hillas analysis with different cut values. Figure taken from de Naurois & Rolland (2009).*

Model++ analysis and the Hillas analysis. In this plot, the energy resolution is defined as the root mean square (rms) of $\Delta E/E$ and the energy bias as $\log(E_{\mathrm{reco}}/E_{\mathrm{true}})$. The improved energy resolution of the Model++ analysis in comparison to the Hillas analysis, especially in the energy range from 500 GeV to 10 TeV is clearly visible.

The angular resolution of the analyses is defined as the 68% containment radius of the PSF. It is displayed in Fig. 4.17 as a function of energy (left plot) and as a function of zenith angle (right plot). For the Model++ analysis the angular resolution is in the order of $0.06°$ and is fairly stable over a large range of energies and up to zenith angles of $\approx 50°$. The superior angular resolution of the Model++ analysis to the Hillas analysis allows for a better study of the morphology of extended sources and also results in an improved sensitivity for the observation of point-like sources.

4.4.2.4 Background Estimation

The parameter cuts for the analysis methods presented in the previous two Sections suppress a large fraction of the dominating air showers of hadronic origin. However, even after these cuts there is still background present from γ-like hadronic air showers and, possibly, from diffuse γ-ray emission. An estimate of the background events contributing to the γ-ray flux of a source is done via the definition of a source region (on region) and background regions (off region). In the latter regions, no contribution of γ-ray events is expected. The number of excess events is then defined as

$$N_{\mathrm{excess}} = N_{\mathrm{on}} - \alpha N_{\mathrm{off}} \,, \qquad (4.20)$$

where N_{on} and N_{off} are respectively the number of events in the source and the background region, and α is a normalization factor which takes into account the differences between the source and the background regions (e.g. size, exposure, zenith angle, acceptance, etc.).

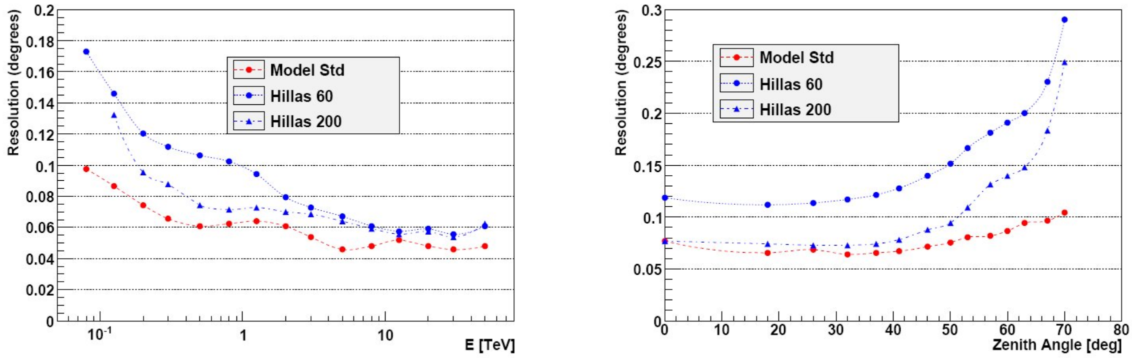

Fig. 4.17: *Comparison of the angular resolution (defined as the* 68% *containment radius of the PSF) between the Model++ analysis and the Hillas analysis. The left plot shows the angular resolution plotted against energy for observations at zenith, the right plot shows the average angular resolution as a function of the zenith angle for a source with a power-law spectrum with an index of 2. The markers have the same meaning as in Fig. 4.16. Figure taken from de Naurois & Rolland (2009).*

The significance of the deviation of the calculated excess of an observation from excess due to statistical background fluctuations is determined using equation 17 by Li & Ma (1983).

A variety of different approaches exists to handle the selection of background regions. For a detailed description of these concepts, see e.g. Berge et al. (2007) and Section 5 in Aharonian et al. (2006a). For the analysis presented in this work (see Section 4.5), the ring-background model and the reflected-background model (also referred to as multiple-off regions background) were used. The two methods are schematically displayed in Fig. 4.18.

In the ring-background model approach, the background for each position on the sky map is determined by using the events contained in a ring around the respective position (and excluding known γ-ray sources). The inner radius is chosen significantly larger than the source extension to avoid contamination of the background region with source events. The method is very robust and well-suited for the generation of sky maps. However, it is less ideal for the spectral analysis, since the acceptance within the ring is not constant and thus might lead to a faulty estimation of the background level. The reflected-background technique uses a number of off-regions that are of equal shape and size as the source region and also have the same distance to the pointing position. All events that fall inside the off-regions are used as background for the calculation of the excess events in the on-region. The big advantage of this approach is, that no correction of the acceptance of the camera is required, making this approach ideally suited for spectral analysis. A disadvantage is, that the method can only be used for observations positions which lie outside the extension of the γ-ray source. For both of these background subtraction methods, the target position of the observation has to lie outside of the source region. Otherwise, no background estimation from the same FOV is possible and dedicated background observations have to be taken. Therefore, data is usually taken in the so-called wobble mode, in which the observation position is wobbled in different offsets around the position of the γ-ray source. Typical offsets are $\pm 0.5°$, but larger offsets are used for large extended sources. Unless otherwise specified, the ring-background model was used for the generation of sky maps and for the morphological studies in the data analysis presented in the next Section. For

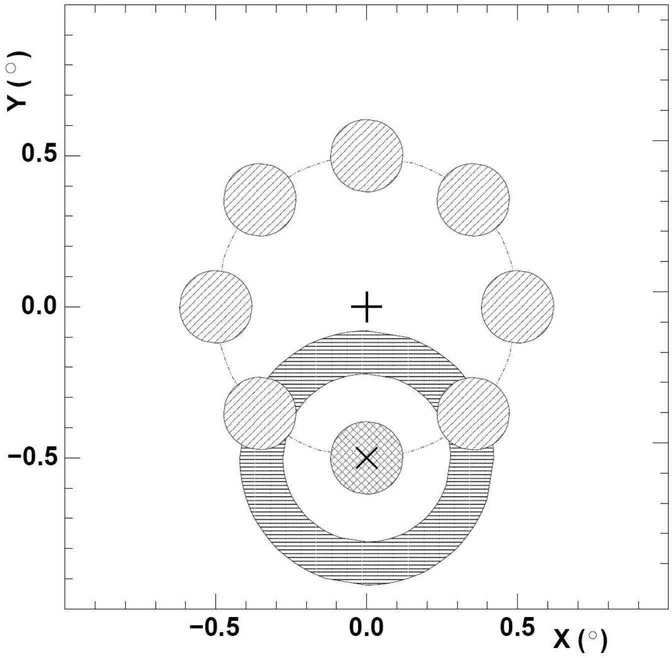

Fig. 4.18: *Illustration of background modeling techniques used in VHE γ-ray astronomy. The cross marks the observation pointing of the telescope and the X marks the position of the target. The hatched circle is the source region (on region). For the reflected-background method, the regions marked with diagonal lines and for the ring-background method, the region filled with horizontal lines are used. Figure taken form Aharonian et al. (2006a).*

spectral analysis, the reflected-background method was applied.

4.5 Analysis of the H. E. S. S. Data Set of MSH 15−52

Now that the techniques used for the analysis of the data taken by the H. E. S. S. experiment have been introduced, the focus of this Section will be the analysis results of the H. E. S. S. observations of the PWN MSH 15−52. A brief introduction to the previous VHE γ-ray observations of this source by H. E. S. S. and other experiments was already given in Chapter 2. In Fig. 2.2 the smoothed H. E. S. S. excess map of the analysis of earlier observations (Aharonian et al. 2005b) is shown. Since then, the data set has been increased and more sensitive data analysis techniques have been developed, as for example the Model++ technique presented in Section 4.4.2.3. These two facts in conjunction allow for an analysis of MSH 15−52 with an unprecedented precision, which will be presented in the following. First an overview of the H. E. S. S. data set is given, followed by the analysis of the morphology and the spectrum of the source. In the last part of the Section, a spatially resolved spectral analysis of the source will be presented. This analysis is part of a H. E. S. S. publication that is currently in preparation (HESS Collaboration et al. in prep.).

4.5.1 Data Set

Already in the early stages of the H. E. S. S. experiment, MSH 15−52 was considered as a prime target for observations, due to the high spin-down luminosity of PSR B1509−58 and the extended nonthermal emission seen at X-ray energies. Therefore, it was one of the first targets to have been observed with the fully completed telescope array in 2004. The detection of MSH 15−52 as the first spatially resolved source of VHE γ-rays was announced by the H. E. S. S. collaboration using 22 hours of observation time (Aharonian et al. 2005b). The data set used in this publication consisted of runs[10] taken between March and June 2004. In these 53 runs, all of the four telescopes were fully operational. The runs were taken as wobble runs on the pointing position ($\alpha_{J2000} = 15^h14^m27\overset{s}{.}12$; $\delta_{J2000} = -59°16'18\overset{''}{.}12$) with offsets of $\pm0.5°$ in declination and $\pm1.0°$ in right ascension, to allow background subtraction from the same field of view. These runs have a mean zenith angle of 37°. For the analysis, only runs passing certain selection criteria, e.g. on the atmospheric condition, were used. More details on the run selection criteria are given in Aharonian et al. (2006a). In Table 4.2 this data set is labeled as "old" and the live time and the live time after correction for the acceptance is given[11].

For the data sets used in the analysis presented here, run lists were used for which the runs satisfied the following quality selection criteria:

- all four telescopes operational,
- run length longer than ten minutes,
- zenith-corrected central trigger rate between 100 and 500 Hz,
- fluctuations of central trigger rate less than 4%,

[10]For the data taking process in H. E. S. S., observation runs are defined in time intervals of typically 28 minutes. Between each run, a short transition time passes, in which the telescope array is made ready for the next observation run.

[11]The acceptance of the camera is lower towards the edges of the camera. Therefore an acceptance-corrected live time is defined, in which the live time of a run is weighted with the relative acceptance of the source position in the camera.

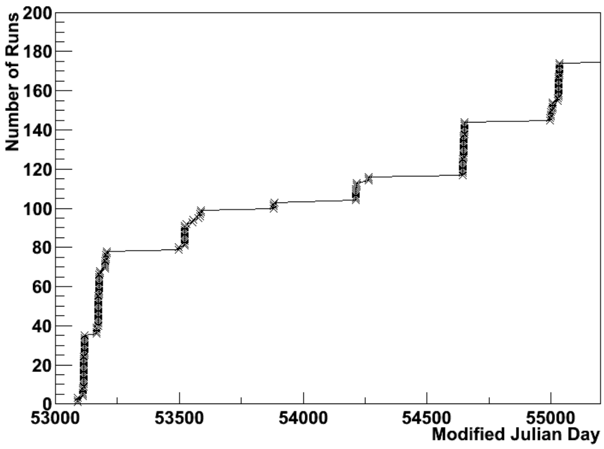

Fig. 4.19: *Number of H. E. S. S. observation runs on MSH 15−52 plotted against the date. The date is given as modified Julian date (MJD). MJD 53000 is equal to 27 December, 2003, MJD 55500 is 31 October, 2010.*

- telescope radiometer stability better than 0.5°C[12],
- fraction of broken pixels less than 10%.

As the central position, the best-fit position of the data analysis in the first publication was used ($\alpha_{J2000} = 15^h 14^m 7^s$; $\delta_{J2000} = 59°9'27''$). All in all 72, 107 and 179 runs pass the selection criteria and have, respectively, a central position with an angular distance of less than 1.0°, 2.0° and 2.5° to this position. The live times for the lists with these runs are given in Table 4.2. The new run lists have live times that are much larger than the live time of the previously used data. Although the number of dedicated runs has also increased by roughly a factor of 1.5, the largest fraction of new data is from runs taken in the context of the H. E. S. S. scan of the Galactic Plane and from observations of other sources in the vicinity of MSH 15−5*2*. Therefore the increase in acceptance-corrected live time is not as noticeable as the increase in the number of runs (cf. Table 4.2). Figure 4.19 shows the cumulative number of runs plotted against the observation date. As stated before, a large fraction of the runs was taken already in 2004. The distribution of zenith angles of the 2.5° run list is plotted in Fig. 4.20. The mean of the distribution lies at 37.2°, close to the value of 37° for the run list of the initial publication.

Table 4.2: *List of the data sets used in the analysis of the H. E. S. S. data on MSH 15−52.*

Data set	No. of Runs	Live time [h]	Acc. corr. live time [h]
Old (Aharonian et al. 2005b)	53	22.1	21.1
New, 1.0°	72	29.8	28.6
New, 2.0°	107	45.2	37.4
New, 2.5°	179	77.2	45.3

[12]Each telescope is equipped with an infrared radiometer to monitor the sky temperature in the FOV. Clouds increase the observed sky temperature and the radiometers therefore provide good means of ensuring cloud-free observation conditions.

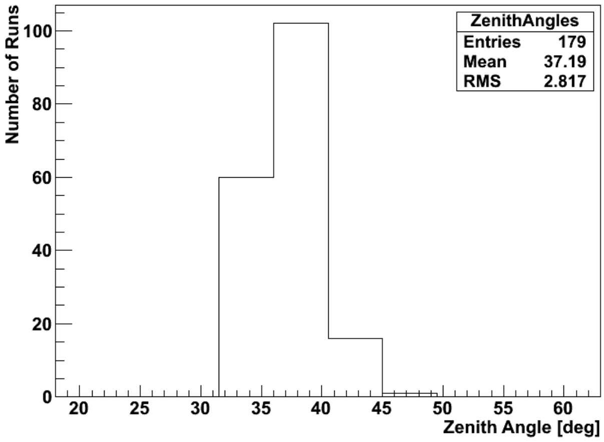

Fig. 4.20: *Distribution of zenith angles for the* 2.5° *run list on MSH 15−52. Most runs were taken at zenith angles between* 30° *and* 40°, *with a mean value of* 37.2° *and an rms spread of* 2.8°.

4.5.2 Comparison of Analysis Configurations

In the following, a comparison of the results obtained with two different analysis methods, Hillas and Model++ analysis, with different configuration of the analysis cuts will be presented. For this analysis, the three different run lists presented above were used. As the source region, a circle around the best-fit position of Aharonian et al. (2005b) with a radius of 0.3° was used, identical to the analysis presented in that publication. Events from a region with a radius of 0.35° around the same position were excluded from the background estimation to avoid contamination of the background with γ-ray events from the source. Table 4.3 lists the results from the different analyses. As can be seen, both cut configurations of the Model++ analysis yield a significance that is a factor of roughly 1.5 larger than the significance above background obtained with the Hillas analysis for the same three run lists. The total number of γ-ray excess events is higher for the Hillas analysis, since more γ-like hadronic events pass the selection cuts as for the Model++ analysis. The rate of γ-ray events that is shown in Table 4.3 is not corrected for acceptance effects. Therefore it decreases systematically for the larger run lists, since MSH 15−52 lies at large offsets for parts of these lists.

A common way to estimate the extension of a source and to check the compatibility of the observed event distribution with point-like emission is to look at the distribution of the radial distance of the events from the centroid position. To avoid geometrical effects in the distribution, the squared radial distance, θ^2, is usually plotted. Figure 4.21 shows the θ^2-plots for the Hillas and Model++ analysis with the position and region as discussed above. On the left hand side, the distribution for the Hillas analysis is plotted, on the right hand side the Model++ results are shown. In both plots, the filled area marks the events from the source region and the black data points the events from the background region. The plots illustrate that the background distribution is flat, as would be expected for a well-understood isotropical background. Beyond the extension of the source region used for the analysis (0.3°, equivalent to 0.09 deg^2 in the θ^2-plot) the source event distribution becomes more and more equivalent to the background. Comparing the two distribution from the Hillas and Model++ analysis one can already see, that the angular resolution of

Table 4.3: *Results of the analysis of MSH 15−52 obtained with different analysis methods and cut configurations.*

Data set	Analysis	Configuration	Excess Events	Significance	Rate [γ/min]
1.0°	Hillas	Std	4132	32.2	2.31 ± 0.08
2.0°	Hillas	Std	5019	37.2	1.85 ± 0.05
2.5°	Hillas	Std	5844	41.6	1.26 ± 0.03
1.0°	Model++	Std	3875	48.0	2.17 ± 0.05
2.0°	Model++	Std	4561	54.2	1.68 ± 0.04
2.5°	Model++	Std	5237	60.2	1.13 ± 0.02
1.0°	Model++	Faint	3196	46.8	1.79 ± 0.04
2.0°	Model++	Faint	3731	52.9	1.37 ± 0.03
2.5°	Model++	Faint	4176	57.6	0.90 ± 0.02

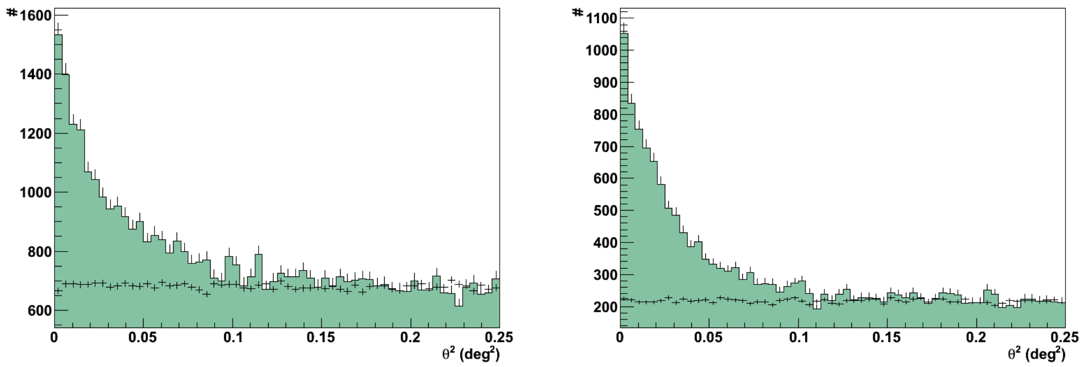

Fig. 4.21: *Plot of the θ^2-distribution of the events around the centroid position of MSH 15−52. The filled area marks the events from the source region (0.3° radius), the black data points mark the distribution of the background events. The left panel shows the distribution for the Hillas analysis with std cuts, on the right panel the result for the Model++ std cuts is plotted.*

the latter analysis is significantly better and the distribution is thus more smeared out for the Hillas analysis.

In Fig. 4.22 the sky maps obtained from the two analysis methods are shown: in the top row the results from the Hillas analysis are displayed and in the bottom row the Model++ results. In each case the left hand map shows the unsmoothed map of the excess events. The color scale indicates the number of excess events in each bin of the map. The size of the bins was chosen as 0.01° for both, right ascension and declination. Comparing the unsmoothed excess maps, one can see the higher background level that is present in the Hillas analysis (also apparent in the θ^2-plots, Fig. 4.21). On the right hand side, sky maps are shown that were smoothed with the point spread function for the respective analysis. The difference in the extension of the PSF between both analyses is apparent ($R_{68} = 0.12°$ for the Hillas analysis, $R_{68} = 0.06°$ for the Model++ analysis). MSH 15−52 appears more circular and shows a less elongated shape in the Hillas analysis, which is due to the lower angular resolution of this analysis method. For the smoothed maps the color scale represents the excess in arbitrary units.

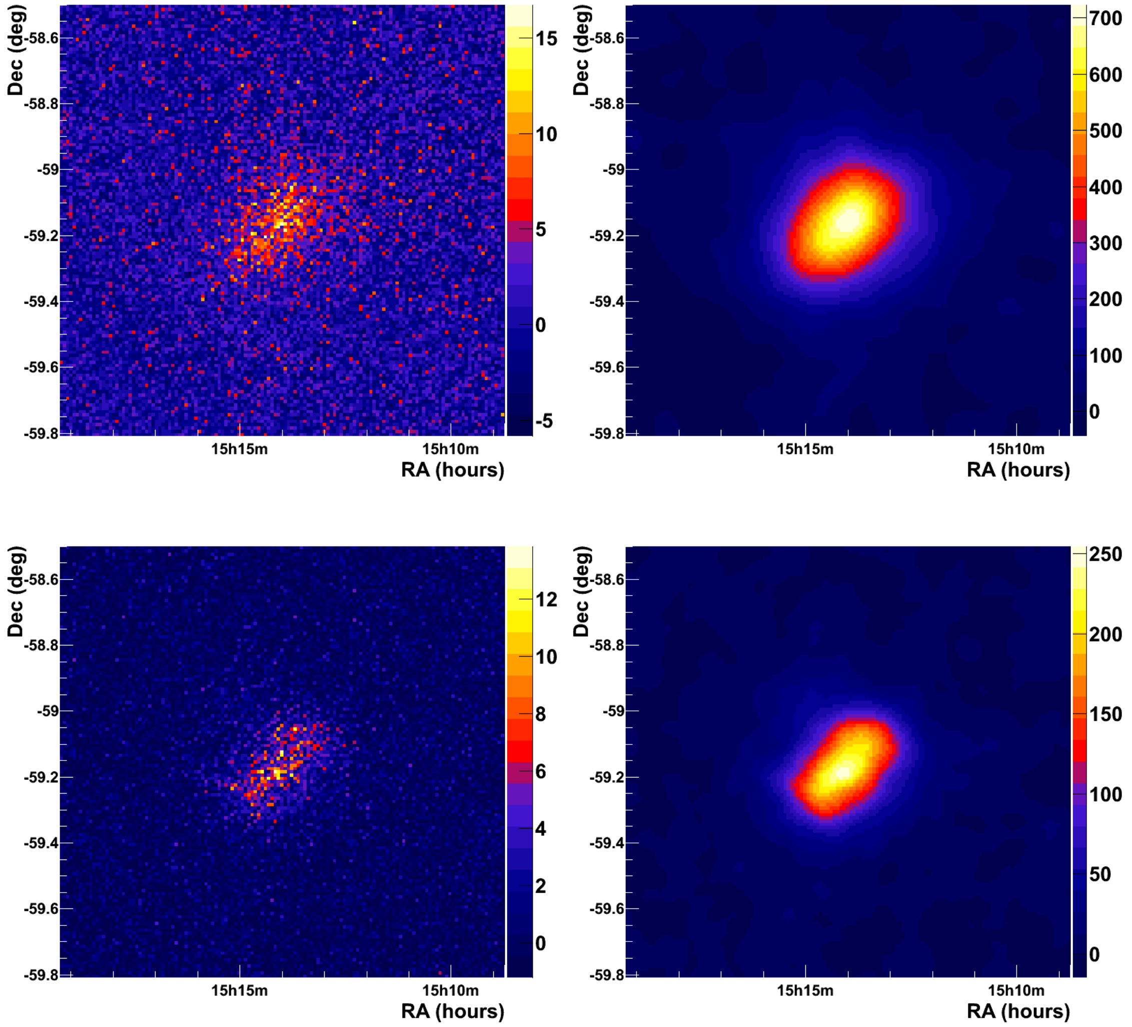

Fig. 4.22: *Sky maps of MSH 15−52 obtained with the Hillas and Model++ analysis. In both rows, the unsmoothed excess map is shown on the left hand side. On the right hand side, smoothed excess maps are shown, which were smoothed with the respective PSF. In the top row, the results from the Hillas analysis with standard cuts are shown. The* 68% *containment radius of the PSF is* 0.12° *for this analysis. In the bottom row, results from the Model++ analysis with faint cuts are shown, for which* $R_{68} = 0.06°$*. The color scale represents excess events in the left hand maps and is in arbitrary units for the right hand side.*

For the further analysis, only the Model++ analysis will be used. Since the faint analysis cuts provide a better angular resolution than the standard configuration, it will be used for the morphological and spectral analysis presented in the following.

4.5.3 Morphology

A first impression of the VHE γ-ray morphology of MSH 15−52 was already given by the sky maps obtained with different analysis methods in Fig. 4.22. To get a feeling of how the source looks at different energies, a multi-wavelength picture of MSH 15−52

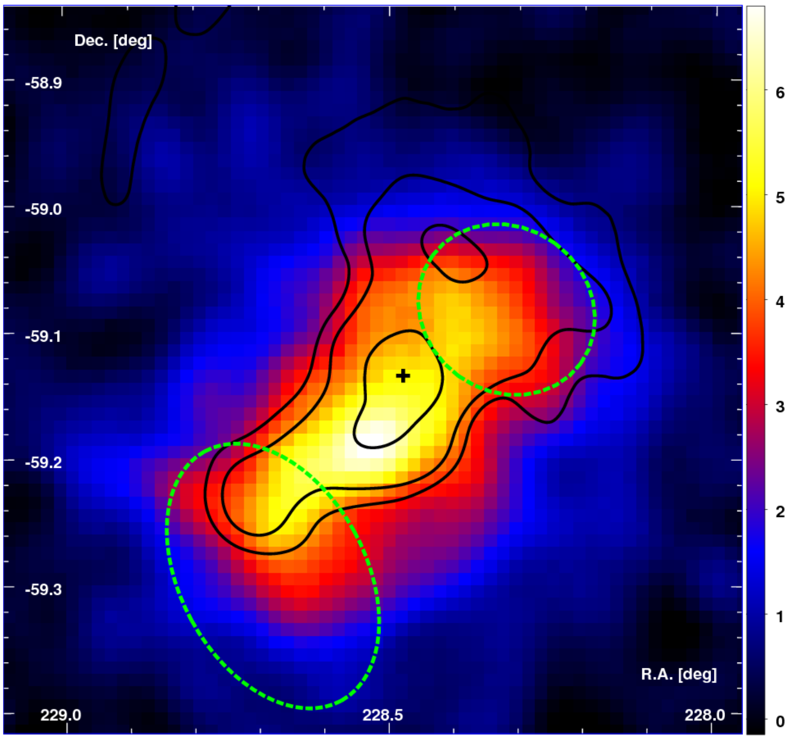

Fig. 4.23: *Multi-wavelength sky map of MSH 15−52. The color scale represents the smoothed excess map observed with the H. E. S. S. experiment. The black contours denote the X-ray emission measured with XMM-Newton and are smoothed to the same angular resolution as the H. E. S. S. data. The two dashed green ellipses denote the fit uncertainty of two sources from the Fermi bright source catalog (Abdo et al. 2009). The position of PSR B1509−58 is marked with a black cross.*

is shown in Fig. 4.23. In this image, the H. E. S. S. excess map is shown in colors and was smoothed with a Gaussian of width $\sigma = 0.04°$. The X-ray data from *XMM-Newton* (cf. Chapter 3) are shown as black contours and are smoothed to the same scale as the H. E. S. S. data. Additionally, the 95% fit uncertainty of the positions of the two objects (1FGL J1513.2−5904 and 1FGL J1514.7−5917) appearing in the *Fermi*-LAT bright source catalog in this field of view are shown as dashed green ellipses (Abdo et al. 2009). The black cross marks the position of the pulsar PSR B1509−58. Both *Fermi* catalog objects have a significance in the order of $5\,\sigma$ and are the brightest points of the extended emission of MSH 15−52 that is visible in the count map above 10 GeV (see Fig. 2.8). Figure 4.23 shows that there is a good general agreement of the source location and morphology at keV, GeV and TeV energies, bearing in mind that the NW part of the X-ray emission is dominated by thermal emission and therefore one does not expect a correlation with VHE emission in this region.

Following this general overview, we will now have a closer look at the VHE morphology of the PWN. Firstly, the general picture is presented, i.e. the morphology is characterized with parameters from a fit of the sky map and profile plots along axes of the systems are shown. Afterwards, an additional cut on the direction error of the reconstructed events in the analysis is discussed, which allows for a more precise reconstruction of the primary direction of the events. In the second part of the Section, an energy-dependent analysis of MSH 15−52 will be presented, in which the γ-ray events are filled into different sky maps, depending on their reconstructed energies. For all of the sky maps presented in the following, the ring background method was used for the estimation of the background.

4.5.3.1 General Picture

A fit routine was used to give a quantitative approach to the analysis of the morphology of the VHE γ-rays from the direction of MSH 15−52. To this end, the observed distribution of events is compared with the predicted event distribution for different morphology shapes and parameters. In this approach, the instrument response is taken into account in the fitting process. A log-likelihood fitting technique is used, which minimizes the difference between the observed and the expected number of events for each bin of the sky map as a function of the morphology of the source. Since Poisson statistics have to be applied, the probability of observing $N_{\rm on}$ and $N_{\rm off}$ events for expected values of n_γ and $n_{\rm hadron}$ is given by (de Naurois 2010):

$$P(N_{\rm on}, N_{\rm off}|n_\gamma, n_{\rm hadron}) = \frac{n_\gamma + \beta n_{\rm hadron}^{N_{\rm on}}}{N_{\rm on}!} e^{-(n_\gamma + \beta n_{\rm hadron})} \times \frac{n_{\rm hadron}^{N_{\rm off}}}{N_{\rm off}!} e^{-n_{\rm hadron}}\,, \tag{4.21}$$

where $\beta = T_{ON}/T_{OFF}$ is the livetime normalization, with T_{ON} and T_{OFF} being the livetime for the source and background data, respectively.

The morphological shape of the source is assumed as an asymmetrical Gaussian which is defined via its centroid position, extension along the major and minor axis and the angle between the major axis and the right ascension axis. The luminosity function for this morphology shape in the coordinates of the binned sky map is given by:

$$L(x, y) = \frac{L_0}{2\pi\sigma^2} \times e^{\frac{((x-x_0)\cos\beta\cos\phi + (y-y_0)\sin\phi)^2}{2\sigma_a^2}} \times e^{\frac{(-(x-x_0)\cos\beta\sin\phi + (y-y_0)\cos\phi)^2}{2\sigma_b^2}}\,. \tag{4.22}$$

In this function, x and y are sky map coordinates and L_0 is a normalization factor. The centroid position of the Gaussian is defined by the coordinates x_0 and y_0, β denotes the declination angle of the source. The shape of the source is given via the length and the width of the asymmetrical Gaussian, σ_a and σ_b, as well as the angle ϕ between the two major axis and the right ascension axis.

The results of the sky map fit are illustrated in Fig. 4.24. In this picture the position from the analysis of Aharonian et al. (2005b) is marked with an “X”, the best-fit position of the 2.5° run list is marked with a cross and the position of PSR B1509−58 with a black circle point. The coordinates of the best-fit centroid position are given in Table 4.4 and have an statistical error of ±0.006° on the right ascension and ±0.003° on the declination. The systematic pointing error of the H. E. S. S. telescope system is around 30″ on each axis (Braun et al. 2008, and references therein). The fitted centroid position is significantly displaced from the position of the pulsar, confirming the previous result of Aharonian et al. (2005b). The white circle in Fig. 4.24 illustrates the 0.3° region which was defined as the source region for the analysis results given in Table 4.2. The dashed ellipse shows the extension of the asymmetrical Gaussian that was fitted to the sky map. Its length and width, as well as the angle between the major axis and the right ascension axis (measured W through N), are given in Table 4.4. In this Table the fit results for the other two run lists analyzed with the Model++ analysis and faint cuts are also shown. No significant change in the morphology parameters is apparent between the different run lists. Moreover, the

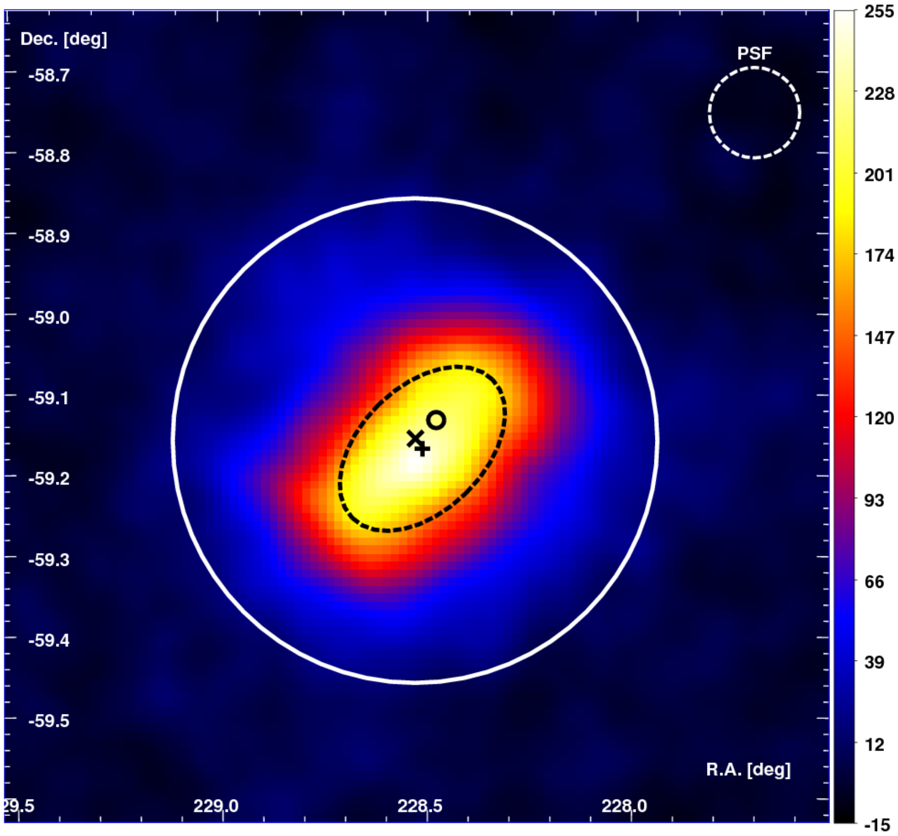

Fig. 4.24: *Sky map of MSH 15−52 that illustrates the result from the fit of the morphology with an asymmetrical Gaussian. The map shows a closer zoom on the PSF-smoothed excess map of MSH 15−52 obtained with the Model++ faint analysis (cf. bottom right in Fig. 4.22). The position from the analysis of Aharonian et al. (2005b) is marked with an "X", the best-fit position of the 2.5° run list is marked with a black cross. The white circle shows the 0.3° region which was defined as the source region for the analysis results given in Table 4.2. The dashed ellipse shows the extension of the asymmetrical Gaussian that was fitted to the unsmoothed sky map. Its length and width, as well as the angle between the major axis and the right ascension axis (measured W through N) are given in Table 4.4. A circle point indicates the position of the pulsar PSR B1509−58. In the upper right corner the extension of the PSF for this analysis is illustrated with its* R_{68}.

Table 4.4: *Morphology results obtained with the Model++ faint analysis for different run lists. An asymmetrical Gaussian was fitted to the sky map for each run list and the parameter values for the best-fit result are shown in the table. The angle is measured W through N and gives the angle between the right ascension axis and the major axis of the ellipse.*

Data set	Position		Extension		Angle
	α_{J2000} [°]	δ_{J2000} [°]	Length [°]	Width [°]	[°]
1.0°	228.520	−59.174	0.122	0.075	44.02
2.0°	228.517	−59.172	0.121	0.077	44.87
2.5°	228.512	−59.170	0.122	0.077	44.51

angular resolution does not change for the larger run lists in which more source events lie at larger offsets to the camera center.

The extension of MSH 15−52 becomes apparent in the projection analysis along the major and minor axis of the fitted two-dimensional Gaussian. The boxes overplotted on the sky map in Fig. 4.25 (which is the same unsmoothed excess map shown in the bottom left of Fig. 4.22) illustrate the regions that were used for this analysis. Both regions are centered on the best-fit position that is given in Table 4.4. The region with the solid line was used for the projection analysis along the major axis of the system, the dashed box for the analysis along the minor axis. Both regions have a length of 1° and a width that is twice the width of the intrinsic Gaussian of the sky map fit[13] and were divided into 25 bins in length. The histograms in Fig. 4.25 show the number of excess events in these bins plotted as a function of the distance to the centroid position. The left histogram corresponds to the white box with solid lines and the direction of the X-axis is from southeast to northwest. The right histogram shows the result for the dashed white box and its X-axis runs from northeast to southwest. The black lines in both histograms show a fit of a Gaussian to the data and the dashed lines illustrate the width of the PSF ($R_{68} = 0.06°$) for this analysis. For the major axis, the Gaussian has a width of 0.13°, which is in good agreement with the intrinsic width of the two-dimensional Gaussian fit convolved with the PSF. The width of the Gaussian along the minor axis (right histogram in Fig. 4.25) is 0.093°. The pulsar PSR B1509−58 has a distance to the centroid position of approximately 0.04° along the major axis and 0.01° along the minor axis. The projection plots provide a further illustration that the VHE γ-ray emission is extended and that the elliptical source shape is similar to the morphology seen at X-ray energies (cf. Fig. 4.23 and Chapter 3).

Due to the selection of γ-ray events with a larger image size, the Model++ analysis with faint cuts provides a better angular resolution than the analysis with standard cuts. However, the statistics decrease with this cut, since there is a fraction of the events that does not pass the tighter cuts. This can be seen in Table 4.3. A further improvement in the angular resolution of the analysis is possible by applying additional cuts in the selection of γ-ray events. The best method to achieve this enhancement is a cut on the error of the reconstructed direction ($dDir$) as pointed out by de Naurois & Rolland (2009). With a cut value of $dDir \leq 0.03°$, the energy threshold is only marginally increased and the angular resolution (R_{68} of the PSF) is in the order of 0.04° in the energy range from 0.5 TeV to 10 TeV. However, two effects have to be kept in mind when applying this cut.

[13]For the major axis the width is $2 \times 0.077°$, for the minor axis the width is $2 \times 0.122°$ (cf. Table 4.4).

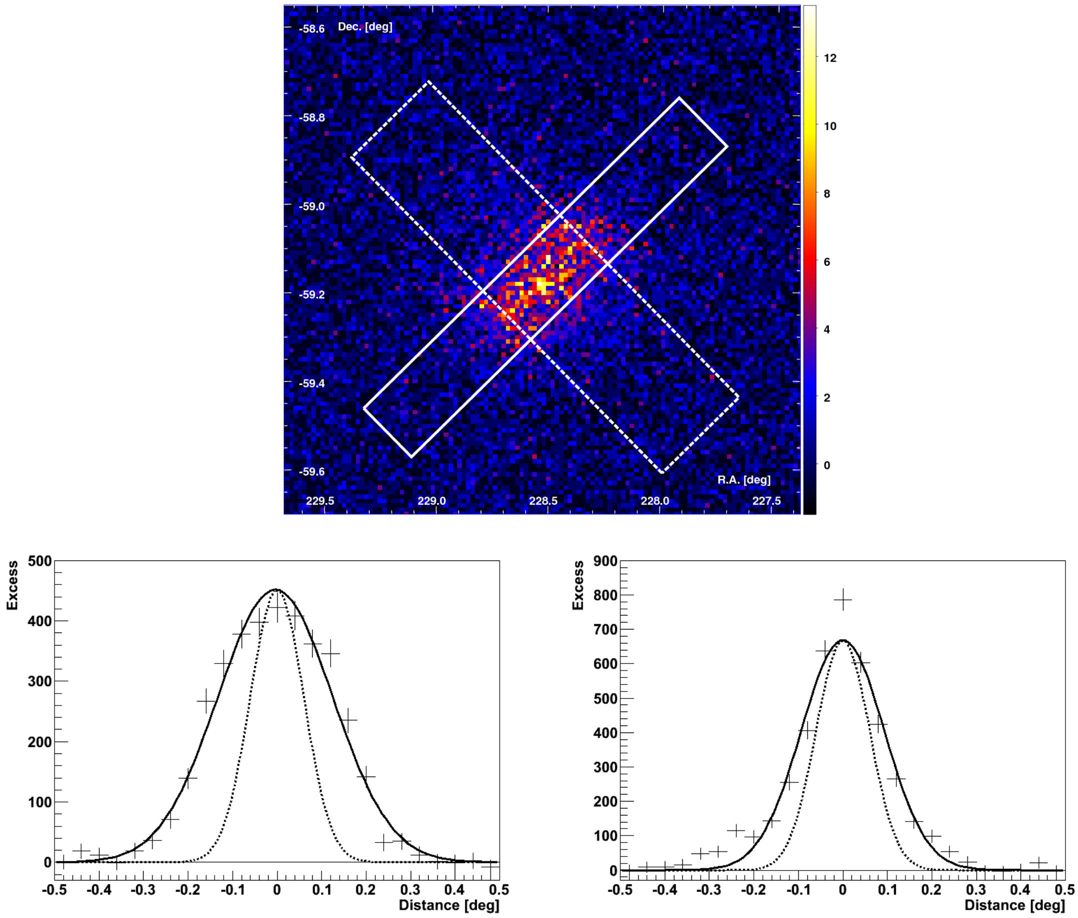

Fig. 4.25: *Projection plots of the unsmoothed excess map of MSH 15−52 along the axes of the fitted two-dimensional Gaussian. The sky map illustrates the box regions that were used for the projections. It is the same unsmoothed excess map shown in the bottom left of Fig. 4.22. The white box with solid lines shows the region for the projection along the major axis of the ellipse, the box with the dashed white lines illustrates the region for the projection along the minor axis. Both regions are centered on the best-fit position of the fitted Gaussian. The histogram on the left side shows the projection along the major axis in 25 bins, going from southeast to northwest. On the right hand side the projection along the minor axis is shown for which the direction is from northeast to southwest.*

Firstly, the statistics of the data set decrease by almost a factor of 2 when applying this cut. Besides, the cut is not independent of the energy of the γ-ray events. Therefore, this cut is very well suited for pin-pointing the exact source location of point-like sources. For extended sources like MSH 15−52, in which the source spectrum cannot be assumed as constant across the source, the drawbacks do not make up for the improvement in angular resolution.

The result of an analysis of the MSH 15−52 data set with this cut ($dDir \leq 0.03°$) is shown in Fig. 4.26, with the unsmoothed map of γ-ray excess events on the left side and the PSF-smoothed sky map on the right side. Within the 0.3° source region the number of events drops to 2370 for the 2.5° run list and 1798 for the 1° run list (in comparison

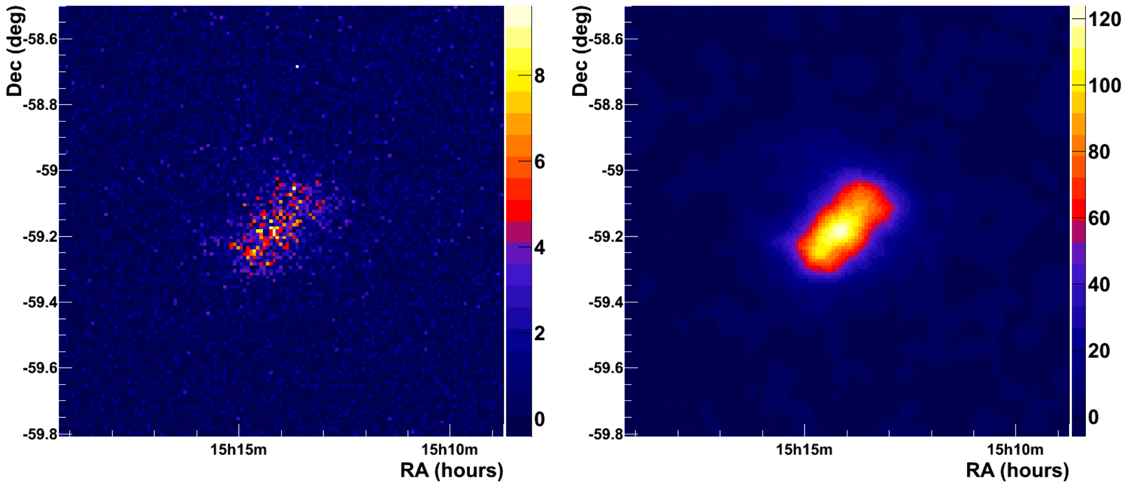

Fig. 4.26: *Sky maps of MSH 15−52 from an analysis with an additional cut on the error of the direction reconstruction using the* 2.5° *run list. On the left-hand panel the unsmoothed sky map of* γ*-ray excess events is shown. On the right-hand side a sky map is displayed that has been smoothed with the PSF for this analysis configuration* ($R_{68} = 0.05°$)*.*

to the values in Table 4.3). The significance of the γ-ray excess drops to 52.2 and 41.2, respectively. However, the angular resolution is lowered to a value of $R_{68} = 0.05°$. All in all, the gain in angular resolution when applying this cut does not outweigh the drawbacks of this cut, especially for an extended source of γ-rays like MSH 15−52.

Another way of improving the angular resolution of the reconstructed γ-ray events is provided by the application of deconvolution algorithms to the γ-ray sky maps. The Richardson-Lucy algorithm was studied in the broader context of this work and is documented in the diploma thesis of Heinz (2008). However, due to the low signal-to-noise ratio in γ-ray astronomy, these algorithms cannot be easily applied to the data. The implications of the high background counts have to be carefully taken into account and further study on this topic is currently in progress. A detailed discussion of the utilization of deconvolution algorithms for VHE γ-ray sky maps is therefore beyond the scope of this thesis and no application of the Richardson-Lucy algorithm on the sky maps of MSH 15−52 will be shown.

4.5.3.2 Energy-dependent Analysis

The morphological analysis shown so far did not take into account a possible variation of the energy spectrum of the γ-rays within the extended source. However, the investigation of the morphology of astrophysical sources at different energies is important to obtain a good understanding of the physical processes in these sources. Therefore, an analysis of the VHE data of MSH 15−52 in three different energy bands was carried out and is presented below. Three energy bands were chosen and were defined with the following energy range:

- above 100 GeV and below 1 TeV,
- between 1 TeV and 3 TeV,

- above 3 TeV and below 100 TeV.

The energy bands were chosen as to have roughly the same statistical significance (≈ 40) for the two ranges at lower energies and one energy band with photons above 3 TeV. The analysis results for these three energy ranges are displayed in Table 4.5. Figure 4.27 shows the corresponding sky maps for these bands. On the left-hand side the unsmoothed excess maps are shown and on the right-hand side the PSF-smoothed excess maps are displayed. Due to the smaller statistics at the highest energies, the sky map with the events above an energy of 3 TeV looks more irregular than the two maps of the events with lower energies. In the map with energies from 1 TeV to 3 TeV there are fewer excess events than at the lowest energies, but due to the lower background the significance of the excess is roughly equal. This can also be seen when comparing the sky maps of these two energy bands in Fig. 4.27.

Table 4.5: *Results of the analysis of MSH 15−52 in different energy ranges for the* 2.5° *run list with the Model++ faint analysis.*

Minimum Energy [TeV]	Maximum Energy [TeV]	Excess Events	Significance	R_{68} [°]
0.1	1.0	2322	39.8	0.064
1.0	3.0	1473	41.7	0.062
3.0	100.0	433	18.4	0.082

Figure 4.28 shows another way of looking at the spectral properties of the morphology. In this sky map, different colors correspond to different energy ranges: colored in red is the emission at the lowest energies, green corresponds to the middle-energy emission and red to the emission at the highest energies. The energy ranges are the same as stated above and for each range the color scale goes linearly from the minimum to the maximum number of excess events per bin. To obtain a meaningful comparison all three sky maps are smoothed to the same angular resolution. If there was a significant change in the morphology for some energy range, then one would see parts of the source dominated by only one color. As this is not the case it can be concluded that no major change of the spectral properties is visible across the source with this method. Two other approaches provide further insight on this topic. First, a look at the source extension of the projections along the major and minor axes is presented, later in Section 4.5.5 an analysis of the spectrum for different sub-regions of the source is presented.

To have a closer look at a possible change of the morphology in different energy bands a similar analysis like the one presented in Fig. 4.25 for the whole energy range was carried out for the three energy band discussed above. The same two box regions as shown in the sky map in Fig. 4.25 were used, divided in 25 bins and the total excess in each bin was summed up. Figure 4.29 shows the result of this analysis. On the left hand side the result for the projection along the major axis is shown. The black data points in this histogram correspond to the lowest energy range, red to the medium energies and blue to the highest energies. The right side shows the projection along the minor axis for which the meaning of the colors is the same. The two histograms show that the extension of MSH 15−52 in the different energy ranges stays constant within the errors. In the projection along the minor axis (right panel in Fig. 4.29) the excess event distribution for the events with energies above 3 TeV is slightly larger than for the two distributions at lower energies. However, when performing a two-dimensional fit of the sky maps and looking at the intrinsic source

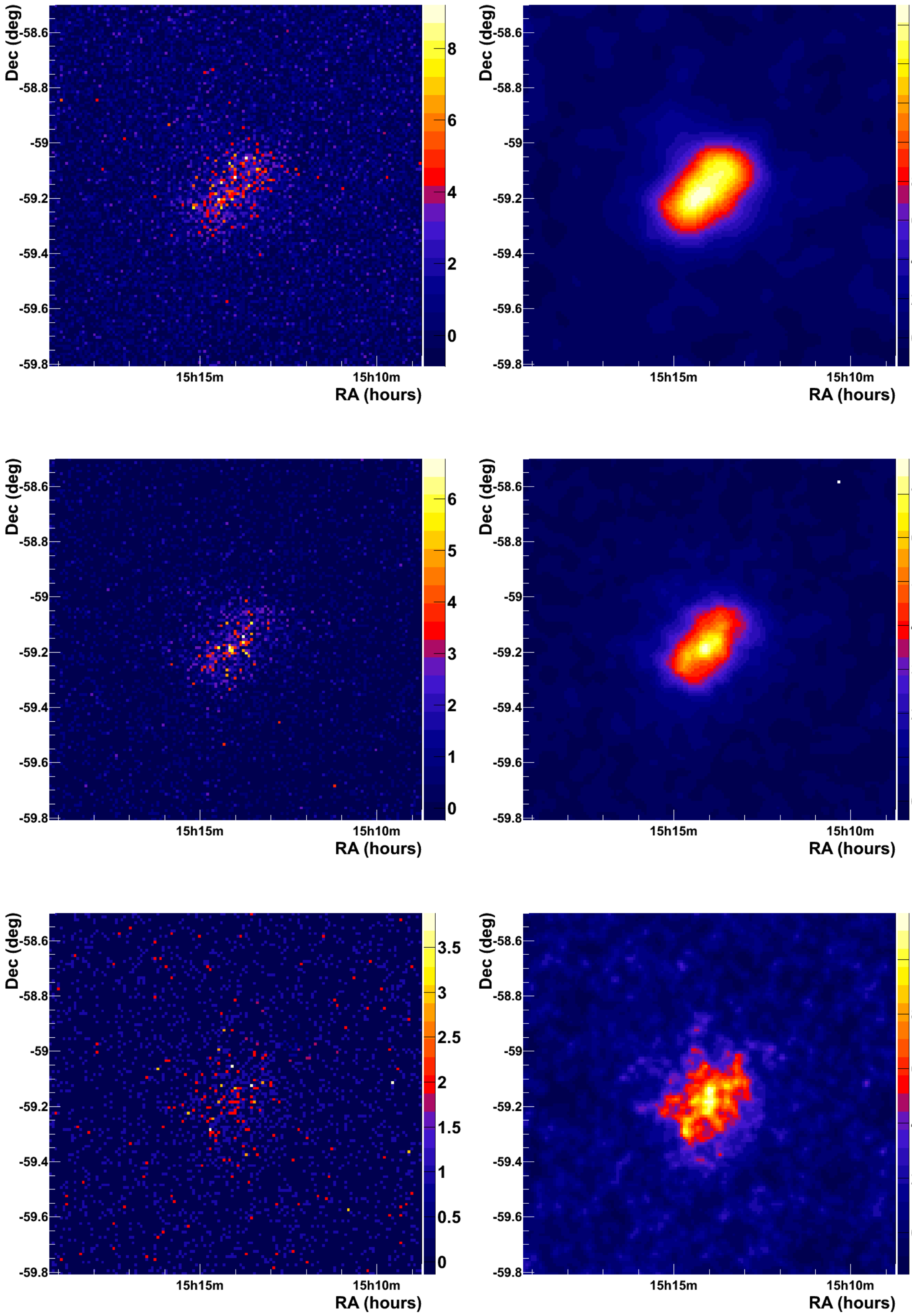

Fig. 4.27: *Unsmoothed (left column) and PSF-smoothed (right column) excess maps of MSH 15−52 in three different energy ranges. The Model++ analysis with faint cuts was used for this data analysis and for each sky map an additional cut on the energy of the primary γ-ray was applied. In the top row, only events with an energy above 100 GeV and below 1 TeV are included. The middle row shows the map for events between 1 and 3 TeV and in the bottom row, events above 3 TeV and with energies up to 100 TeV are included in the sky map.*

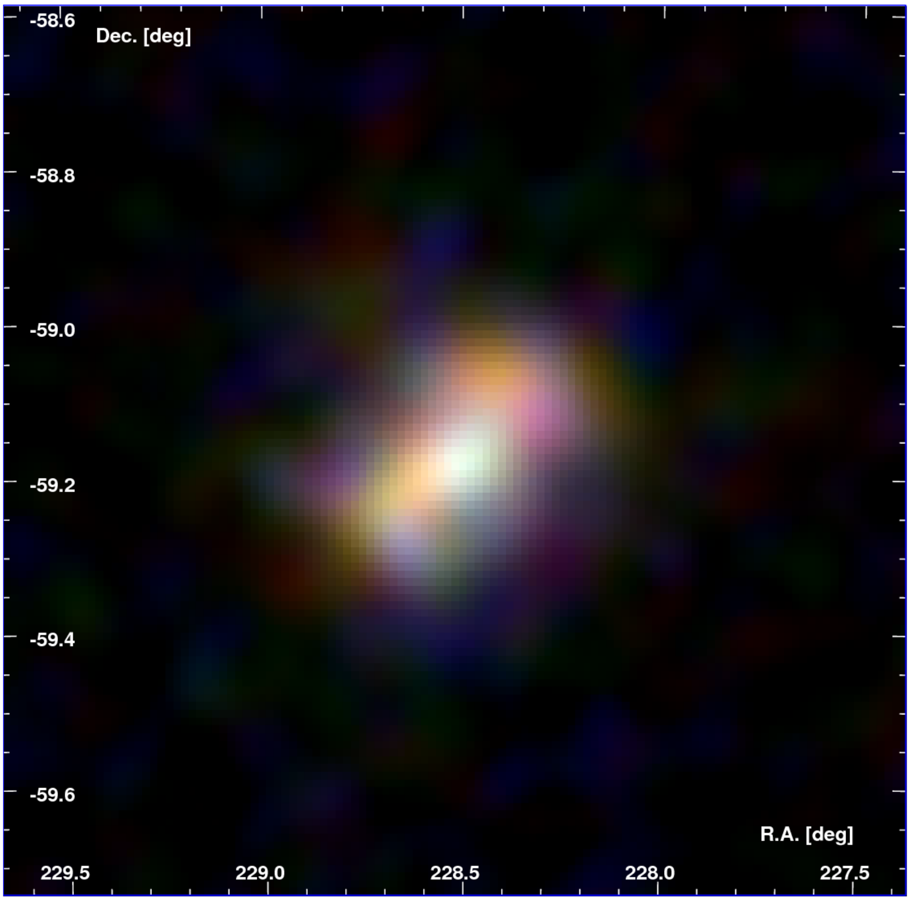

Fig. 4.28: *RGB plot of the VHE γ-rays in three different energy bands. Events with an energy below 1 TeV are display in red color, green corresponds to the events with energies between 1 and 3 TeV and blue shows the events with energies above 3 TeV. Each color scale goes linearly from the minimum to the maximum number of excess events in the respective energy band. Thus, white parts in the image correspond to source regions in which the relative number of excess events is about equal in each energy band.*

distribution, the extension in the medium-energy and high-energy range are statistically compatible ($0.074° \pm 0.003°$ vs. $0.090° \pm 0.008°$). This holds also true for the centroid position of the fitted Gaussian, which does not vary significantly in between the data ranges.

4.5.4 Spectral Analysis

Having discussed the morphological properties of MSH 15−52, the focus in this Section is now the energy spectrum of the VHE γ-ray events from this source. First we will have a look at the spectrum of the events in the 0.3° region around the best-fit centroid position displayed in Fig. 4.24. For all spectral analysis results presented in this and the next Section, the region background method was used for the background estimation (see Section 4.4.2.4 for details).

The spectrum analysis was carried out using a forward-folding technique. It relies on a

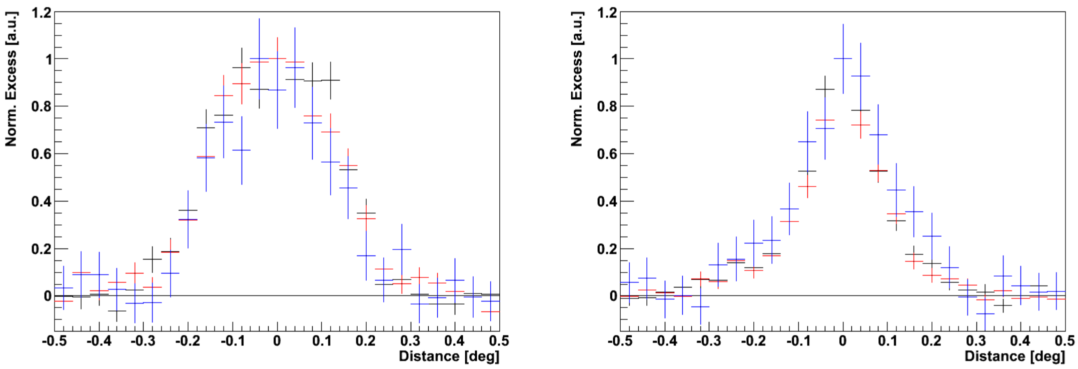

Fig. 4.29: *Projection plots of the unsmoothed excess maps of MSH 15−52 in three different energy bands. The box regions used for the projection are the same as shown in the sky map in Fig 4.25 and were also divided in 25 bins. The left panel shows the projection along the major axis and the right panel the projection along the minor axis of the source. In both histograms the black data points show the excess in the energy range below 1 TeV, red data points correspond to γ-ray energies of 1 – 3 TeV and blue to energies above 3 TeV.*

binned log-likelihood fit of different spectral shapes to the distribution of the reconstructed energy of the events and takes into account Poisson statistics. The expected number of excess events for any bin in reconstructed energy is given by (de Naurois 2010)

$$n_\gamma = \int_{\tilde{E}_1}^{\tilde{E}_2} \mathrm{d}\tilde{E} \int_0^\infty \mathrm{d}E \times \phi(E) \times A(E,\theta,\delta) \times PDF(E,\tilde{E})\,, \tag{4.23}$$

where $\tilde{E}_1$ and $\tilde{E}_2$ are the boundaries of the reconstructed energy bin and E is the true energy of the γ-ray. The source flux is denoted by $\phi(E)$ and depends on the shape of the assumed spectrum. Several different shapes were used and will be discussed in more detail further below. The effective area of the system, $A(E,\theta,\delta)$, is calculated from simulations and depends on the true energy, the zenith angle θ and the off-axis angle δ. The probability density function $PDF(E,\tilde{E})$ gives the probability of observing an event with a reconstructed energy $\tilde{E}$ for a given true energy E. It also depends on the true energy, the zenith angle and the off-axis angle. From the expected number of γ-ray events one can then construct a probability $P(N_{\mathrm{on}}, N_{\mathrm{off}}|n_\gamma, n_{\mathrm{hadron}})$ of observing N_{on} and N_{off} events for expected values n_γ and n_{hadron} using Poisson statistics (equivalent to Eq. 4.21). In the fit procedure the Levenberg-Marquardt algorithm is then used to maximize the likelihood $L = \log(P)$. Since one has the full covariance matrix at hand, it is possible to construct confidence regions for the different spectral shapes.

Figure 4.30 shows the energy spectrum of the events from the 0.3° region discussed above for the 1° run list. The red area denotes the $1\,\sigma$ error band of a power-law fit to the data. The best-fit parameters and the fit quality are given in Table 4.6. The power-law indices of 2.35 ± 0.03 and 2.36 ± 0.03 for the 1° and 2.5° agree well with each other and are within the systematic error of the index that was published in the old analysis. The lower panel of Fig. 4.30 shows the residuals of the power-law fit. Deviations from a good fit are apparent and therefore, the spectrum was also fitted with other spectral shapes. The following spectral shapes were used for the spectral fitting:

- Power law (PL):

$$\frac{\mathrm{d}N}{\mathrm{d}E} = \phi_0 \left(\frac{E}{E_0}\right)^{-\Gamma} , \tag{4.24}$$

- Broken power law (BPL):

$$\frac{\mathrm{d}N}{\mathrm{d}E} = \phi_0 \times \begin{cases} \left(\frac{E}{E_0}\right)^{-\Gamma_1} , & \text{for} \quad E \leq E_\mathrm{B} , \\ \left(\frac{E_\mathrm{B}}{E_0}\right)^{\Gamma_2-\Gamma_1} \left(\frac{E}{E_0}\right)^{-\Gamma_2} , & \text{for} \quad E > E_\mathrm{B} , \end{cases} \tag{4.25}$$

- Exponential cutoff power law (ECPL):

$$\frac{\mathrm{d}N}{\mathrm{d}E} = \phi_0 \left(\frac{E}{E_0}\right)^{-\Gamma} \exp\left(-\frac{E}{E_\mathrm{C}}\right) , \tag{4.26}$$

- Curved power law (CPL):

$$\frac{\mathrm{d}N}{\mathrm{d}E} = \phi_0 \left(\frac{E}{E_0}\right)^{-\Gamma-\beta\log(E/E_0)} . \tag{4.27}$$

The fitting results displayed in Table 4.6 show that a fit with a curved power law or an exponential cutoff or a break in the spectrum is preferred to a simple power law. For the first publication (Aharonian et al. 2005b), the data set was not large and the analysis not sensitive enough to have a statistically significant deviation from a power-law fit. Figure 4.31 shows the spectrum results for the 2.5° run lists with several different shapes. The black area corresponds to the $1\,\sigma$ confidence interval for the power-law fit, the green area shows the result for a curved power law and the blue area for a power law with an exponential cutoff. The lower panel in Fig. 4.31 again shows the residuals from the fit of the energy spectrum with a power law. A broken power law with a break energy of (2.3 ± 0.4) TeV and a change of the spectral index from 2.11 ± 0.06 to 2.79 ± 0.12 gives the best fit to the data. However, the spectrum is almost equally well described by a power-law with an index of 2.06 ± 0.06 and an exponential cutoff at (9.1 ± 2.1) TeV or a curved power-law spectrum. The integral γ-ray flux of MSH 15−52 above an energy of 1 TeV is $(5.3 \pm 0.1) \times 10^{-12}\,\mathrm{cm}^{-2}\,\mathrm{s}^{-1}$ for the power-law fit. This is slightly higher than the result of the old analysis, but within the statistical and systematic errors given for that analysis.

The systematic error on the spectrum is dominated by three contributions, as discussed in more detail in Aharonian et al. (2006a):

- the response of the camera to the Cherenkov light, which is calibrated by so-called single photo-electron runs in which the PMTs are illuminated with LEDs,
- the optical response of the system, calibrated through measurements of local muons in each telescope,
- the interactions of particles and light in the atmosphere, where the main sources of uncertainty are the density profile of the atmosphere and the absorption of Cherenkov light by clouds and dust.

The total systematic error is estimated to be at 20% in the measured flux and at ±0.09 for the spectral index. In the H. E. S. S. publication on MSH 15−52 the estimate of the systematic error was even more conservative at 25% for the flux and ±0.2 for the spectral index.

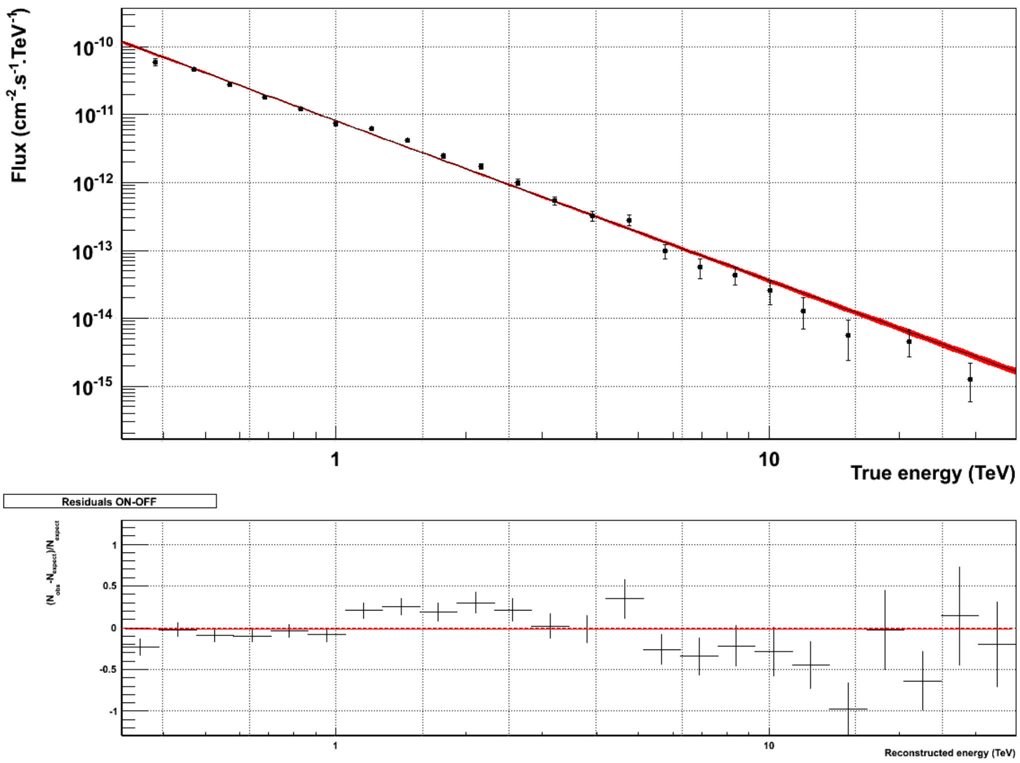

Fig. 4.30: *Energy spectrum of MSH 15−52 for the* 0.3° *region and the* 1° *run list fitted with a power law. The red area corresponds to the* $1\,\sigma$ *confidence interval of the fit. The lower panel shows the residuals of the fit.*

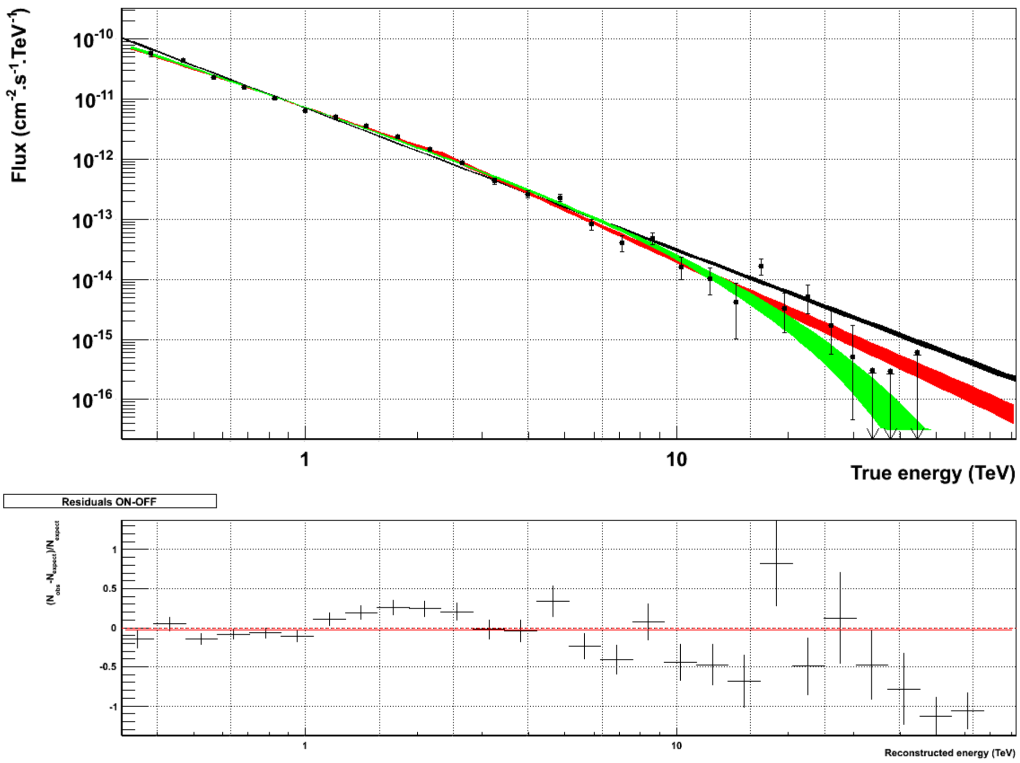

Fig. 4.31: *Energy spectrum of MSH 15−52 for the* 0.3° *region and the* 2.5° *run list fitted with a power law (black), a broken power law (red) and a power law with an exponential cutoff (green). The filled areas correspond to the* $1\,\sigma$ *confidence interval of the respective fit. The lower panel shows the residuals of the fit with the power law.*

Table 4.6: *Results of the spectral analysis of MSH 15−52 for different run lists. The events for this analysis were selected from the region with a radius of* $0.3°$ *centered on the best-fit position indicated in Fig. 4.24.*

List	Shape	F (> 1 TeV) $[10^{-12}\mathrm{cm}^{-2}\,\mathrm{s}^{-1}]$	Norm (@1 TeV) $[10^{-12}\,\mathrm{TeV}^{-1}\mathrm{cm}^{-2}\,\mathrm{s}^{-1}]$	χ^2/dof	Index	Other Parameters
Old	PL	4.5	5.7 ± 0.2	13.3/12	2.27 ± 0.03	none
1°	PL	6.0 ± 0.2	8.2 ± 0.2	60/22	2.35 ± 0.03	none
1°	CPL	6.5 ± 0.3	9.0 ± 0.3	27/21	2.07 ± 0.06	$\beta = 0.19 \pm 0.04$
1°	ECPL	6.5 ± 0.5	8.7 ± 0.2	28/21	1.98 ± 0.07	$E_\mathrm{C} = (6.6 \pm 1.4)$ TeV
1°	BPL	6.6 ± 0.3	8.6 ± 0.3	22/20	2.08 ± 0.06	$\Gamma_2 = 2.90 \pm 0.15$
						$E_\mathrm{B} = (2.3 \pm 0.4)$ TeV
2.5°	PL	5.3 ± 0.1	7.2 ± 0.2	80/25	2.36 ± 0.03	none
2.5°	CPL	5.6 ± 0.2	7.6 ± 0.2	45/24	2.13 ± 0.05	$\beta = 0.15 \pm 0.03$
2.5°	ECPL	5.6 ± 0.4	7.4 ± 0.2	43/24	2.06 ± 0.06	$E_\mathrm{C} = (9.1 \pm 2.1)$ TeV
2.5°	BPL	5.7 ± 0.2	7.4 ± 0.2	38/23	2.11 ± 0.06	$\Gamma_2 = 2.79 \pm 0.12$
						$E_\mathrm{B} = (2.3 \pm 0.4)$ TeV

4.5.5 Spatially Resolved Spectral Analysis

A detailed measurement of the spectral properties in different parts of the pulsar wind nebula is crucial for constraining the various scenarios for the physics in this type of source. In Section 3.6 it was shown that MSH 15−52 shows spectral variation in the X-ray energy range for extraction regions with increasing distance from the pulsar. This might for example be explained by synchrotron cooling of a leptonic outflow. At this point we will now analyze the VHE γ-ray emission measured with H. E. S. S. to check whether a similar effect is seen at energies in the TeV range. To this end, a total of eight extraction regions aligned along the major axis of the system was defined. These regions are centered on the pulsar PSR B1509−58 and depicted in cyan color in Fig. 4.32. The width of the regions was chosen as 0.07°, which is slightly larger than the 68% containment radius of the PSF. For smaller sizes of the regions, the contamination of the regions with events from neighboring regions would be considerably larger.

As a first investigation the energy spectra of the γ-ray events from the regions from Fig. 4.32 were fitted with simple power-law spectra. The best-fit values of the spectral indices from this analysis are plotted in Fig. 4.33 against the distance of the regions from the pulsar. The distance axis is defined along the major axis of the PWN and runs from northwest to southeast, i.e. from the top-right corner to the bottom-left corner of Fig. 4.32. No significant deviation from a constant spectral index across the source is measurable for this analysis. For an accurate statistical analysis one would need to look not only on the index and its error, but also on the correlation between the index and the normalization. One way to look at this is by overplotting the confidence regions from each spectral fit. This is illustrated in Fig. 4.34: in this plot, the confidence regions from the power-law fits to each region in Fig. 4.32 are shown. The spectra were rescaled in order to be able to plot them in one graph. The red, dotted line corresponds to the fourth spectrum from the top, which is the spectrum of the region directly to the southeast of the pulsar in Fig. 4.32. The other spectra are ordered according to the distance from this region. To the top, the distance is increasing towards the northwest, the spectra below are from the regions to the southwest of the pulsar. One can see that the central spectrum is almost within the $1\,\sigma$ confidence region for all of the regions, which underlines the result displayed in Fig. 4.33.

The analysis of the whole source presented in the last Section showed that there is a significant deviation of the spectral shape from a pure power-law spectrum. Therefore, a further approach of analyzing the wedge-like regions was taken for which the spectral data from each region was fitted with a power law with an exponential cutoff. The resulting best-fit parameters for the value of the cutoff and for the spectral index are shown in Fig. 4.35 in the left panel. It is evident that there is no visible trend in the data points and that the statistical errors of the parameters are quite large because of the few events in each region. The right panel shows the result of a spectral fit in which the power-law index of the ECPL was assumed to be constant for all regions at a value of 2.1. This is the best-fit value for the spectral index for the events from the closest region to the southeast of the pulsar. The motivation for this kind of analysis comes from the physics argument, that the uncooled spectrum might exhibit a power-law shape with a certain index (2.1 in this case) and that cooling effects might merely lead to a shift of the cutoff energy to lower energies for regions at larger distances. However, from the results shown in the right panel of Fig. 4.35 it becomes clear that such an effect is not visible in the data and that the distribution of cutoff energies is compatible with a constant. For both analyses shown

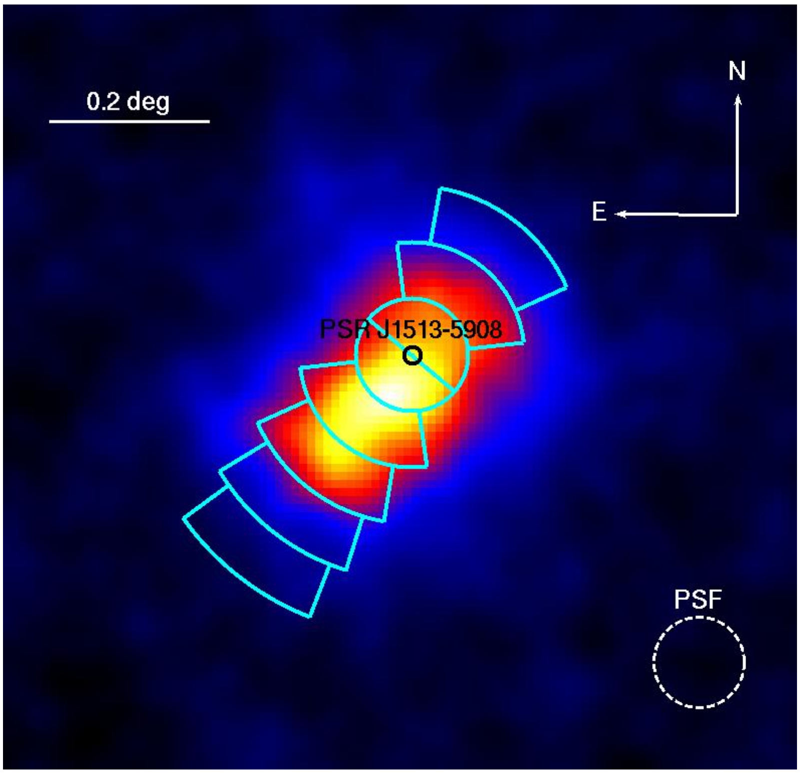

Fig. 4.32: *Sky map of MSH 15−52 with the regions used for the spatially resolved spectral analysis. The black circle marks the position of the pulsar PSR B1509−58 and the cyan-colored regions show the areas from which the events were extracted for the spectral analysis.*

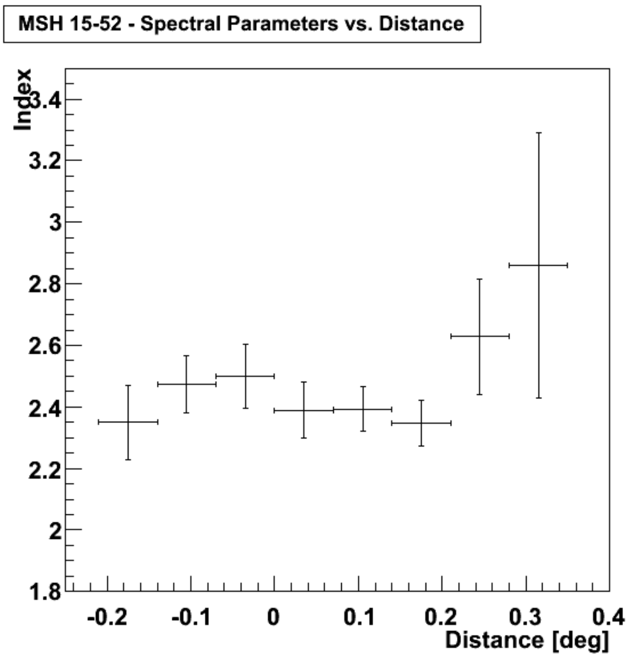

Fig. 4.33: *This graph shows the index of the fitted power-law spectrum for each extraction region (cf. Fig. 4.32) plotted against the distance of the region to the pulsar. The distances on the X-axis are defined from northwest to southeast and the origin is at the position of the pulsar PSR B1509−58.*

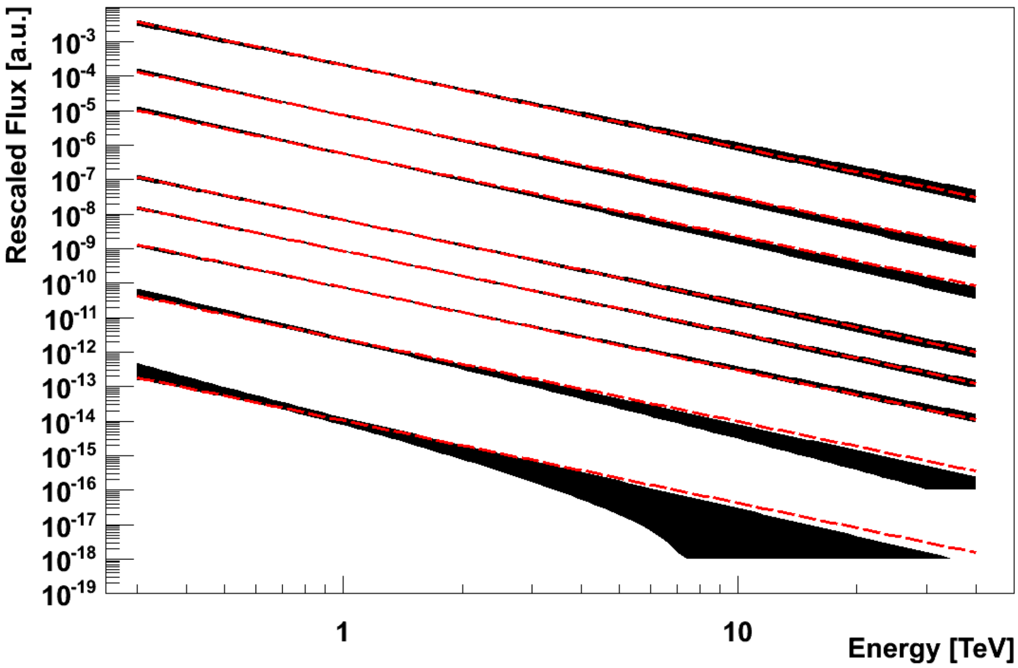

Fig. 4.34: *Confidence intervals of the fitted power laws for the extraction regions shown in Fig. 4.32. The normalization of the individual spectra was rescaled in order to show them in the same plot. The red line marks the spectrum of the closest region to the southeast of the pulsar (cf. Fig. 4.32) and is plotted rescaled for each spectrum to illustrate the evolution of the spectral shape of the individual spectra. The spectra in this plot are ordered according to the distance of the extraction region to the pulsar. The spectra closest to the pulsar are number three and four from the top. The three top-most spectra correspond to the regions to the northwest of the pulsar as shown in Fig. 4.32. The bottom five spectra are from the regions to the southeast of PSR B1509−58.*

in this plot one would need to take into account the full correlation between the index, cutoff energy and normalization for a statistical accurate comparison. As there is not even a trend visible in the simple approach, the correlation plots are not shown here.

To conclude the spatially-resolved analyses presented in this Section one can say, that with the currently available data no significant change in the spectral parameters is visible at any part of the source. This might possibly be due to an intrinsic spectral morphology which really is constant across the source. However, most physical scenarios for PWNe favor a leptonic outflow and thus predict cooling effects due to the synchrotron radiation of the leptons in the magnetic field of the PWN. In this case, the changes in the spectrum are not yet measureable with the current-generation instruments, but future IACT experiments like CTA should be able to address this question in more detail.

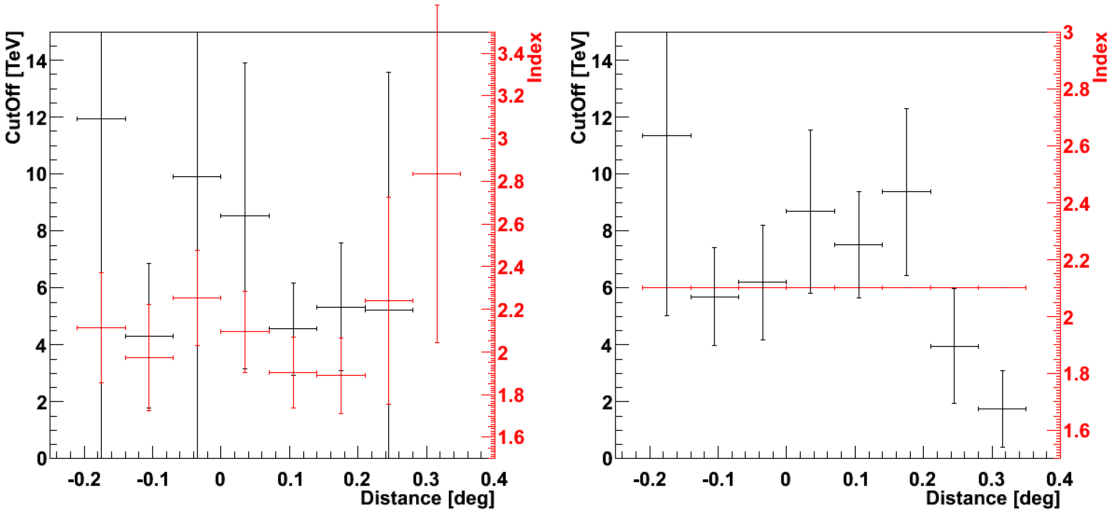

Fig. 4.35: *Plot of the spectral parameters of fitted power-law spectra with exponential cutoffs against the distance of the extraction region from the pulsar. For both plots the black data points show the best-fit values of the cutoff energy and the range of values is shown on the left Y-axis. The right Y-axis, corresponding to the red data points, displays the spectral index. For the left plot the parameters were left unconstrained, whereas the right plot shows the variation of the fitted cutoff energies for a fixed spectral index of* 2.1*.*

5 A Model to Describe the Nonthermal Emission of MSH 15−52

In the previous two Chapters new experimental results from the analysis of the electromagnetic radiation from the direction of MSH 15−52 were presented. The X-ray emission measured by the *XMM-Newton* satellite was discussed in Chapter 3, whereas Chapter 4 dealt with the detection of VHE γ-rays. At this point we will now change our focus from the experimental detection of photons and investigate a theoretical model of the physical processes in the PWN. We presented first results obtained with this modeling approach at the International Cosmic Ray Conference in Lodz for MSH 15−52 (Schöck et al. 2009) and for the compact PWN of the Vela supernova remnant (Vorster et al. 2009). For the latter, the X-ray analysis of Mangano et al. (2005) was used to constrain the free parameters of the model and a more detailed treatment is presented in a Master Thesis (Vorster 2009). Subsequently, we published the final results of the *XMM-Newton* data analysis and the modeling of MSH 15−52 (Schöck et al. 2010). The model and the results of the parameter optimization will be presented in this Chapter.

5.1 Introduction

There are two different possibilities to approach the modeling of a physical system. In a bottom-up approach one starts out at small scales and with the most basic interactions. The complete system comprises many sub-levels of modeling which need to be well-understood for an accurate model. To construct such a model of a pulsar wind nebula, one would need precise information about the nature of the outflow from the pulsar, the wind termination shock and a detailed understanding of the magnetohydrodynamic interactions in the outflow. As the current measurements are not precise enough to yield such information (cf. Chapter 1 for an overview) the modeling here makes use of the other approach, the so-called top-down strategy. In this approach one tries to find a description of the whole system without making assumptions about the exact nature of the low-scale processes. An example for such an approach is the commonly-used one-zone model to describe the nonthermal emission of pulsar wind nebulae. Figure 2.9 on page Fig. 49 shows the spectral energy distribution of the PWN MSH 15−52 obtained with such a model. In the one-zone models it is assumed, that the magnetic field is constant throughout the whole PWN. Furthermore, no energy losses of the particles in the outflow are taken into account. While this is a rather imprecise approach, it is still well-suited for modeling a SED across a broad energy range, as detailed measurements of the spatial and spectral variability are often not feasible for all energy ranges.

The model presented here goes beyond the scope of the one-zone models and aims at providing a more detailed description of the inner part of the system. This part can be probed with great detail by the current-generation X-ray satellites and thus it is possible to constrain free parameters of such a model. The approach in this work assumes that leptons are accelerated according to the so-called lepton injection spectrum at the wind termination shock and flow radially outward to form the PWN. In the downstream flow beyond the termination shock the particles lose energy, causing the shape of the lepton spectrum to change with increasing distance from the shock. In the model presented here a radial symmetry for this outflow is assumed. Looking at the X-ray sky map (e.g. Fig. 3.4), a deviation from a spherical symmetry is apparent. However, compared to current one-zone models in which no change of the properties of the lepton population across the source is taken into account, the radial approach provides a good first estimate of the effects of spatial variation in the PWN. The inner part of the outflow is dominated by leptons which have been freshly injected into the system at the shock. Therefore it is a valid assumption to assume a time-independent injection spectrum and a time-constant magnetic field in the PWN. One has to keep in mind, however, that with this assumption the model is only valid for the inner-most part of the PWN. For the outer parts, the temporal changes of the spin-down behavior of the pulsar and the accumulation of particles from different times play a major role.

If the characteristics of the lepton population and the magnetic field are known, it is possible to calculate the nonthermal emission at each point in the PWN. The predicted emission is then in turn compared to the spatially resolved X-ray emission observed with *XMM-Newton* (see Chapter 3). By minimizing the deviation between the modeled and the measured emission, the best fits for the free parameters of the model are found. As already pointed out in Section 1.4, only the synchrotron radiation of the leptons in the magnetic field and the inverse Compton radiation from the up-scattering of background photons by the high-energy leptons play a role in this system.

A schematic illustration of this procedure is shown in Fig. 5.1. It shows the individual shells, into which the PWN is divided up, labeled from 0 to n. The model starts with a lepton injection spectrum at the termination shock (Q_0), which bases on parameters of the shock that will be discussed in the next Section. From this point on, the leptons are propagated radially outward according to a velocity profile that will be treated in Section 5.3. Due to the expansion and the interaction with the magnetic field, the leptons lose energy, as will be discussed in Section 5.4. Section 5.5 covers the radiation processes that are relevant in the scope of this model and shows examples of emission spectra. The remaining part of the Chapter then deals with the application of this model on the PWN MSH 15−52 and introduces the comparison regions, the optimization procedure and parameter sets, before showing the results and a discussion of the implications of the model for the emission in the TeV range observable with H. E. S. S..

5.2 The Lepton Injection Spectrum at the Termination Shock

At the termination shock of the pulsar wind, particles are accelerated and injected into the PWN (Gaensler & Slane 2006). Commonly, a power-law shape of the energy spectrum is adopted (Kennel & Coroniti 1984b; Reynolds & Chevalier 1984). However, more recent publications on this topic conclude that the injection spectrum should follow a broken power law to account for the observed spectral properties at radio wavelengths (Venter & de Jager 2007). The energy spectrum of the leptons, $Q(E_\mathrm{e}, t)$, is then expressed in the

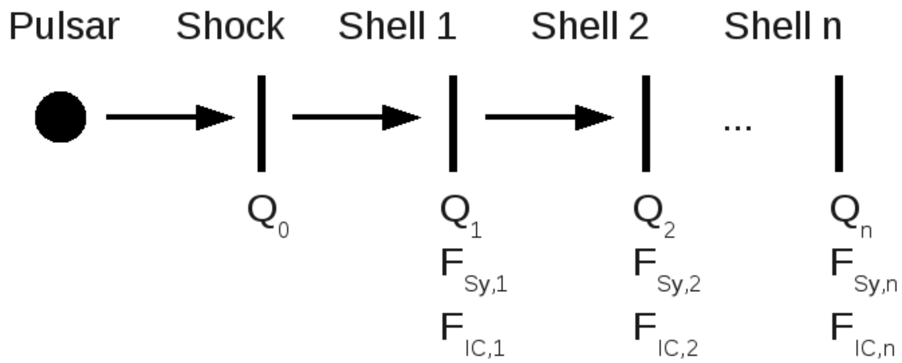

Fig. 5.1: *Sketch of the calculation procedure used in the model. The PWN is divided up into a number of n shells for the calculation of the lepton and the emission spectra. The lepton spectra are labeled with "Q", the synchrotron and IC spectra with "F", each going from 0 to n, where 0 corresponds to the injection spectrum and n marks the farthest position from the pulsar considered in the model.*

time-independent case as a function of the lepton energy, E_e:

$$Q(E_\mathrm{e}) = \begin{cases} Q_{0,\mathrm{R}} \left(\dfrac{E_\mathrm{e}}{E_\mathrm{B}}\right)^{-p_1}, & \text{for} \quad E_\mathrm{e} < E_\mathrm{B}\,, \\ Q_{0,\mathrm{X}} \left(\dfrac{E_\mathrm{e}}{E_\mathrm{B}}\right)^{-p_2}, & \text{for} \quad E_\mathrm{e} \geq E_\mathrm{B}\,. \end{cases} \tag{5.1}$$

In this formula, $Q_{0,\mathrm{R}}$ and $Q_{0,\mathrm{X}}$ respectively are the flux normalization constants for the radio and the X-ray part of the spectrum. E_B is the break energy of the spectrum, p_1 and p_2 denote the spectral indices of the power-law components before and after the spectral break. As the model focuses on the high-energy part of the spectrum beyond the spectral break in the lepton energy spectrum, we will set $p = p_2$ for the further context and treat this part of the spectrum as a single power law.

The normalization of the injection spectrum is related to the energy emitted from the pulsar's spindown, $\dot{E}$, by

$$\int_{E_\mathrm{e,min}}^{E_\mathrm{e,max}} Q(E_e) E_e \mathrm{d}E_e = \eta \dot{E}\,, \tag{5.2}$$

where η denotes the conversion efficiency. Again, we are interested in the spectrum beyond the break energy and in this case $E_\mathrm{e,min} = E_\mathrm{B}$. The expression for the conversion efficiency of the spin-down luminosity to the energy contained in the leptons with energies above E_B is then:

$$\int_{E_\mathrm{B}}^{E_\mathrm{e,max}} Q_{0,\mathrm{X}} \left(\frac{E_\mathrm{e}}{E_\mathrm{B}}\right)^{-p} E_e \mathrm{d}E_e = \eta \dot{E}\,. \tag{5.3}$$

Integrating this expression and transposing for $Q_{0,\mathrm{X}}$ one finds

$$Q_{0,\mathrm{X}} = \frac{(2-p)\eta\dot{E}}{E_\mathrm{B}^p (E_\mathrm{e,max}^{2-p} - E_\mathrm{B}^{2-p})}\,. \tag{5.4}$$

If the index of the lepton spectrum is $p = 2$, then the equation above is not defined and the appropriate expression for $Q_{0,\mathrm{X}}$ comes down to

$$Q_{0,\mathrm{X}} = \frac{\eta\dot{E}}{E_\mathrm{B}^2 \ln\left(E_\mathrm{e,max}/E_\mathrm{B}\right)}\,. \tag{5.5}$$

Making use of these expressions for $Q_{0,\mathrm{X}}$, the lepton spectrum above the break energy is given by

$$Q(E_\mathrm{e}) = \frac{(2-p)\eta\dot{E}}{E_{\mathrm{e,max}}^{2-p} - E_\mathrm{B}^{2-p}} E_\mathrm{e}^{-p}\,, \tag{5.6}$$

for $p \neq 2$ and by

$$Q(E_\mathrm{e}) = \frac{\eta\dot{E}}{\ln\left(E_{\mathrm{e,max}}/E_\mathrm{B}\right)} E_\mathrm{e}^{-2}\,, \tag{5.7}$$

for an index of $p = 2$.

The lepton injection spectrum defined by the Equations 5.6 and 5.7 has several free parameters which define the shape and the intensity of the spectrum. Fortunately, observational results provide constraints on some of these parameters. The index of the injection spectrum can be deduced from X-ray observations close to the pulsar. The analysis of *Chandra* data by Yatsu et al. (2009) discussed in Section 2.2 shows that the spectral index of the X-ray spectrum is around 1.5 at a distance of $10''$ to the pulsar. Under the assumption that the lepton population emitting this synchrotron radiation has not yet undergone significant cooling, the index of the lepton spectrum at this point is given via the relation $p = 2\Gamma - 1$ that was derived in Section 1.4. An index of the synchrotron spectrum of $\Gamma = 1.5$ thus corresponds to an index of $p = 2$ for the lepton spectrum. This value was adopted for the further modeling and the expression for the lepton spectrum is therefore given by Eq. 5.7. The energy range of the spectrum is defined by $E_{\mathrm{e,max}}$ and E_B. A variation of these parameters does not change the shape of the spectrum and only alters the normalization logarithmically. The value for the maximal energy that the leptons can reach in the shock is constrained by two limits, the gyroradius limit and the synchrotron limit. These limits are discussed in more detail in Section 1.3.3. The lower value of the maximum lepton energy from these two limits is taken as $E_{\mathrm{e,max}}$ for the modeling. A constraint for the break energy in the lepton spectrum was given by Gaensler et al. (2002): to connect the observed radio spectrum from the PWN MSH 15−52 with the X-ray spectrum, the break energy in the synchrotron spectrum has to lie just below the energy range detectable with X-ray satellites[1]. The break energy is thus not fixed, but is in the order of TeV energies. As pointed out before, a change in this energy only enters the spectrum as a logarithmic factor. In the theoretical introduction on pulsars, Eq. 1.7 was introduced, which gives the spin-down luminosity as a function of the moment inertia and the angular rotation frequency of the pulsar. For PSR B1509−58, $\dot{E}$ is equal to

$$\dot{E} = I_{45}\; 1.8 \times 10^{37}\,\mathrm{erg\,s^{-1}}\,, \tag{5.8}$$

where I_{45} is the moment of inertia in units of $10^{45}\,\mathrm{g\,cm^2}$ and is stated as $I_{45} = 3$ by Zhang et al. (2008). This leaves the conversion efficiency as the last parameter without an observational constraint. The only limit on this parameter comes from the condition that the total energy in particles accelerated in the termination shock should be less than the energy output of the pulsar ($\eta < 1$).

5.3 Evolution of the Lepton Population and the Magnetic Field

In the last section the derivation of the injection spectrum for the leptons accelerated in the termination shock was laid out. At this point we will discuss how the leptons propagate

[1] The energy threshold of current-generation instruments is in the order of a couple of hundred electronvolt.

in the PWN once they leave the shock. Since the model assumes spherical symmetry, the bulk velocity of the leptons at each point in the PWN only depends on the radial distance to the termination shock. For the expression of the bulk velocity of the leptons in the nebular flow we assume a profile of the form

$$v(r) = v_{\mathrm{S}} \left(\frac{R_{\mathrm{S}}}{r} \right)^{\alpha} , \tag{5.9}$$

that has only a radial component. In this equation v_{S} is the bulk velocity of the leptons at the shock, α is the exponential index of the velocity profile and r is the distance of the bulk to the pulsar. The index of the velocity profile is a free parameter in the subsequent parameter optimization and is, in principle, unconstrained. However, $\alpha < 0$ would correspond to an acceleration of the bulk movement in the PWN and this is not expected from the physics in the nebular outflow. The value of the shock velocity has been the topic in earlier publications on the modeling of PWN. Kennel & Coroniti (1984a) found a value of $v_{\mathrm{S}} = c/3$ in their model of the Crab Nebula. This value was also adopted by Gaensler et al. (2002) and Yatsu et al. (2009) for MSH 15−52 and was used in the modeling described here.

In the ideal MHD limit discussed in Section 1.1.4 the magnetic field is frozen in the plasma of the outflow and moves along with it. This is also known as Alfvén's theorem of flux-freezing and assumes infinite conductivity (i.e. zero resistivity) for the plasma. In the steady-state approach that can be assumed for the young lepton population close to the pulsar, the ideal MHD limit can be expressed as:

$$\nabla \times (\mathbf{v} \times \mathbf{B}) = 0 \, . \tag{5.10}$$

Assuming that the magnetic field in the PWN is toroidal, the product of the flow velocity v, the distance from the pulsar r and the magnetic field strength B is a constant (Kennel & Coroniti 1984a):

$$Bvr = B_{\mathrm{S}} v_{\mathrm{S}} R_{\mathrm{S}} = \mathrm{constant} \, . \tag{5.11}$$

Here the subscripted parameters denote the parameters at the termination shock. This is a quite useful result as it allows to evaluate the value of the magnetic field strength at each point in the PWN if the parameters at the shock and the velocity profile of the outflow is known. The velocity of the bulk flow was already discussed in the last paragraph and inserting Eq. 5.9 in the equation above, one finds

$$r = \left[(1+\alpha) v_{\mathrm{S}} R_{\mathrm{S}}^{\alpha} t + R_{\mathrm{S}}^{1+\alpha} \right]^{1/(1+\alpha)} , \tag{5.12}$$

as the relation for the distance of the leptons from the pulsar and the travel time t. For the magnetic field strength in the PWN one needs to know its value at the shock, which is given by (Kennel & Coroniti 1984a; Sefako & de Jager 2003):

$$B_{\mathrm{S}} = \frac{\xi}{R_{\mathrm{S}}} \sqrt{\frac{\dot{E}}{c}} \, . \tag{5.13}$$

In this equation and for the parameter optimization presented later in this Chapter, we define

$$\xi = \kappa \sqrt{\frac{\sigma}{1+\sigma}} \tag{5.14}$$

as a combined parameter for the shock compression κ and the magnetization σ. The range of values for the parameter κ is between 1 and 3, whereas the only constraint for σ is, that it is far greater than 1 for the unshocked wind and less than 1 for the outflow in the PWN behind the termination shock (see Section 1.1.4 for more details). Unfortunately, the wind termination shock around PSR B1509−58 has not yet been clearly resolved. Ng & Romani (2004) used a modeling approach to determine the shock radius for a number of PWN, but did not include MSH 15−52 in their work. However, there are constraint on the radius from the analyses by Gaensler et al. (2002) and Yatsu et al. (2009). These will be discussed later in Section 5.6.

For the calculation of the lepton spectra at each location in the PWN, a numerical scheme was used which is already schematically illustrated in Fig. 5.1. The calculation starts with the injection spectrum, which is denoted here as Q_0. The total lepton spectrum in the first of the n shells into which the PWN is divided up, N_1, is calculated by multiplying the injection spectrum with the residence time t_1 of the leptons in the first shell

$$N_1 = Q_0 t_1 \,. \tag{5.15}$$

This is a valid approach as long as the size of shells (and therefore the residence time of the particles in the shell) is chosen small enough. The injection spectrum for the next shell is then calculated by dividing the spectrum in the previous shell by the residence time in that shell, so for shell 2, the injection spectrum is calculated as:

$$Q_1 = \frac{N_1}{t_1} \,. \tag{5.16}$$

This iterative scheme is then repeated for all of the n shells. In the next Section it will then be illustrated how the shape of the lepton spectrum changes because of the energy losses that the particles undergo in each shell.

5.4 Energy Losses of the Leptons in the PWN

During the bulk movement of the leptons outward from the termination shock into the PWN, the leptons lose energy through expansion and radiation processes. This changes the shape of the lepton spectrum and therefore also the resulting radiation spectra. The total energy loss of the particles due to the adiabatic expansion is given by (de Jager & Harding 1992):

$$\frac{\mathrm{d}E}{\mathrm{d}t} = -\frac{1}{3} E_\mathrm{e} (\nabla \cdot \mathbf{v}) \,. \tag{5.17}$$

Under the assumption that the bulk motion follows the velocity profile given in Eq. 5.9, the adiabatic energy losses can then be written as

$$\left(\frac{\mathrm{d}E}{\mathrm{d}t}\right)_\mathrm{Ad} = -\frac{1}{3}(2-\alpha) E_\mathrm{e} v_\mathrm{S} R_\mathrm{S}^{\alpha} r^{-(1+\alpha)} \,. \tag{5.18}$$

From this equation it is apparent, that there are no adiabatic losses for the leptons for a velocity profile with an index of $\alpha = 2$.

The energy losses of the leptons due to the interaction with electromagnetic fields are dominated by the synchrotron radiation emitted in the magnetic field in the PWN. They are given by (de Jager & Harding 1992):

$$\left(\frac{\mathrm{d}E}{\mathrm{d}t}\right)_\mathrm{Sy} = -2.368 \times 10^{-3} B^2 E_\mathrm{e}^2 \,\mathrm{erg}\,\mathrm{s}^{-1} \,. \tag{5.19}$$

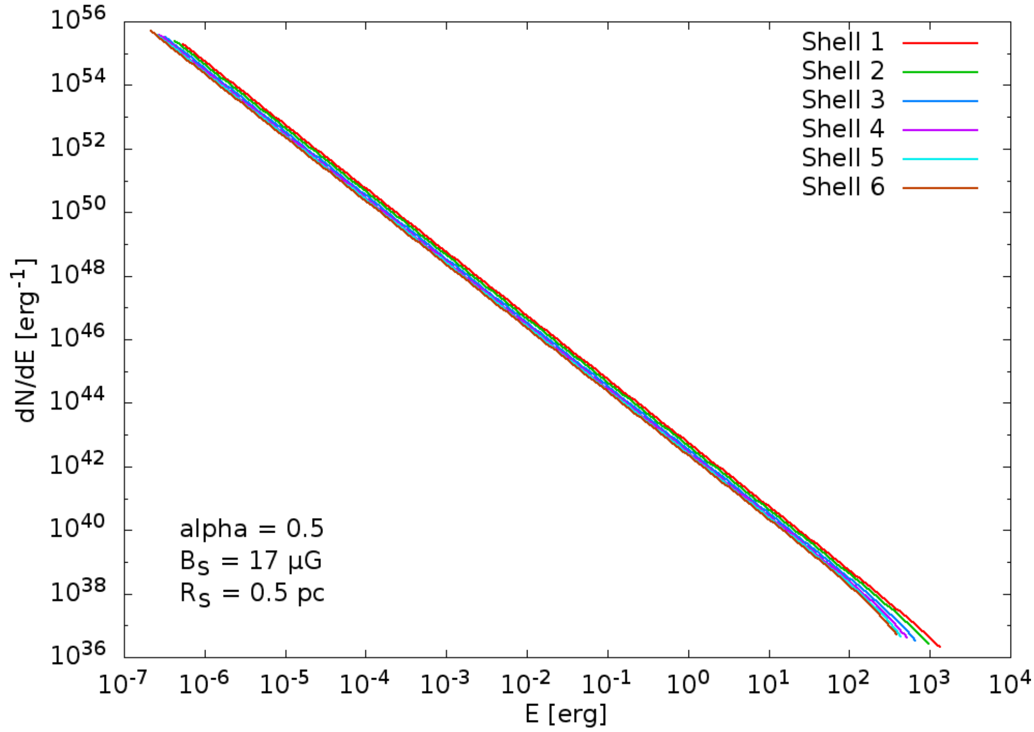

Fig. 5.2: *Illustration of the adiabatic energy losses as described by the model. The plot shows the lepton spectra at different distances from the pulsar, labeled "Shell 1" through "Shell 6" and drawn in different colors. The top-most spectrum (red color) is for the region closest to the pulsar and the differential flux of the spectra decreases with larger distance. The magnetic field strength for this calculation is* $17\,\mu G$*, the index of the velocity profile is* 0.5 *and the shock radius is* $0.5\,pc$*. The injection spectrum for this plot is a power law with an index of* 2 *and is then propagated radially outward according to the velocity profile and the energy losses discussed in the text.*

Compared to the losses due to synchrotron radiation, the energy losses via other radiation mechanisms, e.g. IC radiation, can be neglected as they are smaller by far (cf. Section 1.4). The total energy loss of the leptons in the PWN is then given by the sum:

$$\left(\frac{\mathrm{d}E}{\mathrm{d}t}\right)_{\mathrm{Total}} = \left(\frac{\mathrm{d}E}{\mathrm{d}t}\right)_{\mathrm{Ad}} + \left(\frac{\mathrm{d}E}{\mathrm{d}t}\right)_{\mathrm{Sy}} . \tag{5.20}$$

The evolution of the lepton spectrum due to the cooling mechanisms in the PWN is illustrated in Fig. 5.2 and Fig. 5.3. The first plot shows lepton spectra at different distances from the pulsar that undergo mainly adiabatic cooling. The initial injection spectrum for this plot is a power law with an index of $p = 2$. Six spectra are drawn in the plot for increasing distances, as labeled in the legend. The velocity profile for the propagation of the leptons has an index of $\alpha = 0.5$, the magnetic field strength at the shock is $B_{\mathrm{S}} = 17\,\mu\mathrm{G}$ and the shock radius is $R_{\mathrm{S}} = 0.5\,\mathrm{pc}$. For this set of parameters the adiabatic losses dominate over the synchrotron losses. This is apparent as a shift of the spectra to lower energies for the shells at greater distances. As there is no energy-dependence in the adiabatic cooling, the overall shape of the spectra in Fig. 5.4 stays unaltered, except at the highest energies, where a slight bending of the spectrum is visible. This is due to the cooling of the highest-energy leptons in the magnetic field of the PWN. The effect of the synchrotron cooling is

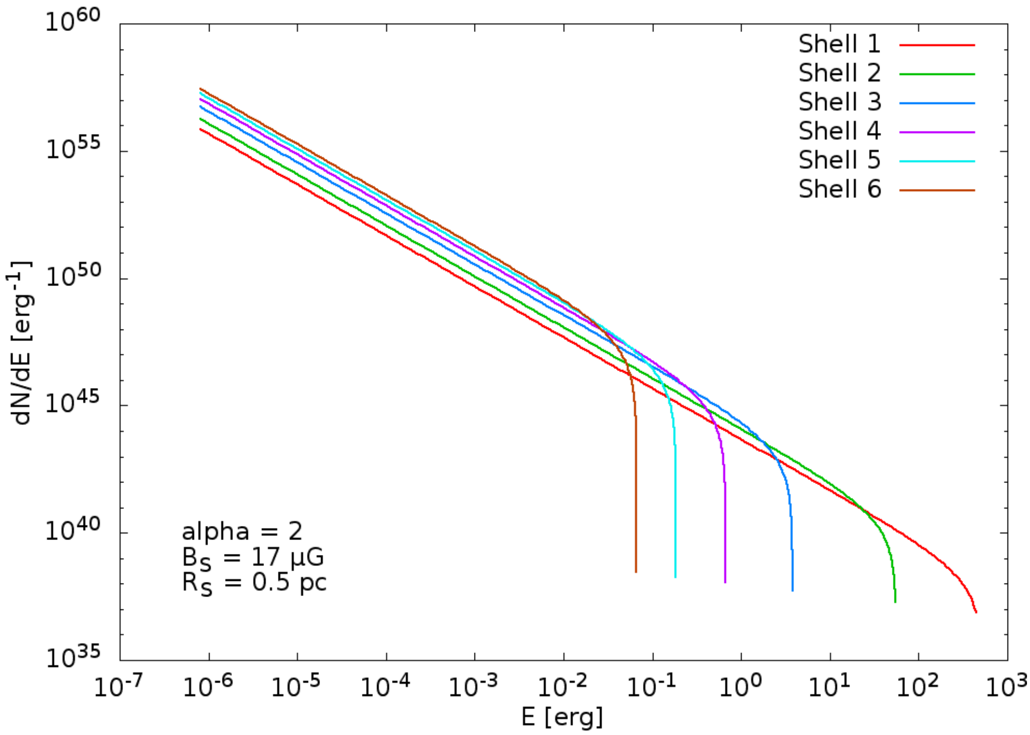

Fig. 5.3: *Illustration of the energy losses due to synchrotron radiation as described by the model. The plot shows the lepton spectra at different distances from the pulsar, labeled "Shell 1" through "Shell 6" and drawn in different colors. The spectrum with the cutoff at the highest energy (red color) is for the region closest to the pulsar, for larger distances the cutoff lies at subsequently lower energies. The magnetic field strength for this calculation is 17 μG, the index of the velocity profile is 2 and the shock radius is 0.5 pc. The injection spectrum for this plot is a power law with an index of 2 and is then propagated radially outward according to the velocity profile and the energy losses discussed in the text.*

better illustrated in Fig. 5.3. For this plot the parameters are essentially the same, except for the index of the velocity profile, which is $\alpha = 2$. This index means that the outflow velocity of the leptons drops off rapidly after the injection at the termination shock. Since the bulk velocity is slower, the leptons undergo synchrotron cooling for a longer time. The effect of this cooling is a shift of the high-energy leptons to lower energies. This is illustrated in Fig. 5.3 by the cutoff that is shifted to lower energies for the higher shell numbers. Accordingly, the intensity at lower energies for the outer shells is increasing.

In the calculation procedure the energy loss of the particles is calculated in binned energy intervals. For each energy bin the average energy loss of the mean energy is calculated. The energy bin is then shifted by the energy loss that the particles with this energy sustain. This is a reasonable approach as long as the two following conditions are met. The number of shells into which the PWN is divided up has to be great enough, i.e. the residence time in each calculation shell is small enough. If this criterion is not met, then the energy losses calculated with this approach are overestimated. This results in the worst case in an energy loss which is greater than the particle's primary energy. The second condition is that the number of bins for the lepton spectra has to be great enough. If the spectra

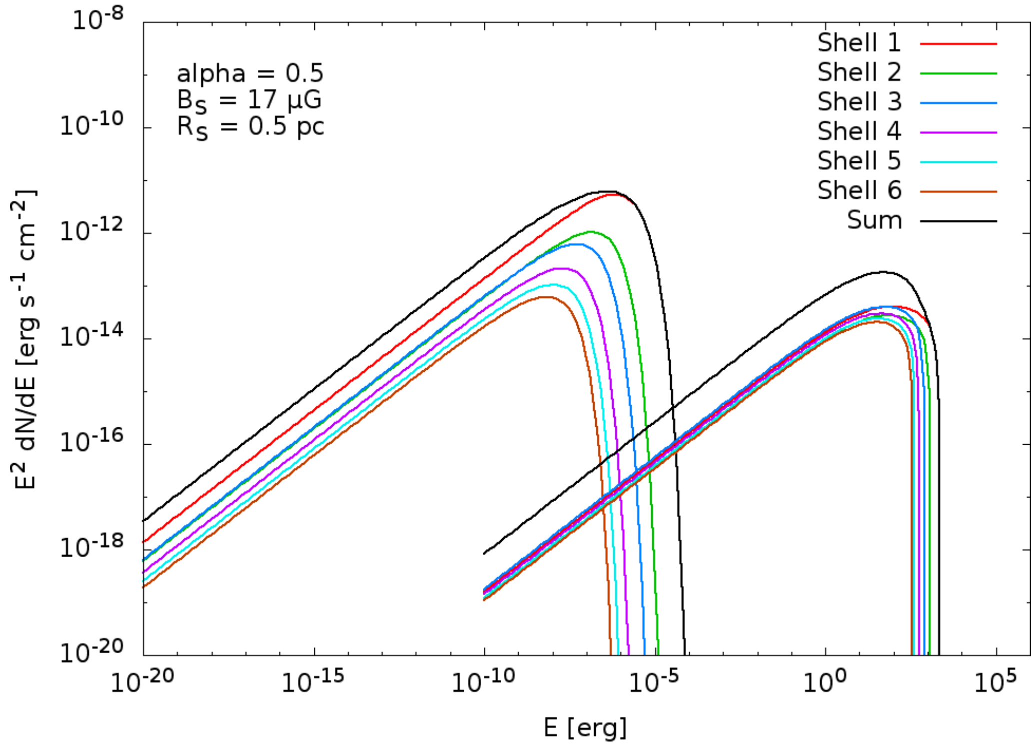

Fig. 5.4: *Synchrotron and IC emission spectra for the scenario with dominating adiabatic energy losses ($\alpha = 0.5$), corresponding to the lepton spectra shown in Fig. 5.2. The plot shows the differential energy spectrum multiplied with the squared energy. The synchrotron spectra are at lower energies, whereas the IC spectra peak at roughly 10^2 erg. The emission spectra from six shells with increasing distance from the pulsar are shown in colored lines and the summed emission from the individual spectra is plotted as the black line.*

are binned too scarce, then the averaged energy loss for each energy bin is not a valid approach any more. The computation precision and the required calculation time have to be carefully weighted against each other to allow on the one hand an extensive scan of the parameter space of the model and on the other hand provide precise results. For the first parameter scans typically a lower precision was chosen, whereas the final results were then computed with high precision. More details on the applied calculation precision are given in Section 5.6.

5.5 Radiation Mechanisms in the Model

The description of the model in the last Sections gives us the energy spectrum of the leptons at each point in the PWN at hand. However, we are not able to probe the leptons directly, but have to rely on the measurement of the electromagnetic radiation that the leptons emit. An introduction of the relevant radiation processes in the PWN MSH 15−52 was given in Section 1.4. The nonthermal radiation observed from MSH 15−52 at X-ray and TeV γ-ray energies is mainly due to synchrotron and inverse Compton radiation. As the model gives us the magnetic field strength at each point of the PWN, we can calculate the expected synchrotron emission for any location. The parameters of the model are then

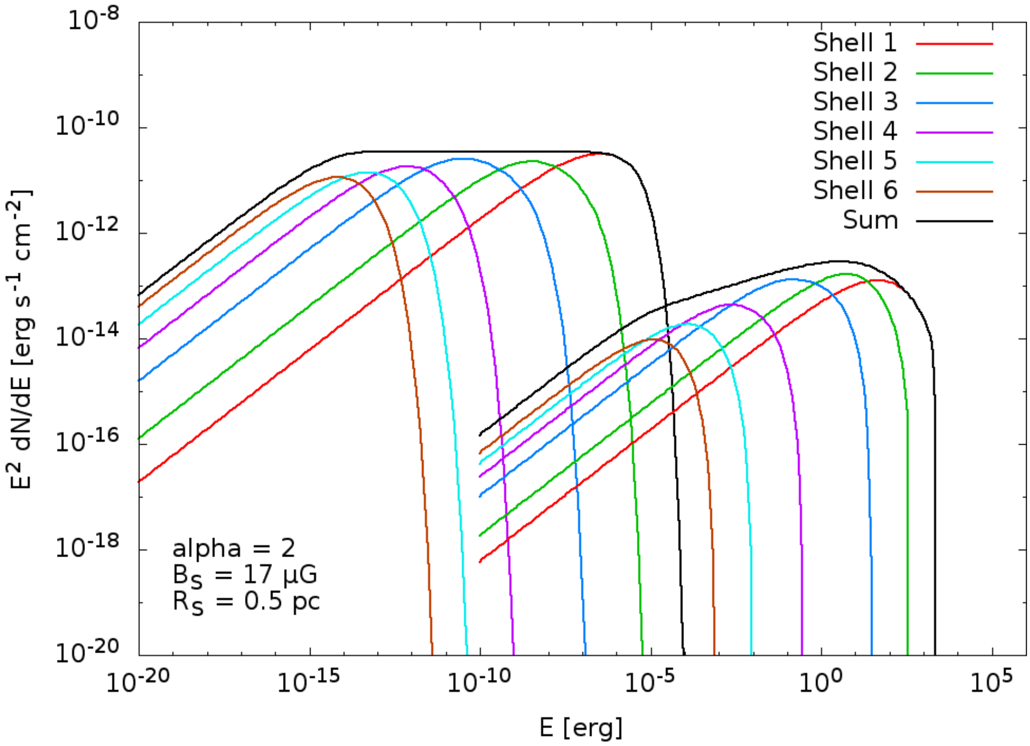

Fig. 5.5: *Synchrotron and IC emission spectra for the scenario with only synchrotron energy losses ($\alpha = 2$), corresponding to the lepton spectra shown in Fig. 5.3. The plot shows the differential energy spectrum multiplied with the squared energy. The synchrotron spectra are at lower energies, whereas the IC spectra peak at roughly 10^2 erg. The emission spectra from six shells with increasing distance from the pulsar are shown in colored lines and the summed emission from the individual spectra is plotted as the black line.*

optimized based on the comparison of the predicted X-ray emission in a certain region to the measured signal in the same region.

The resulting synchrotron and IC emission spectra of a PWN are illustrated in Figs. 5.4 and 5.5 for the two scenarios already used for the lepton spectra that are shown in Figs. 5.2 and 5.3. Both plots show the resulting emission spectra of a lepton population with a power-law injection spectrum with an index of $p = 2$ that is propagated radially outward. Different colors represent the emission from different shells that have an increasing distance from the pulsar and the termination shock. On the Y-axis of the plots, the differential flux ($\mathrm{d}N/\mathrm{d}E$) multiplied with the squared energy is plotted. The curves at lower energies with a peak around 10^{-5} show the synchrotron emission, while the curves at higher energies show the IC emission from the same regions. The CMB photon field was used as the only target photon field for these plots. On top of the spectra of the individual regions, the sum over all six regions is plotted with a black line. In Fig. 5.4 (with $\alpha = 0.5$) the adiabatic energy losses play the major role and result in a shift to lower energies and lower intensities for the regions that are lying at a larger distance from the pulsar. The plot illustrates that for a power-law lepton spectrum with an index of $p = 2$, the emitted synchrotron spectrum has an index of $\Gamma = (p + 1)/2 = 1.5$ up to the cutoff at the maximum lepton energy. The IC emission in Fig. 5.4 is only from the interaction with CMB photons and, therefore, treated in the Thomson regime. In this case, the spectral index of the IC spectrum is the same as for the synchrotron spectrum and is also equal to 1.5.

For the case of strong synchrotron cooling and no adiabatic energy losses ($\alpha = 2$) displayed in Fig. 5.5, the resulting spectra look different. In this scenario, the cutoff in the lepton spectrum rapidly moves to lower energies for the more distant shells due to the strong synchrotron cooling. The sum of the individual synchrotron spectra, shown as the black curve on top, illustrates that the superposition of these spectra results in a power-law spectrum with an index of $\Gamma = 2$ over a large range of energies. At energies below $\approx 10^{-14}$ erg, the synchrotron spectrum again has the index that is characteristic of the uncooled lepton spectrum ($\Gamma = 1.5$). The same is also valid for the IC emission spectra at energies below $\approx 10^{-5}$ erg.

5.6 Optimization Procedure and Parameters in the Model

At this point, the model now allows us to extract the emission spectra at each location in the PWN. The emission from the different locations is then summed up to correspond to the regions from measurements. In the case presented here, the spatially resolved analysis of the X-ray emission conducted with the *XMM-Newton* satellite presented in Chapter 3 was used to constrain the free parameters in the model. The six regions used in the analysis are shown in the X-ray sky map in Fig. 3.4 on page 56. The measured evolution of the spectral index of the power-law spectrum in the X-ray energy range and the evolution of the surface brightness are shown in Figs. 3.6 and 3.7, respectively.

The parameters of the model were already introduced and briefly discussed in the last Sections. The injection spectrum is assumed as a power-law spectrum which is defined by the spectral index and the normalization. Following the measurements of Yatsu et al. (2009), the index of the lepton injection spectrum is chosen as $p = 2$. The normalization is derived from the parameters $E_{\mathrm{e,min}}$, $E_{\mathrm{e,max}}$, $\dot{E}$ and η. The minimum energy is in the order of 1 erg and constrained by the condition that a break in the lepton spectrum is required to connect the synchrotron spectrum seen at radio and X-ray energies (Gaensler et al. 2002). Towards higher energies, $E_{\mathrm{e,min}}$ is limited by the energy threshold of the X-ray instruments, as no break is seen by X-ray satellites. $E_{\mathrm{e,max}}$ is defined by the limits discussed in Section 1.3.3 and therefore depends on the parameters of the shock, which are combined as one parameter ξ (cf. Eq. 5.14) and left unconstrained for the optimization. The velocity profile of the leptonic outflow is characterized by three parameters, α, v_{S} and R_{S}. While α is unconstrained for the optimization, the shock radius and shock velocity have been restricted by observations. For v_{S}, Gaensler et al. (2002) and Yatsu et al. (2009) both assume a shock velocity of $v_{\mathrm{S}} \approx c/3$ based on the analysis of *Chandra* data. This value is also in good agreement with the lower limit that Gaensler et al. (2002) derived from the energetics of MSH 15−52. Furthermore, this value has also been proposed for other PWN, e.g. the Crab Nebula (Kennel & Coroniti 1984a). Therefore, we adopted $v_{\mathrm{S}} = c/3$ for the model calculations shown here.

The radius of the termination shock around PSR B1509−58 has also been estimated by Gaensler et al. (2002) and Yatsu et al. (2009) using *Chandra* X-ray data. However, both authors arrive at differing conclusions. Gaensler et al. (2002) favor a scenario in which a feature at 0.5 pc corresponds to an internal structure in the termination shock (see Fig. 2.4 for the detailed *Chandra* sky map of this analysis). They also estimated the value of the magnetization parameter σ for several compact knots of emission less than 0.5 pc away from PSR B1509−58 and concluded that the transition to a particle-dominated wind

Table 5.1: *Model parameters for the different scenarios as discussed in the text.*

Parameter	Scenario		
	I	II	III
R_S [pc]	< 0.1	0.5	0.225
v_S [c]	1/3		
α	no constraint		
η	0 –1		
ξ	no constraint		

should occur at a distance of less than 0.1 pc from the pulsar. Yatsu et al. (2009) analyzed a larger data set of *Chandra* observations and used image enhancement techniques to resolve the detailed structure of the inner region around PSR B1509−58 (cf. Fig. 2.5). According to their results, the termination shock is located at a distance of $9''$ to the pulsar. This corresponds to a termination shock radius of $R_S = 0.225$ pc. For the magnetization parameters, Yatsu et al. (2009) derived a value of $\sigma \approx 0.01$, which is about a factor of 2 greater than the result obtained by Gaensler et al. (2002).

Based on the two *Chandra* analyses, we considered three scenarios with different values of R_S for the optimization procedure of our model. In Scenario I we assume that the termination shock is unresolved in the *Chandra* observations and thus is at a distance closer than 0.1 pc to the pulsar. For Scenario II we follow the arguments of Gaensler et al. (2002) and choose a value of $R_S = 0.5$ pc, while for Scenario III we adopt the value of $R_S = 0.225$ pc, as stated by Yatsu et al. (2009). An overview of the free parameters in the model is given in Table 5.1. The constraint on the conversion efficiency to a range of $\eta = 0-1$ follows straightforward from the assumption that the energy in the particles of the injection spectrum cannot be greater than the spin-down luminosity of the pulsar.

For the three Scenarios listed in Table 5.1 the parameter space was scanned and the emission spectra in the regions corresponding to the regions shown in Fig. 3.4 were calculated. From these spectra the flux was calculated in the same energy range as the flux points from the *XMM-Newton* analysis shown in Fig. 3.8 exemplary for the rings 1 and 6. This gives a total of 24 points that were used for the comparison of the model emission to the measured emission. The deviation between these two, in units of the statistical fit error on the X-ray data, was calculated as:

$$X^2 = \sum_{i=1}^{n} \left(\frac{F_{\mathrm{model},i} - F_{\mathrm{X},i}}{\sigma_i} \right)^2 , \tag{5.21}$$

where $F_{\mathrm{model},i}$ is the flux of the model, $F_{\mathrm{X},i}$ the flux from the X-ray measurement and σ_i the statistical error in the respective energy range of the current flux point.

Due to the partially strongly correlated parameters of the model, the parameter optimization does not lead to a singular best-fit result. Therefore, we chose intervals of parameters within a certain percentage range around the minimum value of X^2. For the broad scan of the parameter space, 500 bins were used for the lepton and photon spectra. The number of calculation shells was set to 500. Both numbers were increased for the cross-check of the optimal set of the parameters that was found in the three scenarios. However, the higher precision did not lead to a significant change in the results.

5.7 Results of the Modeling

Using the model presented and the parameter constraints discussed in this Chapter, the optimum parameters were calculated for the three scenarios that were defined in the last Section and are listed in Table 5.1. Already in the broad scan of the parameter space it becomes apparent, that Scenario II and III (larger shock radius) yield a much better fit to the *XMM-Newton* data than Scenario I (small shock radius).

Scenario I

For Scenario I it is assumed that the termination shock has not been resolved by the high-resolution *Chandra* analysis. As discussed by Gaensler et al. (2002), the dimension of the shock radius must then be smaller than $R_\mathrm{S} \lesssim 0.1\,\mathrm{pc}$ and this value is taken as an upper limit for this case (see Table 5.1). The best fit for Scenario I is obtained for a value of $R_\mathrm{S} = 0.1\,\mathrm{pc}$. This is the upper limit of the value and even the best fit is far worse than for the other two scenarios. An explanation for this result is, that due to the small shock radius in this scenario, the synchrotron cooling is very efficient and leads to strong cutoffs in the X-ray spectra, especially for the outer rings. This is not compatible with the observed *XMM-Newton* spectra.

Scenario II

The results obtained for Scenario II yield a better fit to the data. In this scenario the shock radius is considerably larger ($R_\mathrm{S} = 0.5\,\mathrm{pc}$). Thus, the leptons accelerated at the termination shock suffer from less synchrotron cooling up to ring 1 of the *XMM-Newton* measurement. Figure 5.6 shows as an example the data and model synchrotron spectra for rings 1 and 6 for the optimum set of parameters found in Scenario II. The best-fit power law from the X-ray observations is plotted as a solid line for ring 1 and as a dashed line for ring 6. The error bands of the statistical fit error are drawn as gray regions. While this regions is clearly visible for the ring 6 spectrum, it is very small and thus hardly visible for ring 1, due to the small statistical errors on the X-ray spectrum. The calculated spectra from the model with the best-fit parameters for Scenario II are drawn as a dotted line for the region corresponding to ring 1 and as a dashed-dotted line for ring 6. Even these best-fit model spectra deviate significantly from the *XMM-Newton* spectrum, but this is expected due to the simplifications of our model. In the general trend, however, the model reproduces the spectral shape and the flux level of the *XMM-Newton* data. The variation of the spectral index with increasing distance of the extraction region from the pulsar is plotted in Fig. 5.7 for the same set of parameters. The plot shows the spectral index of the power-law fit of the *XMM-Newton* data (cf. Fig. 3.6) marked with blue "x" points and the respective statistical error. The filled box points show the spectral index of a power-law fit to the calculated model spectra in the energy range of $0.5 - 9.0\,\mathrm{keV}$. The general trend of the development of the spectral index with increasing index is reproduced, although several model points are outside of the narrow statistical fit error of the *XMM-Newton* measurement. A similar picture is obtained for the variation of the surface brightness. This is illustrated in Fig. 5.8, in which the surface brightness in the energy range from 0.5 to 9 keV is plotted against the distance of the extraction region from the pulsar PSR B1509−58. Blue points and error bars represent again the *XMM-Newton* data and filled black box points the result from the model calculation in the same energy range. The surface brightness shows a monotonic decrease from the inner regions to ring 6 in both, data and model calculations.

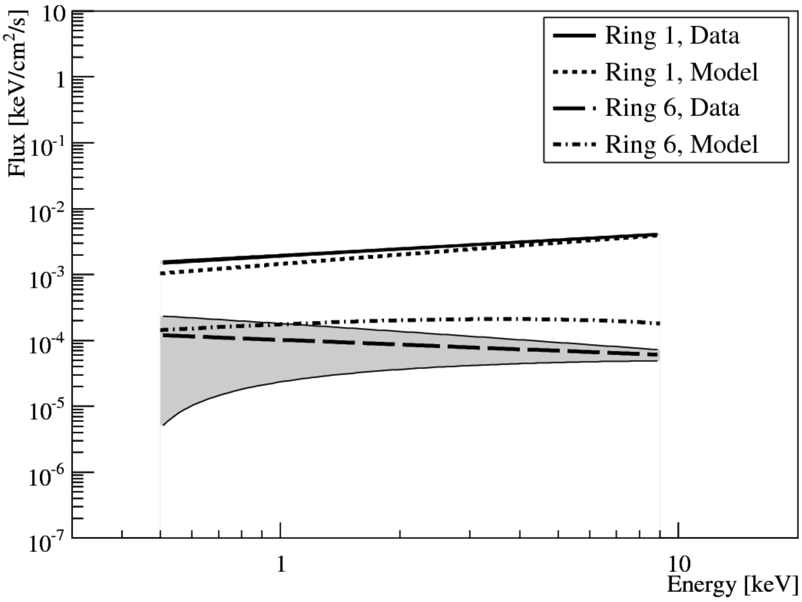

Fig. 5.6: *Data and model spectra for the ring 1 and 6 regions for Scenario II. The meaning of the different lines is indicated in the legend. The shaded regions mark the error bands of the XMM-Newton measurement of ring 1 and 6. For ring 1 the error band is very narrow and thus hardly visible.*

The plots in Figs. 5.6 to 5.8 show the best-fit results for the Scenario II of the model. In this set of parameters, the velocity profile has an index of $\alpha = 0.47$. For ξ, a value of $\xi = 0.56$ is found. Taking into account that the compression parameter κ varies between 1 and 3 for relativistic shocks and using the relation between σ and κ given in Eq. 5.14, this translates to a range for the magnetization σ from 0.04 to 0.46. Since the parameters of the model are correlated, a different set of parameters can yield similar values of X^2. We therefore state parameter ranges of the model parameters for which the value of X^2 is within 10% of the minimum value found. For Scenario II this leads to a range of the index of the velocity profile of $\alpha = 0.4-0.6$ and a conversion efficiency that is greater than $\eta \geq 0.3$. This lower limit matches the limit that Zhang et al. (2008) found in their time-dependent one-zone model of MSH 15−52. The combined parameter ξ has a range of $\xi = 0.3-1.3$, which results in a lower limit of $\sigma \geq 0.01$. This lower limit on σ is a factor of 2 greater than the lower limit on σ previously stated by Gaensler et al. (2002).

Scenario III

The range of minimum values of X^2 found in the parameter optimization for Scenario III is in the same range as the values for Scenario II. Therefore, it is not possible to favor one scenario over the other. For this scenario the termination shock lies at a distance of 0.225 pc from the pulsar, following the *Chandra* data analysis of Yatsu et al. (2009). The synchrotron spectra for the ring 1 and ring 6 regions are shown in Fig. 5.9, along with the calculated model spectra for the optimum set of model parameters. The meaning of the different lines is the same as in Fig. 5.6 for the results of Scenario II. Similarly to that figure, the error band of the X-ray measurement that indicates the statistical fit error is only visible for the ring 6 data, as it is very narrow for the data from ring 1.

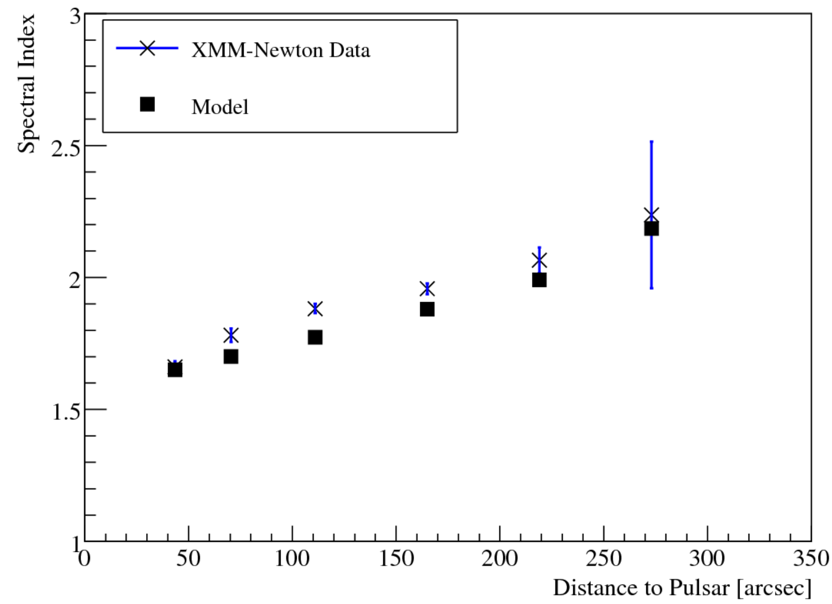

Fig. 5.7: *Spectral indices of power-law fits to the XMM-Newton data of the different regions in the energy range of* $0.5-9.0\,keV$ *(cf. Fig. 3.6). The model points shown are calculated for the best fit of Scenario II and use the same energy range for the fit as the X-ray data.*

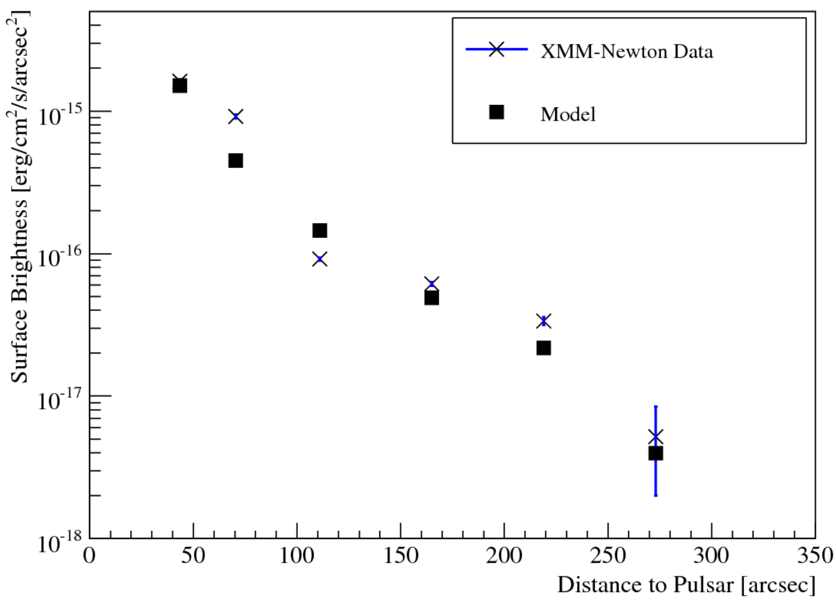

Fig. 5.8: *Variation of the surface brightness for the XMM-Newton data and the model in the energy range of* $0.5-9.0\,keV$ *with increasing distance from the pulsar (cf. Fig. 3.7). The model points shown are calculated for the best fit of Scenario II.*

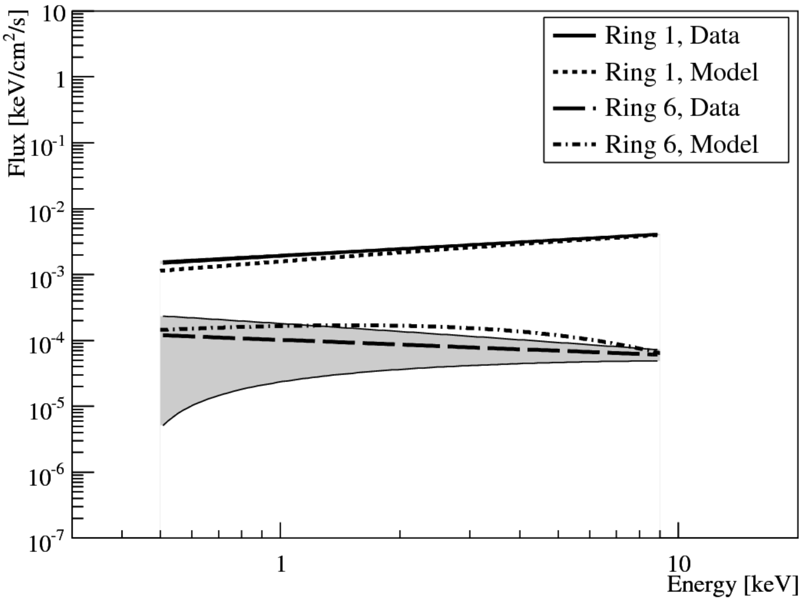

Fig. 5.9: *Data and model spectra for the ring 1 and 6 regions for Scenario III. The meaning of the different lines is indicated in the legend. The shaded regions mark the error bands of the XMM-Newton measurement of ring 1 and 6. For ring 1 the error band is very narrow and thus hardly visible.*

The calculated model spectrum for ring 6, drawn as a dash-dotted line, exhibits a more pronounced curvature than that of the same spectrum in Fig. 5.6. This already illustrates the effect that for the smaller shock radius ($R_{\mathrm{S}} = 0.225\,\mathrm{pc}$) of this scenario the cooling of the high-energy leptons plays a larger role. Fig. 5.10 shows the variation of the spectral index of the *XMM-Newton* data and the calculated model spectra. The *XMM-Newton* data points and error bars are, again, drawn in blue and the filled black box points correspond to the model. While the spectral indices in the inner regions agree very well, the more effective synchrotron cooling leads to a systematic steeping of the spectral index for the outer regions. The variation of the surface brightness in the energy range of $0.5-9.0\,\mathrm{keV}$ is shown in Fig. 5.11. The calculated model values exhibit the same monotonic decrease in surface brightness as the *XMM-Newton* data points that are drawn in blue.

The optimum parameters for Scenario III for which the plots are shown have values of $\alpha = 0.5$ and $\xi = 0.3$, corresponding to range of σ from 0.01 to 0.1. Defining a range of parameters in the same fashion as for Scenario II delivers a range of the velocity profile index of $\alpha = 0.4-0.6$ and a conversion efficiency that is greater than 0.3. The lower limit for the magnetization is $\sigma \geq 0.005$. This smaller than the value of Yatsu et al. (2009), but in the same order of magnitude. They used the equipartition assumption to estimate a magnetization parameter of $\sigma \approx 0.01$.

Spatial Evolution of the Magnetic Field

Besides the calculation of the emission spectra from different regions around the pulsar, the model that is presented in this Chapter also make predictions for the spatial evolution

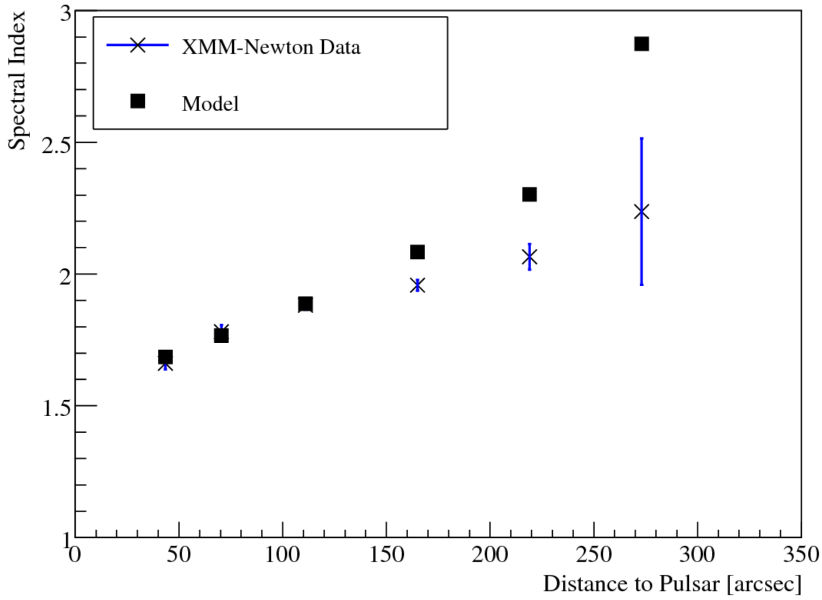

Fig. 5.10: *Spectral indices of power-law fits to the XMM-Newton data of the different regions in the energy range of* 0.5 – 9.0 *keV (cf. Fig. 3.6). The model points shown are calculated for the best fit of Scenario III and use the same energy range for the fit as the X-ray data.*

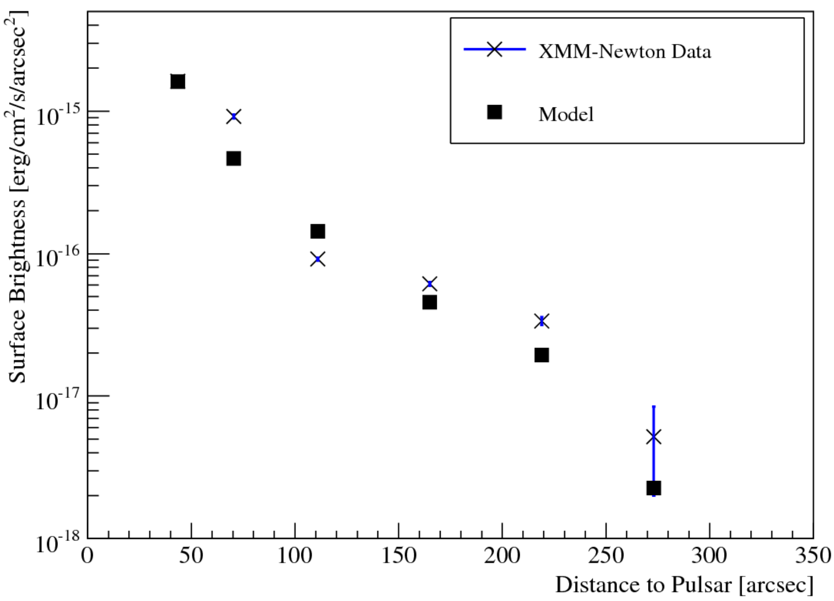

Fig. 5.11: *Variation of the surface brightness for the XMM-Newton data and the model in the energy range of* 0.5 – 9.0 *keV with increasing distance from the pulsar (cf. Fig. 3.7). The model points shown are calculated for the best fit of Scenario III.*

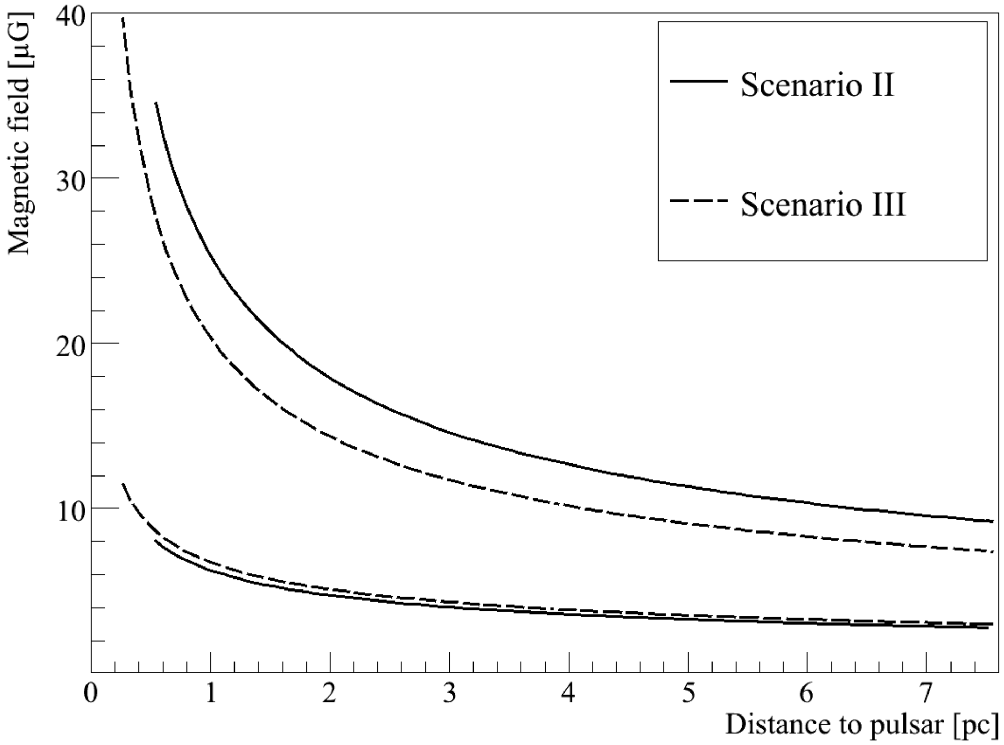

Fig. 5.12: *Spatial evolution of the magnetic field with distance from the pulsar. The two solid lines denote the upper and lower range of values of the magnetic field strength for Scenario II (based on the range for α and ξ that was found in the optimization). The two dashed lines mark the upper and lower limit of B for Scenario III.*

of the magnetic field with increasing distance. Since the magnetic field strength is a key parameter for the established one-zone models, we calculated its variation for the Scenarios II and III that yield the best fit to the X-ray data. The result of this calculation is shown in Fig. 5.12, where the ranges of the magnetic field strength for the two scenarios is plotted against the distance from the pulsar. The two solid lines denote the range of values that was found for the range of optimum parameters in Scenario II ($R_S = 0.5$ pc), whereas the dashed lines shows the upper and lower limits for Scenario III ($R_S = 0.225$ pc). The magnetic field estimates for MSH 15−52 that have been found in previous one-zone modeling approaches range from 8 μG (Gaensler et al. 2002) to 25 μG (Zhang et al. 2008). This is in excellent agreement with the spatial evolution of the magnetic field that we find our calculations.

5.8 Predictions of the Model for the TeV γ-ray Emission

Besides the calculation of the synchrotron emission that was used to optimize the free parameters of the model, as shown in the last Section, we also calculated the inverse Compton emission that is emitted, when the leptons in the outflow interact with target photon fields (see Section 1.4 for more details). In the case of MSH 15−52, contributions

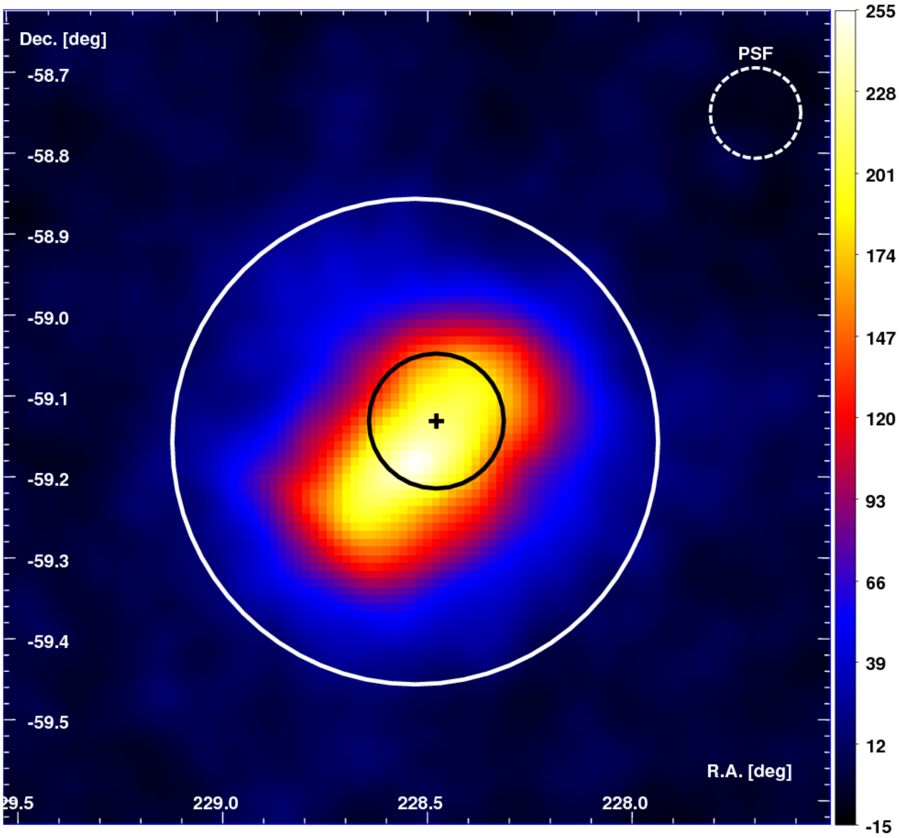

Fig. 5.13: *Smoothed H. E. S. S. excess map of the VHE γ-rays from MSH 15−52. The map was smoothed with the H. E. S. S. point spread function (illustrated by the dashed white circle in the upper right) to reduce statistical fluctuations and is the same map as is shown in Fig. 4.24. The extraction region for the published H. E. S. S. spectrum has a radius of $0.3°$ and is marked with a white line (cf. Section 4.5). It is centered on the centroid of the VHE γ-ray emission. The black circle denotes the $300''$ region used for the modeling in this paper. It is centered on the position of the pulsar PSR B1509−58, which is indicated by a black cross.*

from photons of the cosmic microwave background radiation (CMBR), infrared (IR) photons emitted by dust and starlight play a role. Based on the optimized parameters of the model that were described in the previous Section, we calculated the resulting IC emission from these fields. The energy density of the individual components was held fixed on the values stated by Zhang et al. (2008):

- $U_{\mathrm{CMB}} = 0.25\,\mathrm{eV\,cm^3}$ for the 2.7 K CMBR,
- $U_{\mathrm{IR}} = 4\,\mathrm{eV\,cm^3}$ for the 40 K IR radiation, and
- $U_{\mathrm{Starlight}} = 1.4\,\mathrm{eV\,cm^3}$ for the 5000 K starlight component.

The energy density of the IR component is rather high, but might be explained by material swept up by MSH 15−52, as suggested by Du Plessis et al. (1995).

A detailed analysis of the VHE γ-ray emission from MSH 15−52 was given in Chapter 4. The emission in this energy band is far more extended than at X-ray energies. This is again illustrated in Fig. 5.13, where the H. E. S. S. γ-ray excess map of MSH 15−52 is shown.

The map is smoothed with the PSF for these observations, which is indicated with its R_{68} as a dashed white circle in the upper right corner. The white circle in this map marks the extraction region used for the spectral analysis in (Aharonian et al. 2005b) and in Chapter 4 of this work. The black cross indicates the position of the pulsar PSR B1509−58 and the black circle the outer boundary of the regions used for the modeling of the source.

Two different approaches were used to obtain the H. E. S. S. spectrum of the inner region of MSH 15−5*2* for the comparison with the model. For the publication of the model in Schöck et al. (2010), we used the published excess map of Aharonian et al. (2005b) and rescaled the data to obtain the spectrum of the central 300″ region around PSR B1509−58. The ratio of excess events in the two regions displayed in Fig. 5.13 is 3.42 and this results in a normalization of the γ-ray spectrum at 1 TeV of $(1.67 \pm 0.06_{\mathrm{stat}} \pm 0.41_{\mathrm{sys}}) \times 10^{-12}\,\mathrm{TeV}^{-1}\,\mathrm{cm}^{-2}\,\mathrm{s}^{-1}$, where the error is rescaled with the same factor. This scaling assumes, that there is no significant spectral variation of the H. E. S. S. spectrum across the source, which is fortified by the analysis presented in Section 4.5. Due to the size of the H. E. S. S. PSF, which is in the same order of magnitude as the inner region considered for the modeling, we expect contamination of the the inner region with events from the outer regions of the PWN. About 30% of the emission from inside the PSF will fall outside of the region defined by the rings 1 to 6. However, a similar amount from the emission outside this region will fall into the central part. To a first order these effects will cancel out, although a systematic steepening in the spectrum is expected if the TeV photon index also steepens.

With the analysis results presented in Chapter 4, and by using a smaller extraction region around PSR B1509−58, we can now also directly use the H. E. S. S. analysis results for a comparison with the model calculation. For an analysis region with a size of 300″ that is centered on PSR B1509−58, a broken power-law spectrum gives the best fit to the data. The fitted spectrum has a break at (2.35 ± 0.67) TeV, where the spectral index changes from 2.07 ± 0.09 to 2.85 ± 0.21. The differential flux at 1 TeV for this spectrum is $(1.84 \pm 0.08) \times 10^{-12}\,\mathrm{TeV}^{-1}\,\mathrm{cm}^{-2}\,\mathrm{s}^{-1}$ and therefore consistent within errors with the differential flux of the rescaled spectrum.

The spectral energy distribution (SED) of MSH 15−5*2* in the X-ray and TeV γ-ray band is shown in Fig. 5.14. The experimental data shown in the X-ray energy range in this plot are the sum of the emission of the shells from the *XMM-Newton* analysis (see Chapter 3). For the TeV range, the rescaled H. E. S. S. spectrum as discussed above, is shown as a solid black line and the $1\,\sigma$ confidence region of the new Model++ analysis is shown as a red region. The model SED was obtained with the best-fit parameters of Scenario II ($R_{\mathrm{S}} = 0.5$ pc) for a conversion efficiency of $\eta = 0.4$. For this set of parameters, the fitted spectral index of the IC emission in the energy range from 300 GeV to 30 TeV is 1.8. This is slightly below the statistical and systematic error of the measured H. E. S. S. spectrum. The normalization of the power-law fit of the model at 1 TeV is $3.1 \times 10^{-12}\,\mathrm{TeV}^{-1}\,\mathrm{cm}^{-2}\,\mathrm{s}^{-1}$ and hence also below the 1σ error of the measurement. The ratio of the predicted flux above 300 GeV to the observed flux is 0.3 for this set of parameters.

The predicted variation of the spectral index in the TeV energy range for the regions used in the modeling is illustrated in Fig. 5.15. The black points show the spectral index of a power-law fit to the model spectrum in the energy range of 300 GeV to 30 TeV for the best-fit parameters of Scenario II with a conversion efficiency of $\eta = 0.4$. It can be seen that the spectral indices of the model are below the measured index for the whole MSH 15−5*2* region. This result might be compatible with the previous H. E. S. S. measurement of the 0.3° region around MSH 15−5*2*, if there is a very drastic steepening of the spectrum outside of the region used for the modeling. However, the analysis presented in Section 4.5

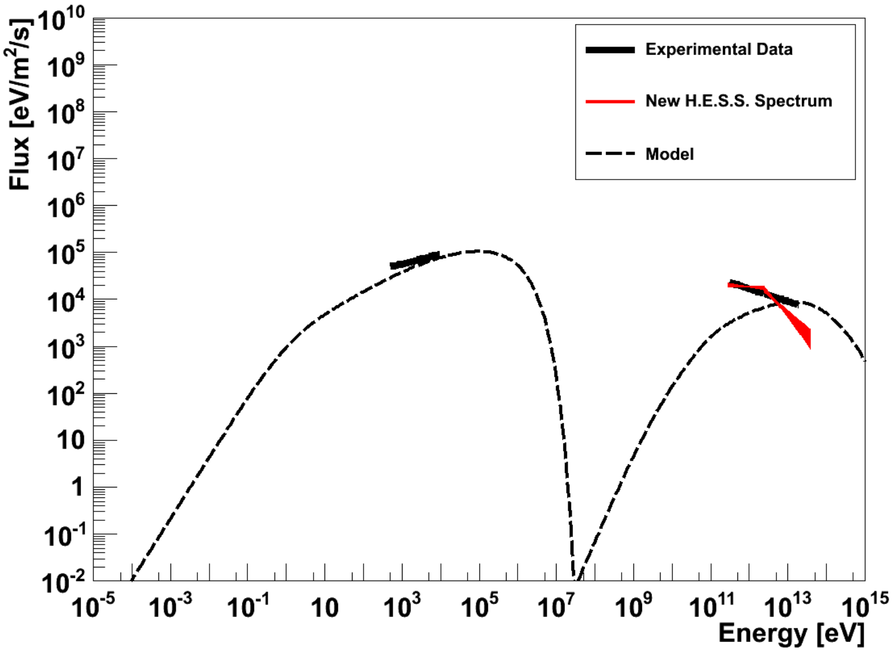

Fig. 5.14: *Spectral energy distribution (SED) of the emission from the inner region of MSH 15−52 as marked by the solid black line in Fig. 5.13. The summed XMM-Newton spectrum of the analysis of the regions presented in Chapter 3 and the H. E. S. S. data from the rescaled old analysis are marked as solid black lines. The red area denotes the $1\,\sigma$ confidence region from the new analysis of the inner region of MSH 15−52. The model result for the best-fit values of Scenario II with a conversion efficiency of $\eta = 0.4$ is drawn as a dashed black line.*

shows that this is not the case. Therefore, this can not explain the apparent deviation.

In Fig. 5.16 the variation of the surface brightness for the same set of parameters is shown. The flux was calculated in the energy range of 0.3 – 30.0 TeV and for the same ring regions as used in the X-ray analysis. Compared to the X-ray surface brightness shown in Figs. 5.8 and 5.11, which drops by three order of magnitude from ring 1 to ring 6, the decrease in surface brightness is considerably smaller for the IC emission. However, from looking at the H. E. S. S. sky map (Fig. 5.13) it is apparent that there is large component of the emission that is not inside the central region and thus not described by our model. This might, for example, be due to an older population of leptons that accumulate in the outer parts of the PWN, as discussed e.g. by de Jager & Djannati-Ataï (2009).

Both predictions, the variation of the spectral index and the surface brightness in the TeV energy range, are stated for the inner 300″ around the pulsar. Unlike the instruments in the X-ray energy range, the current generation of VHE γ-ray experiments does not have the necessary angular resolution to probe the inner structure around the pulsar with such great detail. Therefore, it is currently not possible to test the model against the data. However, future IACT telescopes like the Cherenkov Telescope Array (CTA, Wagner et al. 2009) will have a resolution around one arcminute and will allow for a test of these predictions.

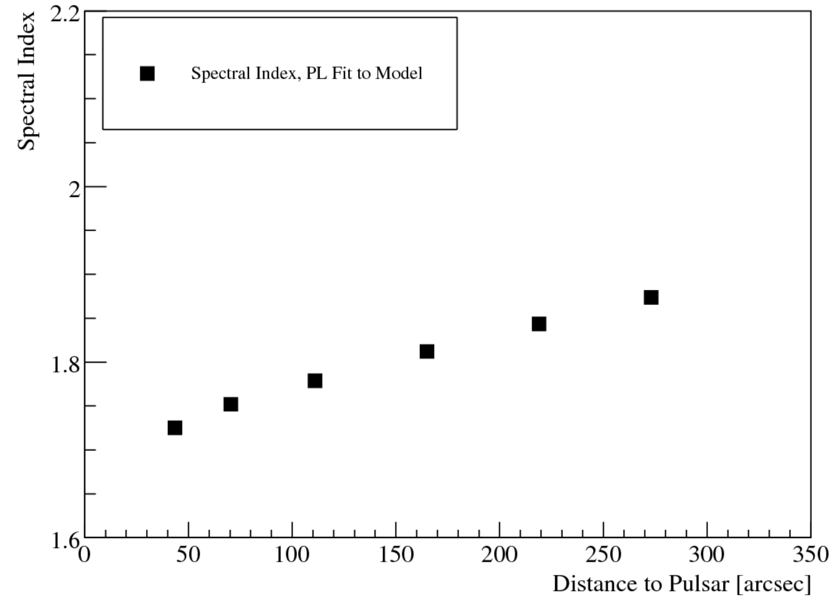

Fig. 5.15: *Plot of the spectral index of a power-law fit to the IC emission calculated in the model with increasing distance from the pulsar. The fit range was from* 300 *GeV to* 30 *TeV. Plotted is the result of the model with the best-fit parameters for Scenario II for a conversion efficiency of* $\eta = 0.4$.

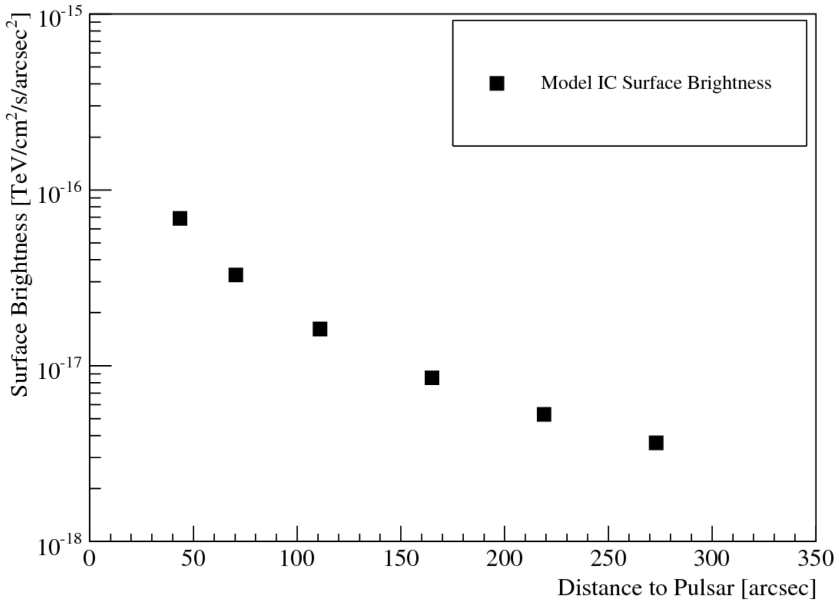

Fig. 5.16: *Plot of the surface brightness of the IC emission with increasing distance from the pulsar. The surface brightness was calculated for a power-law fit to the data in an energy range of* 300 *GeV to* 30 *TeV. Plotted is the emission from the model calculations with the best-fit parameters for Scenario II for a conversion efficiency of* $\eta = 0.4$.

5.9 Implications of the Model

The numerical model described in the previous Sections is able to reproduce the general trend of the observed synchrotron spectra in the X-ray energy range. The results of the optimization procedure suggest, that the termination shock is in the range of 0.225 pc to 0.5 pc, without being able to discriminate between these values that have been proposed by Yatsu et al. (2009) and Gaensler et al. (2002). The lower limit on the magnetization parameter is at $\sigma \geq 0.005$ and the lower limit for the conversion efficiency is at $\eta \geq 0.3$. In this context, only the leptons beyond the break energy are taken into account for the conversion efficiency. One can derive the total energy emitted by the leptons via synchrotron and IC emission by integrating over the SED that is shown in Fig. 5.14. The integrated emission amounts to $7.6 \times 10^{35}\,\mathrm{erg\,s^{-1}}$, which is about 4% of the current spin-down luminosity of the pulsar PSR B1509−58. However, when making this comparison one has to be aware, that the integrated emission comes from a population of leptons with different lifetimes and cannot be directly linked to the current spin-down luminosity. Furthermore, there is also significant emission in the X-ray band and at TeV energies outside of the central $300''$ region considered in our modeling approach (see e.g. Figs. 3.4 and 5.13). This increases the percentage of the lepton energy that is converted to radiation.

The modeling presented in this Chapter supports the case that the VHE γ-ray emission observed from this source can be explained by a purely leptonic scenario, in which the γ-rays are from the interaction of high-energy leptons with target photon fields. This has already been proposed e.g. by Aharonian et al. (2005b), Zhang et al. (2008) and Abdo et al. (2010b) based on one-zone models of the PWN. In this Chapter we showed, that a model which is based on the parameters of the termination shock and takes into account a velocity profile for the leptonic outflow can reproduce the observed characteristics of the synchrotron emission and the approximate flux level of the VHE γ-ray emission.

However, the model spectra calculated with the best-fit parameters still show deviations from the measured spectra. Possible causes for this are the assumption of radial symmetry and of ideal magnetohydrodynamics in the model. Although the radial symmetry provides an improvement to current one-zone models, the X-ray and TeV γ-ray sky maps of MSH 15−5*2* (Figs 3.4 and Fig. 5.13) suggest that the morphology is more complicated than this. A jet-like feature is apparent at X-ray energies and is possibly linked to the orientation of the rotational axis of PSR B1509−58, as argued by Gaensler et al. (2002). The same authors also discuss a potential sub-structure of MSH 15−5*2*, denser regions within the PWN that might be the site of re-acceleration processes, which could also be responsible for a deviation of the data from the model. In the calculation of the IC spectra, the target photon fields were fixed to the values stated by Zhang et al. (2008). A difference in the photon fields would also directly change the IC spectrum of the model and could account for the deviations between the model and the data. If one assumes a larger contribution of the CMB target photons for the overall spectrum (relative to the IR and starlight component), then the index of the model IC spectrum would become greater, and thus closer to the index of H. E. S. S. observations. However, since the energy density of the CMB is well-known and fixed, the overall IC flux of the model spectra would then be even lower than what is shown in Fig. 5.14 and one would need a conversion efficiency of more than one hundred percent for PSR B1509−58.

6 Summary and Conclusions

In the present thesis a detailed study of the pulsar wind nebula (PWN) MSH 15−52 in X-rays and TeV γ-rays is introduced. This study encompasses the first analysis of observations of the *XMM-Newton* satellite on MSH 15−52 in the X-ray energy range. For very high-energy γ-rays, the most sensitive analysis of MSH 15−52 so far was carried out, using data taken with the H. E. S. S. telescope system. Finally, a leptonic model of the PWN was constructed, which allows to investigate the physics of the particles in the outflow. The results of the X-ray analysis were used to constrain the parameters of this model. Using the optimized parameters, the model is able to reproduce the spatial evolution of the spectral characteristics. The model prediction for the flux in the TeV energy range is in the same order of magnitude as the observed flux, the exact shape of the spectrum, however, is not reproduced.

The region known as MSH 15−52 is a rather complex one. It comprises a shell-type supernova remnant that is visible at radio wavelengths, a central pulsar wind nebula that emits nonthermal radiation in a broad energy range and the pulsar PSR B1509−58 for which pulsed emission has been detected in the radio and X-ray bands. With a spin-down luminosity of $\dot{E} = I_{45}\ 1.8 \times 10^{37}\,\mathrm{erg\,s^{-1}}$, PSR B1509−58 is one of the most energetic pulsars known and therefore the region around it has been intensively studied for a long time. The different components of the supernove remnant are most likely associated and lie at a distance of $5.2 \pm 1.4\,\mathrm{kpc}$. The nonthermal emission seen from the different parts of the source is powered by the energy which the pulsar losses via its rotational slowdown.

In Chapter 3 the first analysis of *XMM-Newton* observations of the pulsar wind nebula MSH 15−52 was presented. *XMM-Newton* is an X-ray satellite that was launched in 1999. It measures the X-ray emission from astrophysical sources in the energy range from 0.1 to 10 keV with three telescopes. The data from the most sensitive camera, the EPIC-pn camera, was used for the analysis. The observations were affected by background-flaring and the net exposure time of high-quality data is 11.5 ks. The high sensitivity of *XMM-Newton* allows for a spectral analysis of the source in ring-like regions around the pulsar PSR B1509−58 up to a distance of $300''$. The energy spectra of the individual extraction regions are all well-fit with absorbed power-law spectra. The fitted absorption density is $N_{\mathrm{H}} = (1.15 \pm 0.03) \times 10^{21}\,\mathrm{cm^{-2}}$, which is in good agreement with previous measurements. The index of the power-law spectra steepens from 1.66 ± 0.02 in the innermost region to 2.24 ± 0.28 in the farthest region, while the surface brightness exhibits a decrease by almost three orders of magnitude. The variation of the spectra with increasing distance of the extraction regions from the pulsar was then used to constrain the free parameters of the model introduced in Chapter 5.

The second data analysis part in this thesis covers the analysis of the observations on MSH 15−52 carried out with the H. E. S. S. experiment. H. E. S. S. is an array of four imaging air Cherenkov telescopes that is located in Namibia and has been fully operational since 2004. It measures photons in the energy range of around $0.1 - 100\,\mathrm{TeV}$ with a ground-based, indirect detection technique. Due to the high spin-down power of PSR B1509−58 and the nonthermal emission observed at X-ray energies, the region around MSH 15−52 was one of the first targets of the H. E. S. S. experiment. The detection was announced in 2005 based on 22 hours of observation time (Aharonian et al. 2005b). Since then, the data set has significantly increased and more sensitive analysis methods have been developed. The H. E. S. S. analysis that is presented in Section 4.5 of this thesis uses a total of 179 runs and the data set has a total live time of more than 77 hours. A comparison of two H. E. S. S. analysis methods, the standard Hillas analysis and the new Model++ analysis method, shows, that the latter yields a significance that is about 1.5 times larger. For the further analysis only the Model++ reconstruction method was used. MSH 15−5*2* is one of the brightest sources observed with H. E. S. S. and the signal has a significance of around $60\,\sigma$ above background. The source exhibits an elliptical shape that is extended beyond the point-spread function. The morphology in VHE γ-rays is similar to the one seen at X-ray energies and in the GeV energy range, taking into account the differing angular resolution of the instruments in each energy band. The intrinsic length of a two-dimensional Gaussian fit to the source morphology is 0.12°. The width is 0.08° and the angle between the major axis of the Gaussian and the right ascension axis is 45°. The centroid of the source lies at a position of 228.51° in right ascension and −59.17° in declination. An energy-dependent analysis of the source, in which the events were binned in three separate energy bands, did not show any significant variation in the extension of the source, neither in the profile plots along the axes of the system, nor in the intrinsic dimension of the two-dimensional Gaussian fit. The energy spectrum of the source was first analyzed in the same 0.3°-radius region as in the first H. E. S. S. publication. The enlarged data set allows a more detailed spectral analysis and shows that a simple power law does not yield the best fit to the data anymore. Different spectral shapes are statistically preferred, however it is not possible to discriminate between a broken, curved or exponential-cutoff power-law fit. The measured flux above 1 TeV is compatible within statistical and systematic errors to the previously published flux and lies at $(5.6 \pm 0.4) \times 10^{-12}\,\mathrm{cm}^{-2}\,\mathrm{s}^{-1}$ for the power law with an exponential cutoff at (9.1 ± 2.1) TeV. A fit with a broken power law yields a break energy of $E_\mathrm{B} = (2.3 \pm 0.4)$ TeV and a spectral index that changes from 2.11 ± 0.06 to a value of 2.79 ± 0.12 beyond the break. The spectral index of a simple power-law fit to the data is 2.36 ± 0.03 and thus slightly steeper than the previously published one, but compatible within errors. To investigate the spectral properties in different parts of the source, the γ-rays from sub-regions along the major axis of the system were analyzed. However, no significant variation in the spectral parameters was found. The presented analysis is the most sensitive analysis of MSH 15−5*2* in this energy range up to now. A more detailed analysis of the source will only be possible with the next generation of VHE γ-ray experiments that is currently either under construction (H. E. S. S. phase II) or in the design phase (CTA).

Following the two Chapters on the data analysis in the X-ray and TeV γ-ray energy bands, a model of the nonthermal emission in the inner region of pulsar wind nebulae was introduced. The model goes beyond the current standard approach of one-zone models and treats the dynamics and radiation processes of leptons in an approach that assumes radial symmetry. The whole model rests on two components: the injection spectrum of the leptons at the termination shock of the pulsar wind and the velocity profile of the leptons as they move away from the pulsar. The injection spectrum is assumed to be time-independent and is linked to the parameters of the termination shock, which are typically unknown. As there is usually also no information about the distribution of leptons in the PWN, a power-law distribution is adopted for the velocity profile with the index as a free parameter of the model. In the ideal magnetohydrodynamics approach, which assumes infinite conductivity of the lepton plasma, the magnetic field and the bulk velocity of the particles can then be derived for each distance from the pulsar. The emission spectra were calculated and were added up for those regions that match the analysis regions of the X-ray analysis from Chapter 3. The optimum range of values for the free parameters of the model was then found by scanning the parameter space for three different scenarios. These scenarios are based on the different values of the shock radius of MSH 15−5*2* that were derived in the *Chandra* data analyses of Gaensler et al. (2002) and Yatsu et al. (2009). It shows that the best fit of the model is for a shock radius between 0.225 and 0.5 pc. Our model excludes a shock radius at smaller distances to the pulsar, but we are not able to discriminate between the other two scenarios. The index of the velocity profile has a value in the range of 0.4 − 0.6 and we find a lower limit on the conversion efficiency of $\eta \geq 0.3$. For the magnetization parameter we arrive at a lower limit of 0.005. Based on the optimum parameters we calculated the inverse Compton emission for MSH 15−5*2* predicted by the model. It shows that the model reproduces the right order of magnitude for the flux, but differs in the spectral shape of the emission. This deviation might, for example, be caused by the simplifying assumptions of the model (radial symmetry and ideal MHD) or a difference in the relative strength of the individual components of the IC target photon fields, as discussed in Section 5.9. The model prediction for the spatial variation of the IC spectra in the inner parts of MSH 15−5*2* may be tested with future VHE γ-ray instruments that will have the necessary angular resolution.

In summary, the model describes the nonthermal emission of the inner region of MSH 15−5*2* in the X-ray band. Although there are a number of simplifying assumptions, the model reproduces the change in the spectral index and the surface brightness. The predicted IC flux is in the same order of magnitude as the observed flux, which supports the argument that the IC emission from leptons in the nebular wind is the main component of the observed emission in the TeV energy range. Following the successful modeling of MSH 15−5*2*, the model is currently applied to other pulsar wind nebulae for which a spatially-resolved spectral analysis of the X-ray data is feasible. A diploma thesis and a publication on the analysis and the modeling of G0.9 + 0.1 are currently in preparation (Holler in prep.; Holler et al. in prep.). The study of further PWNe will show, whether the optimum parameters of the model of different PWNe exhibit a coherent behavior and if the prediction of the TeV emission matches the observed flux levels of these sources.

7 Zusammenfassung und Ausblick

In der vorliegenden Dissertation wurde eine detaillierte Studie der Röntgen- und TeV-Gammastrahlung des Pulsarwindnebels (PWN) MSH 15−5*2* vorgestellt. Im Rahmen der Arbeit wurde die erste Analyse der Beobachtungen von MSH 15−5*2* mit dem Röntgensatelliten *XMM-Newton* präsentiert. Im Energiebereich der hochenergetischen Gammastrahlung ermöglichte die Analyse von Beobachtungen mit dem H. E. S. S. Teleskopsystem die bisher präziseste Vermessung dieses Pulsarwindnebels. Um ein besseres Verständnis der physikalischen Prozesse in MSH 15−5*2* zu erlangen, wurde ein theoretisches Modell entwickelt. Dieses Modell beruht auf der Annahme, dass die beobachtete elektromagnetische Strahlung von Leptonen im Pulsarwind emittiert wird. Die freien Parameter des Modells wurden anhand der Ergebnisse der Analyse der Röntgendaten optimiert. Es zeigt sich, dass das Modell die ortsabhängigen spektralen Eigenschaften der Röntgenemission gut beschreiben kann. Die Vorhersage des Modells für den Fluss der hochenergetischen Gammastrahlung ist in der selben Größenordnung wie der mit H. E. S. S. gemessene Fluss, es gibt allerdings Unterschiede im Verlauf der Energiespektren.

Die Region um MSH 15−5*2* besteht aus mehreren Objekten, die sehr wahrscheinlich miteinander assoziiert sind. Im Radiobereich kann man die Struktur eines schalenartigen Supernovaüberrestes erkennen. In dessen Mitte befindet sich der PWN, der über einen weiten Energiebereich hin sichtbar ist. Die gemessene Strahlung des PWN weist ein nichtthermisches Energiespektrum auf. Der Pulsar PSR B1509−58 liegt im Zentrum des PWN und emittiert im Radio- und Röntgenbereich gepulste Strahlung. PSR B1509−58 ist von besonderem Interesse, da er im Vergleich zu anderen Pulsaren sehr viel Energie an seine Umgebung abgibt ($\dot{E} = I_{45}\ 1.8 \times 10^{37}\,\mathrm{erg\,s^{-1}}$). Deshalb wurde diese Region bereits von vielen verschiedenen Instrumenten beobachtet. Die Ergebnisse dieser Beobachtungen lassen darauf schliessen, dass die verschiedenen Komponenten Teil eines Supernovaüberrestes sind, der in einer Entfernung von 5.2 ± 1.4 kpc liegt und dass der Pulsar die Energiequelle für die elektromagnetische Strahlung in den verschiedenen Wellenlängenbereichen ist.

In Kapitel 3 wird die erste Datenanalyse der Beobachtungen des Pulsarwindnebels MSH 15−5*2* mit dem Röntgensatelliten *XMM-Newton* vorgestellt. *XMM-Newton* ist ein Röntgensatellit, der seit 1999 im Weltall ist. Mit den drei Teleskopen an Bord des Satelliten kann die Röntgenstrahlung astrophysikalischer Quellen im Energiebereich von etwa 0.1 bis 10 keV vermessen werden. In der vorliegenden Analyse der Energiespektren wurden die Daten der sensitivsten Kamera des Satelliten, der EPIC-pn Kamera, verwendet. Während der Datennahme gab es eine erhöhte Untergrundrate, weshalb die Dauer der nutzbaren, qualitativ hochwertigen Messzeit bei 11.5 ks liegt. Aufgrund der hohen Sensitivität von *XMM-Newton* konnte eine räumlich aufgelöste Analyse der Spektren um PSR B1509−58 herum durchgeführt werden. Dafür wurden Ring-Regionen verwendet, die bis zu einem Abstand von $300''$ zum Pulsar liegen. Die einzelnen Energiespektren können durch ein absorbiertes Potenzgesetz gut gefittet werden. Dabei zeigt sich, dass die Absorption gut mit bisherigen Messungen übereinstimmt ($N_{\mathrm{H}} = (1.15 \pm 0.03) \times 10^{21}\,\mathrm{cm^{-2}}$). Der Index des Potenzgesetzes hat für den innersten Ring einen Wert von 1.66 ± 0.02 und steigt bis zum äußersten Ring auf einen Wert von 2.24 ± 0.28 an. Die Oberflächenhelligkeit fällt von innen nach außen um fast drei Größenordnungen ab. Anhand der beobachteten spektralen Parameter der Röntgenanalyse wurden die Parameter des Modells, das in Kapitel 5 vorgestellt wurde, optimiert.

Kapitel 4 beinhaltet die Datenanalyse der hochenergetischen Gammastrahlung des PWN MSH 15−5*2*. Die Daten wurden mit dem H. E. S. S. Experiment erfasst. H. E. S. S. ist ein System von abbildenden Cherenkov Teleskopen das in Namibia steht und seit dem Jahr 2004 voll funktionsfähig ist. Mit H. E. S. S. wird die hochenergetische Gammastrahlung im Energiebereich von etwa 100 GeV bis 100 TeV gemessen. Eine direkte Messung dieser Strahlung ist mit Satelliten aufgrund des niedrigen Flusses nicht sinnvoll möglich. Daher verwendet H. E. S. S. eine bodengebundene, indirekte Messmethode. Die Region um MSH 15−5*2* war eines der ersten Beobachtungsziele für das H. E. S. S. Experiment, da der Pulsar PSR B1509−58 sehr hochenergetisch ist und im Röntgenbereich bereits nichtthermische Strahlung des PWN detektiert worden war. Die Entdeckung von hochenergetischer Gammastrahlung von MSH 15−5*2* wurde 2005 bekannt gegeben (Aharonian et al. 2005b). Die Analyse in dieser Veröffentlichung basierte auf 22 Stunden Beobachtungsdaten. Seitdem wurde die Quelle weiter beobachtet und effektivere Analysemethoden entwickelt. Die H. E. S. S. Datenanalyse, die in Abschnitt 4.5 dieser Arbeit präsentiert wird, beinhaltet einen Datensatz aus 179 Beobachtungseinheiten mit jeweils 28 Minuten Dauer. Insgesamt ergibt sich daraus eine effektive Beobachtungszeit von mehr als 77 Stunden. Ein Vergleich zweier H. E. S. S. Analysemethoden, der standardmäßigen Hillas Analyse und der neueren Model++ Analyse, zeigt, dass die neue Methode etwa um einen Faktor 1.5 sensitiver ist. Die weitere Analyse wurde daher ausschließlich mit der Model++ Analyse durchgeführt.

MSH 15−5*2* ist eine der hellsten Quellen im Energiebereich von H. E. S. S. und hat eine Signifikanz von mehr als $60\,\sigma$ über dem Untergrund. Die Quelle hat eine elliptische Form und ist deutlich ausgedehnter als die PSF des Teleskopsystems. Die Morphologie zeigt im Vergleich zwischen Röntgen- und Gammastrahlung eine gute Übereinstimmung, wenn man die unterschiedliche Auflösung der Instrumente in den verschiedenen Energiebereichen berücksichtigt. Die Parameter der Quellmorphologie wurden durch einen Fit einer zweidimensionalen Gauß-Funktion bestimmt. Die Position liegt demnach bei einer Rektaszension von 228.51° und einer Deklination von −59.17°. Die intrinsische Länge der Quelle beträgt 0.12° und ihre Breite 0.08°. Der Winkel zwischen der Hauptachse und der Rektaszensions-Achse liegt bei 45°. Um die spektralen Eigenschaften der Quelle zu untersuchen wurde eine Analyse durchgeführt, bei der die Gammastrahlung in drei unterschiedliche Energiebereiche eingeteilt wurde. Eine signifikante Änderung der Morphologie in den verschiedenen Energiebereichen war jedoch nicht messbar. Auch in den Quellprofilen entlang der beiden Hauptachsen des Systems waren keine Unterschiede bei verschiedenen Energien erkennbar. Das Energiespektrum von MSH 15−5*2* wurde zuerst in einer Region mit einem Radius von 0.3° analysiert, welche auch in der ersten H. E. S. S. Publikation zu dieser Quelle verwendet wurde. Der größere Datensatz ermöglichte nun eine genauere Analyse des Energiespektrums und es zeigte sich, dass eine signifikante Abweichung der Spektren von einem reinen Potenzgesetz zu beobachten ist. Fit-Funktionen verschiedener Art wurden an die Daten angepasst, aber eine Unterscheidung zwischen einem gekrümmten Potenzgesetz, einem gebrochenen Potenzgesetz oder einem Potenzgesetz mit einer exponentiellen Abschwächung ist nicht signifikant möglich. Der gemessene Fluss oberhalb einer Energie von 1 TeV liegt innerhalb der statistischen und systematischen Fehler der veröffentlichten Messung, die auf dem kleineren Datensatz basierte. Für ein Potenzgesetz mit exponentieller Abschwächung liegt der Fluss bei $(5.6 \pm 0.4) \times 10^{-12}\,\mathrm{cm}^{-2}\,\mathrm{s}^{-1}$ und die Cutoff-Energie bei (9.1 ± 2.1) TeV. Im Fall des gebrochenen Potenzgesetzes liegt der Übergang zwischen den beiden Potenzgesetzen bei einer Energie von $E_\mathrm{B} = (2.4 \pm 0.4)$ TeV. Der Index verändert sich dabei von 2.11 ± 0.06 auf einen Wert von 2.79 ± 0.12. Der beste Fit mit einem reinen Potenzgesetz hat einen Index von 2.36 ± 0.03 und ist damit etwas höher als der Wert aus der alten Veröffentlichung, allerdings noch im Rahmen der systematischen Fehler. In einer weiteren Analyse wurden Spektren aus verschiedenen Unterregionen der Quelle extrahiert. Diese Regionen wurden entlang der Hauptachse des Systems definiert. Eine signifikante Variation der spektralen Parameter in den verschiedenen Teilregionen ist jedoch nicht nachweisbar. Die im Rahmen dieser Arbeit präsentierte Analyse ist die bis dato genaueste Vermessung der hochenergetischen Gammastrahlung von MSH 15−5*2*. Die noch offenen Fragen zu den Eigenschaften der Quelle werden erst mit der nächsten Generation von abbildenden Cherenkov Teleskopen, die derzeit entweder im Bau (H. E. S. S. Phase II) oder in Entwicklung (CTA) sind, genauer untersucht werden können.

Im Anschluß an die beiden Kapitel über die Datenanalyse im Röntgen- und TeV-Bereich wurde ein neuentwickeltes Modell vorgestellt, das der Beschreibung der nichtthermischen Strahlung aus dem inneren Bereich des PWN dient. Im Gegensatz zu den derzeitig üblichen Modellen, in denen der gesamte PWN räumlich und zeitlich gemittelt betrachtet wird, simuliert das Modell auch die räumliche Verteilung und die Emission der Leptonen im Pulsarwind in einem radialsymmetrischen Ansatz. Das Modell wird durch zwei Komponenten bestimmt. Zum einem durch das Injektionsspektrum der Leptonen am Schock des Pulsarwindes, zum anderen durch das Geschwindigkeitsprofil der Leptonen das eine radiale Abhängigkeit vom Abstand zum Pulsar hat. In unserem Modell wird ein zeitunabhängiges Injektionsspektrum angenommen, das von den, üblicherweise unbekannten, Parametern des Schocks abhängt. Da es typischerweise auch keinen Einblick in die Verteilung der Leptonen innerhalb des PWN gibt, wurde für das Geschwindigkeitsprofil ein Potenzgesetz angenommen, dessen Index ein freier Modellparameter ist. Unter der Annahme idealer Magnetohydrodynamik, in der das Lepton-Plasma eine unendliche Leitfähigkeit besitzt, kann für jeden Punkt innerhalb des PWN das Magnetfeld und die Geschwindigkeit der Leptonen bestimmt werden. Dadurch ist es auch möglich die Emissionsspektren zu berechnen, für die die Synchrotronstrahlung und die Strahlung auf Grund des inversen Compton-Effekts der Leptonen mit den Hintergrundphotonen die wesentliche Rolle spielen. Für die Optimierung in Kapitel 5 wurden die Emissionsspektren so aufsummiert, dass ein Vergleich mit den gemessenen Spektren im Röntgenbereich (Kapitel 3) möglich ist. Die freien Modellparametern wurden anschließend anhand der Messdaten optimiert. Dazu wurden drei Szenarien anhand unterschiedlicher Werte für den Schockradius definiert. Diese wurden anhand einer Analyse von Daten des *Chandra* Röntgensatelliten von Gaensler et al. (2002) und Yatsu et al. (2009) bestimmt. Die Ergebnisse der Optimierung zeigen, dass das Modell für die Szenarien mit einem Schockradius von 0.225 pc (Szenario III) und 0.5 pc (Szenario II) am besten zu den gemessenen Daten passt. Ein kleinerer Schockradius (Szenario I) wird durch die Ergebnisse der Modellierung ausgeschlossen, allerdings ist eine Entscheidung zwischen Szenario II und III nicht möglich. Der Index des Geschwindigkeitsprofils liegt im Bereich von 0.4 bis 0.6, die untere Schwelle für die Effizienz der Umwandlung von Rotationsenergie des Pulsars in die Energie der Leptonen im Pulsarwind liegt bei $\eta \geq 0.3$. Für den Magnetisierungsparameter σ wurde eine untere Schwelle von 0.005 bestimmt. Mit den optimierten Parametern wurde dann die Strahlung von MSH 15−5*2* aufgrund des inversen Compton-Effekts der Leptonen mit den Hintergrundphotonen berechnet. Der berechnete Fluss liegt in der gleichen Größenordnung wie der mit H. E. S. S. gemessene Fluss. Allerdings gibt es Unterschiede in der Form des Spektrums. Diese Unterschiede können sich zum einen durch die vereinfachenden Annahmen des Modells (radiale Symmetrie und ideale Magnetohydroydynamik) ergeben. Andererseits könnten auch andere Photonfelder die Abweichungen in den vorhergesagten IC-Spektren erklären, wie in Abschnitt 5.9 diskutiert. Die Vorhersage für die räumliche Variation des IC-Spektrums im inneren Bereich des PWN kann mit den derzeitigen Instrumenten nicht überprüft werden, zukünftige Experimente wie zum Beispiel CTA werden aber die nötige Winkelauflösung dafür haben.

Zusammenfassend lässt sich sagen, dass das Modell die nichtthermische Emission der inneren Region des PWN MSH 15−5*2* im Röntgenbereich gut beschreibt. Obwohl in dieser Modellierung einige vereinfachende Annahmen stecken, wird der Verlauf der Indices der Röntgenspektren und der Verlauf der Oberflächenhelligkeit treffend beschrieben. Die Vorhersage für den IC-Fluss liegt in der gleichen Größenordnung wie der gemessene Fluss. Damit liefert die Modellierung ein weiteres Indiz dafür, dass die hochenergetische Gammastrahlung des PWN MSH 15−5*2* durch den inversen Compton-Effekt der Leptonen mit den Hintergrundphotonen erklärt werden kann und dass dies der wesentliche Prozess für die beobachtete TeV-Strahlung in Pulsarwindnebeln ist. Nach der erfolgreichen Modellierung von MSH 15−5*2* wird das Modell derzeit auf andere PWN angewandt, für die es im Röntgenbereich die Möglichkeit der ortsaufgelösten Spektroskopie gibt. Eine Diplomarbeit und eine Veröffentlichung über die Röntgenanalyse und Modellierung des PWN G0.9+0.1 sind derzeit in Bearbeitung (Holler in prep.; Holler et al. in prep.). Die Untersuchung weiterer Pulsarwindnebel wird zeigen, ob die optimalen Parameter des Modells im gleichen Bereich liegen und ob sich die Modell-Vorhersagen für die Gammastrahlungs-Flüsse dieser Quellen als zutreffend erweisen.

List of Figures

List of Tables

Bibliography

Abdo, A. A., Ackermann, M., Ajello, M., et al. 2010a, ApJS, 188, 405

Abdo, A. A., Ackermann, M., Ajello, M., et al. 2010b, ApJ, 714, 927

Abdo, A. A., Ackermann, M., Ajello, M., et al. 2009, ApJS, 183, 46

Aharonian, F., Akhperjanian, A. G., Aye, K., et al. 2005a, Science, 307, 1938

Aharonian, F., Akhperjanian, A. G., Aye, K., et al. 2004, Astroparticle Physics, 22, 109

Aharonian, F., Akhperjanian, A. G., Aye, K.-M., et al. 2005b, A&A, 435, L17

Aharonian, F., Akhperjanian, A. G., Bazer-Bachi, A. R., et al. 2006a, A&A, 457, 899

Aharonian, F., Akhperjanian, A. G., Bazer-Bachi, A. R., et al. 2006b, ApJ, 636, 777

Aharonian, F., Buckley, J., Kifune, T., & Sinnis, G. 2008, Reports on Progress in Physics, 71, 096901

Aharonian, F. A. 2004, Very high energy cosmic gamma radiation : a crucial window on the extreme Universe, ed. Aharonian, F. A.

Aharonian, F. A. & Bogovalov, S. V. 2003, New Astronomy, 8, 85

Albert, J., Aliu, E., Anderhub, H., et al. 2008, ApJ, 674, 1037

Amato, E. & Arons, J. 2006, ApJ, 653, 325

Arnaud, K. A. 1996, in Astronomical Society of the Pacific Conference Series, Vol. 101, Astronomical Data Analysis Software and Systems V, ed. G. H. Jacoby & J. Barnes, 17

Arons, J. 2002, in Astronomical Society of the Pacific Conference Series, Vol. 271, Neutron Stars in Supernova Remnants, ed. P. O. Slane & B. M. Gaensler, 71

Baade, W. & Zwicky, F. 1934, Proceedings of the National Academy of Science, 20, 254

Bamba, A., Mori, K., & Shibata, S. 2010, ApJ, 709, 507

Bednarek, W. & Bartosik, M. 2003, A&A, 405, 689

Berge, D. 2006, Dissertation, Ruprecht-Karls-Universität, Heidelberg, Germany

Berge, D., Funk, S., & Hinton, J. 2007, A&A, 466, 1219

Bernlöhr, K. 2000, Astroparticle Physics, 12, 255

Bernlöhr, K. 2010, Monte-Carlo Images of Air Showers, Website, `http://www.mpi-hd.mpg.de/hfm/~bernlohr/HESS/MC_images/`

Blackburn, J. K. 1995, in Astronomical Society of the Pacific Conference Series, Vol. 77, Astronomical Data Analysis Software and Systems IV, ed. R. A. Shaw, H. E. Payne, & J. J. E. Hayes, 367

Blumenthal, G. R. & Gould, R. J. 1970, Reviews of Modern Physics, 42, 237

Braun, I., Bolz, O., van Eldik, C., et al. 2008, Journal of Physics Conference Series, 110, 062003

Camilo, F., Kaspi, V. M., Lyne, A. G., et al. 2000, ApJ, 541, 367

Caraveo, P. A., Mereghetti, S., & Bignami, G. F. 1994, ApJ, 423, L125

Caswell, J. L., Milne, D. K., & Wellington, K. J. 1981, MNRAS, 195, 89

Chaves, R. C. G., H. E. S. S. Collaboration, Aharonian, F., Akhperjanian, A. G., & et al. 2009, in Proceedings of the International Cosmic Ray Conference

Chevalier, R. A. 1977, in Astrophysics and Space Science Library, Vol. 66, Supernovae, ed. D. N. Schramm, 53

Chevalier, R. A. 1998, Memorie della Societa Astronomica Italiana, 69, 977

Clark, D. H. & Caswell, J. L. 1976, MNRAS, 174, 267

Daugherty, J. K. & Harding, A. K. 1982, ApJ, 252, 337

Daum, A., Hermann, G., Hess, M., et al. 1997, Astroparticle Physics, 8, 1

de Jager, O. C. 2005, in American Institute of Physics Conference Series, Vol. 801, Astrophysical Sources of High Energy Particles and Radiation, ed. T. Bulik, B. Rudak, & G. Madejski, 298–303

de Jager, O. C. & Djannati-Ataï, A. 2009, Neutron Stars and Pulsars, ASSL 357, Springer, ed. Becker, W., 451

de Jager, O. C. & Harding, A. K. 1992, ApJ, 396, 161

de Jager, O. C., Harding, A. K., Michelson, P. F., et al. 1996, ApJ, 457, 253

de Naurois, M. 2005, in Proc. Conf. Towards a Network of Atmospheric Cherenkov Detectors VII

de Naurois, M. 2010, Internal Documentation, Website

de Naurois, M., Aharonian, F., & Akhperjanian, A. G. H. 2003, in International Cosmic Ray Conference, Vol. 5, Proceedings of the International Cosmic Ray Conference, 2907

de Naurois, M. & Rolland, L. 2009, Astroparticle Physics, 32, 231

DeLaney, T., Gaensler, B. M., Arons, J., & Pivovaroff, M. J. 2006, ApJ, 640, 929

Drake, S. A. 2007, How Many Known X-Ray (and Other) Sources Are There?, Website, `http://heasarc.gsfc.nasa.gov/docs/heasarc/headates/how_many_xray.html`

Du Plessis, I., de Jager, O. C., Buchner, S., et al. 1995, ApJ, 453, 746

Dubner, G. M., Gaensler, B. M., Giacani, E. B., Goss, W. M., & Green, A. J. 2002, AJ, 123, 337

Fermi, E. 1949, Physical Review, 75, 1169

Forot, M., Hermsen, W., Renaud, M., et al. 2006, ApJ, 651, L45

Funk, S. 2005, Dissertation, Ruprecht-Karls-Universität, Heidelberg, Germany

Gaensler, B. M., Arons, J., Kaspi, V. M., et al. 2002, ApJ, 569, 878

Gaensler, B. M., Brazier, K. T. S., Manchester, R. N., Johnston, S., & Green, A. J. 1999, MNRAS, 305, 724

Gaensler, B. M. & Slane, P. O. 2006, ARA&A, 44, 17

Goebel, F., MAGIC Collaboration, Albert, J., et al. 2009, in International Cosmic Ray Conference, Vol. 3, Proceedings of the International Cosmic Ray Conference, 1485–1488

Gold, T. 1968, Nature, 218, 731

Goldreich, P. & Julian, W. H. 1969, ApJ, 157, 869

Harding, A. K. & Gaisser, T. K. 1990, ApJ, 358, 561

Haslam, C. G. T., Salter, C. J., Stoffel, H., & Wilson, W. E. 1982, A&AS, 47, 1

Heinz, S. 2008, Diploma thesis, Friedrich-Alexander-Universität, Erlangen, Germany

Heitler, W. 1954, Quantum theory of radiation, ed. Heitler, W.

HESS Collaboration, Abramowski, A., Acero, F., et al. in prep., in preparation

Hewish, A., Bell, S. J., Pilkington, J. D. H., Scott, P. F., & Collins, R. A. 1968, Nature, 217, 709

Hillas, A. M. 1985, in International Cosmic Ray Conference, Vol. 3, Proceedings of the International Cosmic Ray Conference, ed. F. C. Jones, 445–448

Hinton, J. A. & Hofmann, W. 2009, ARA&A, 47, 523

Hirotani, K. 2008, ApJ, 688, L25

Hofmann, W., Jung, I., Konopelko, A., et al. 1999, Astroparticle Physics, 12, 135

Holder, J., Acciari, V. A., Aliu, E., et al. 2008, in American Institute of Physics Conference Series, Vol. 1085, American Institute of Physics Conference Series, ed. F. A. Aharonian, W. Hofmann, & F. Rieger, 657–660

Holler, M. in prep., Diploma thesis, Friedrich-Alexander-Universität, Erlangen, Germany

Holler, M., Eger, P., Kiessling, D., Schöck, F. M., & Stegmann, C. in prep., in preparation

Hoppe, S. 2008, in International Cosmic Ray Conference, Vol. 2, International Cosmic Ray Conference, 579–582

Hupfer, M. 2008, Diploma thesis, Friedrich-Alexander-Universität, Erlangen, Germany

Jackson, J. D. 1998, Classical Electrodynamics, 3rd Edition, ed. Jackson, J. D.

Jansen, F., Lumb, D., Altieri, B., et al. 2001, A&A, 365, L1

Jansky, K. G. 1933, Nature, 132, 66

Kaplan, D. L. & Moon, D. 2006, ApJ, 644, 1056

Kaspi, V. M., Manchester, R. N., Siegman, B., Johnston, S., & Lyne, A. G. 1994, ApJ, 422, L83

Kawai, N., Okayasu, R., Brinkmann, W., et al. 1991, ApJ, 383, L65

Kennel, C. F. & Coroniti, F. V. 1984a, ApJ, 283, 694

Kennel, C. F. & Coroniti, F. V. 1984b, ApJ, 283, 710

Kirk, J. G., Lyubarsky, Y., & Petri, J. 2009, in Astrophysics and Space Science Library, Vol. 357, Astrophysics and Space Science Library, ed. W. Becker, 421

Klein, O. & Nishina, T. 1929, Zeitschrift fur Physik, 52, 853

Kramer, M., Lyne, A. G., Hobbs, G., et al. 2003, ApJ, 593, L31

Kuiper, L., Hermsen, W., Krijger, J. M., et al. 1999, A&A, 351, 119

Lattimer, J. M. & Prakash, M. 2001, ApJ, 550, 426

Le Bohec, S., Degrange, B., Punch, M., et al. 1998, Nuclear Instruments and Methods in Physics Research A, 416, 425

Li, T. & Ma, Y. 1983, ApJ, 272, 317

Livingstone, M. A., Kaspi, V. M., Gavriil, F. P., & Manchester, R. N. 2005, ApJ, 619, 1046

Longair, M. S. 2004a, High energy astrophysics. Vol.1: Particles, photons and their detection, ed. Longair, M. S.

Longair, M. S. 2004b, High energy astrophysics. Vol.2: Stars, the galaxy and the interstellar medium, ed. Longair, M. S.

Lorimer, D. R. & Kramer, M. 2005, Handbook of Pulsar Astronomy, ed. Lorimer, D. R. and Kramer, M.

Lyne, A. G. & Graham-Smith, F. 2006, Pulsar Astronomy, ed. Lyne, A. G. & Graham-Smith, F.

Lyne, A. G., Pritchard, R. S., & Graham-Smith, F. 1993, MNRAS, 265, 1003

Lyne, A. G., Pritchard, R. S., Graham-Smith, F., & Camilo, F. 1996, Nature, 381, 497

Manchester, R. N., Hobbs, G. B., Teoh, A., & Hobbs, M. 2005, VizieR Online Data Catalog, 7245

Manchester, R. N., Tuohy, I. R., & Damico, N. 1982, ApJ, 262, L31

Mangano, V., Massaro, E., Bocchino, F., Mineo, T., & Cusumano, G. 2005, A&A, 436, 917

Mills, B. Y., Slee, O. B., & Hill, E. R. 1961, Australian Journal of Physics, 14, 497

Mineo, T., Cusumano, G., Maccarone, M. C., et al. 2001, A&A, 380, 695

Muslimov, A. G. & Harding, A. K. 2004, ApJ, 606, 1143

Ng, C. & Romani, R. W. 2004, ApJ, 601, 479

Nowak, T. 2008, Diploma thesis, Friedrich-Alexander-Universität, Erlangen, Germany

Otte, N., VERITAS collaboration, Holder, J., et al. 2009, in Proceedings of the International Cosmic Ray Conference

Pacini, F. 1967, Nature, 216, 567

Particle Data Group, Amsler, C., Doser, M., et al. 2008, Physics Letters B, 667, 1

Pétri, J. & Lyubarsky, Y. 2007, A&A, 473, 683

Punch, M., H.E.S.S. Collaboration, Aharonian, F., Akhperjanian, A. G., & et al. 2005, in Proc. Conf. Towards a Network of Atmospheric Cherenkov Detectors VII

Rees, M. J. & Gunn, J. E. 1974, MNRAS, 167, 1

Reynolds, S. P. 2008, ARA&A, 46, 89

Reynolds, S. P. & Chevalier, R. A. 1984, ApJ, 278, 630

Rybicki, G. B. & Lightman, A. P. 1979, Radiative processes in astrophysics, ed. Rybicki, G. B. & Lightman, A. P.

Sako, T., Matsubara, Y., Muraki, Y., et al. 2000, ApJ, 537, 422

Schöck, F. M., Büsching, I., de Jager, O. C., et al. 2009, in Proceedings of the International Cosmic Ray Conference

Schöck, F. M., Büsching, I., de Jager, O. C., Eger, P., & Vorster, M. J. 2010, A&A, 515, A109

Sefako, R. R. & de Jager, O. C. 2003, ApJ, 593, 1013

Seward, F. D. & Harnden, Jr., F. R. 1982, ApJ, 256, L45

Seward, F. D., Harnden, Jr., F. R., Murdin, P., & Clark, D. H. 1983, ApJ, 267, 698

Staelin, D. H. & Reifenstein, III, E. C. 1968, Science, 162, 1481

Strüder, L., Briel, U., Dennerl, K., et al. 2001, A&A, 365, L18

Tamura, K., Kawai, N., Yoshida, A., & Brinkmann, W. 1996, PASJ, 48, L33

Tanimori, T., Sakurazawa, K., Dazeley, S. A., et al. 1998, ApJ, 492, L33

Truemper, J., Pietsch, W., Reppin, C., et al. 1978, ApJ, 219, L105

Trussoni, E., Massaglia, S., Caucino, S., Brinkmann, W., & Aschenbach, B. 1996, A&A, 306, 581

Turner, M. J. L., Abbey, A., Arnaud, M., et al. 2001, A&A, 365, L27

van der Swaluw, E. & Wu, Y. 2001, ApJ, 555, L49

Venter, C. & de Jager, O. C. 2007, in Proceedings of the 363. WE-Heraeus Seminar on Neutron Stars and Pulsars 40 years after the discovery. Edited by W. Becker and H. H. Huang. MPE-Report 291. ISSN 0178-0719. Published by the Max Planck Institut für extraterrestrische Physik, Garching bei München, Germany, 2007., p.40, ed. W. Becker & H. H. Huang, 40

Vincent, P., Denanca, J., Huppert, J., et al. 2003, in International Cosmic Ray Conference, Vol. 5, Proceedings of the International Cosmic Ray Conference, 2887

Vorster, M. J. 2009, Master thesis, North-West University, Potchefstroom, South Africa

Vorster, M. J., de Jager, O. C., Büsching, I., & Schöck, F. M. 2009, in Proceedings of the International Cosmic Ray Conference

Wagner, R. M., Lindfors, E. J., Sillanpää, A., et al. 2009, in Proceedings of the 2009 Fermi Symposium

Wagner, S. J. & Seifert, W. 2000, in Astronomical Society of the Pacific Conference Series, Vol. 202, IAU Colloq. 177: Pulsar Astronomy - 2000 and Beyond, ed. M. Kramer, N. Wex, & R. Wielebinski, 315

Wakely, S. & Horan, D. 2010, TeVCat - Online Gamma-Ray Catalog, Website, `http://tevcat.uchicago.edu/`

Weekes, T. C., Cawley, M. F., Fegan, D. J., et al. 1989, ApJ, 342, 379

Weiler, K. W. & Panagia, N. 1978, A&A, 70, 419

Whiteoak, J. B. Z. & Green, A. J. 1996, A&AS, 118, 329

Wilms, J., Allen, A., & McCray, R. 2000, ApJ, 542, 914

Wolter, H. 1952, Annalen der Physik, 445, 94

Yatsu, Y., Kawai, N., Shibata, S., & Brinkmann, W. 2009, PASJ, 61, 129

Zhang, L., Chen, S. B., & Fang, J. 2008, ApJ, 676, 1210

Zombeck, M. V. 2010, Designations of Astronomical Catalogs, Website, `http://www.astrohandbook.com/ch19/catalog_desig.pdf`

Acknowledgement/Danksagung

"Ich sage nur ein Wort: Vielen Dank!"

Horst Hrubesch

An dieser Stelle möchte ich mich bei einigen Personen bedanken, die einen wesentlichen Beitrag zum Gelingen dieser Arbeit geleistet haben.

Zuerst möchte ich mich bei meinem Doktorvater, Prof. Christian Stegmann, für die Möglichkeit zur Promotion in seiner Arbeitsgruppe und die gewährten Freiräume bei der wissenschaftlichen Arbeit bedanken. Die Gespräche und Diskussionen waren stets sehr hilfreich und es hat mir großen Spaß gemacht, beim Aufbau der Erlanger H. E. S. S. Gruppe mitzuwirken.

Bedanken möchte ich mich auch bei allen derzeitigen (und ehemaligen) Kollegen aus der Erlanger H. E. S. S. Gruppe. Die Liste der Namen ist lang, aber trotzdem möchte ich mich bei Arnim, Bernhard, Daniel, Kathrin, Ira, Markus, Michi, und Sebastian nochmal besonders für die gute Zusammenarbeit, Hilfe in Computer-Fragen und das Korrekturlesen der Arbeit bedanken. Hervorheben möchte ich auch unseren "in-house astronomer" Peter, ohne den die *XMM-Newton* Analyse in dieser Form nicht möglich gewesen wäre und der auch auf den Kollaborationstreffen stets interessante Beiträge lieferte.

Nicht nur in der H. E. S. S. Gruppe, sondern auch im gesamten ECAP war die Arbeitsatmosphäre immer sehr gut. Deswegen auch ein herzlicher Dank an die Kollegen von Acoustics, Antares, KM3NeT und Co., besonders an die langjährigen Computer-Admins Claudio, Max und Ralf.

Mein Aufenthalt an der NWU in Potchefstroom in Südafrika war aus fachlicher und menschlicher Hinsicht sehr bereichernd. Deshalb bedanke ich mich bei Prof. Okkie de Jager, Ingo Büsching, Michael Vorster und den anderen Kollegen von der NWU für die gute Zusammenarbeit und die tolle Gastfreundschaft während meiner Zeit dort. Baie dankie vir alles!

Ohne die Unterstützung meiner Familie wäre weder mein Studium noch meine Doktorarbeit möglich gewesen. Vielen Dank für den bedingungslosen, fortwährenden Rückhalt den ich immer genießen durfte und der mich stets bestärkt hat.

Den größten Beitrag zum Gelingen dieser Arbeit hat mit Sicherheit meine Frau geleistet. Sie hat es auch in schwierigen Phasen immer geschafft mich aufzubauen, auch wenn Sie sich manchmal wie Rudi Völler gefühlt haben muss ("Ein Tiefpunkt und nochmal ein Tiefpunkt. Da gibt's nochmal einen niedrigeren Tiefpunkt. Ich kann diesen ganzen S..... nicht mehr hören."). Vielen Dank!